

Diss. ETH No. 20835

# On-Machine Wire Electrical Discharge Dressing of Metal Bonded Grinding Wheels

A dissertation submitted to  
ETH ZURICH

for the degree of  
Doctor of Sciences

presented by  
Eduardo Weingärtner  
M. Eng. Mec. UFSC

Date of birth  
08<sup>th</sup> January 1978

citizen of  
Brazil

accepted on the recommendation of

Prof. Dr.-Ing. Konrad Wegener

Dr. sc. techn. Friedrich Kuster

Dipl. El. Ing. ETH Marco Boccadoro

2013



# Acknowledgements

This thesis was developed during my tenure as a scientific research assistant at the Institute of Machine Tools and Manufacturing (IWF) at the Swiss Federal Institute of Technology (ETH) Zurich. It is the result of intense work with contribution from numerous individuals.

Primarily, I would like to express my gratefulness to my supervisor, Prof. Dr.-Ing. Konrad Wegener, for his guidance, inspiration and encouragement to reach my goals. Throughout the course of my thesis I was challenged and motivated by his inquiries, which were not always easy but have certainly contributed to make my work more consistent and innovative. I also want to thank him in his position as the director of the IWF, for having given me the valuable opportunity to work at this world-accredited research institute.

My thesis has also significantly benefited from the co-direction of Dr. Fredy Kuster and Mr. Marco Boccadoro. To Fredy, Chief Engineer and Research Coordinator at IWF, special thanks for his advice, support and cheer throughout the course of my work. Fredy has always been willing to help and support colleagues and students, and I am grateful for his technical advice and for the exciting moments of brainstorming ideas. My gratitude also to Mr. Marco Boccadoro, head of EDM Research and Innovation at GF AgieCharmilles, for his availability and accessibility in co-supervising the development of my work. His valuable knowledge was an asset and indispensable to develop a grounded understanding of various technical contents I dealt with in my study, especially the ones related to electrical discharge machining.

In 2010, I was fortunate to be nominated Research Affiliate of the International Academy for Production Engineering – CIRP, and I thank Dr. Wolfgang Knapp, head of Metrology Division at IWF and CIRP fellow, for this nomination. The numerous CIRP-related events were occasions of learning and sharing knowledge with peers and I thank Dr. Wolfgang Knapp and also IWF support for this opportunity.

Special moments of learning, mutual support and playfulness were shared with Fabio Wagner Pinto, Jérémie Monnin, Mohammad Rabiey, Adam Gontarz, Nikolas Schaal, Raoul Roth, Ricardo Knoblauch and Umang Maradia, colleagues with whom I shared my office during the years at IWF and I had the pleasure to become friends. A special thanks to my friend Fabio for his ‘hand’ in the early stages of my doctoral studies.

Other IWF colleagues from whom I appreciate the inputs and contributions to my work are Guilherme Vargas, Angelo Boeira, Rolf Schroeter, Carl Wyen, Sebastian Buhl, Claus Dold, Christian Walter, Michael Gull, Josef Meile, Albert Weber, Sandro Wigger, Sherline Wunder, Martin Suter, Thomas Liebrich, Jens Boos, Josef Mayr, Josef Stirnimann, Robert Transchel and Silvio Burg.

Among several research activities undertaken at IWF, I had the opportunity to take the lead in two CTI projects which focused on topics related to my thesis. I want to express my sincere thanks and appreciation to all project team members who actively participate in these challenging projects: Dr. Fiebelkorn, Mr. Klotz and Mr. Stüssi from Fritz Studer AG; Mr. Boccadoro, Mr. Baumeler, Mr. Tobler and Mr. Wehrli from GF AgieCharmilles; Mr. Gilomen from Diametal AG; Mr. Eglin and Mrs. Fischer from Blaser Swissslube; Mr. Weikert from CeramTec AG; and Mr. Sascha Jaumann from inspire AG. Special thanks to Sascha, for his great job in designing the first wire electrical discharge dressing unit for these projects.

I would like to express my appreciation to the Commission for Technology and Innovation - CTI and all aforementioned project partners, without whose generous financial support this work could not have been realized.

Special thanks to Prof. Walter L. Weingaertner, who has directly and indirectly contributed to my work. From the outset, Prof. Weingaertner played a supportive role in the choices that have defined the course of my career, since the time as graduate and master student at the Federal University of Santa Catarina in Brazil until the decision to undertake my doctoral studies at ETH in Switzerland. I greatly thank prof. Weingaertner for his advice and for sharing his cutting-edge knowledge on machining processes.

To my family, my parents Valmor and Sonia, my sister Andrea and my brother Gustavo, an enormous thank for all their love and unconditional support. The distance may have made contacts less frequent but never less intensive. It is rewarding to know that I can count on you and I am extremely grateful for that.

One last and very meaningful word to thank Fernanda Lonardoni, the woman, partner and friend I have had on my side. I have counted on her strength, determination and support and I am proud of what we have gone through and built together all along these years, in the pursuit of mutual and individual goals. This thesis is one important achievement of this trajectory.

# Contents

<b>Symbols and Acronyms .....</b>	<b>viii</b>
<b>Abstract.....</b>	<b>xiii</b>
<b>Kurzfassung .....</b>	<b>xiv</b>
<b>1. Introduction.....</b>	<b>1</b>
<b>2. State of the art .....</b>	<b>3</b>
2.1 Grinding wheel wear .....	3
2.2 Grinding wheel conditioning .....	5
2.3 Metal bonded diamond wheels .....	7
2.4 Conditioning of metal bonded diamond wheels.....	11
2.4.1 Mechanical conditioning methods.....	12
2.4.2 Laser beam dressing.....	15
2.4.3 Electro chemical dressing .....	16
2.4.4 Electrical discharge dressing.....	18
2.4.5 Electro chemical discharge dressing.....	25
2.4.6 On-machine dressing .....	26
2.5 EDM modeling.....	29
<b>3. Problem description and objectives .....</b>	<b>35</b>
<b>4. Conventional versus WED-dressing .....</b>	<b>37</b>
4.1 Materials, equipment and methods.....	37
4.1.1 Metal bonded diamond wheels .....	37

4.1.2	Conventional dressing .....	38
4.1.3	Electrical discharge dressing.....	38
4.1.4	Equipment for on-machine dressing and grinding tests.....	41
4.1.5	Metrology equipment .....	42
4.2	Evaluation of dressing methods.....	43
4.2.1	Grinding wheel topography .....	44
4.2.2	Grinding forces.....	48
4.2.3	Grinding wheel wear .....	52
4.2.4	Workpiece surface quality .....	56
4.2.5	Discharge concentration around diamonds in EDD.....	58
4.2.6	WEDD – Process limitations.....	62
<b>5.</b>	<b>On-machine WED-dressing.....</b>	<b>65</b>
5.1	WEDD with a free stretched wire .....	65
5.2	WEDD with a special wire guide .....	69
5.3	Dressing material removal rate.....	74
5.3.1	MRR in conventional dressing.....	74
5.3.2	MRR in WED-dressing .....	76
5.4	Influence of $v_{fad}$ and $a_{ed}$ on dressing accuracy.....	79
5.5	In-process-dressing .....	83
<b>6.</b>	<b>Modeling and simulation of WEDM .....</b>	<b>90</b>
6.1	WEDM model approach.....	90
6.1.1	Finite-difference method.....	91
6.2	Model inputs.....	95
6.2.1	Discharge duration and pulse interval time .....	95
6.2.2	Discharge current waveform.....	97
6.2.3	Thermophysical properties of workpiece materials.....	99
6.2.4	Latent heat of fusion and vaporization.....	100
6.2.5	Energy distribution and recast layer.....	101
6.3	Single discharge experiments.....	103

Contents	vii
6.3.1 Characterization of eroded craters.....	103
6.3.2 Influence of relative speed on eroded craters.....	105
6.3.3 Plasma expansion.....	109
6.4 Numerical results .....	111
6.4.1 Erosion power factor .....	112
6.4.2 Influence of heat source type.....	112
6.4.3 Thermophysical properties of workpiece materials.....	115
6.4.4 High relative speeds in WEDM .....	119
6.4.5 WED-dressing strategy .....	123
6.4.6 Diamond graphitization.....	126
<b>7. Conclusions and outlook.....</b>	<b>134</b>
7.1 Outlook .....	138
<b>References .....</b>	<b>140</b>

# Symbols and Acronyms

## Latin symbols

$a_{ed}$	$\mu\text{m}$	Depth of dressing cut
$a_{ed,ges}$	$\mu\text{m}$	Total depth of dressing cut
$a_{pd}$	$\mu\text{m}$	Active width of cut
$b_s$	$\text{mm}$	Grinding wheel width
$b_w$	$\text{mm}$	Workpiece width
$c$	$\text{Ns/m}$	Damping coefficient
$c_p$	$\text{J}/(\text{kg}\cdot\text{K})$	Specific heat at constant pressure
$d_c$	$\mu\text{m}$	Crater diameter
$d_e$	$\mu\text{m}$	Equivalent grain diameter
$d_s$	$\text{mm}$	Grinding wheel diameter
$d_w$	$\text{mm}$	Workpiece diameter
$f_a$	$\text{mm}$	Radial feed per grinding wheel revolution
$f_{ad}$	$\text{mm}$	Dressing feed per grinding wheel revolution
$f_e$	$\text{kHz}$	Effective pulse frequency
$f_p$	$\text{kHz}$	Theoretical pulse frequency
$h_c$	$\mu\text{m}$	Crater depth
$k$	$\text{W}/(\text{m}\cdot\text{K})$	Thermal conductivity
$l_w$	$\text{mm}$	Free stretched wire length
$m$	$\text{kg}$	Mass
$m, n, p$	-	Indices in finite difference equations
$n_s$	$\text{rpm}$	Grinding wheel rotational speed
$q_y$	$\text{N}$	External force applied to wire



$q_s$	-	Grinding speed ration
$\dot{q}$	W/m <sup>3</sup>	Rate of energy generation per unit volume
$q''$	W/m <sup>2</sup>	Heat flux
$r_s$	mm	Grinding wheel radius
$t$	s	Time
$t_d$	s	Time per dressing pass
$t_e$	s	Machining cycle time
$t_{er}$	s	Machine idle time
$t_g$	s	Sum of $t_h$ and $t_n$
$t_h$	s	Main production time
$t_n$	s	Non-productive time
$t_o$	μs	Pulse interval time
$t_v$	s	Downtime
$u_e$	V	Discharge voltage
$v_D$	mm/min	Wire run-off speed
$v_f$	mm/min	Grinding radial feed rate
$v_{fad}$	mm/min	Axial dressing feed rate
$v_r$	m/s	Relative speed during single discharge experiments
$v_s$	m/s	Grinding wheel circumferential speed
$v_{sd}$	m/s	Grinding wheel speed during dressing
$v_{s.SiC}$	m/s	SiC-wheel circumferential speed during dressing
$v_w$	m/s	Workpiece rotating speed
$A$	mm <sup>2</sup>	Area
$A_s$	mm <sup>2</sup>	Total grinding wheel wear (edge + radial wear)
$A_{sk}$	mm <sup>2</sup>	Grinding wheel edge wear
$A_{sr}$	mm <sup>2</sup>	Grinding wheel radial wear
$E$	GPa	Young's modulus
$F_c$	-	Erosion power factor
$F_D$	N	Wire pretensioning force
$F'_n$	N/mm	Specific normal force
$F_o$	-	Fourier number
$F'_t$	N/mm	Specific tangential force

G	-	G-ratio (wear ratio)
I	kg·m <sup>2</sup>	Moment of inertia
I <sub>e</sub>	A	Discharge current
I <sub>peak</sub>	A	Discharge peak current
L	kJ/kg	Latent heat
L <sub>f</sub>	kJ/kg	Latent heat of fusion
L <sub>v</sub>	kJ/kg	Latent heat vaporization
P <sub>t</sub>	μm	Profile height
Q <sub>d</sub>	mm <sup>3</sup> /min	Dressing material removal rate
Q <sub>l</sub>	L/min	Oil flow rate during grinding
Q' <sub>w</sub>	mm <sup>3</sup> /mms	Specific material removal rate
R <sub>a</sub>	μm	Roughness average
R <sub>k</sub>	μm	Core roughness
R <sub>pk</sub>	μm	Reduced peak height
R <sub>t</sub>	μm	Maximum height of the profile
R <sub>vk</sub>	μm	Reduced valley depths
R <sub>z</sub>	μm	Average maximum height of the profile
S	mm <sup>2</sup>	Wire cross section
S <sub>a</sub>	μm	Average height of measured area
S <sub>k</sub>	μm	Core roughness depth
S <sub>pk</sub>	μm	Reduced peak height
S <sub>vk</sub>	μm	Reduced valley height
T	K	Temperature
T <sub>boil</sub>	K	Boiling temperature
T <sub>graph</sub>	K	Graphitization temperature
T <sub>melt</sub>	K	Melting temperature
U <sub>d</sub>	-	Overlapping rate
V <sub>a</sub>	%	Volume percentage of abrasives in the bond
V <sub>c</sub>	μm <sup>3</sup>	Effective eroded volume per crater
V <sub>d</sub>	mm <sup>3</sup>	Dressing material removal
V <sub>s</sub>	mm <sup>3</sup>	Volume of grinding wheel wear
V <sub>sd</sub>	mm <sup>3</sup>	Grinding wheel dressed volume
V <sub>w</sub>	mm <sup>3</sup>	Volume of workpiece material removed

$V'_w$	mm <sup>3</sup> /mm	Specific material removal
$V_{wear}$	mm <sup>3</sup>	Wear volume of dressing tool
$W_e$	J	Discharge energy
$W_t$	μm	Waviness

### Greek symbols

$\alpha$	m <sup>2</sup> /s	Thermal diffusivity
$\epsilon_r$	-	Relative permittivity
$\rho$	kg/m <sup>3</sup>	Mass density
$\Delta r_s$	μm <sup>2</sup>	Grinding wheel radial wear
$\Delta r_{sk}$	μm <sup>2</sup>	Grinding wheel edge wear
$\Delta t$	s	Time step (simulation)
$\Delta T_m$	K	Equivalent melting temperature
$\Delta T_v$	K	Equivalent evaporation temperature
$\Delta x$	μm	Distance between nodal points in x direction
$\Delta y$	μm	Distance between nodal points in y direction
$\Delta z$	μm	Distance between nodal points in z direction
$\lambda$	-	Pulse frequency ratio

### Acronyms

AISI	-	American Iron and Steel Institute
Al <sub>2</sub> O <sub>3</sub>	-	Aluminum oxide
CBN	-	Cubic boron nitride
CH	-	Hydrocarbon (CH-based = oil-based)
CNC	-	Computer numerical control
CWEDT	-	Cylindrical wire electrical discharge turning
ECCD	-	Electro chemical in-process control dressing
ECDD	-	Electrochemical discharge dressing
ECDM	-	Electro chemical discharge machining
ECHSM	-	Expanding-circle heat source model
ECM	-	Electrochemical machining
EDD	-	Electrical discharge dressing
EDM	-	Electrical discharge machining

---

ELID	-	Electrolytic in-process dressing
ETH	-	Swiss Federal Institute of Technology
Gap	$\mu\text{m}$	Distance between electrodes during erosion
GF	-	Georg Fischer
HSG	-	High speed grinding
IEDD	-	In-Process Electro Discharge Dressing
IWF	-	Institute of Machine Tools and Manufacturing
MEDD	-	Mist-jetting electrical discharge dressing
MRR	$\text{mm}^3/\text{min}$	Material removal rate
PFE	-	Plasma flushing efficiency
PHSM	-	Point heat source model
PMEDM	-	Powder mixed electric discharge machining
SEDD	-	Sinking electrical discharge dressing
SEM	-	Scanning electron microscope
SiC	-	Silicon carbide
Si <sub>3</sub> N <sub>4</sub>	-	Silicon nitride
US	-	Ultrasonic
VDI	-	Verein Deutscher Ingenieure
ZrO <sub>2</sub>	-	Zircon oxide
WEDD	-	Wire electrical discharge dressing
WEDM	-	Wire electrical discharge machining
WL	-	White layer

# Abstract

Metal bonded diamond wheels, due to their strong grain retention, wear resistance and thermal conductivity are frequently used for grinding difficult-to-cut materials, such as advanced ceramics. On the other hand, the poor dressability of this type of grinding wheel limits its application. This study aims to evaluate the use of wire electrical discharge machining for truing and dressing metal bonded grinding wheels. In electrical discharge dressing (EDD), grain protrusion is generated while the electrically conductive bond material is eroded. Aiming to evaluate this dressing process, a wire electrical discharge dressing unit was designed, manufactured and integrated into a universal cylindrical grinding machine. Grinding oil is used for both dressing and grinding processes. High dressing material removal rates were achieved. Cylindrical plunge grinding tests on silicon nitride workpieces indicated that, in comparison to conventionally dressed wheels, lower cutting forces and wheel wear (higher G-ratio) are achieved by using ED-dressed grinding wheels, since ED-dressing creates grinding wheels with higher grain protrusion. To improve dressing accuracy a special wire guide was developed. It guides the wire directly at the erosion zone and is responsible for delivering dielectric to the erosion process. In comparison to free-stretched wires, considerably better dressing accuracy and erosion material removal rates were achieved. It was also found that better dressing accuracy is achieved when small depth of dressing cuts and constant axial dressing feed rates are applied in WED-sharpening. A thermal model was proposed aiming to help understand the erosion process and minimize the amount of time-consuming experiments necessary to generate suitable dressing data. The model is used to simulate the shape and volume of craters generated by single discharges. As a result, erosion material removal rates can be predicted, WEDM at high relative speeds can be better understood and even diamond graphitization can be analyzed.

Keywords: Electrical Discharge Dressing; Grinding; Diamond Wheels; Metal Bond; Ceramics

## Kurzfassung

Aufgrund der festen Anbindung des Kornes, der Verschleissbeständigkeit und der guten Wärmeleitfähigkeit werden metallisch gebundene Diamant-Schleifscheiben bevorzugt für die Bearbeitung von schwerzerspanbaren Materialien, wie Hochleistungskeramiken eingesetzt. Andererseits, wird ihre Anwendung durch die schlechte Abrichtbarkeit begrenzt. Das Ziel dieser Arbeit ist die Untersuchung von Drahterosion als Alternativprozess für das Abrichten von metallisch gebundenen Diamant-Schleifscheiben. Beim funkenerosiven Abrichten (EDD) wird der Kornüberstand durch die Erosion der elektrisch leitfähigen Bindung erzeugt. Um diesen Abrichtprozess untersuchen zu können, wurde eine funkenerosive Abrichteinheit entwickelt und gefertigt, welche in eine universelle Rundschleifmaschine integriert wurde. Schleiföl wird als Kühlschmiermittel beim Schleifen und auch als Dielektrikum beim Erodieren angewendet. Hohe Erosionsabtragsleistungen konnten erreicht werden. Die Ergebnisse beim Schleifen von Siliziumnitrid zeigen auf, dass durch die Anwendung von funkenerosiv abgerichteten Schleifscheiben kleinere Prozesskräfte und höhere Verschleissverhältnisse (G-Wert) erzielt werden können. Dies wird den höheren Kornüberständen und damit geringeren Reibkräften zugeschrieben, die durch die Funkenerosion im Vergleich zu konventionellen Abrichtprozessen erzeugt werden. Um die Abrichtgenauigkeit zu verbessern, wurde eine spezielle Drahtführung entwickelt, welche den Draht direkt an die Erosionsstelle führt und welche auch für die Zuführung des Dielektrikums verantwortlich ist. Eine bessere Abrichtgenauigkeit und Erosionsabtragsleistung wurden im Vergleich zum Abrichten mit frei gespannten Drähten erreicht. Ausserdem konnte gezeigt werden, dass die Abrichtgenauigkeit grösser wird, wenn beim EDM-Schärfen eine geringere Abrichtzustellung und eine konstante Drahtvorschubgeschwindigkeit eingesetzt wird. Ein thermoelektrisches Modell wurde entwickelt mit dem Ziel den Abrichtprozess besser verstehen zu können und gleichzeitig die Anzahl von zeitintensiven Versuchen zu minimieren. Das Modell wird benutzt um die Kraterform und das Kratervolumen von Einzelfunken zu simulieren. Als Ergebnis kann die Erosionsabtragsleistung vorausgesagt, der Einfluss der Relativgeschwindigkeit auf den Erosionsprozess besser verstanden und die Graphitisierung der Diamanten analysiert werden.

Kennwörter: Funkenerosives Abrichten; Diamantschleifscheiben; Metallische Bindung

# 1. Introduction

Metal bonded diamond wheels are frequently used for grinding difficult-to-cut materials, since diamonds have key properties such as high wear resistance, high hardness, very high thermal conductivity, low friction and thermal expansion coefficients, and the metal bond possesses properties such as high grain retention forces, high wear resistance and high thermal conductivity. One particular application is thus grinding of advanced ceramics, which are materials with several exceptional properties such as high hardness, high stiffness and good thermal and chemical stability. When grinding advanced ceramics, the grinding wheel is subjected for instance to high mechanical and thermal loads, and depending on the type of bond material, high wear rates occur. If a profiled grinding wheel is used, its shape can be quickly compromised, and consequently ground workpieces are machined out of tolerances. Therefore, the right choice of bond material is essential to minimize wear. Metal bonded grinding wheels are the right choice in this case.

Apart from the above mentioned advantages of metal bonded grinding wheels, carrying out a proper dressing method is the main challenge when using these tools. Dressing must provide the grinding wheel with sufficient grain protrusion and chip space to transport the chips as well as the coolant through the grinding zone. Usually, a silicon carbide wheel is used for truing and dressing metal bonded diamond wheels. The dressing mechanism consists basically in the abrasion of the silicon carbide grains and filler material on the metal bond. In other words, the main objective of this dressing method is not to crush the grains but to set back the bond. This method has, however, limitations. High wear of the silicon carbide wheel limits dressing accuracy, so that usually only non-complex wheel profiles are dressed by this method. In addition, it is very time consuming, the reason why metal bonded diamond wheels are in many cases conditioned on independent dressing machines. In this case, however, another problem arises, since after dressing the grinding wheel has to be carefully reassembled

to the grinding machine, to avoid clamping errors, which can cause wheel wear and deteriorates accuracy.

Aiming to improve the dressability of metal bonded wheels, several methods have been proposed so far, such as electrolytic in-process dressing (ELID), electrochemical discharge machining (ECDM) and electrical discharge dressing (EDD). ELID leads to an anodic dissolution of the metal bond, producing high grain protrusion. However, only low material removal rates are achieved and water based fluids (electrolyte) must be used. In ECDM, the anodic dissolution is assisted by electrical discharges. Higher material removal rates are achieved, but such as in ELID, a special fluid has to be used, which restricts its application within a grinding machine. In electrical discharge dressing (EDD), bond removal occurs by the thermal effect of electrical discharges. High macro-geometrical accuracy and, due to high pulse frequencies, high material removal rates can be achieved. Grain protrusion is generated since diamonds are not electrically conductive, i.e. diamonds should not be eroded by means of EDM. Two different electrical discharge machining processes, wire EDM and die-sinking EDM, can be used for truing and dressing metal bonded grinding wheels. In general, electrical discharge dressing is carried out in EDM machines, i.e. EDD is not integrated in grinding machines. In these cases, standard EDM dielectric liquids such as oil (die-sinking EDM) and deionized water (wire EDM) are used.

On-machine wire electrical discharge dressing (WEDD) of metal bonded grinding wheels is the focus of this work. First an overview of the state of the art on conditioning technologies applied to metal bonded grinding wheels is presented. Thereafter, a wire electrical discharge dressing unit is presented, which was designed, manufactured and integrated into a universal cylindrical grinding machine, so that on-machine dressing experiments can be performed. In this study, WED-dressing is mainly compared to SiC-dressing, regarding the topography of the conditioned grinding wheel, dressing material removal rates, accuracy and its influence on grinding performance. A special wire guide is proposed in this work, which is mostly responsible for reducing wire vibrations and thus increasing dressing accuracy and material removal rates. In-process dressing is also evaluated, and shows potential for future applications. In addition, a thermal model is proposed, so that simulation of material removal rates for different materials can be performed. Single discharge experiments were carried out to help validate the model. The erosion model is also used to describe and understand EDM with high relative speeds between workpiece and electrode. Moreover it helps to calculate the constant axial dressing feed rate used in WED-sharpening and to explain the reason why little or no thermal damages occur to diamond grains when EDM is applied for dressing metal bonded diamond wheels.



## 2. State of the art

The conditioning technology plays a decisive role in grinding. Within the grinding community the slogan “grinding is dressing” [WEGE11] points out that the preparation of the grinding tool has a significant influence on grinding results. Depending on the type of workpiece material, special grinding wheels are required. Hence, the right choice of both the abrasive and the bond material is important. According to Klocke and Kuchie [KLOC09a], metal bonded diamond wheels are the first choice when advanced ceramics has to be ground. This bond material offers advantages especially regarding grain retention and thermal conductivity, which is important to keep the grinding wheel profile within the pre-specified tolerances and help to dissipate generated heat. Moreover, diamond is the hardest material found in nature [FIEL79], being appropriate to grind difficult-to-cut materials like ceramics. Apart from the aforementioned advantages, some authors [DERK08, SCHO01a, WEGE11] emphasize the fact that metal bonded diamond wheels are difficult-to-dress tools. They have no pores and consequently bond material has to be removed between the diamonds to create chip pockets and provide the grinding wheel with sufficient grain protrusion. Thus, the main challenge in using metal bonded diamond wheels is to have an efficient conditioning process. In this chapter, conditioning is the main focus. First, grinding wheel wear is discussed, since it represents the main reason why grinding wheels have to be conditioned. Subsequently, metal bonded diamond wheels are highlighted and different conditioning methods are illustrated. At this point, electrical discharge machining is presented as an alternative to conventional dressing. Finally, some EDM modeling approaches are discussed.

### 2.1 Grinding wheel wear

Grinding wheel wear is the consequence of mechanical, thermal and chemical loads to which the grinding wheel is subjected during grinding [WEGE11]. The macro geometry

of the grinding wheel, i.e. its shape and dimensions, is thus affected by wear. According to König and Schulz [KOEN94] the total area of grinding wheel wear  $A_s$  comprises the sum of the radial wear area  $A_{sr}$  and the edge wear area  $A_{sk}$ , as illustrated in Figure 2.1. It indicates the minimum dressing depth necessary to restore the shape of the grinding wheel, here represented by the total depth of dressing cut  $a_{ed.ges}$ . As reported by Klocke and Kuchie [KLOC09b], macroscopic wear is responsible for causing deficient accuracy of ground workpieces, which are in general specified with tight tolerances, so that only little macroscopic wear is tolerated.

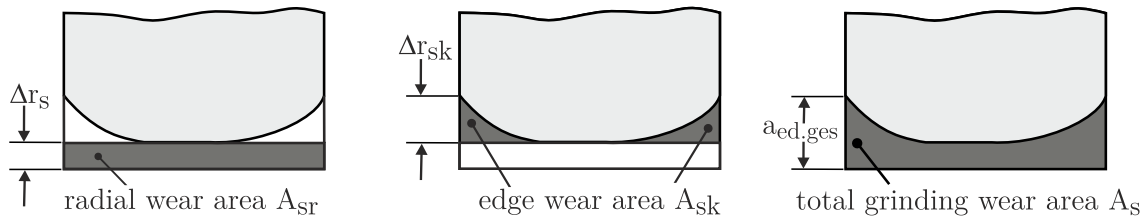


Figure 2.1 – Macroscopic types of grinding wheel wear [KOEN94]

According to Stetiu and Lau [STET74], microscopic grinding wheel wear can be divided into three different types, namely attrition wear, partial fracture of grain and fracture of bond. König and Schulz [KOEN94] use a similar nomenclature, distinguishing microscopic grinding wheel wear in grain wear, where micro and macro fracture occur, bond wear, which is subdivided in bond bridge wear and bond breakage, and pullout, where total grain loss occurs (Figure 2.2).

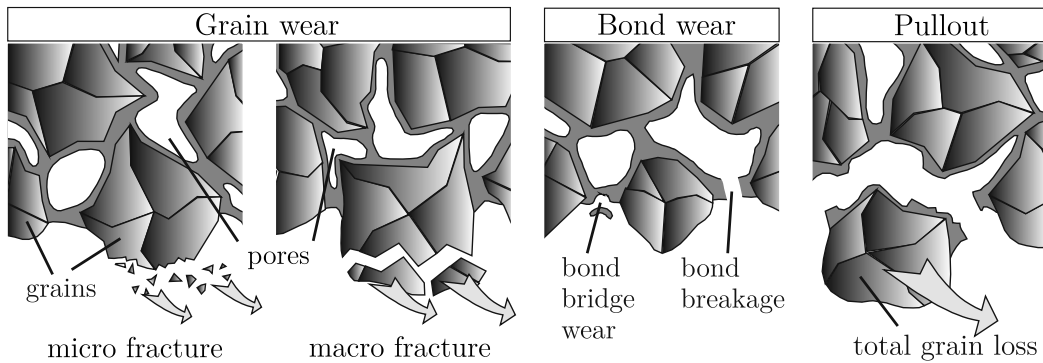


Figure 2.2 – Microscopic types of grinding wheel wear [KOEN94]

Attritious wear occurs directly at the interface between grain and workpiece, where abrasion, crumbling and chemical wear take place. When this type of wear is predominant, the grinding ratio  $G$ , which is defined as the ratio of ground volume  $V_w$  to wheel wear volume  $V_s$  as presented in equation (2.1), is usually high (the higher the better). The grinding wheel, however, loses its sharpness, and consequently grinding forces increase and more heat is generated, which ends in break off or pullout of grains, when they become overloaded [STET74]. Bond wear occurs mainly due to contact between chips and bond, which in fact weakens grain retention. Grain pullout occurs

when bond material bursts or the interface between bond and grain fails [WEGE11]. When bond wear and pullout mechanisms are predominant, lower G-ratios are expected. Still, a self-sharpening effect can occur, which helps keeping the grinding wheel sharp. On the other hand, this mechanism deteriorates accuracy.

$$G = \frac{V_w}{V_s} \quad (2.1)$$

To compensate the above mentioned wheel wear and therefore restore the grinding capability of grinding wheels, these tools have to be conditioned from time to time, i.e. a specific amount of volume has to be removed from the grinding wheel ( $a_{ed,ges}$  in Figure 2.1). Thus, conditioning is highly necessary and therefore considered, as stated by Wegener et al. [WEGE11], the most important enabling factor in grinding.

## 2.2 Grinding wheel conditioning

The term conditioning refers to different processes used to create and restore the macro and micro geometry of grinding wheels. According to the VDI guideline 3392 [VDI07], conditioning is divided into cleaning and dressing, and the latter is classified into profiling and sharpening, as illustrated in Figure 2.3. Since different bond materials and abrasives are used to compose different grinding wheels, several conditioning methods were developed to suit these different grinding wheel specifications. Regarding bond materials, ceramic, resin and metal bonds are typically used. Abrasives are in general classified into conventional, i.e. silicon carbide (SiC) and aluminum oxide ( $Al_2O_3$ ), and superabrasives, namely Cubic Boron Nitride (CBN) and diamond. As reported by Madison [MADI96], seven out of ten grinding wheels are ceramic bonded. Better dressability, good stiffness and self-sharpening are some reasons for this fact.

Depending on the type of material to be ground, wheel loading can occur, i.e. workpiece material adheres to the grinding wheel surface blocking its pores. Cleaning processes serve to remove residual chips, grains and bond material from the grinding wheel surface. For this reason, cleaning is considered a conditioning method, since it helps to restore the grinding capability of grinding wheels.

Regarding dressing, profiling is used to obtain the macro geometry of the grinding wheel, i.e. its dimensions and form in radial and axial directions. When a new grinding wheel is mounted inside the grinding machine, run-out errors have to be eliminated, i.e. profiling has to be performed. Furthermore, structuring also belongs to the profiling processes, which is used for structuring ceramic or resin bonded grinding wheels in order to enhance the cutting condition of the abrasive grains and decrease heat generation, as stated by Oliveira et al. [OLIV10] and Piotr [PIOT07].

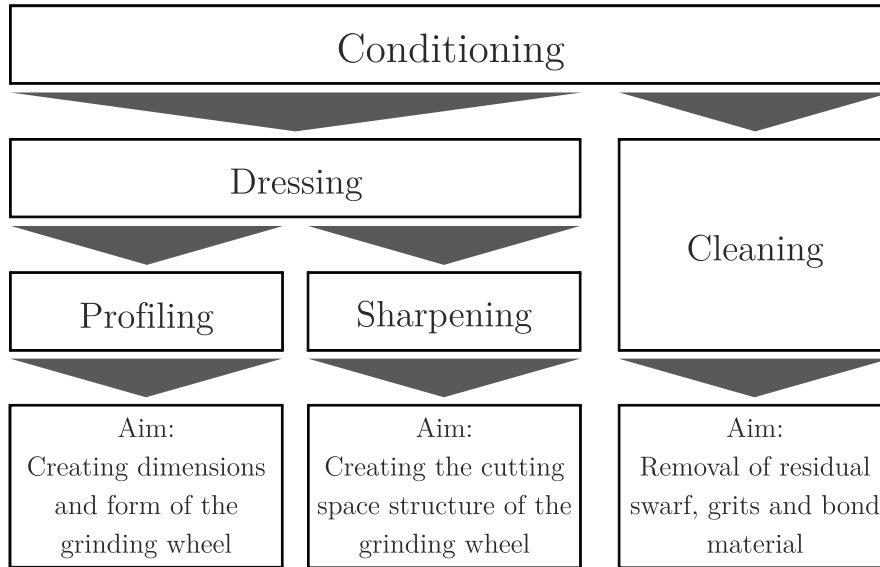


Figure 2.3 – Conditioning according to VDI guideline 3392 [VDI07]

Sharpening is used to generate the grinding wheel micro geometry, in which bond material between grains as well as worn grains are removed or partially broken and new cutting edges as well as chip pockets are generated. However, not all types of bond materials require this process. Ceramic bonded wheels, for example, are manufactured with pores, and for this reason chip pockets are already available after profiling. On the other hand, bronze bonded and resin bonded grinding wheels usually have to be sharpened, since after profiling grains and bond material are mainly at the same radial level, i.e. there is nearly no grain protrusion.. In this case, high friction between bond and workpiece can occur, generating heat and increasing wear.

Several conditioning methods have been proposed so far. Many of them were especially developed due to the spread of CBN and diamond abrasives in industry. Wegener et al. [WEGE11] carried out a detailed study on conditioning of grinding wheels and proposed a classification of different processes in four main categories, namely mechanical, thermal, chemical/ECM and hybrid methods (Figure 2.4).

Mechanical methods are the most consolidated and can be applied for all different types of grinding wheels. Conventional grinding wheels of aluminum oxide and silicon carbide are generally conditioned with mechanical methods. CBN grinding wheels are also often mechanically conditioned, although metal bonded CBN grinding wheels can also be conditioned with other methods. Diamond wheels are more difficult to dress, especially when metal bonded diamond wheels are used, and therefore different methods other than mechanical were especially designed for these tools.

In general, the choice of an appropriate conditioning method depends on the type of grinding wheel, which is mainly chosen based on the type of material to be ground. Advanced ceramics, for instance, have exceptional properties such as high

hardness and stiffness and good thermal and chemical stability, finding an increasing number of applications in the automotive, aerospace, medical, electronics and machine-tool industries [LAUW07, LIAN01, PARK06]. Grinding with metal bonded diamond wheels is the major machining process for advanced ceramics. This work focuses on this type of grinding wheel, and consequently metal bonded diamond wheels are discussed in more details in the following section of this chapter.

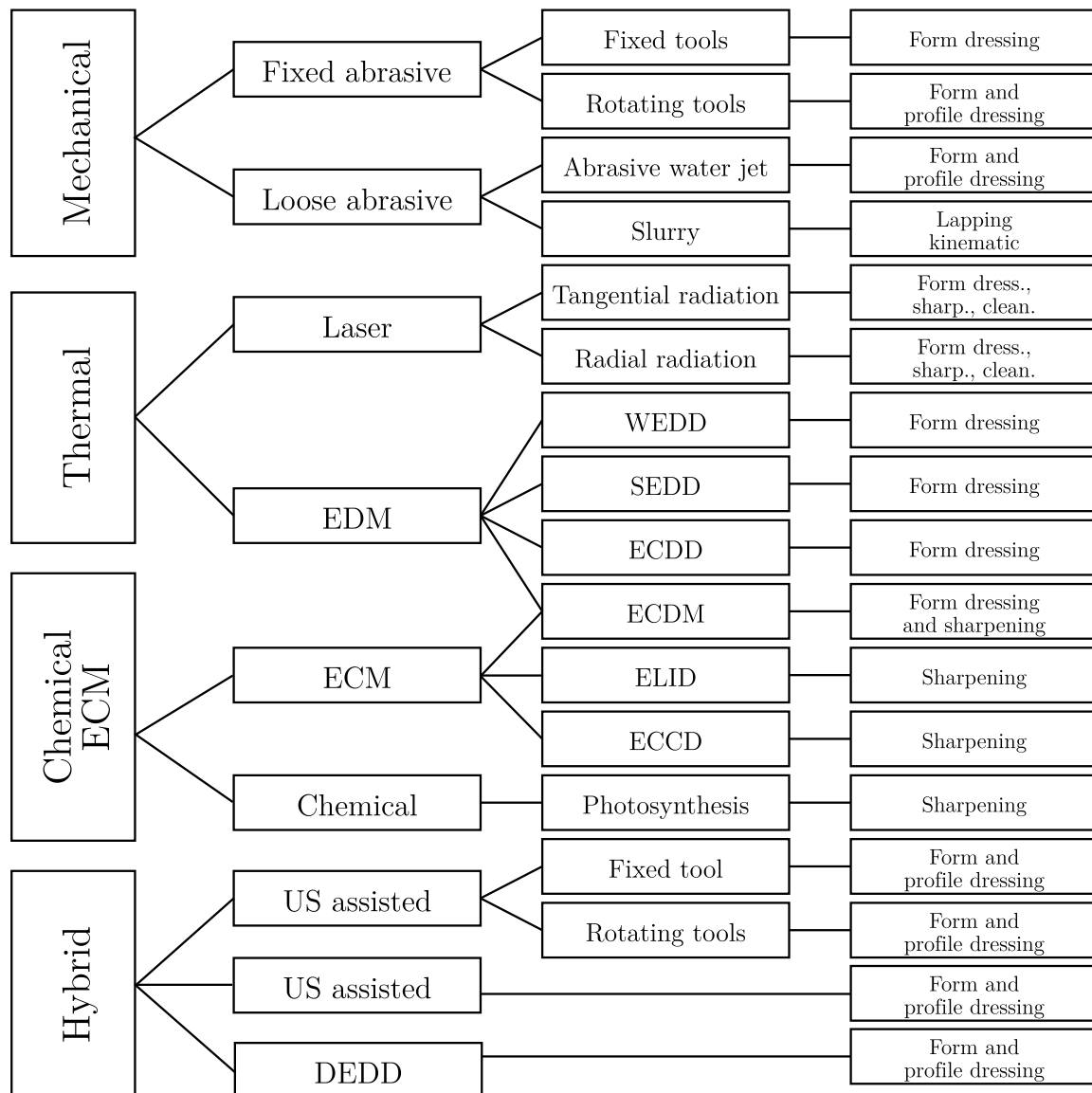


Figure 2.4 – Conditioning methods according to Wegener et al. [WEGE11]

## 2.3 Metal bonded diamond wheels

Diamond is the hardest material found in nature, as stated by Field [FIEL79], and therefore is called “superabrasive” in the context of grinding. Diamonds have key properties such as high wear resistance, high hardness, very low coefficient of friction and low thermal expansion, which are important properties for grinding abrasives

[ELEM12, HUAN03, LEE00b]. Moreover, Element Six [ELEM12] states that diamonds have excellent electrical insulator properties, the highest known thermal conductivity and resistance to thermal shocks. Accordingly, diamond grinding wheels are suitable for grinding materials that can only hardly or even cannot be ground using conventional abrasives such as aluminum oxide or silicon carbide [DIAM09, KLOC09d]. Figure 2.5 illustrates a comparison between diamond and other grinding and workpiece materials regarding hardness and fracture toughness, clearly showing the superior properties of diamond and CBN, the superabrasives, in comparison to conventional grinding materials ( $\text{Al}_2\text{O}_3$  and SiC). Diamond has a wider spectrum of hardness, since both natural and synthetic diamonds (with inclusions and crystallographic defects) can be used as grinding material. Higher fracture toughness is also a desired property, since the grains have to withstand consecutive collisions with the workpiece, and despite this remain sharp over a long time.

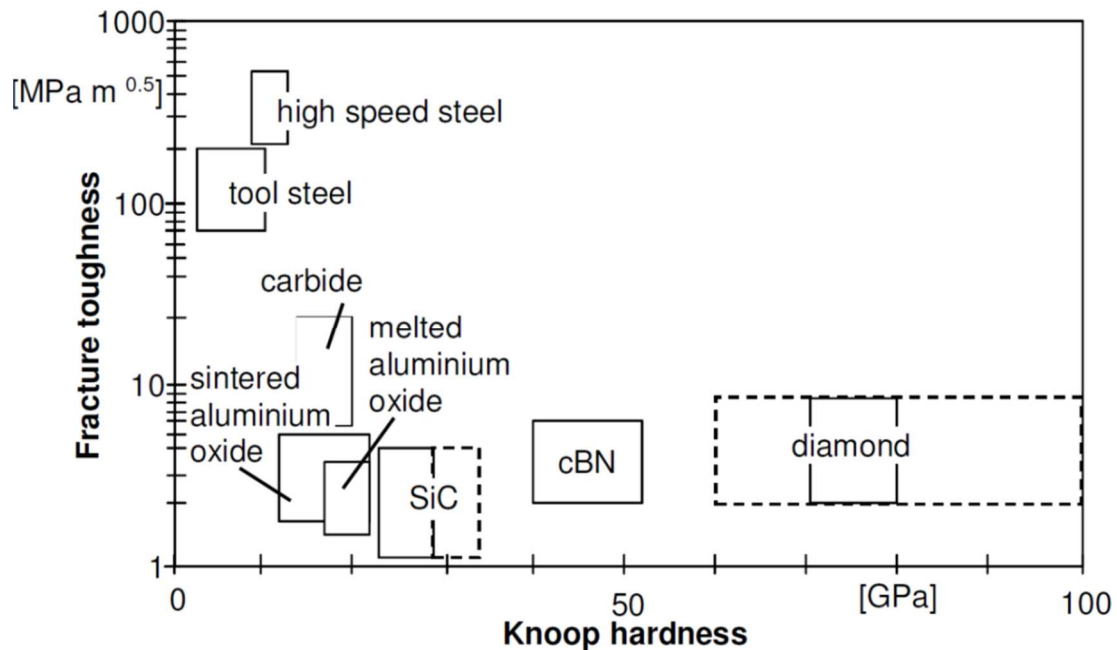


Figure 2.5 – Properties abrasive materials [KLOC09b]

According to Klocke and Kuchie [KLOC09c], the great majority of natural diamonds, more than 80%, are not used to manufacture jewelry because they are either too small or do not have the required purity. For this reason, they can be used in other applications such as in grinding. Synthetic diamond, however, is the most dominant type of diamond used in grinding. Pressures of 70 to 120 kbar and temperatures around 2,000° C are applied in the presence of metallic catalysts to transform graphite into diamond. Due to the chemical affinity of iron to carbon, diamonds are not applied to grind steel, and rather find its main applications in grinding ceramics, glass, carbides, plastic and concrete. As reported by Holz and Sauren [HOLZ88], diamond grains can be used combined with ceramic, resin and metal bonds.

Synthetic diamonds can be manufactured in different forms and with different properties, according to specific grinding applications and depending on different existing bond materials. Figure 2.6 shows two different diamond grains manufactured by Element Six [ELEM12]. The diamond type PDA 989 is designed to be used with metal bonds in high-productivity grinding applications. It is a blocky, crystalline material with a high impact strength and high thermal stability. PDA 446, on the other hand, is a sharp-shaped diamond, used to ensure free-cutting characteristics.

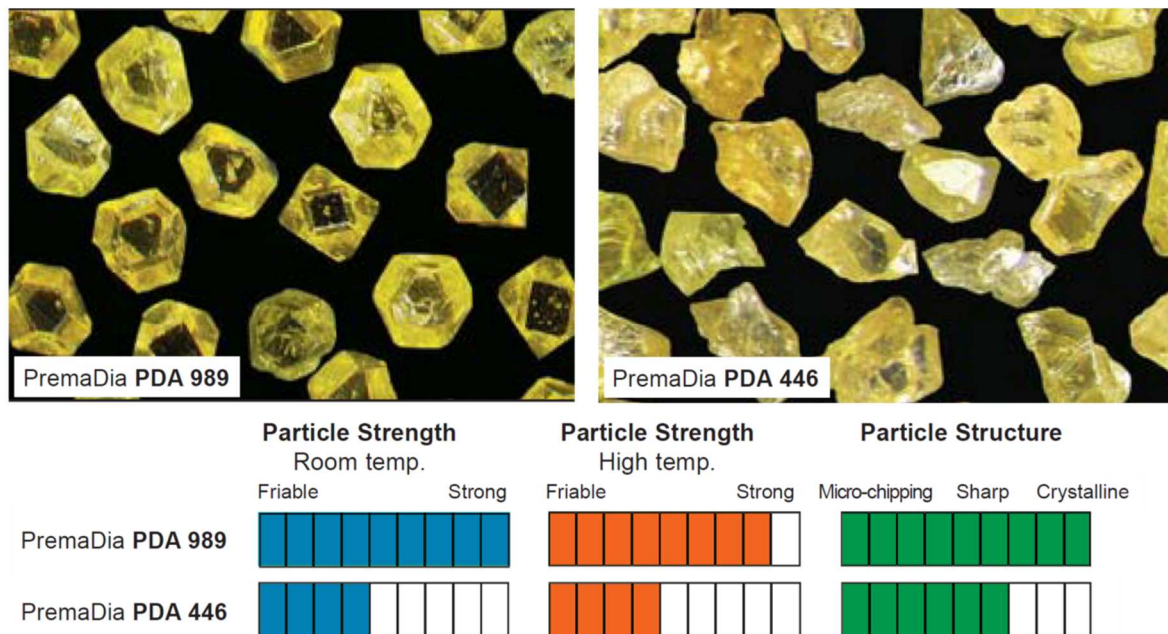


Figure 2.6 – Different types of synthetic diamonds [ELEM12]

Sintered metal bonds are generally made out of different modified copper/tin and cobalt bronze alloys. They can be manufactured in a variety of different wear resistance, toughness and brittleness, depending on the alloy composition and sintering process parameters. Metal bonded diamond wheels are normally produced by first mixing metallic powder and diamond grains, followed by cold pressing in steel or graphite molds, sintering and hot pressing, as described by Klocke [KLOC09d]. Diametal AG [DIAM09] states that metal bonded grinding wheels have an excellent stability of shape, mainly due to its strong grain retention forces and wear resistance, which make this grinding tool especially suitable in profile grinding applications. Additionally, metal bonded grinding wheels have a high thermal conductivity, as stated by Lin et al. [LIN08], which is important to help dissipate heat generated during grinding. Figure 2.7 shows a comparison between different bond materials and highlights some properties of metal bonded grinding wheels, e.g. high diamond bonding or retention forces, good profile stability and high toughness, high thermal conductivity, and good thermal and chemical stability, as reported by Noichl [NOIC12].

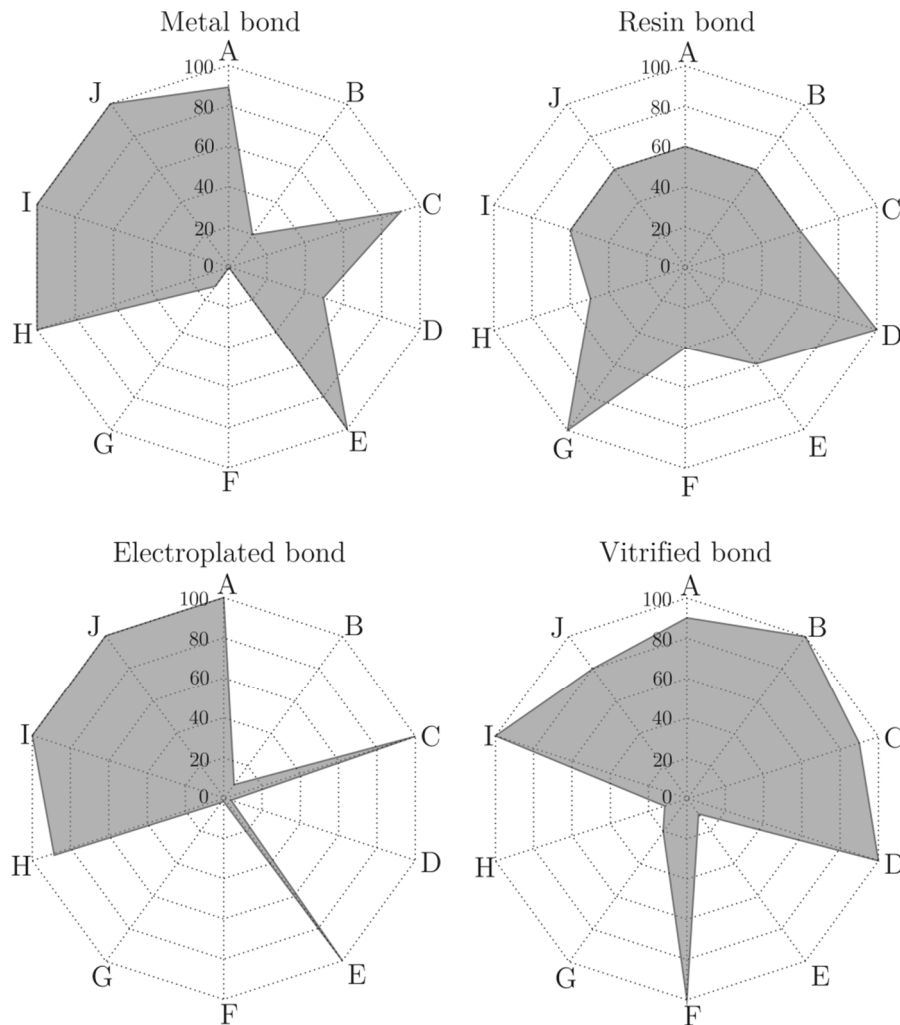


Figure 2.7 – Properties of different bond materials: **A.** Diamond bonding; **B.** Profiling; **C.** Profile holding; **D.** Sharpening; **E.** Toughness; **F.** Brittleness; **G.** Damping; **H.** Thermal conductivity; **I.** Thermal stability; **J.** Chemical stability [NOIC12]

According to several authors [KLOC09b, KLOC09d, OHMO96, SCHO01a, SCHO01b], the main application fields of metal bonded wheels are found in grinding difficult-to-cut materials such as hard-metal and advanced ceramics. Among several different compositions of ceramics, special attention can be given for silicon nitride ( $\text{Si}_3\text{N}_4$ ), aluminum oxide ( $\text{Al}_2\text{O}_3$ ) and zircon oxide ( $\text{ZrO}_2$ ). Figure 2.8 shows some applications of advanced ceramics [CERA11]. In Figure 2.8a, components used in welding are shown, namely welding rollers, welding pins and gas nozzles, where the ceramic material, due to its hardness and wear resistance, high temperature and chemical resistance, helps increasing tool life. Figure 2.8b shows knee replacement components, where the application of ceramics helps reduce wear rate and the risk of allergic response from the human body. Figure 2.8c shows ceramic forming tools which have advantages concerning friction characteristics, low diffusion and adhesion and high hot hardness, and are used in tube drawing, bending, widening and welding applications.



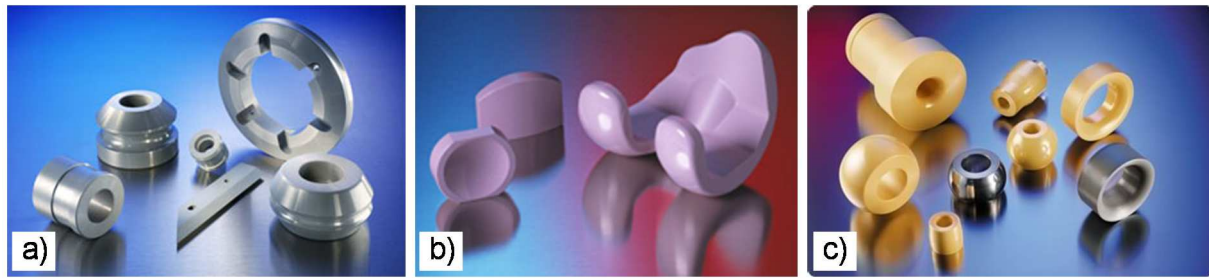


Figure 2.8 – Some applications of advanced ceramics: a) welding components; b) knee replacement components; c) forming tools [CERA11]

Rödel et al. [RODE09] drew a roadmap for advanced ceramics covering the period 2010-2025 and stated that these materials represent an important enabling technology with considerable impact on a large variety of industries and have potential to deliver high-value contributions for solving the challenges of future. To generate the expected progress at all levels, from ceramic materials to applications, various breakthrough developments are still required. Improving grinding performance of metal bonded diamond wheels is without any doubt an important requirement to achieve such goals.

Although metal bonded diamond wheels have several advantages over other types of grinding wheels, they also have disadvantages. The main drawback lies in their poor dressability (see Figure 2.7). Thus, dressing is still the main barrier to increase the use of metal bonded diamond wheels, as stated by Derzy et al. [DERK08]. Conventional dressing using silicon carbide wheels is inefficient and not very accurate. Consequently, different non-conventional dressing methods have been proposed so far. Some of these methods as well as conventional dressing are discussed in the following section.

## 2.4 Conditioning of metal bonded diamond wheels

In view of the classification shown previously in Figure 2.4, metal bonded grinding wheels can be conditioned by methods belonging to the four mentioned categories. This is not applicable to ceramic and resin bonded grinding wheels, since in some methods an electric conductive bond material is required. Several dressing methods were especially designed for metal bonded grinding wheels, and much research has been done in this field lately, indicating a growing interest in this type of grinding tool. According to Wegener et al. [WEGE11], metal bonded grinding wheels are the most critical to dress grinding tools. Therefore, the dressability of metal bonded grinding wheels has to be improved so that its advantages can be better exploited in the industry.

### 2.4.1 Mechanical conditioning methods

With regard to mechanical conditioning, metal bonded grinding wheels are generally conditioned by ceramic bonded silicon carbide wheels [DIAM09, KLOC05]. In this case, the dressing wheel acts primarily on the removal of bond material. Diamond grains are not necessarily broken to form new cutting edges (although mechanical damages also occur), but rather grain pullout is the primary mechanisms of grain removal. Indeed, metal bonded diamond wheels can be mechanically profiled and at least some grain protrusion can be generated using a SiC-wheel, even though chip pockets are mainly created in the sides of the grains.

According to Diametal AG [DIAM09], a reciprocating method is usually applied in SiC-dressing. In roughing, dressing depth of cuts ranging from 0.02 to 0.05 mm are commonly used, while in finishing dressing depth of cuts between 0.01 and 0.02 mm are applied. The grain size and hardness of the silicon carbide wheel have to be chosen according to the diamond grain size. As a recommendation given by Diametal AG [DIAM09], for example, D46 and D91 metal bonded grinding wheels are conditioned with silicon carbide wheels of grain mesh sizes 320 and 120 and hardness G and H respectively. SiC-dressing can be carried out inside the grinding machine, using a specific dressing spindle or even by mounting the dressing wheel on the workpiece spindle. Nevertheless, only relatively simple geometries can be profiled in this case. Figure 2.9a shows a SiC-dressing wheel, mounted on the workpiece spindle of a grinding machine, which is used for dressing a diamond wheel of straight profile (type A1A). Figure 2.9b illustrates a cup dressing wheel mounted in a dressing spindle, which is used for dressing the lateral face of a diamond grinding wheel. Klocke and Kuchie [KLOC09b] pointed out that profiled SiC-dressing wheels can be used as an alternative to the reciprocating dressing method, which, however, must be continuously dressed with a diamond roller.

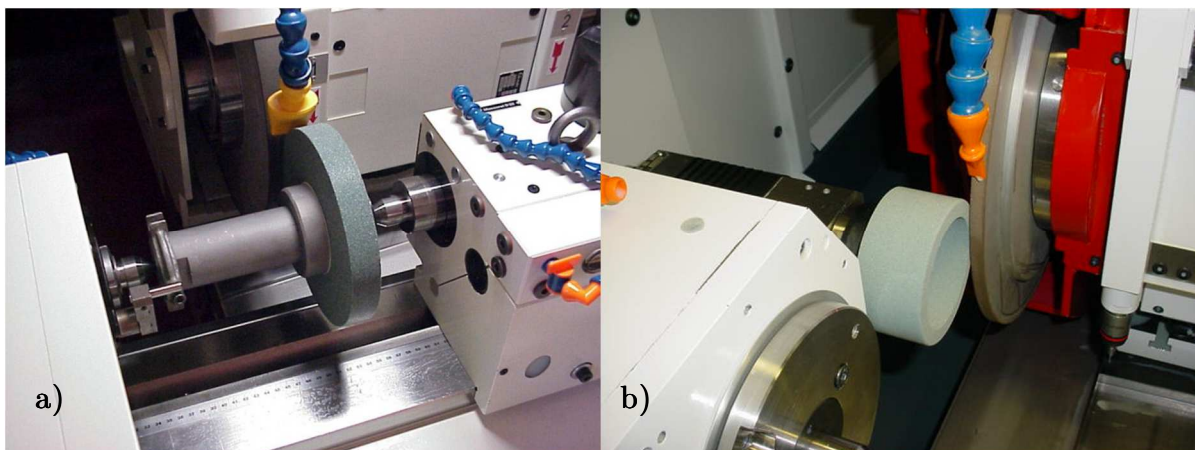


Figure 2.9 – Conventional dressing using ceramic bonded silicon carbide wheels. a) Frontal dressing b) Lateral dressing [FIEB09]

In SiC-dressing of metal bonded diamond wheels high wear occurs to the dressing tool, as reported by Suzuki et al. [SUZU87]. According to Diametal AG [DIAM09], a dressing ratio  $G_d$ , as defined in equation (2.2), of only 0.025 is expected, meaning that during dressing the removal of each cubic millimeter from the diamond tool ( $V_{sd}$ ) requires approximately forty cubic millimeters from the dressing wheel ( $V_{wear}$ ). As a consequence, high dressing times are required, there are limitations concerning dressing accuracy and the generation of abrasive dust in the grinding machine is not beneficial at all. Wimmer [WIMM95] stated that qualitative problems such as loss of contour accuracy can easily occur in SiC-dressing. Irregular removal of bond material is also possible in SiC-dressing due to the small dressing ratio, meaning that traces can be generated on the surface of the grinding wheel where the dressing direction can be recognized. To minimize this problem, Nagase [NAGA12] developed a dressing process using double cup dressers of SiC for face grinding. In this process, the relative speed between grinding wheel and dressing cup wheels gives a cross with adjustable angle to the grinding speed direction, grooving the grinding wheel surface in those directions, giving beneficial surface topography and minimizing the generation of undesired traces on the grinding wheel.

$$G_d = V_{sd}/V_{wear} \quad (2.2)$$

Sharpening is normally required after SiC-dressing, since in general small grain protrusion is generated. Ceramic bonded  $Al_2O_3$  wheels are applied in this case or sharpening stones are used to set bond material back and generate the desired micro geometry. This process also contributes to increase non-productive time.

To minimize the negative impact of non-productive times associated to this type of dressing method, metal bonded grinding wheels are often conditioned outside the grinding machine. Several dressing machines are available on the market. Figure 2.10 shows two examples, a 3M™ machine type E339V [3M2011], and a Atrump machine type TD1 [ATRU12]. In both cases it is possible to import CAD drawings and to quick-change spindle systems. Moreover, a high-resolution LCD monitor is used for monitoring the process. Special profiles can be generated and different grinding wheel clamping systems can be used. However, the main drawback in the case of using an external dressing machine is the reassembly of the grinding wheel on the grinding machine with its attributed inaccuracies, which can lead to irregular wear, chatter and therefore deteriorate grinding accuracy.



Figure 2.10 – Dressing machines for conditioning metal bonded grinding wheels: 3M™ type E339V (left) [3M2011] and Atrump type TD1 (right) [ATRU12]

In addition to SiC-dressing, other mechanical methods can be applied in some special cases. According to Derkx et al. [DERK08], form crush dressing, which is a dressing method usually applied to ceramic bonded wheels, can be used with some special crushable bronze bonded wheels. In form crushing, the surface speeds of the dressing tool and grinding wheel have to be synchronized, so that only normal forces are applied to the diamonds. Dressing occurs when high stresses cause the bond material to fail, and consequently even whole diamonds can pull out of the grinding wheel (the diamonds can undergo splintering and thus sharp cutting edges are generated). Touch dressing is another process used for conditioning metal bonded wheels, as reported by Ghosh and Chattopadhyay [GHOS07]. In this case, single layer wheels are conditioned, in which a diamond dressing wheel is used to homogenize grain protrusion. Only very small dressing depths of cut are used, the reason why this process is known as touch dressing. According to Shen et al. [SHEN01], abrasive water jet is another method that can be applied for dressing metal bonded grinding wheels. In this case, a high pressure jet of water mixed with abrasives is used to remove bond material out of the grinding wheel. However, it is very aggressive to the grinding machine, so that it is better to be carried out in special designed devices. Another method, as described by Klocke and Kuchie [KLOC09b], uses long-chipping steels as dressing tools, in which the steel chips remove bond material from the grinding wheel due to friction wear.

In order to profit more from the application of metal bonded diamond wheels, attempts to improve its dressability have become an important research issue. Different truing and dressing methods have been proposed so far, including the application of

laser, electro chemical machining (ECM), electrical discharge machining (EDM) and electro chemical discharge machining (ECDM), among others. These different dressing methods are discussed in the following sections.

### 2.4.2 Laser beam dressing

Following the classification presented in Figure 2.4, laser beam dressing belongs to the category thermal conditioning, and can be further divided according to the direction of the laser beam in tangential and radial radiation. In general, a Nd:YAG laser is used in continuous wave or pulsed mode [WEGE11]. According to Wang et al. [WANG07], by adjusting the laser beam intensity, selective removal of material takes place. Thus, the process can be controlled for avoiding thermal damages to the abrasive grains while the bond material is removed. It can be reached by adjusting the intensity of the laser source in such a way that the laser energy is above the threshold for ablating the bond material and below the threshold for ablating the grain.

Hosokawa et al. [HOSO06] investigated laser-dressing of bronze bonded diamond wheels by applying pulsed-Nd:YAG laser. Laser was irradiated in radial direction to the grinding wheel. The authors claim that when a critical laser power is not exceeded no thermal damages occur to the diamonds. Moreover, grinding forces are similar when laser conditioned wheels and conventionally conditioned grinding wheels are used, showing that this method can really create grain protrusion and thus be used for conditioning metal bonded grinding wheels.

Laser touch dressing can be applied for conditioning electroplated diamond grinding wheels. In this case, the main goal is not to remove bond material but rather to cut the diamond grains within a defined grain protrusion and avoid damages to the bond material, since the grinding wheel is made out of one single layer of diamonds. Dold et al. [DOLD11] evaluated this dressing method by applying a picosecond pulsed Yb:YAG-laser beam tangentially to the grinding wheel. According to the authors, high accuracy can be achieved and no thermal damages were observed to the abrasive grains and bond material. The laser-dressed wheel was then used for dressing a SiC-wheel, and comparisons with a mechanically dressed diamond wheel revealed better dressing efficiency in laser dressing.

Rabiey et al. [RABI11] investigated the dressability of hybrid bonded CBN grinding wheels using a Q-switched fiber laser system. By applying the laser in radial direction the grinding wheel can be sharpened, i.e. grain protrusion is generated. They found that the use of laser-dressed wheels leads to lower grinding forces and consequently lower specific energies and heat generation when compared to conventionally SiC-dressed hybrid bonded grinding wheels. However, a poorer G-ratio and higher workpiece surface roughness were achieved using this method. According to

the authors, accurate profiles can be generated in small grinding wheels diameters by applying the laser in tangential direction. Walter et al. [WALT12] applied a Q-switched fiber laser system for dressing and truing of hybrid bonded CBN grinding tools and found that complex profiles with sharp edges can be created with this method, as shown in Figure 2.11, where an internal corner radius of around  $20\ \mu\text{m}$  was created in a B126 grinding wheel.

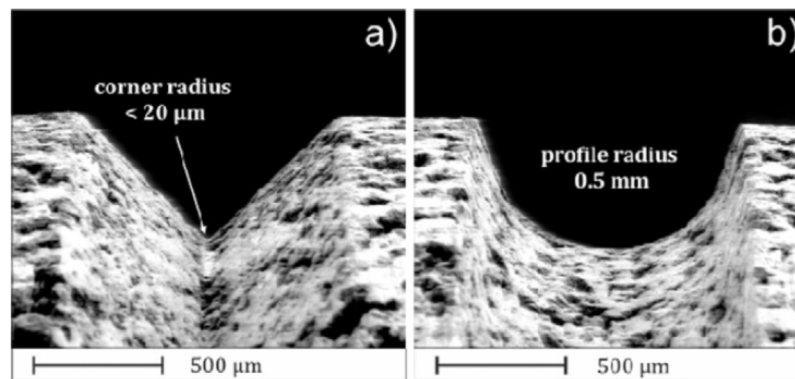


Figure 2.11 – SEM micrograph of a laser trued  $90^\circ$ -kerf (left) and a  $0.5\ \text{mm}$  tool profile radius (right) [WALT12]

Although laser beam conditioning is an alternative for metal bonded grinding wheels in comparison to the conventional dressing method, this process has some drawbacks. First, it is time-consuming, since only low material removal rates can be achieved without damaging the grains. Second, the integration of a laser system into a grinding machine is complex, and several safety measures have to be adopted to allow this integration. Moreover, the costs associated to this method can be very high and therefore unattractive to many potential users of metal bonded grinding wheels [RABI11].

### 2.4.3 Electro chemical dressing

Metal bond, in contrast to ceramic and resin bond, is an electric conductive material, and can be machined by means of electro chemical processes. Diamond and CBN, on the other hand, are electrical insulators, so that grain protrusion is generated when bond material between the grains is chemically removed. Electro chemical dressing can be further classified into electrolytic in-process dressing (ELID) and electro chemical in-process control dressing (ECCD), as described by Wegener et al. [WEGE11]. Figure 2.12 shows a schematic representation of both electro chemical processes according to Ohmori and Nakagawa [OHMO90].

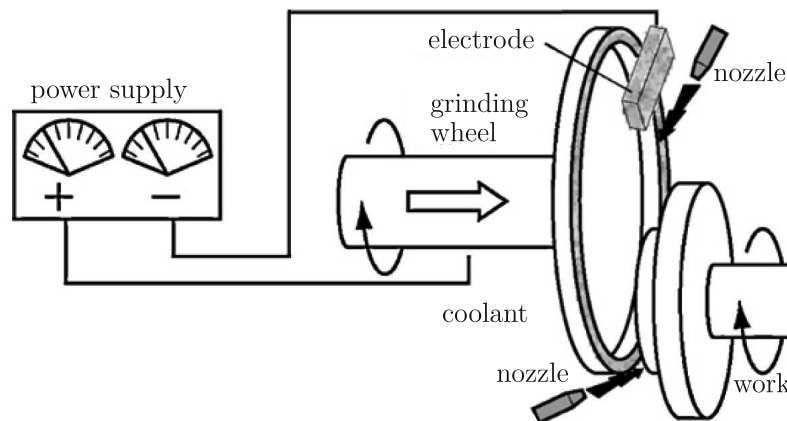


Figure 2.12 – Schematic representation of system setup for chemical dressing process (ELID and ECCD) [OHMO90]

In electrolytic in-process dressing (ELID), electrolysis occurs between the anodic metal bond and an electrically conductive cathode, normally copper. According to Rahman et al. [RAHM09], the cathode is positioned at a distance of 0.1 to 0.5 mm from the grinding wheel, and a special electrolyte is supplied to the gap. Electrical potential is applied between the electrode and grinding wheel, and electrical current flows through the electrolyte, leading to the dissolution of the bond material. During dressing, as a result of electrolysis, a soft, brittle, and electrically insulating layer of anodic oxide is formed, which is then removed during grinding, so that grain protrusion is generated. Because ELID is carried out during grinding, it is important that the bond removal rate is in accordance with the wear rate of the diamonds, to maximize grinding performance [CHEN00a]. Prior to ELID, the grinding wheel must be profiled by means of another dressing method, since ELID is only suitable as a sharpening process. Moreover, after profiling, the grinding wheel must be first pre-dressed by electrolysis to obtain a stable oxide layer before grinding. The process is then defined as a self-controlled process, since when the oxide layer increases, electrolysis decreases due to the non-electrical property of the oxide layer. According to several authors [LIM02, OHMO90, OHMO97, OHMO07], the main advantages of ELID grinding are lower grinding forces and excellent ground surface qualities. The latter because the chips and debris of grain pullout are sucked off by the gel-like hydroxide layer.

Electrochemical in-process control dressing (ECCD) is similar to ELID in its concept, but does not require an oxide or hydroxide layer for a self-control dressing process. The grinding process is monitored, and the rate of dissolution is adjusted, by changing the current density of the power source, in accordance with the sharpness of the wheel and the workpiece material. According to Kramer et al. [KRAM99], ECCD enables to keep the grinding wheel in an optimum state of sharpness and achieve thus

a more reliable grinding process, so that workpieces with better dimensional stability, conformity of shape and superior surface quality can be manufactured.

Apart from the aforementioned advantages, electro chemical dressing processes have also disadvantages. First of all, these processes are very time consuming and not sufficiently accurate for being used as a profiling method, as stated by Schöpf et al. [SCHO01a]. Thus only sharpening is suitable with ELID and ECCD. The electrolyte is in general not appropriate as a grinding cutting fluid. The use of two different fluids inside the grinding machine is not always feasible, since it is difficult to ensure the separation of these fluids. In addition, the electrolyte is hazardous and must be handled with care [SCHO01a].

#### 2.4.4 Electrical discharge dressing

In electrical discharge machining (EDM) discharges occur between two electrical conductive electrodes, the tool electrode and the workpiece, in a gap filled with dielectric fluid, i.e. an insulating medium, which prevents electric current to flow directly from one electrode to another. At the beginning, high voltage is applied between the electrodes, the open circuit voltage, so that after a certain delay time the breakdown strength of the dielectric is overcome. It occurs at a specific location within the gap, where conditions are proper for a discharge. At this moment, the plasma channel starts forming, i.e. a highly ionized gas with high temperatures is created, and electric current flows between both electrodes. Workpiece material is thus locally heated and a certain volume of molten material can be ejected from the melting pool, especially at the end of the discharge, when the voltage is switched off and the plasma channel/bubble collapses. Since only a small volume of material is removed per single discharge, high pulse frequencies have to be applied aiming to achieve sufficient material removal rates. Pulse frequencies ranging from 1 kHz to 1 MHz are commonly applied. Between consecutive discharges a pulse interval time is needed to allow the dielectric strength to be recovered and to cool down the electrodes.

Electrical discharge machining is almost exclusively used to erode electrically conductive materials, and therefore metal bonded grinding wheels can be conditioned by means of this method [KLOC07a]. Thus, grain protrusion can be generated, since diamonds are electric insulators and cannot be directly eroded [KLOC09d]. Accordingly, bond material between abrasive grains is removed, and sharp grinding wheels are created.

The work carried out by Lazarenko [LAZA43] in 1943 marked the beginning of the development of electrical discharge machining (EDM). Electrical discharge dressing (EDD), however, was first proposed only approximately 45 years later, in the late 80's, by Suzuki et al. [SUZU87]. At that time, EDD was developed aiming to improve the



grinding performance of metal bonded diamond wheels for grinding ceramics, such as silicon nitride. Suzuki et al. [SUZU87] suggested the integration of electrical discharge machining into a grinding machine and pointed out that both variants of EDM could be used for conditioning metal bonded grinding wheels. Electrical discharge machining has basically two variants, namely sinking EDM and wire EDM, which are called respectively sinking and wire electrical discharge dressing (SEDD and WEDD) when used in the context of conditioning.

In sinking electrical discharge dressing (SEDD), a shaped tool electrode, normally copper or graphite, is used and its negative shape is copied to the grinding wheel. Figure 2.13 illustrates the SEDD method, in which both the shaped electrode and the grinding wheel rotate, dielectric is supplied to the erosion gap via external free jet nozzles and the grinding geometry is created by plunging the shaped electrode into the grinding wheel, in radial direction. This process is therefore similar to mechanical form dressing, in which a profiled diamond roller is used as dressing tool.

One of the main disadvantages of SEDD is electrode wear. In electrical discharge machining, material is not only removed from the workpiece but also from the tool electrode, causing wear and consequently dressing inaccuracies [SANC08, SUZU87]. Moreover, dressing accuracy depends directly on the accuracy of the manufacturing process used for shaping the tool electrode. Thus, in SEDD wear compensation plays a decisive role, so that after some dressing cycles the electrode must be reshaped or replaced.

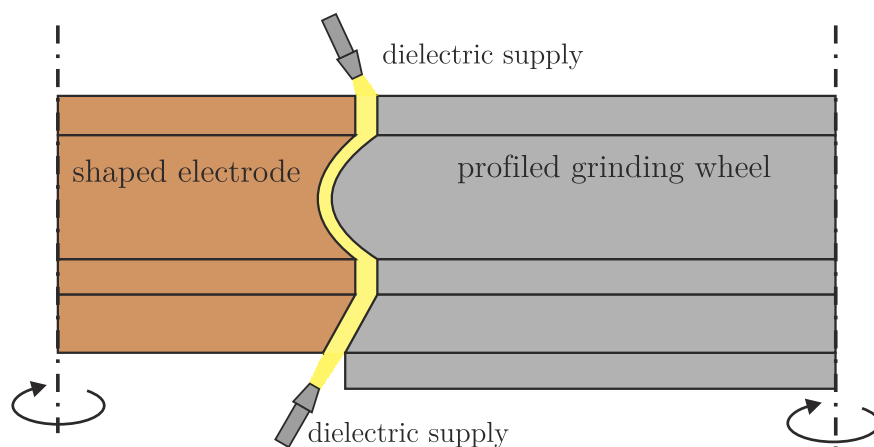


Figure 2.13 – Schematic representation of sinking electrical discharge dressing [SUZU87]

Suzuki et al. [SUZU87] suggested the integration of a turning tool inside the grinding machine to compensate for electrode wear in sinking electrical discharge dressing. In this case, however, conditioning needs both an EDM unit and a kind of lathe within the grinding machine, which makes this process excessively expensive. Sanches et al. [SANC08] proposed a new method of SEDD, in which a single-point

electrode of copper is used for conditioning metal bonded CBN grinding wheels. Single-point electrodes with a diameter of only 60  $\mu\text{m}$  were applied. A schematic representation of the proposed experimental setup is shown in Figure 2.14. A mathematical model was derived to compute the electrode path, axial dressing feed rate and to compensate electrode wear. This dressing process is, however, not enough accurate, very time-consuming and difficult to be implemented, especially because it requires the prior knowledge of the grinding wheel profile so as to generate the CNC path and to calculate the dressing feed rates. Grinding wheel profile has to be constantly monitored by means of a profilometer, as illustrated in Figure 2.14.

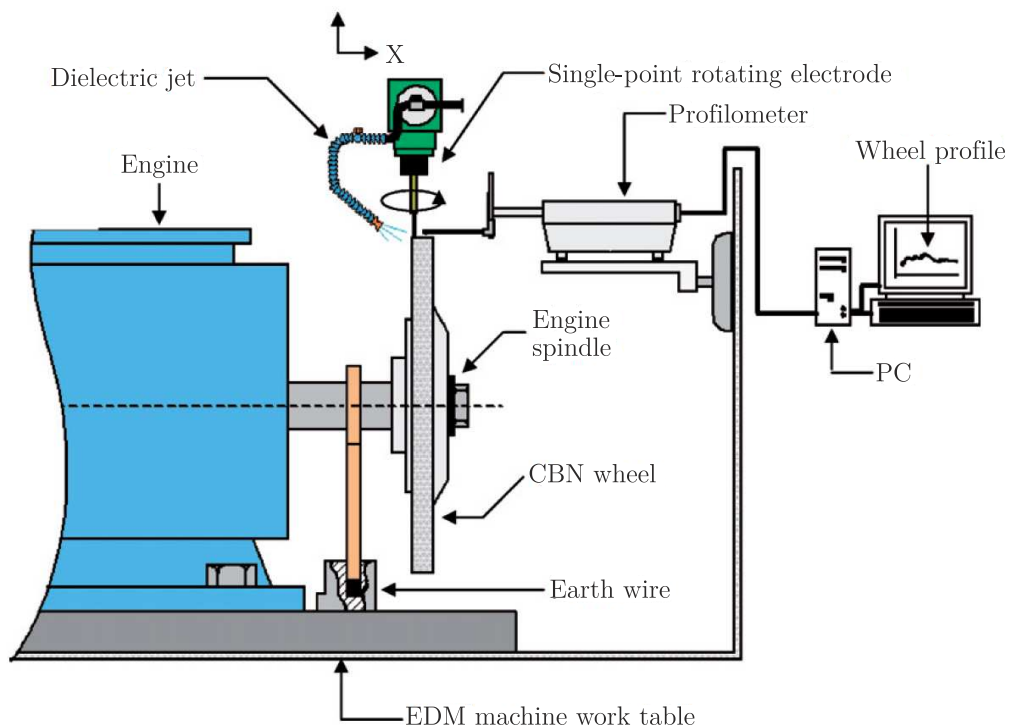


Figure 2.14 – Experimental setup for SEDD with a single-point electrode [SANC08]

Ohmori et al. [OHMO00] developed an ELID centerless grinding system for precision grinding of small, hard and brittle cylindrical parts, such as hardened steel, silicon nitride and zirconium oxide, and used sinking electrical discharge dressing (SEDD) to first profile the grinding wheel. SEDD was performed at low dressing speeds, approximately 2.5 m/s, using a copper tungsten electrode for dressing a bronze bonded grinding wheel. Fine grained wheels were dressed, i.e. mesh sizes of 800, 2,000, 4,000 and 8,000 were tested. The authors claim that a good dressing accuracy was achieved, namely a straightness of 6  $\mu\text{m}$  over a wheel width of 50 mm and roundness of 2  $\mu\text{m}$  in a grinding wheel diameter of 150 mm.

In wire electrical discharge dressing (WEDD), different wheel profiles can be manufactured with the same wire electrode and wear compensation is guaranteed by using a continuous unwinding wire supplied from a spool [KLIN10, SUZU87, WEIN10a,

WEIN10b]. This process is thus more flexible in comparison to sinking electrical discharge dressing, since for the latter new shaped electrodes are required for every different grinding wheel profile. Figure 2.15 shows a schematic representation of the wire electrical discharge dressing process. In this case, the tool electrode, the wire, is not fed only in radial direction as in SEDD, but rather works as a reciprocating process, in which the wire travels in both radial and axial direction at a specific dressing feed rate. A dressing depth of cut  $a_{ed}$  is incremented after each dressing pass. It is therefore similar to mechanical form dressing, in which the dressing tool follows a CNC path to create the wheel profile. Different wire types can be used (diameter and materials), influencing, for example, the sharpness of internal profile edges and achievable material removal rates.

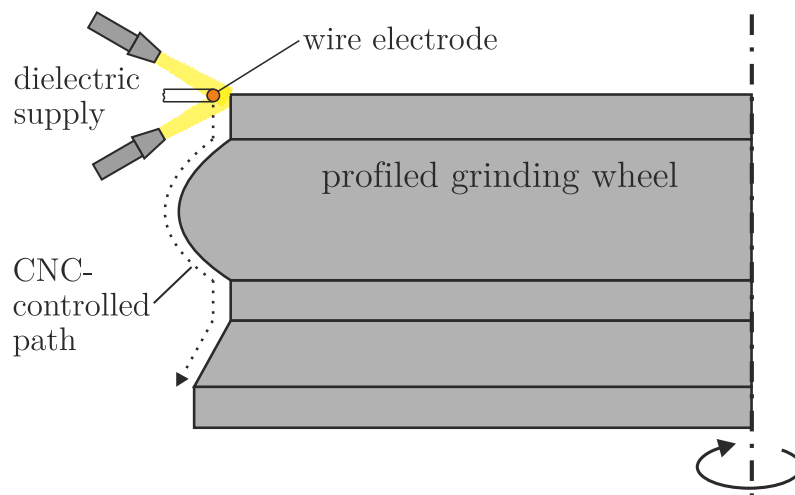


Figure 2.15 – Schematic representation of wire electrical discharge dressing (WEDD)

In contrast to SEDD, tool electrode wear does not play the same major role in WEDD, since the wire is continuously renewed. Wire breakage, however, can occur, and lead to an interruption of the erosion process. This problem can be minimized by choosing the right set of erosion parameters and the type of wire electrode material. In WEDD, dressing accuracy does not depend on the process used to manufacture the tool electrode anymore, but rather on the accuracy of the wire positioning system and the erosion process itself. Therefore, when working with wire electrodes, special attention should be given to wire deviations [DAUW89, DAUW94, WEIN10a]. In particular when dressing grinding wheels, small wire deflections, i.e. a few micrometers, are not acceptable, since very tight tolerances are usually required in grinding processes.

Wire deflection is mainly caused by different forces acting in the erosion gap, such as hydraulic, electro static and electro dynamic forces. As a result, geometrical errors are generated on eroded workpieces. To improve the accuracy of very thin rods (diameter of less than 50  $\mu\text{m}$ ) machined by WEDM, Masuzawa et al. [MASU85] have initiated the application of a wire guide at the erosion zone, a method named wire

electrical discharge grinding (WEDG). By reducing wire vibrations and deflections, wire electrical discharge grinding guarantees better machining accuracy, and therefore has been mainly used in micro-EDM applications [MASU05]. Figure 2.16 shows a schematic representation of WEDG and a micrograph of a thin rod of only 30  $\mu\text{m}$  in diameter manufactured by this method. The same WEDG principle can be applied in WEDD, in which a wire guide can be used for guiding the wire in the dressing zone. This method is proposed in this work and discussed later in Chapter 5.

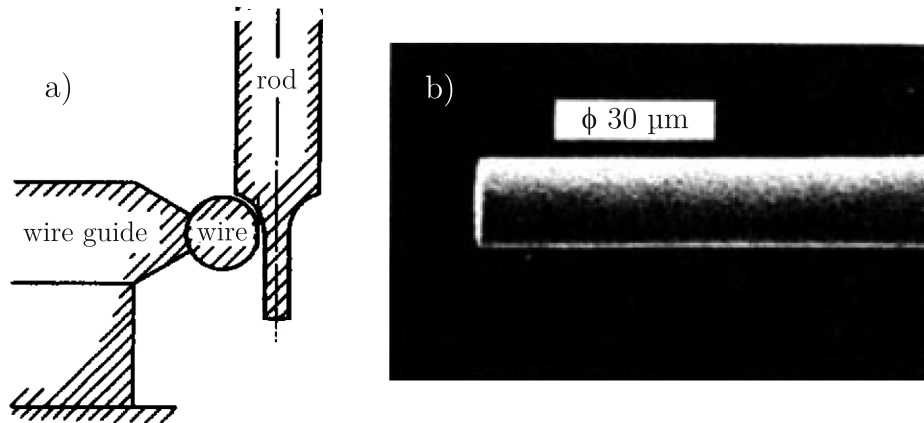


Figure 2.16 – Wire electrical discharge grinding (WEDG): a) Schematic representation; b) Rod of diameter 30  $\mu\text{m}$  manufactured using WEDG [MASU85]

Wire electrical discharge dressing was investigated by Rhoney et al. [RHON02a, RHON02b]. A flexible and corrosion resistant spindle was first designed and integrated into a wire cut machine. Deionized water was used as dielectric in all experiments and a metal bonded diamond wheel with diamonds of equivalent diameter of 54  $\mu\text{m}$  was dressed. High protrusion was achieved, such as 60% in some cases. WEDD was compared to a mechanical dressing process, in which a stationary diamond pin was used for conditioning the grinding wheel. Regarding surface quality of ground silicon nitride workpieces, better results were achieved using mechanical dressing. Grinding forces were in general similar for grinding wheels conditioned by means of both dressing methods, although, in some cases, higher forces were achieved using the WED-dressed grinding wheel. Wheel wear was higher when the mechanically-conditioned grinding wheel was used, although very low G-ratios were achieved in both cases. G-ratios no higher than 180 were achieved, which is very little for metal bonded diamond wheels.

Klocke et al. [KLOC07a, KLOC07b, KLOC07c] also investigated wire electrical discharge dressing, focusing the work on fine grained bronze bonded diamond wheels (diamonds between D7 and D20). Two conventional WEDM machines were used to carry out dressing experiments, one using deionized water and other hydrocarbon-based dielectric. A special rotating device was mounted in both WEDM machines to allow for accurate clamping of the grinding wheel. A free stretched wire was used as electrode

tool in all experiments. Only low discharge energies were applied, aiming not to introduce thermal damages to the diamonds. The authors stated that both dielectrics are suitable for WEDD, although the use of hydrocarbon-based dielectric leads to smaller gaps, and so to more restrictions regarding applicable grain sizes. According to Klink et al. [KLIN09, KLIN10], virtually any profile can be created on the grinding wheel using Wire-EDM, which represents an important advantage in comparison to conventional mechanical dressing methods such as SiC-dressing. Figure 2.17 shows some profiles generated in fine grained grinding wheels by means of WEDD.

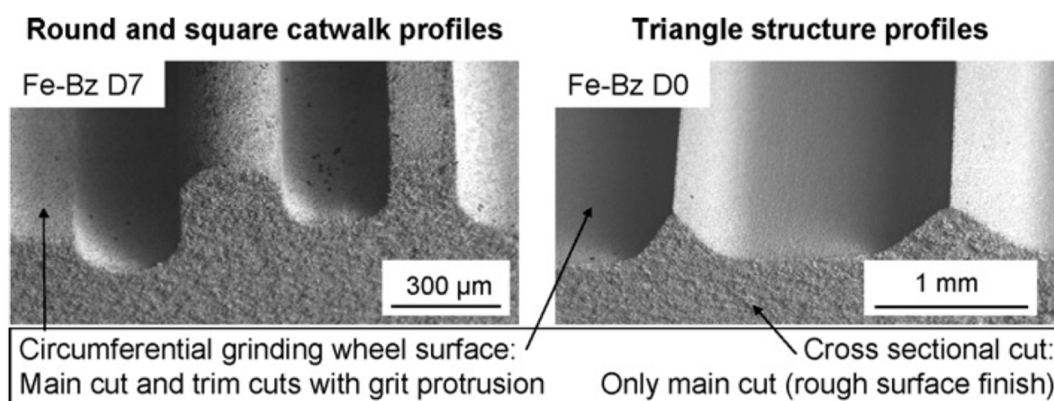


Figure 2.17 – WED-dressed grinding wheels with different profiles [KLIN09, KLIN10]

Tönshoff and Friemuth [TONS00] proposed the use of in-process electro contact discharge dressing (ECDD) to enhance cutting performance of fine grained diamond wheels in grinding ceramics. In ECDD, which is in fact a variant of the SEDD process, the tool electrode is constantly ground by the grinding wheel. Chips removed from the tool electrode trigger discharges that dress the grinding wheel. The authors claim that it is possible to use ECDD to help keep grinding wheels sharper for longer time and consequently work with lower grinding forces. Moreover, lower wear is achieved in comparison to conventional in-process abrasive dressing using sharpening stones.

In electrical discharge dressing, different dielectrics can be applied. Generally, the dressing process is carried out inside an EDM machine, so that, in most cases, deionized water is applied in WEDD and hydrocarbon-based dielectric in SEDD. Wang et al. [WANG06] investigated the dry-electrical discharge assisted truing and dressing process for conditioning metal bonded diamond wheels. A standard stationary diamond tool was used for truing the grinding wheel and this process was assisted by sinking EDM, where metal bond could be additionally removed by means of erosion. It is considered thus a dry-SED-sharpening process. According to Wang et al. [WANG06] wear rate of diamond dresser was reduced, lower dressing forces were achieved, and the grinding wheel was kept sharper for longer time. Cai et al. [CAI09] showed that mist-jetting electrical discharge dressing (MEDD) can be used for conditioning superabrasive

grinding wheels. Emulsion mist instead of hydrocarbon-based dielectric was used in a sinking EDM machine, to avoid fire. It was shown that high grain protrusion can be achieved by means of this dressing method. Uematsu et al. [UEMA99] indicated that EDD can be carried out using conventional dielectrics as well as mist air, dry, compressed air and cold air. The authors claim that when cold air is used, wear of the SED-dressed wheel is lower in comparison conventionally conditioned wheels. Iwai et al. [IWAI01] tested SEDD using compressed air and a water-based dielectric. Graphite electrodes were used and experiments were carried out in a vertical machining center, especially modified for this purpose. According to the authors, dressing efficiency is very low when compressed air is used in comparison to wet conditions and the type of dielectric (dry or wet) does not influence grinding forces and wheel wear.

As mentioned before, diamonds are generally not eroded in electrical discharge dressing, since they are not electrical conductors [FIEL79, SEAL92]. Therefore, grain protrusion is generated, which is an important characteristic of grinding wheels. Suzuki et al. [SUZU04, SUZU05], however, developed a grinding wheel with electrically conductive diamonds for precision grinding of ceramics, carbides and glasses. An SEDD process was used and both bond material and diamonds were conditioned. The authors reported a significant decrease in grinding forces (about 21%) when grinding tungsten carbides with conductive diamond wheels in comparison to non-conductive diamond ones. According to the authors, sharpened diamond edges are created in SED-dressed wheels with conductive diamonds (also all negative flank angles are at least transformed into zero flank angles), the reason why lower forces were achieved.

Electrical discharge machining is a thermal removal process, in which discharges with highly concentrated energies warm-up, melt and evaporate material from the workpiece [KUNI05]. Depending on the discharge energy, craters with diameters up to a few hundreds of micrometers are created. When conditioning of metal bonded diamond wheel is assisted by means of electrical discharge machining, one would expect thermal damages to the diamonds, especially if high discharge energies are applied. Klink et al. [KLIN09, KLIN10, KLOC07a, KLOC07b] measured a graphite layer of about 0.5  $\mu\text{m}$  on small diamond grains (ranging from 5 to 20  $\mu\text{m}$ ) after wire electrical discharge dressing in deionized water. Schöpf [SCHO01b] stated that holes caused by discharges were found in diamonds after ECDM. In spite of that, different studies [CAI09, RHON02a, RHON02b, WEIN10a, WEIN10b] have shown that EDM is a suitable dressing process for conditioning metal bonded diamond wheels. Although several studies already addressed electrical discharge dressing for metal bonded diamond wheels, the reason why these processes do not severely affect the diamonds is still unclear. This topic is addressed later in Chapter 6.

EDD can also be designed as in-process dressing (In-Process Electro Discharge Dressing, IEDD), as reported by Lee [LEE00a]. In this case the grinding wheel is sharpened during grinding, and wear can be continuously compensated. Lee [LEE00a] mounted a SEDD-prototype on a face grinding machine and used deionized water as dielectric. Bronze bonded diamond grinding wheels with equivalent diamond diameters ranging from 20 to 40  $\mu\text{m}$  were used. It was reported that IEDD is feasible and can bring benefits during grinding. Sudiarso and Atkinson [SUDI08] carried out in-process sinking electrical discharge dressing to shape metal bonded grinding wheels (macro geometry) and simultaneously electro chemical dressing for sharpening (micro geometry). A special fluid, designed to be used as dielectric, electrolyte and cutting fluid, was used and experiments were performed in a face grinding machine. According to the authors, higher dressing accuracy and better ground surface quality were achieved by means of this non-conventional dressing method in comparison to conventional SiC-dressing.

### 2.4.5 Electro chemical discharge dressing

Electro chemical discharge dressing (ECDD) combines electro chemical machining (ECM) and electrical discharge machining (EDM), allowing for truing and dressing of metal bonded superabrasives wheels [SCHO01a, SCHO01b]. Figure 2.18 shows the voltage and current waveforms during ECDD. The electro chemical process, which is responsible for sharpening the metal bonded grinding wheel, is assisted by a pulse of electrical discharge machining, which helps to profile the tool. Thus, profiling and sharpening occur simultaneously in ECDD.

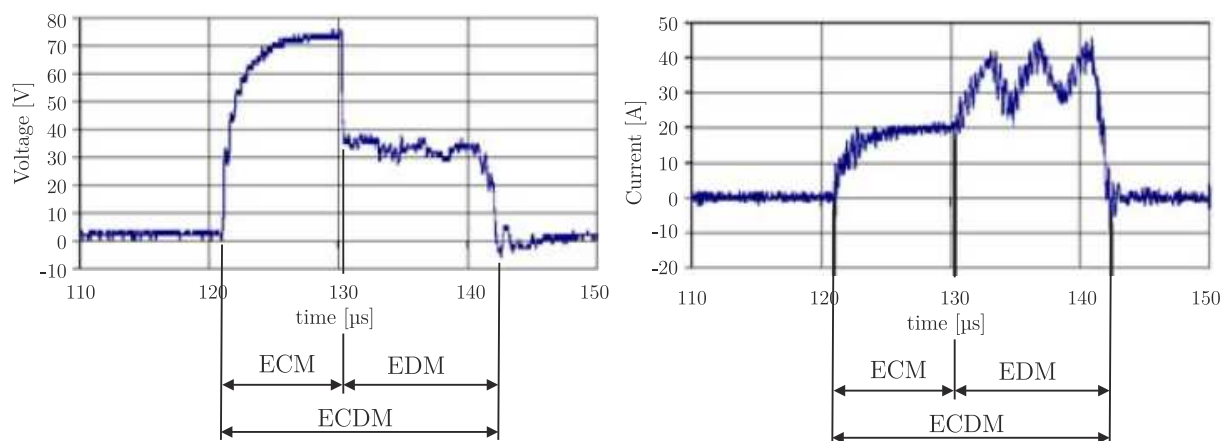


Figure 2.18 – Voltage and current waveforms during ECDD [SCHO01a]

Schöpf et al. [SCHO01a] applied ECDD to prepare metal bonded grinding wheels for centerless grinding. A fully synthetic water-soluble concentrate (mixed to deionized water in a 3% solution), special manufactured by Blaser Swissslube to reach the required electrical conductivity, was used for both dressing and grinding. According to

the authors, either only sharpening (ECM) or the combined process (ECDD) could be adjusted. Moreover, dressing was designed as an on-machine process, in which the grinding wheel is conditioned from time to time on pre-defined time steps, rather than during grinding (in-process dressing). Regarding surface quality of ground workpieces, i.e. surface roughness and roundness, ECDD showed advantages in comparison to conventional SiC-dressing.

As a main disadvantage, the process uses a fluid that was developed to suit both dressing and grinding processes, i.e. it is not ideal for grinding. Furthermore, this fluid (electrolyte) is hazardous, and like in ECD has to be handle with care.

### 2.4.6 On-machine dressing

The time associated to dressing is, in general, seen as a non-productive time. Dressing is just an auxiliary process, since the final goal is essentially to grind workpieces with a pre-defined specification, and thus, the time necessary to carry out wheel preparation generally reduces the time available for grinding. As shown before, electrical discharge dressing (EDD) is normally performed in EDM machines, as an offline process. This happens because on-machine electrical discharge dressing requires the integration of an EDM unit inside the grinding machine, what is normally seen as difficult and costly. Thus, after reaching a certain wear, the grinding wheel has to be removed from the grinding machine and assembled in the EDM machine to be conditioned. After dressing, the reverse way is also necessary, and the grinding wheel is reassembled in the grinding machine. In this back-and-forth, not only non-productive time increases, representing high costs, but also clamping errors are more likely to occur (errors in the order of 2 to 5  $\mu\text{m}$  can occur), as already emphasized by some authors [KLOC09b, SUZU87, WEIN10a, WEIN10b]. According to Badger et al. [BADG11] grinding wheel eccentricity and run-out errors have a negative impact on grinding forces and wheel wear, especially because chatter is more likely to occur.

To illustrate how even small grinding wheel run-out errors can influence grinding, radial feed per grinding wheel revolution was plotted for some different grinding parameters (Figure 2.19). Grinding wheel and workpiece diameters of 400 mm and 50 mm, respectively, and three different specific material removal rates were considered. In plunge grinding, radial feed per grinding wheel revolution  $f_a$ , wheel circumferential speed  $v_s$  and specific material removal rate  $Q'_w$  are written as follows

$$f_a = v_f / n_s \quad (2.3)$$



$$v_s = \pi \cdot d_s \cdot n_s \quad (2.4)$$

$$Q'_w = \pi \cdot d_w \cdot v_f \quad (2.5)$$

where  $n_s$  is the wheel rotation and  $v_f$  the radial grinding feed rate in plunge grinding. Substituting equations (2.4) and (2.5) into (2.3),  $f_a$  can be rewritten as

$$f_a = \frac{Q'_w \cdot d_s}{v_s \cdot d_w} \quad (2.6)$$

According to Figure 2.19, in many cases, the radial feed rate per grinding wheel revolution is lower than 2  $\mu\text{m}$ . Specific material removal rates lower than 20  $\text{mm}^3/\text{mms}$  were chosen since they represent values often used in grinding advanced ceramics, although material removal rates up to 50  $\text{mm}^3/\text{mms}$  can be found in some applications, as mentioned in [KLOC09a]. When grinding wheel speed is increased and/or specific material removal rate is decreased, even lower values of  $f_a$  are reached. This points out how accurate the grinding wheel clamping system must be to avoid grinding problems, such as irregular wheel wear and chatter, which together can deteriorate the quality of ground workpieces. Thus it is recommended to keep the grinding wheel on the spindle in order to limit non-productive times and minimize clamping errors.

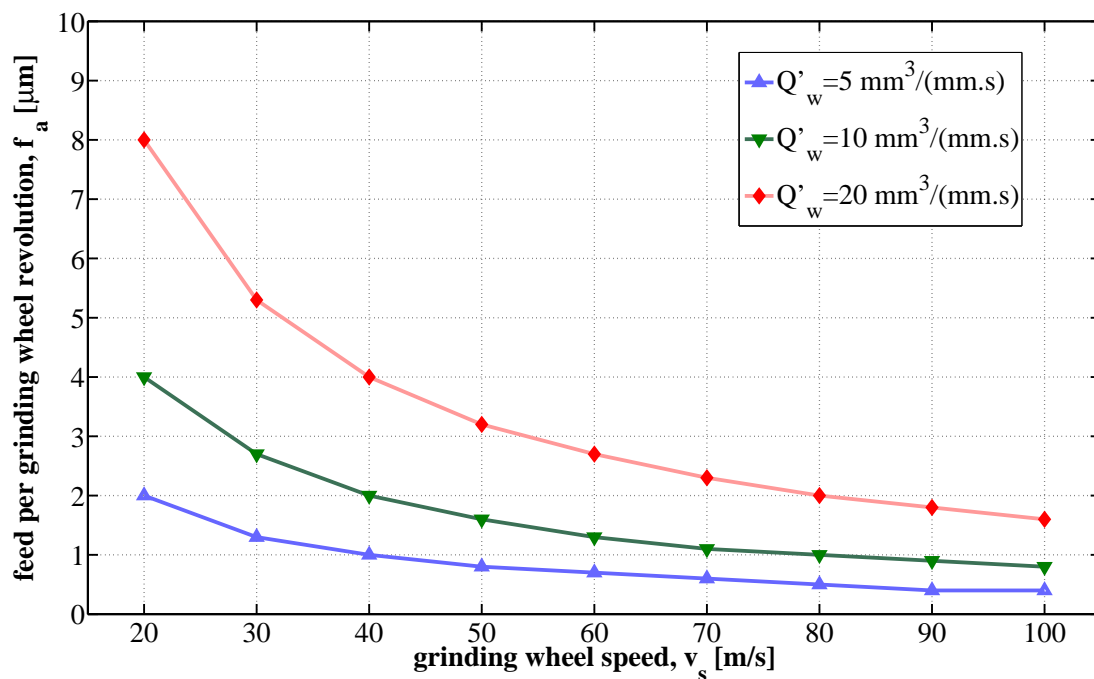


Figure 2.19 – Feed per wheel revolution in plunge grinding as a function of grinding wheel speed, for different specific material removal rates ( $d_s = 400 \text{ mm}$ ;  $d_w = 50 \text{ mm}$ )

In on-machine electrical discharge dressing, another issue is important, namely the relative speed between tool electrode and grinding wheel. In general, electrical

discharge machining is applied with no or very low relative speeds between tool electrode and workpiece. The workpiece normally remains fixed and the tool electrode, the shaped electrode or wire, moves toward the workpiece. In some applications, however, the workpiece also rotates. Cylindrical wire electrical discharge turning (CWEDT) is one example [HADD08a, HADD08b, MOHA08]. In this process a rotary axis is added to the EDM machine aiming to produce axisymmetric parts. Wire electrical discharge grinding (WEDG) also deals with rotating workpieces. Still, in both cases relatively slow rotation speeds are applied. In on-machine EDD, however, high relative speeds can be used, and the grinding wheel, in general, has to be conditioned using the same rotating speed as for grinding, to avoid errors caused by centrifugal forces. Dressing is also carried out at grinding speeds during in-process EDD. According to Uhlman et al. [UHLM05], high speed relative movement between workpiece and tool electrode can significantly influence electrical discharge machining. It was stated that small crater areas are created by increasing speeds above 2.5 m/s (measurements up to 5 m/s were carried out on electrical discharge turning process [UHLM05]). Some authors [HADD08a, HADD08b, WANG96] claim that relative speed affects efficiency of EDM to a great extent, pointing out that material removal rate decreases as relative speed is increased. On the other hand, Matorian et al. [MATO08] described the opposite, indicating that MRR can be increased by means of increasing relative speed. According to Kunieda et al. [KUNI10] the discharge plasma slides easier over the cathode rather than over the anode, as shown in Figure 2.20 for a relative speed of 16 m/s. They carried out die-sinking erosion experiments using relatively long discharge pulses (discharge duration of about 200  $\mu$ s), during which the anode was kept stationary while the cathode was rotating. According to the authors, tool wear (cathode) can be reduced when relative speed is increased, since less material per discharge is removed from the cathode, where the discharge plasma slides the most.

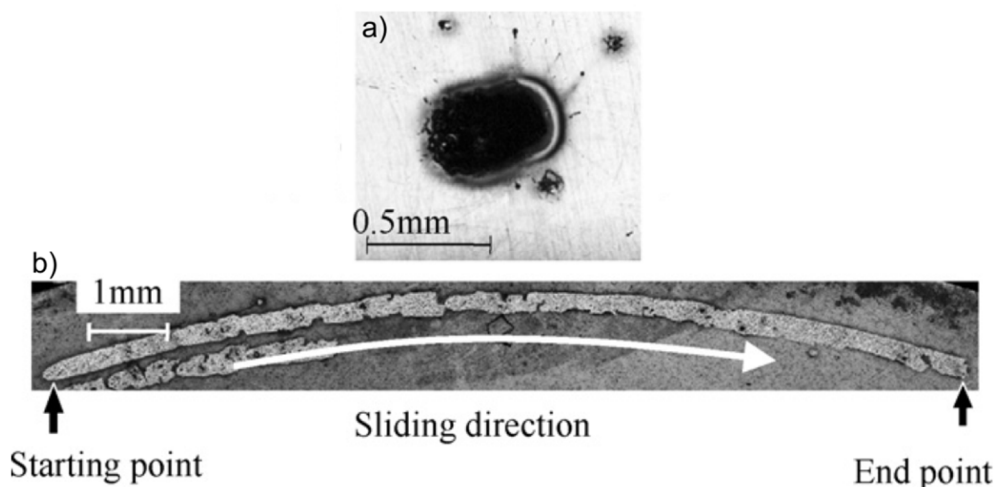


Figure 2.20 – Influence of relative speed on eroded craters (16 m/s): a) discharge crater on anode; b) elongated discharge crater on cathode

## 2.5 EDM modeling

Electrical discharge machining is a complex process in which several disciplines are involved, such as electrodynamics, electromagnetism, thermodynamics and hydrodynamics, so that it is still difficult to combine everything in a comprehensive model [YEO08]. In general, attempts are focused in modeling the plasma channel, material removal rate, tool wear and discharge location.

To calculate the material removal rate, electrical discharge machining is generally modeled based on an electro-thermal mechanism [BECK81b, BECK81a, DIBI89, JENN84, JOSH10, MARA06, PAND86, PATE89, SPUR93, TAN10, TARI82, TARI83, VAN74, VAND74, YEO07]. In this case, material is removed due to high temperatures achieved in the plasma channel during the discharge (high electrical current densities). In most cases, the main goal is to compute the temperature distribution as a consequence of different input parameters and estimate the amount of molten material. Single discharge experiments are usually taken as reference for modeling the process. Analytical and numerical models that describe this process have been derived so far.

Regarding modeling of the material removal rate, one of the main challenges lies in the way how the heat source is described. DiBitonto et al. [DIBI89] suggested a schematic representation of EDM processes, as shown in Figure 2.21, pointing out different types of melting cavities on the anode and cathode electrodes. As stated by DiBitonto et al. [DIBI89], craters created on the anode are generally shallower and larger in comparison to craters created on the cathode electrode, since the plasma radius is much smaller at the cathode. Therefore, the heat source applied to the cathode and anode generally differs considerably. Several approaches are described in the literature, where point or disc heat sources are more commonly applied, but approaches using an expanding-circle heat source or a Gaussian heat source can also be found. The amount of energy that flows to the cathode and anode, the so called erosion power factor  $F_c$ , also represents a challenge in modeling EDM. No consensus is found in the literature, and completely divergent values are used in different models, depending on the preliminary assumptions made by the authors. The power factor  $F_c$  can vary from a low percentage of the discharge energy being distributed to the anode or cathode (and consequently the rest to the plasma formation and dielectric), up to 50% of the available energy for each electrode.

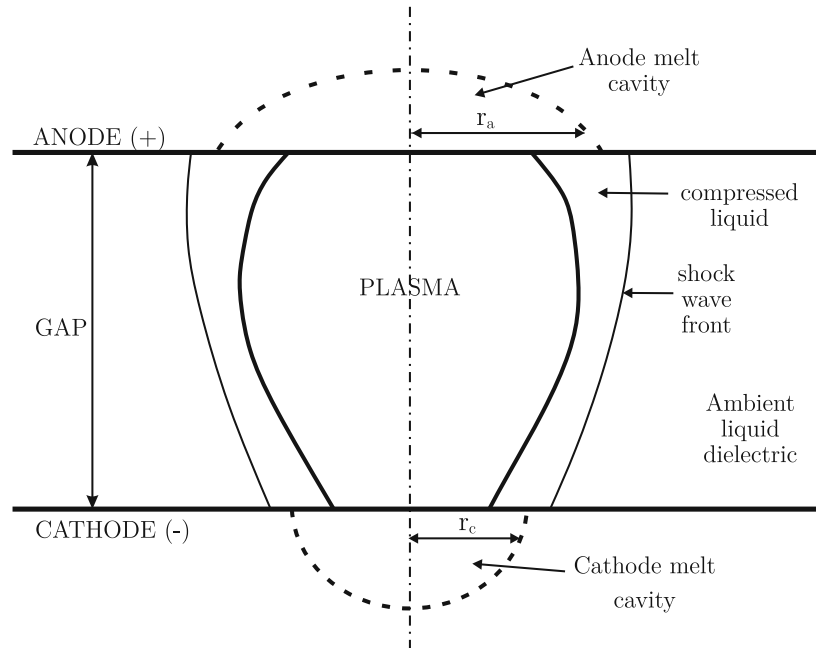


Figure 2.21 – Schematic representation of EDM discharge, showing a shallower and larger ( $r_a$ ) melt cavity on the anode electrode and a deeper and smaller ( $r_c$ ) melt cavity on the cathode electrode [DIBI89, PATE89]

DiBitonto et al. [DIBI89] proposed an point heat source model (PHSM) for the cathode, assuming that 18% of the discharge energy is transmitted to this electrode ( $F_c = 0.18$ ). Figure 2.22 illustrates a schematic representation of DiBitonto's model, showing some calculated isotherms, such as the melting front in  $T = T_{melt}$ . The temperature distribution is calculated based on an analytical solution given by Carslaw and Jaeger [CARS05], which can be expressed as

$$T(r, z, t) = T_0 + \frac{q'' \cdot r}{k} \operatorname{erfc}\left(\frac{r}{2\sqrt{\alpha \cdot t}}\right) \quad (2.7)$$

where  $r$  and  $z$  are the radial and vertical distances to the origin,  $t$  represents time,  $T_0$  is the ambient temperature,  $q''$  is the heat flux,  $k$  and  $\alpha$  represent respectively, the thermal conductivity and thermal diffusivity of the material.

In the erosion model proposed by DiBitonto et al. [DIBI89] latent heats of fusion and vaporization are not considered and averaged thermophysical properties of the workpiece material is assumed over the whole temperature regime (from ambient up to melting temperature). Regarding material removal rates, discrepancies between simulation and experimental results up to 98% were found, particularly when less energetic erosion pulses were used. The plasma flushing efficiency (PFE), which describes the ratio between measured and simulated material removal rate, i.e. PFE represents which fraction of the theoretical molten volume is removed/ejected, was calculated for thirteen different erosion pulses (discharge currents between 2.34 A and

68 A), showing a variation from 2% up to 96%, with an average value of 46% and standard deviation of 28% when all results of PFE are considered within the statistics. These results indicate a poor correlation between experimental and simulation results. For example, for a discharge current of 2.34 A, a material removal rate of 0.3 mm<sup>3</sup>/min was measured while simulation output revealed a MRR of 13.82 mm<sup>3</sup>/min (PFE of 2%). Moreover, simulated craters were very different from measured ones, since a point heat source creates hemispherical crater profiles, and in reality eroded craters are less deep in comparison to their diameters.

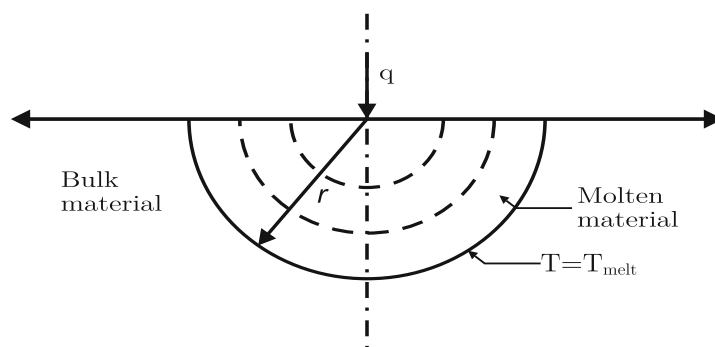


Figure 2.22 – Schematic representation of DiBitonto's cathode point heat source model (PHSM) [DIBI89]

Similarly to the cathode erosion model, Patel et al. [PATE89] proposed an expanding-circle heat source model (ECHSM) for the anode, assuming that only 8% of the available discharge energy flows into this electrode ( $F_c = 0.08$ ). The temperature distribution was again calculated based on an analytical solution given by Carslaw and Jaeger [CARS05]. The authors neglected the effects of latent heats of fusion and vaporization and used averaged material properties over the whole temperature regime. The disc radius was assumed to grow proportional to  $t^{3/4}$  ( $r \propto t^{3/4}$ ), which is in accordance to experiments on exploding wires in water carried out by Robinson (cited in Patel et al. [PATE89]). By comparing experimental and simulation results, discrepancies up to 85% regarding material removal rates were verified, especially for low energetic erosion pulses. The same set of experimental results used by DiBitonto [DIBI89] was taken as reference and the plasma flushing efficiency (PFE) was again computed. Among thirteen different erosion pulses, from 2.34 A up to 68 A, PFEs from 15% up to 94% were achieved, with an average value of 52% and standard deviation of 23% when all results of PFE are computed together.

Joshi and Pande [JOSH10] proposed a Gaussian distribution of the heat flux to describe the disc heat source used for modeling die-sinking EDM (Figure 2.23). Furthermore, temperature-dependent thermal conductivity of the material and the latent heat of fusion were considered. The latent heat of fusion was considered to be distributed over the whole temperature regime, from ambient temperature to the

melting point, incorporated in the specific heat. The temperature distribution inside the workpiece was computed and material removal rates were calculated based on theoretical discharge frequencies. The authors compared simulation results with the same set of experimental results used by DiBitonto et al. [DIBI89] and Patel et al. [PATE89], and assumed that 18% of the available discharge energy was transmitted to the cathode ( $F_c = 0.18$ ). The authors claim that better correlation between experimental and simulation results were achieved. Nevertheless, plasma flushing efficiencies between 2.5% and 153% were achieved when the latent heat of fusion was neglected and between 2.5% and 207% when it was considered. To correct these discrepancies, the authors recommend the use of different erosion power factors  $F_c$  for different erosion pulses, depending on the energy level of each pulse.

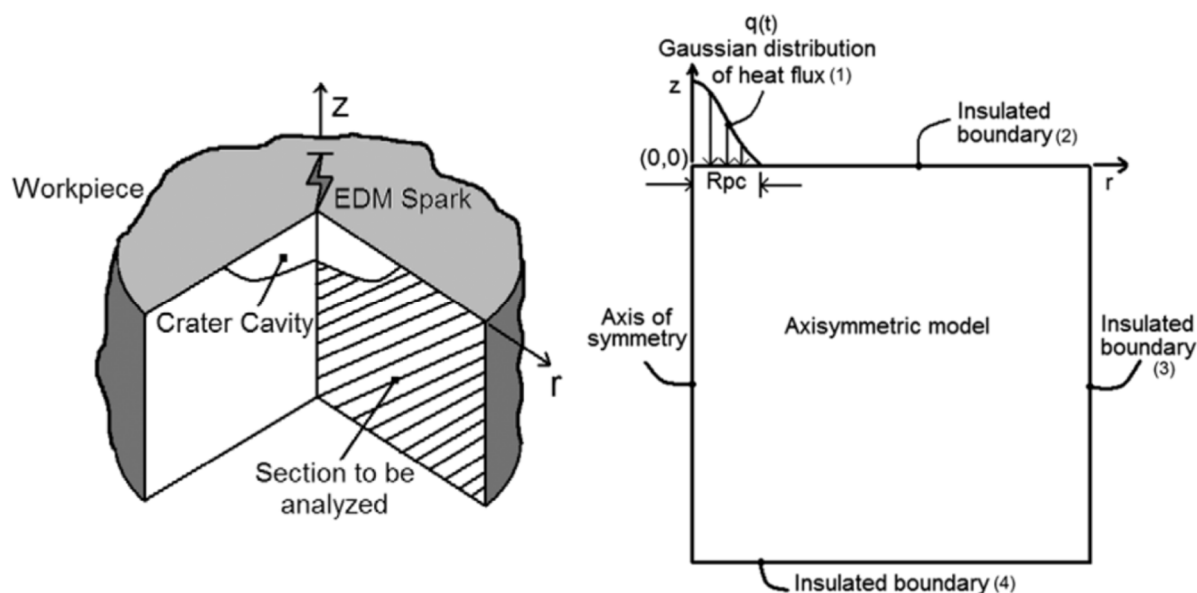


Figure 2.23 – Schematic representation of Joshi and Pande's thermo-physical model for die-sinking EDM using a Gaussian distributed heat source [JOSH10]

In Jilani's model [TARI82] and Beck's model [BECK81a] a disc heat source was used for modeling the heat flow into the workpiece. Figure 2.24 shows a schematic representation of the assumptions made in these models. In both cases an erosion power factor of  $F_c = 0.5$  was assumed, i.e. it is considered that 50% of the available discharge energy flows into the workpiece. As a consequence, the simulated material removal rates were far higher than those obtained experimentally. None of these models considered temperature-dependent properties of the involved materials as well as latent heats of fusion and vaporization. Apart from both aforementioned models, different works describe mathematical solutions for using a disc heat source in modeling EDM [BECK81b, MARA06, TARI83, VAN74, YEO07].

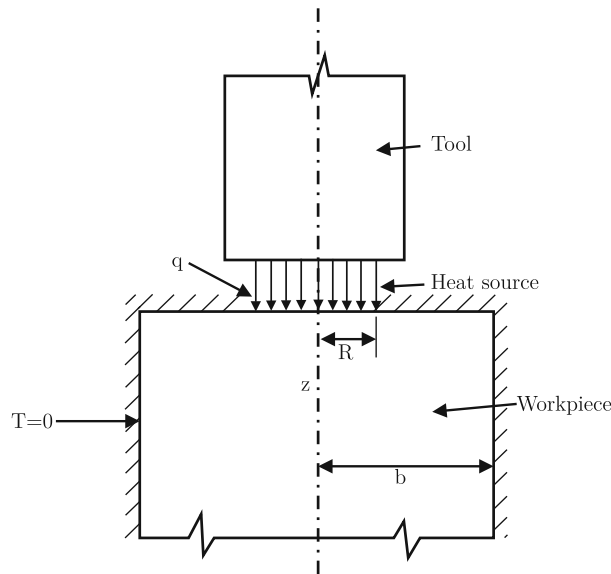


Figure 2.24 – Schematic representation of Jilani's disc heat source model [TARI82]

Pandey and Jilani [PAND86] compared experimental and simulation results of material removal per single discharge assuming stationary and expanding disc heat sources (Figure 2.25). It can be seen that simulation results are improved when an expanding heat source is considered, although still poor correlation is shown. Expanding disc heat sources were also used in other models [JENN84, SPUR93, TAN10], showing improvements in comparison to models that considered heat sources as stationary.

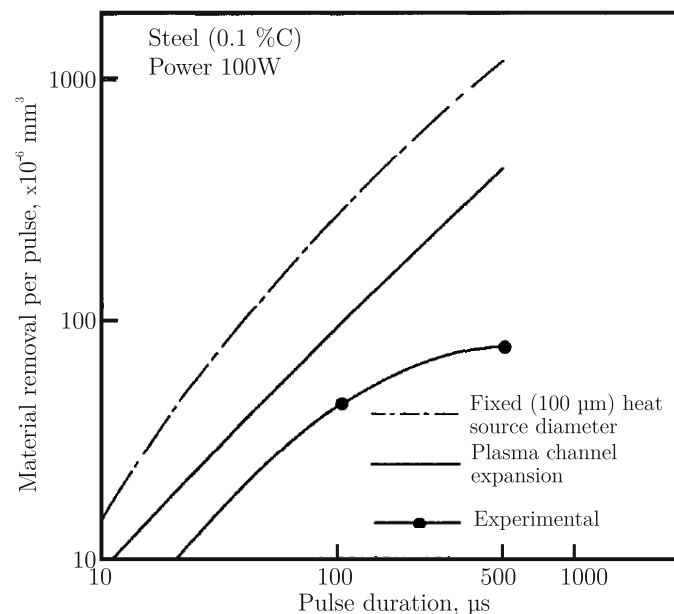


Figure 2.25 – Comparison between experimental results and simulation results with static and expanding disc heat sources [PAND86]

Klink [KLIN10] calculated the electric field distribution inside the erosion gap in EDD, considering diamonds embedded in one of the metallic electrodes and the gap

filled with different dielectric fluids (deionized water and hydrocarbon-based dielectric). The author considered the following relative permittivities  $\epsilon_r$  when performing the calculations: 2.4 for the hydrocarbon-based dielectric, 80 for the deionized water and 5.5 for the diamond. Based on that, it was stated that when deionized water is used, an electric field concentration can occur just on the border between the diamond and the metal, since deionized water has a higher relative permittivity in comparison to the diamonds. On the other hand, when hydrocarbon-based dielectric is used there is a risk of damaging the diamond, since the electric field concentrates on the diamond, which has a higher relative permittivity than the hydrocarbon-based dielectric. Figure 2.26 shows some results obtained pointing out the concentration of electric field around the diamond for deionized water and on the tips of the diamonds for hydrocarbon-based dielectric. Moreover, Klink [KLIN10] stated that for hydrocarbon-based dielectrics too many finishing cuts can result in a flat surface without grain protrusion, i.e. in a surface where the diamonds were removed by means of EDM.

Chen and Li [CHEN00a, CHEN00b] used a similar approach as Klink [KLIN10] to calculate the electric field distribution inside the gap, in this case, however, for ELID instead of EDM. The authors found that a concentration of electric field occurs just at the diamond/metal boundary and causes the metal dissolution to be the highest at these locations.

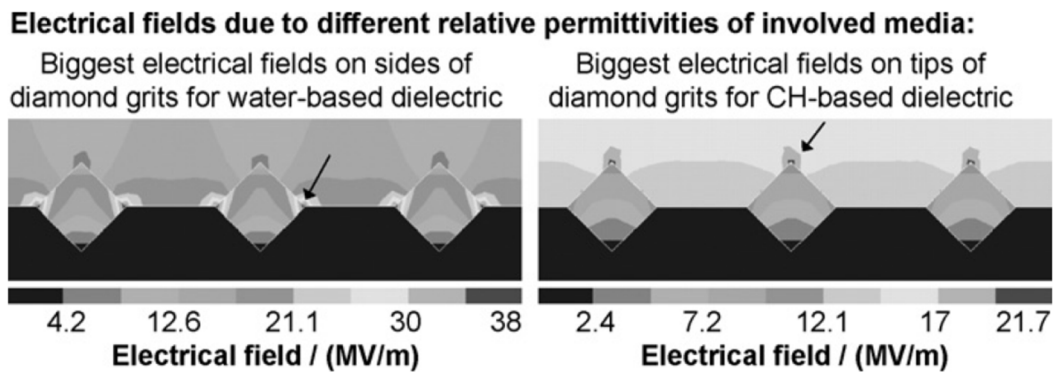


Figure 2.26 – Formation of the electric field in hydrocarbon-based and water-based dielectrics after the supply of voltage and before dielectric breakdown [KLIN10]

In summary, it can be concluded from this section that regarding EDM modeling, the erosion power factor and the way how the heat source is described play a decisive role in achieving accurate simulation results. Moreover, temperature-dependent material properties and the latent heats of fusion and vaporization must be taken into consideration to further increase accuracy of simulation results. Regarding the electric field distribution, special attention has to be paid to the type of dielectric used during erosion, to avoid or minimize damages to the diamonds and ensure that they are kept strongly attached to the metal matrix after dressing.



### 3. Problem description and objectives

According to the state of the art presented in the previous chapter, it can be stated that the application of metal bonded diamond wheels still find limitations especially due to its poor dressability. Conventional dressing using SiC-wheels is very limited, the reason why several non-conventional dressing methods are under investigation. Among them, EDD appears as a real potential for future industrial applications. Bond material is removed while non-electrically conductive diamonds are not eroded. In contrast to the conventional ECM process, high material removal rates can be achieved in EDM. Hydrocarbon-based dielectrics are also very often used in EDM, which have lots of similarities with grinding oils. Moreover, electrical discharge machining is an accurate manufacturing process by which small machining tolerances can be met.

Based on the literature review presented before, some interesting aspects concerning electrical discharge dressing were found:

- In virtually all research work done in this field, electrical discharge dressing is carried out in conventional electrical discharge machines. This is fact for both EDD variants, namely sinking and wire electrical discharge dressing;
- Dressing material removal rates are rarely addressed. Since in most research works EDD is carried out outside the grinding machine, dressing non-productive time does not appear to be an important issue;
- Dressing accuracy is practically neglected in most of the research works. When sinking electrical discharge dressing is used, electrode wear is mostly not mentioned. When wire electrical discharge dressing is applied, issues regarding wire deviation are not addressed;
- In-process dressing is a method by which dressing non-productive time can be reduced and the quality of the grinding wheel can be kept more constant over time. Since most research works focused on offline EDD, in-process

dressing is practically not addressed. ELID, on the other hand, is often applied as a sharpening process (not for profiling);

- Information regarding wheel wear of EDD-dressed grinding wheels is nearly not found in literature;
- Electrical discharge dressing is in general carried out using low relative speeds between tool electrode and the grinding wheel. This is again the consequence of focusing on offline dressing processes;
- In EDM, several model approaches were already proposed. However, there is not a model of material removal that deals with dressing and takes diamond graphitization into account.

The main objectives of this work are thus associated to the above mentioned aspects (research gaps). The main focus is therefore on on-machine electrical discharge dressing of metal bonded grinding wheels. To assess this process, the following aspects have to be taken into consideration:

- An electrical discharge dressing unit is needed and has to be integrated into a grinding machine;
- The dressing process has to suit the grinding process, not the opposite. This means that standard grinding oil has to be used as dielectric fluid for dressing metal bonded grinding wheels;
- Dressing accuracy must be addressed and non-productive times associated to dressing have to be analysed;
- SiC-dressing is a reference process, to which electrical discharge dressing is compared. The topography of the dressed grinding wheel as well as its influence on grinding results has to be assessed;
- The feasibility of in-process electrical discharge dressing has to be evaluated. Therefore, the EDD unit must be mounted on the clamping system of an internal grinding spindle, to allow the utilization of small grinding wheels;
- A thermal model is needed, aiming to assist in understanding electrical discharge dressing and to help reduce the amount of necessary time-consuming experiments;
- EDM at high relative speeds has to be addressed, since EDD should be performed at grinding speeds for both in-process and on-machine dressing.

As a global objective, this work intends to contribute to improve the dressability of metal bonded grinding wheels, and bring electrical discharge dressing one step closer to real industrial applications.

## 4. Conventional versus WED-dressing

In order to evaluate the feasibility of wire electrical discharge machining for truing and dressing metal bonded diamond wheels, dressing and grinding tests were carried out. In this chapter, the materials and methods used for carrying out these experiments are first presented. A brief description of the wire electrical discharge dressing unit used in this work is also shown. Dressing and grinding results are discussed, and wire electrical discharge dressing is mainly compared with conventional dressing, in which a silicon carbide wheel is used as dressing tool.

### 4.1 Materials, equipment and methods

This section describes the materials and methods used in all dressing and grinding tests carried out in this work. For performing dressing tests different EDM machines were primarily used. Additionally, a wire electrical discharge dressing unit (WEDD unit) was designed and integrated into a grinding machine for carrying out on-machine and in-process WED-dressing tests. The same grinding machine was used to perform all grinding tests that are described later.

#### 4.1.1 Metal bonded diamond wheels

The principal metal bonded diamond wheel used in this study was chosen according to recommendations given by the company Diametal AG, whose expertise, among others, is the manufacture of precision grinding tools in diamond and CBN. The grinding wheel has the following specification: 1A1 50x10x5x20 D46 C125 B1. It consists basically of a bronze bond material (B1 is a copper-tin-silver alloy) impregnated with synthetic diamond grains (D46), at a grain concentration of 30% in volume (C125). The diameter of the grinding wheel is 50 mm, and the width is 10 mm. Moreover,

grinding wheels with different diamonds grain sizes and bond materials were also used, and are specified in the text where appropriate.

### 4.1.2 Conventional dressing

All conventional dressing experiments were carried out using a silicon carbide wheel, which was chosen according to recommendations given by Diametal AG. For dressing diamond grinding wheels of grain size D46, a silicon carbide of grain mesh size 320 and hardness G is recommended. The complete specification of the dressing wheel is the following: A1A 500x20x203.2 11C320 G12VPS81 50-m/s. It has a straight profile (A1A), a diameter of 500 mm and width of 20 mm and is a ceramic bonded wheel. A reciprocating dressing method was applied for the conditioning metal bonded grinding wheels, i.e. the dressing wheel moves back and forth in axial direction with a specific axial dressing feed rate, and a dressing depth of cut  $a_{ed}$  is incremented in radial direction after each axial movement.

### 4.1.3 Electrical discharge dressing

Sinking electrical discharge dressing (SEDD) was carried out in an EDM machine type Agitron SPIRIT 2 from GF AgieCharmilles. Figure 4.1 shows a dressing spindle (a) mounted inside this machine, a small metal bonded grinding wheel (b) clamped to the spindle and a rotating copper electrode (c), which was used to perform SEDD experiments. Dielectric fluid was supplied to the erosion zone via free jet nozzles positioned tangentially to the grinding wheel at the erosion zone, from both sides back and front. Thus, the grinding wheel was not eroded submerged into dielectric. Sorepi LM was used as dielectric fluid, which is an oil specially developed for EDM sinking operations. This dielectric is suitable for roughing, finishing and superfinishing with copper and graphite electrodes.

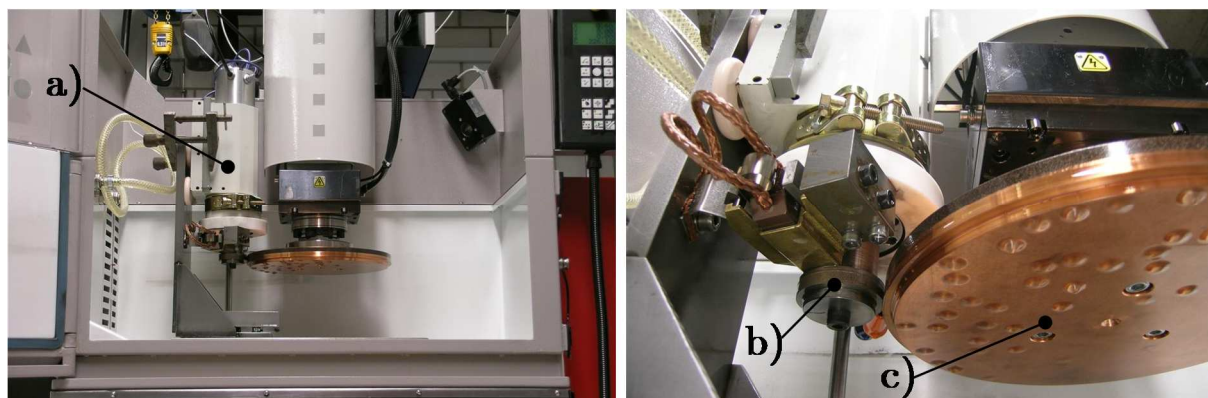


Figure 4.1 – Experimental setup for SEDD in an EDM machine Agitron SPIRIT 2:  
a) dressing spindle; b) metal bonded grinding wheel; c) rotating copper electrode

Wire electrical discharge dressing (WEDD) was first carried out in a wire cut EDM machine type AC Progress VP4 from GF AgieCharmilles (Figure 4.2). Similarly to the experimental setup shown in Figure 4.1, a dressing spindle was mounted inside the machine and dressing experiments were carried out using different types of wire electrodes. Profiling and sharpening tests using different dressing strategies were performed. Dielectric was supplied coaxially to the wire by a flushing system integrated on the upper and lower guide heads and further free jet nozzles were positioned perpendicular to the wire in the radial direction to the grinding wheel to ensure dielectric to reach the erosion zone effectively. Dielectric fluid was deionized water with electrical conductivity lower than 5  $\mu\text{S}/\text{cm}$ .



Figure 4.2 – Wire cut EDM machine type AC Progress VP4 from GF AgieCharmilles

To enable on-machine and in-process wire electrical discharge dressing (WEDD), a dressing unit was designed and manufactured at the Institute of Machine Tools and Manufacturing (IWF/ETH) and integrated inside a grinding machine [WEIN10b]. One advantage of WEDD over SEDD concerns the reduction of unwanted effects caused by electrode wear on dressing accuracy, since new wire electrode is continuously feed from a spool. Thus, the macrogeometry of grinding wheels can be better generated, without requiring the use of a complex device to compensate electrode wear, which would be the case in sinking EDM. In addition, wire EDM is more flexible, since different wheel profiles can be created using the same tool electrode, not requiring the use of different shaped electrodes for every new type of wheel profile as for SEDD.

Figure 4.3 illustrates the CAD design of the WEDD unit, highlighting the wire drive unit, the two axes feed system and the wire guide. It was mounted on the support of the internal grinding spindle, allowing for in-process dressing experiments to be carried out. The feed system is equipped with roller guideways on both horizontal and vertical directions, which allows for relative displacement from wire electrode to grinding wheel in axial and radial directions respectively, enabling the erosion of different profiles. Servo feed control on both axes uses discharge voltage as sensing parameter, enabling the achievement of a stable electrical discharge dressing condition. Actual positions of the axes are measured by two absolute linear encoders model LC 483 (Heidenhain). The axes are controlled by an Adaptive Control System “AC Progress VP4” - GF AgieCharmilles, which allows high dynamic erosion gap regulation.

The wire drive system adjusts and maintains a constant wire run-off speed  $v_D$  and wire pretensioning force  $F_D$  and is responsible for supplying and disposing the wire electrode. It is located on the vertical stage of the two axis NC-controlled positioning unit and is basically composed of one DC servo motor and a permanent magnetic hysteresis clutch. Different torques can be adjusted in this hysteresis clutch, so that constant wire tension is guaranteed by keeping constant clutch torques. The wire guide, a key part of the unit, is also located on the vertical stage. It is responsible for reducing wire vibration and deflection by guiding the wire directly at the erosion zone, as well as for delivering dielectric to the erosion gap. The wire guide is described in more details in Chapter 5.

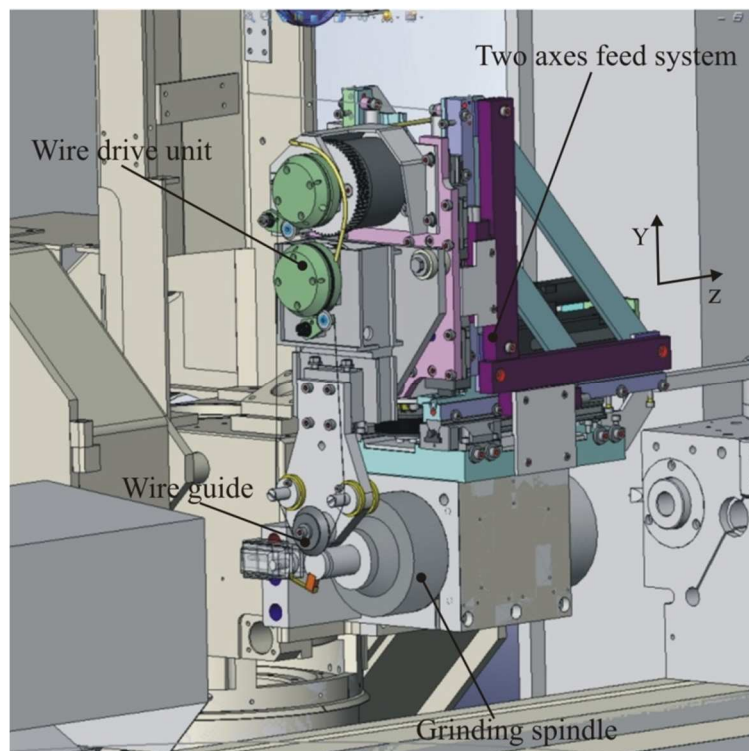


Figure 4.3 – Wire drive unit and feed system of WEDD unit

Figure 4.4 shows the WEDD unit assembled and integrated into the grinding machine. It is covered with an enclosure to protect its components from grinding fluid as well as abrasive grains and removed material chips. In this figure, the wire drive unit, grinding spindle, grinding wheel and wire guide are highlighted.

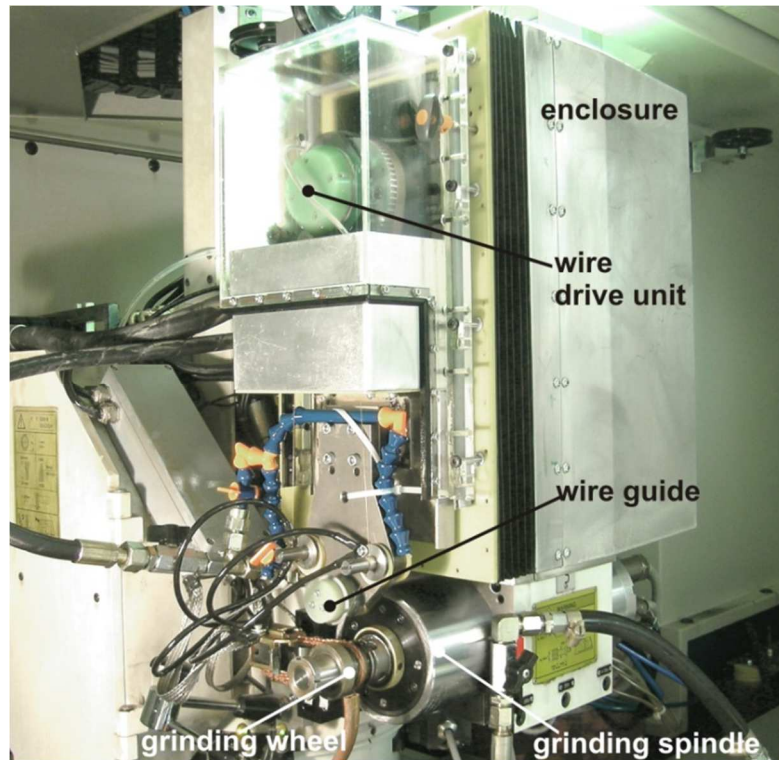


Figure 4.4 – WEDD unit integrated into the grinding machine.

Standard grinding oil type Blasogrand HC5 manufactured by Blaser Swisslube AG was used for all erosion and grinding experiments inside the grinding machine. It is a universal high performance synthetic grinding oil with low viscosity, low misting and high flashpoint, suited to practically all materials. The high flashpoint of 165°C is also very important for EDM, especially when no-submerged WEDD experiments are carried out. In WEDD, the dielectric is delivered to the erosion zone through the wire guide and additionally via free jet nozzles positioned tangentially to the grinding wheel.

#### 4.1.4 Equipment for on-machine dressing and grinding tests

All on-machine dressing tests and grinding experiments were performed on a CNC universal cylindrical grinding machine Studer type S31 (Figure 4.5). The internal grinding spindle (Fischer type MFM-1224/42) was used in both cases, allowing the use of metal bonded grinding wheels of small diameters. This grinding spindle enables rotations up to 42,000 rpm, and uses a tool holder type HSK40-A for clamping the grinding wheels.

High performance silicon nitride ( $\text{Si}_3\text{N}_4$ ) manufactured by CeramTec AG was chosen as workpiece material for most of the grinding tests (in some cases aluminum oxide was used and is specified in the text where appropriate). These workpieces were manufactured in cylindrical shape with a diameter of  $d_w = 51.5$  mm and width of  $b_w = 7.5$  mm. Silicon nitride is a material with high strength over a wide temperature range, high fracture toughness, high hardness, outstanding wear resistance, good thermal shock resistance and chemical resistance, which poses a challenge for efficient grinding. Plunge grinding tests were performed. Grinding oil was supplied to the grinding zone via a shoe nozzle especially designed for the applied grinding wheels.



Figure 4.5 – Universal cylindrical grinding machine type Studer S31 [STUD11]

#### 4.1.5 Metrology equipment

To evaluate the results obtained with WED-dressed and SiC-dressed metal bonded grinding wheels as well as in single discharge experiments, different measurement equipment were used.

For measuring the grinding wheel topography after dressing and grinding as well as wheel wear, a 3D optical device Alicona InfiniteFocus was used. The volume and shape of craters generated in single discharge experiments were also measured with this equipment. It consists in an optical 3D micro coordinate system for form and roughness measurement. It works with a focus-variation technique, in which a 3D image is built step by step by varying the vertical position of the lens and acquiring information that is sharp on each measurement. Vertical resolution of up to 10 nm can be achieved [INFI11]. Figure 4.6 shows this device and a three-dimensional measurement of a crater eroded on copper in a single discharge experiment.



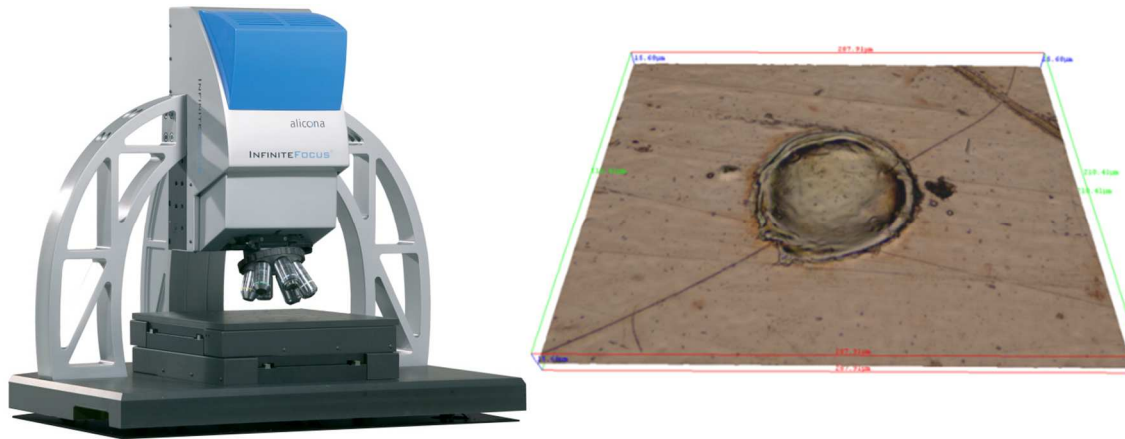


Figure 4.6 – Optical measurement device Alicona InfiniteFocus (left) and a 3D measurement of a crater eroded in an single discharge experiment in copper (right) using a discharge peak current of  $I_{peak} = 73$  A and discharge duration  $t_e = 1.25$   $\mu$ s (crater diameter  $d_c = 72$   $\mu$ m; crater depth  $h_c = 5.5$   $\mu$ m; eroded volume 8,500  $\mu$ m<sup>3</sup>)

A scanning electron microscope (SEM) type ZEISS DSM962 was used to qualitatively characterize different grinding wheels and pellets used in this work. In some cases the grinding wheels were coated with a thin layer of gold to improve the quality of SEM micrographs.

The ground workpiece quality was assessed using two different roughness measurement devices, namely Taylor Hobson Precision type Form Talysurf series 2, and Taylor Hobson Precision type "Talyrond 365". Roughness, waviness and roundness measurements were performed using these devices.

An oscilloscope type LeCroy WaveRunner 44MXi-A was used to monitor the erosion process. The discharge duration and peak currents were measured for different types of EDM pulses and pulse frequencies were assessed using this equipment.

Grinding was mainly monitored by measuring cutting forces. A rotating dynamometer type Z15168 SN473735 from Kistler was used clamped to the workpiece spindle of the grinding machine. It consists of a 4-component force-torque measurement system. Tangential and normal grinding forces could thus be monitored.

## 4.2 Evaluation of dressing methods

One advantage of wire electrical discharge dressing in comparison to SiC-dressing is the possibility of applying this method inside the grinding machining for dressing different profiles in a flexible way, where non-productive time can be reduced. Besides this fact, it is important to evaluate to which extend dressing influences grinding. In this section, wire electrical discharge dressing is compared to SiC-dressing regarding grinding wheel topography, grinding forces, grinding wear and ground workpiece quality.

### 4.2.1 Grinding wheel topography

Grinding performance is intimately related to grain protrusion. The existence of sufficient porosity guarantees the collection of chips as well as the transportation of cutting fluid into the grinding zone. Hence, high grain protrusion brings benefits to grinding, representing thus a desired property in grinding wheels.

The dressing method was found to have a significant influence on the grinding wheel's surface topography. Figure 4.7 shows the topography of a conventionally dressed metal bonded grinding wheel, conditioned by a silicon carbide dressing tool. This grinding wheel has only low grain protrusion, which means it exhibits a low effective surface roughness. In other words, the metal bond can easily rub against the workpiece, causing an increase in grinding wheel wear and heat generation, so that damages can occur to both the workpiece and the grinding wheel. Traces can be seen in the surface of the SiC-dressed wheel, clearly pointing out the dressing direction. These traces can negatively affect workpiece surface quality, since in plunge grinding, for instance, the macrogeometry of the grinding wheel is directly reproduced on the workpiece surface. Moreover, bond material is not effectively removed exactly there where it should, between the diamonds, where the chips are formed during grinding, which represents another disadvantage of this conventional method.

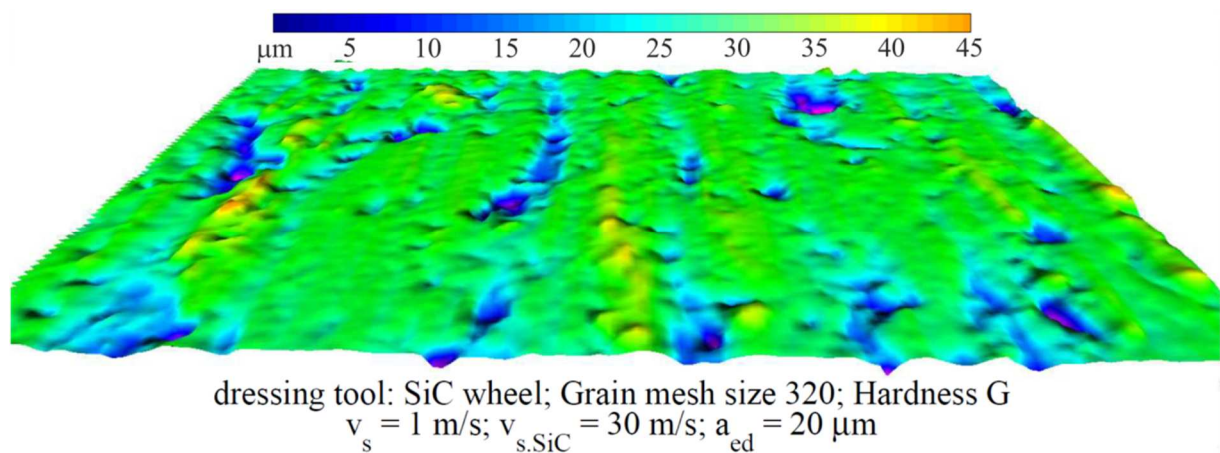


Figure 4.7 – Surface topography of a SiC-dressed metal bonded grinding wheel

On the other hand, Figure 4.8 shows the same metal bonded grinding wheel, now conditioned by means of WEDD. Higher grain protrusion in comparison to the conventional dressed wheel is achieved. The grinding wheel has a well-homogenized distribution of grains and chip spaces in front of the grains, where the chip material is collected in grinding, independent on the dressing direction. A zinc-coated brass wire of 0.33 mm in diameter, type CobraCut S from Bedra, was used for conditioning this grinding wheel inside the grinding machine Studer S31.

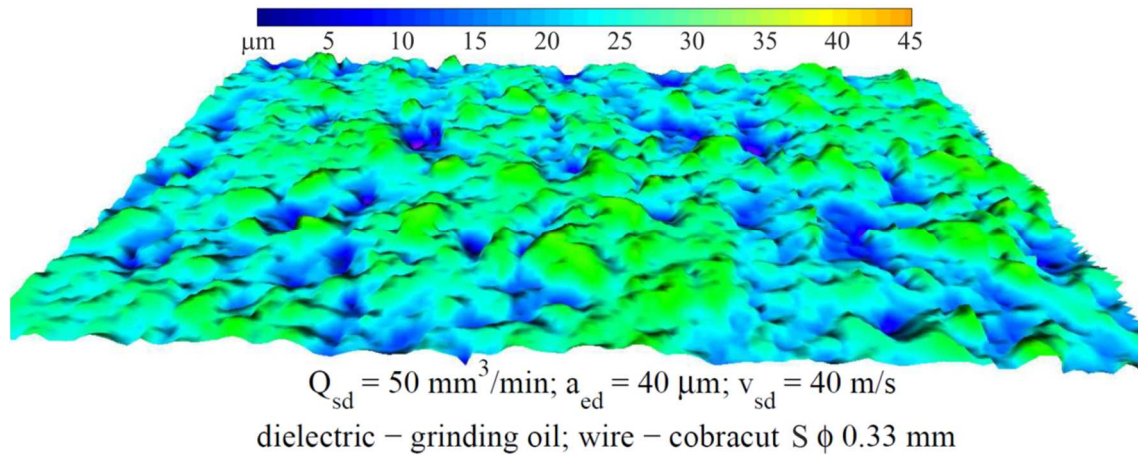


Figure 4.8 – Surface topography of a WED-dressed metal bonded grinding wheel eroded using a discharge peak current of 188 A and discharge duration of 1.55  $\mu\text{s}$

Figure 4.9 and Figure 4.10 illustrate the Abbott–Firestone curve and show some three-dimensional surface parameters used to describe the topographies previously illustrated in Figure 4.7 and Figure 4.8, respectively. The presented three-dimensional parameters are similar in definition to two-dimensional parameters, but are calculated over an area rather than only over a line. Thus, the values of  $S_a$ ,  $S_k$ ,  $S_{pk}$ , and  $S_{vk}$  are analogues to  $R_a$ ,  $R_k$ ,  $R_{pk}$ , and  $R_{vk}$ . The parameter  $S_a$  indicates the average height of the selected area,  $S_k$  the core roughness depth,  $S_{pk}$  the reduced peak height, and  $S_{vk}$  the reduced valley height. The higher value of average height  $S_a$  for the WED-dressed wheel underlines the efficiency of wire electrical discharge dressing in producing a very rough topography in comparison to the conventional method. Secondly, the WED-dressed wheel encompasses higher reduced peak height  $S_{pk}$  values, indicating a surface with higher peaks. The profile depth distribution of the WED-dressed wheel extends over a wider range, resulting in a higher core roughness depth  $S_k$ . Higher core roughness depths  $S_k$  points out higher grain protrusion, indicating higher efficiency in removing material during grinding. The reduced valley height  $S_{vk}$  is similar in both topographies. It can be interpreted as corresponding to pores on the grinding wheel surface. The SiC-dressed wheel has lots of craters left by diamonds that pulled-out during dressing, so influencing the value of reduced valley height. In short, it can be stated that WED-dressing generates grinding wheels with a more open structure in comparison to conventionally dressed wheels, which is a desired characteristic, especially important when grinding advanced ceramics.

Grain protrusion was measured in a D46 grinding wheel, which was eroded by means of different discharge pulses ( $I1 - I6$ ), with peak currents varying between 88 A for  $I1$  and 223 A for  $I6$ , and discharge duration time from 1 to 1.8  $\mu\text{s}$ . Figure 4.11 shows the results obtained, where grain protrusion is represented as a percentage of the equivalent diamond diameter, in this case  $d_e = 46 \text{ } \mu\text{m}$ . It can be seen that average

grain protrusion slightly varies between 40% and 46% with broad standard deviations. Grain protrusion cannot be manipulated after the grinding wheel has already been eroded, i.e. it is not possible to set the erosion process to achieve, for instance, 10, 20 or 30% of grain protrusion. This would only be possible if at the beginning grains and bond would be at the same radial level (not the case after EDD). For D91 and D126 grinding wheels, average grain protrusion of 47% and 50% respectively were measured.

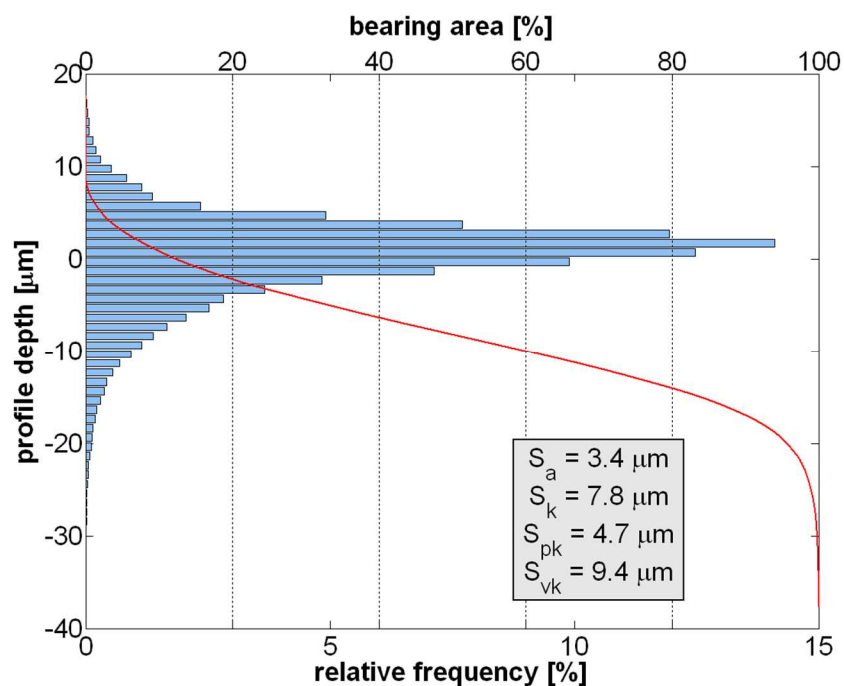


Figure 4.9 – Abbot-Firestone curve of a SiC-dressed metal bonded grinding wheel

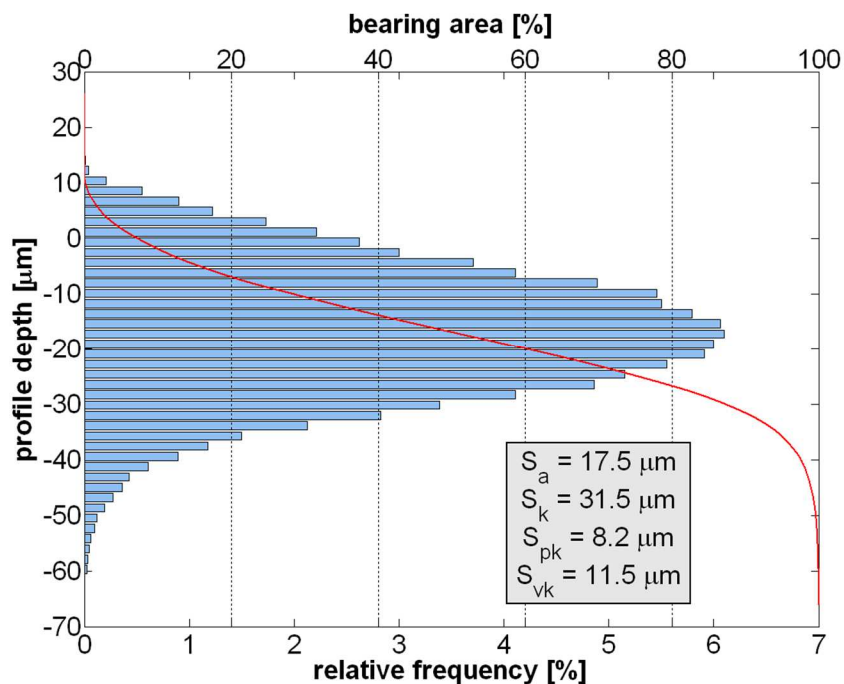


Figure 4.10 – Abbot-Firestone curve of a WED-dressed metal bonded grinding wheel

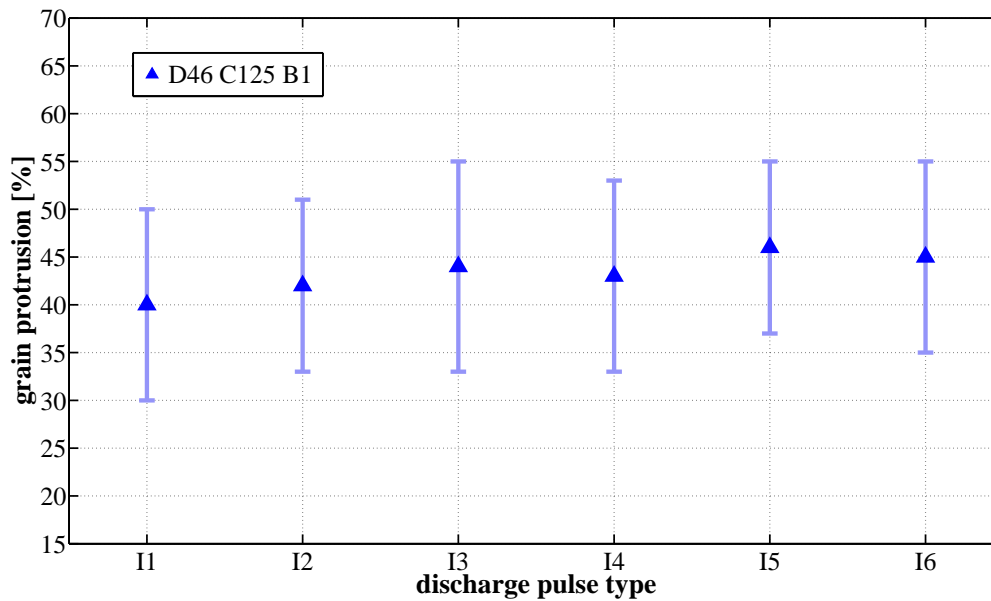


Figure 4.11 – Grain protrusion of a D46 grinding wheel for different discharge pulses

In electrical discharge dressing, diamonds are not eroded during dressing but are rather pulled out after achieving a certain protrusion, since at this point the grains no longer have a sufficient retention force to the bond. For this reason, EDM can be used for both profiling and sharpening of metal bonded grinding wheels. In comparison to other dressing methods, which attack the cutting edges of the abrasives, EDD attacks only the binder and installs the profile of the grinding wheel indirectly. Considering a metal bonded grinding wheel type 1A1 400x10x5x203.2 D46 C125 B1, which means diamonds of equivalent diameter of 46  $\mu\text{m}$  and volumetric concentration of 30%, wheel diameter of 400 mm and width of 10 mm, the removal of a dressing depth of cut  $a_{ed}$  of only 10  $\mu\text{m}$  would represent the removal of about 800,000 diamonds, assuming the diamonds as octahedrons. The whole grinding wheel, in this case with a layer height of 5 mm, has a total of approximately 400 million diamonds. This means that a considerably amount of diamonds is removed during dressing, and that new grain protrusion is generated by this mechanism. The effect of this removal mechanism can be observed in Figure 4.12, a SEM-micrograph of a WED-dressed grinding wheel surface. Marks left by removed diamonds can be clearly identified on the surface of the metal bond (red arrows), indicating that diamond grains were removed during the dressing process.

Figure 4.13a shows another SEM micrograph of a WED-dressed grinding wheel. In the center, three geometrically well-defined diamond grains with high protrusion are visible, while on the top of the figure, new grains are starting to emerge from the metal bond. A typically EDM molten surface is shown, where, for example, resolidified spherical particles were reattached to the wheel surface as well as to the diamonds. No damages were found on the diamonds surfaces after erosion. According to Klocke et al.

[KLOC07a], thermal damage of the diamond grains takes place after EDM dressing. However, graphitization is limited to a very thin layer on the surface of the diamond, so that grinding can still be performed (diamond graphitization is further discussed in Chapter 6). Finally, Figure 4.13b shows a SEM-micrograph of a SiC-dressed metal bonded grinding wheel. One can see that the diamonds were mechanically damaged and pulled out, and grain protrusion is much lower than for WED-dressed wheels.

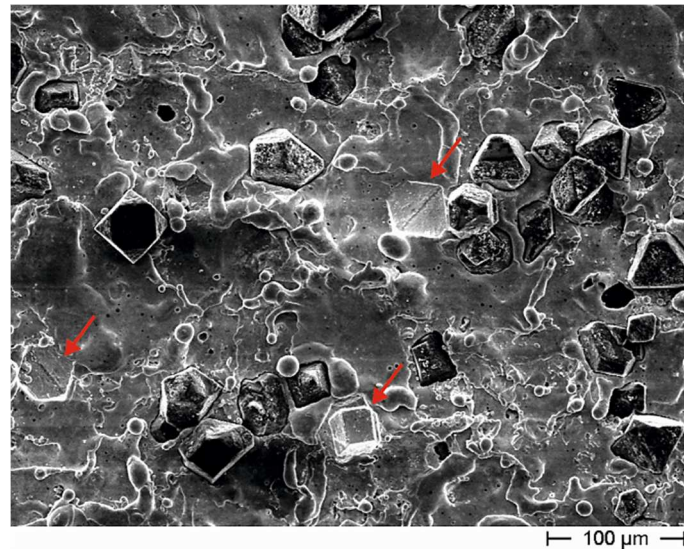


Figure 4.12 – Grain pull-out as a result of wire electrical discharge dressing

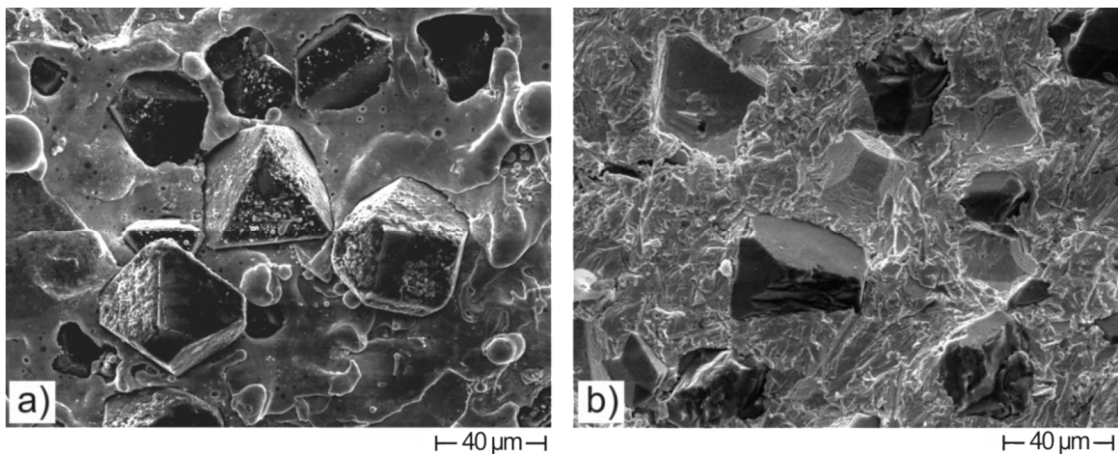


Figure 4.13 – SEM micrographs of a metal bonded grinding wheel D46 after a) WEDD-Dressing and b) conventional dressing with a SiC-Wheel

### 4.2.2 Grinding forces

In order to evaluate the influence of dressing on grinding wheel performance, plunge grinding tests were carried out on silicon nitride workpieces. Figure 4.14 shows results of tangential grinding forces for both dressing methods, WEDD and SiC-dressing. A total specific material removal  $V'_w$  of 2,000 mm<sup>3</sup>/mm was ground. Table 4.1 shows erosion and grinding parameters used in these experiments. Lower grinding

forces were achieved by using the WED-dressed grinding wheel. This better performance is a direct consequence of higher grain protrusion generated in WEDD. In this case, chip space helps cooling and lubricating the grinding zone and inhibits stuffing of chips [BRIN99, PINT08]. Both help to reduce grinding forces. Moreover, less heat is generated and consequently wheel wear is lower.

Table 4.1 - Erosion parameters, grinding wheel, dielectric and wire specifications

WEDD erosion			Plunge Grinding		
discharge current	$I_{peak}$	223 A	1A1-50-5-20-D46-C125-B1		
discharge duration	$t_e$	1.45 $\mu$ s	wheel speed	$v_s$	60 m/s
pulse interval time	$t_o$	18.5 $\mu$ s	specif. MRR	$Q'_w$	10 mm <sup>3</sup> /mms
wheel speed	$v_{sd}$	20 m/s	speed ratio	$q_s$	100
wire electrode	CobraCut S 0.33 mm		wheel width	$b_s$	10 mm
dielectric	Blasogrind HC5		cutting fluid	Blasogrind HC5	

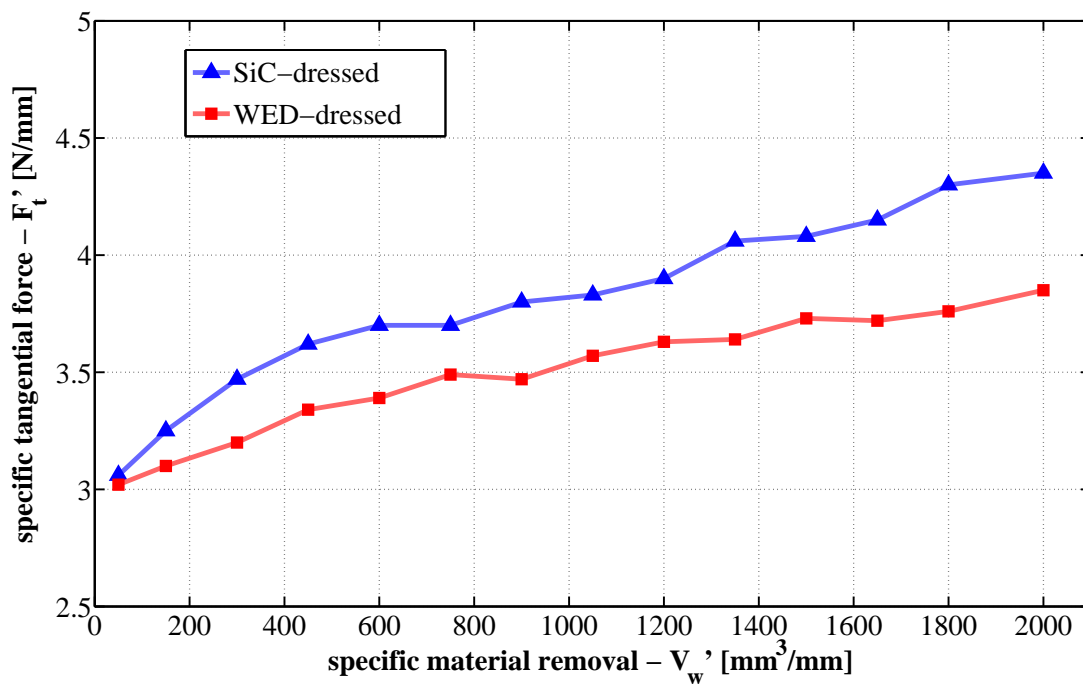


Figure 4.14 – Influence of dressing methods on tangential grinding forces.

The normal forces were also monitored and are presented in Figure 4.15. Similar results to those presented in Figure 4.14 were achieved, in which grinding forces are lower when a WED-dressed wheel is used. Consequently, it can be stated that regarding grinding forces wire electrical discharge dressing is more suitable than SiC-dressing for conditioning metal bonded grinding wheels.

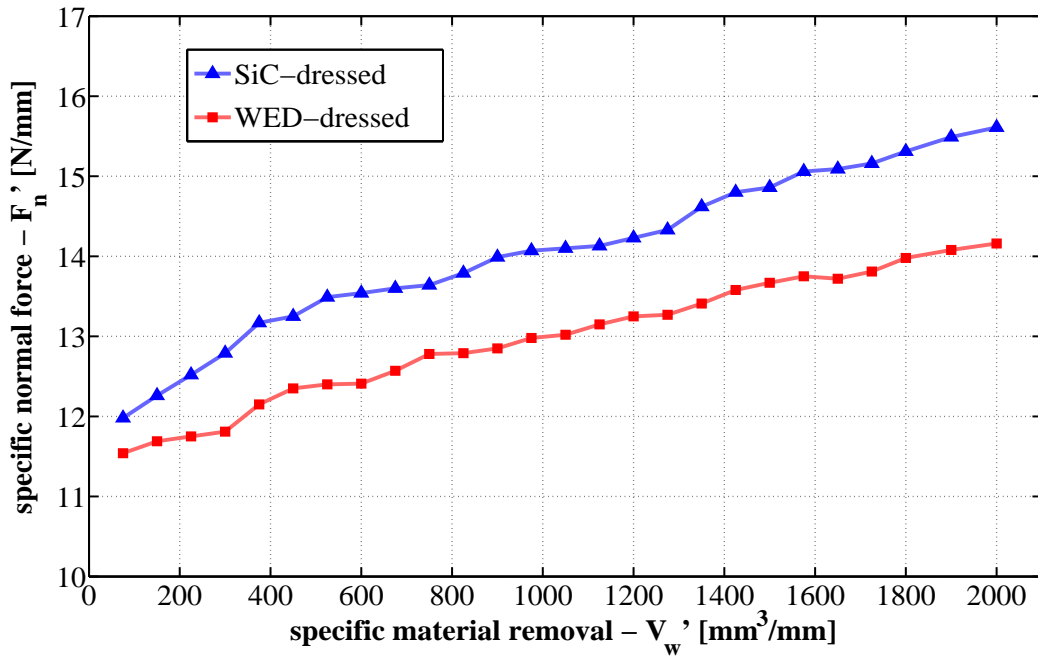


Figure 4.15 – Influence of dressing methods on normal grinding forces

The type of metal bond material also significantly influences grinding forces. In a bronze-based metal bond, for instance, different volume percentage of copper and tin create a wide range of different bond properties, where especially the hardness, ductility and toughness can vary. In general, when the amount of tin is increased and copper decreased a grinding wheel with lower toughness and strength and higher hardness is obtained. According to Madison [MADI96], metal bonds with higher toughness and strength help retain the costly diamonds firmly throughout their entire useful life. More tin also decreases the melting temperature of the bronze alloy. The type of bond has thus an influence on grinding forces, since it impacts the grinding wear rate, i.e. the way how new cutting edges are created during grinding and how worn grains are removed from the bond. Different bronze alloys also influence the dressability of metal bonded grinding wheels, since material removal rates depend among others on the thermo-electrical properties of the material to be eroded. Three different types of bond materials were used in this work, and its characteristics are summarized in Table 4.2. The exact composition of these bond materials is not revealed in this work, as agreed with the grinding wheel supplier, but the relative composition, i.e. which bond material has a higher volume percentage of a specific component is also presented in Table 4.2 (relative composition). Figure 4.16 and Figure 4.17 show respectively results of specific tangential and normal grinding forces obtained using these different bond materials, which were eroded on a sinking EDM machine. In addition, the B1-bonded grinding wheel was conventionally dressed, using a SiC-wheel, and results obtained with this grinding wheel are also presented in the following figures. Table 4.3 shows erosion and grinding parameters used in these experiments.



Table 4.2 – Bond materials and relative composition (for example, B1 has less copper than B3 and more than B2 in its composition)

Bond type		Relative bond composition	
B1	copper-tin-silver alloy	Copper	B3 > B1 > B2
B2	copper-tin-silver alloy	Tin	B2 > B1 > B3
B3	copper-tin alloy	Silver	B1 > B2

Table 4.3 - Erosion parameters, grinding wheel, dielectric and electrode specifications

SEDD erosion			Plunge Grinding		
discharge current	$I_e$	8 A	1A1-50-5-20-D46-C125-(B1-B2-B3)		
discharge duration	$t_e$	2,7 $\mu$ s	wheel speed	$v_s$	45 m/s
pulse interval time	$t_o$	13 $\mu$ s	specif. MRR	$Q'_w$	5 mm <sup>3</sup> /mms
wheel speed	$v_{sd}$	20 m/s	speed ratio	$q_s$	100
wire electrode	Copper disc		wheel width	$b_s$	10 mm
dielectric	Sorepi		cutting fluid	Blasogrind HC5	

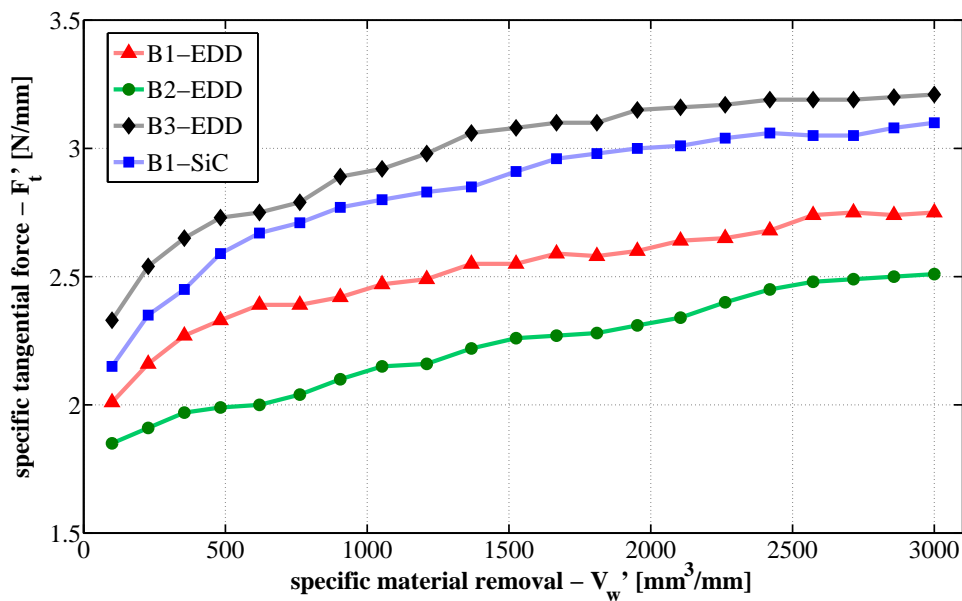


Figure 4.16 – Tangential forces using different types of bond materials (see Table 4.2 for details about the different bond materials)

In comparison to B1, bond type B2 has a higher amount of tin, being thus harder, less ductile and with a lower strength. Bond type B3 has a higher volume percentage of copper, having thus higher toughness and strength (more wear resistant). According to Figure 4.16 and Figure 4.17, it can be seen that higher tangential and

normal forces were measured when using the tougher variant of bond material, i.e. bond type B3. Generation of new grain protrusion due to a self-sharpening process is less likely to occur in this case, leading to more friction between bond and workpiece and consequently higher forces. However, the profile geometry of B3-bonded grinding wheels can be kept for longer time, as presented later in Figure 4.19. Lower grinding forces were achieved using the B2-bonded grinding wheel, which is less wear resistant, resulting in less friction during grinding. Comparing SEDD and SiC-dressing for a B1-bonded grinding wheel, it can be seen that lower grinding forces occur when SEDD is applied.

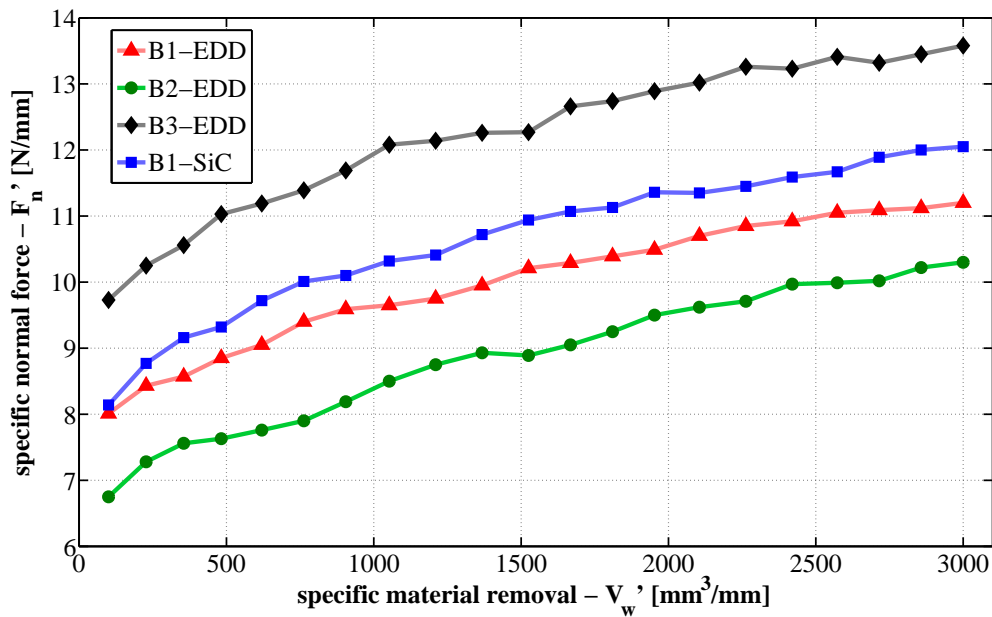


Figure 4.17 – Normal forces using different types of bond materials (see Table 4.2 for details about the different bond materials)

### 4.2.3 Grinding wheel wear

Dressing also influences grinding wheel wear, which occurs due to mechanical, thermal and chemical loads during grinding. A more open grinding wheel structure can lead to less mechanical load, since more space for collecting ground material between the grains are available (more chip pockets). Friction between bond and workpiece can also be reduced in this case, resulting in less heat generation. Moreover, grinding fluid can be more efficiently transported to the cutting zone, reducing friction and increasing the cooling effect on the cutting zone. All this together can lead to a better cutting condition, resulting in lower grinding wear rates. The G-ratio is a common way to describe wheel wear, and is defined as the ratio of volume of ground material to volume of wheel wear. The higher the G-ratio the lower is the wheel wear, indicating a more efficient cutting process. Figure 4.18 shows results obtained using a WED-dressed and a SiC-dressed grinding wheel when grinding silicon nitride workpieces. Erosion and

grinding parameters used in these experiments are the same presented previously in Table 4.1. Again, better results were obtained using WED-dressed grinding wheels. In fact these results are consistent with the grinding forces presented before, where higher forces were reached using a SiC-dressed grinding wheel.

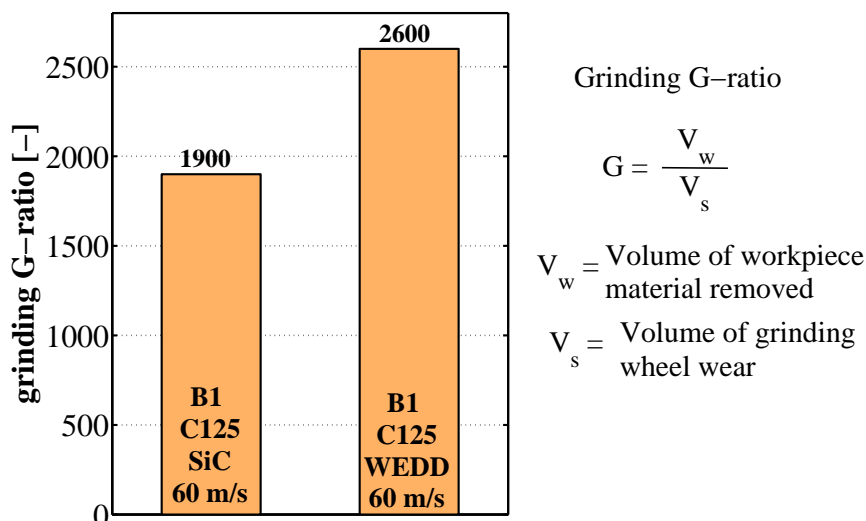


Figure 4.18 – Grinding wheel wear of WED-dressed and SiC-dressed wheels

Additionally, grinding wheel wear was also measured for different metal bonded diamond wheels, conditioned by SEDD and conventionally (SiC-dressing), after grinding aluminum oxide, and the results of G-ratios are presented in Figure 4.19. Erosion and grinding parameters are presented in Table 4.3. B1-bonded grinding wheels with different diamond concentrations, namely C75 and C125, different grinding wheels speeds, 45 and 60 m/s, and different conditioning methods, SEDD and SiC-dressing, were used. First, when comparing SEDD and SiC-dressing, one can see that higher G-ratios were achieved using the first method. Again, a grinding wheel with higher surface roughness leads to less wheel wear, since higher grain protrusion helps reduce friction and improve the efficiency of cutting fluid reaching the grinding zone. The concentration of abrasives significantly influences grinding wheel wear. A considerably higher G-ratio was achieved using a C125 grinding wheel in comparison to a C75 one, since for the C125 wheel a much larger amount of diamonds is active and consequently the material removal is distributed over more diamonds in comparison with the C75 grinding wheel. Moreover, wheel wear can also be reduced by increasing grinding wheel speeds. A higher G-ratio was achieved with a grinding wheel speed of 60 m/s in comparison to 45 m/s. The different types of bond materials also influence wheel wear. A higher G-ratio was achieved using the B3-bonded grinding wheel, decreasing respectively for B1 and B2-bonded wheels. These results are consistent with those presented in Figure 4.16 and Figure 4.17, where higher grinding forces were measured for B3-bonded grinding wheels, in comparison to B1 and B2-bonded wheels.

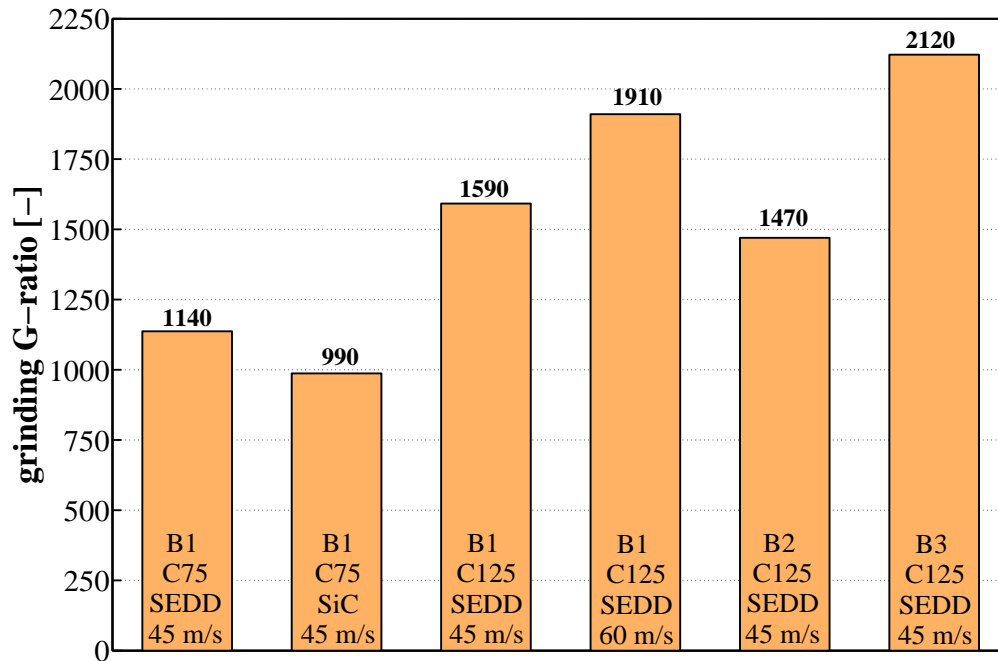


Figure 4.19 – Wheel wear for different bond materials, abrasive concentration, wheel speed and dressing methods (see Table 4.2 for details about the bond materials)

Corner wear was also measured in a profiled grinding wheel with a geometry as schematically illustrated in Figure 4.20. A taper angle of  $45^\circ$  connects two parallel surfaces which differ one from each other by a radial distance of 1 mm. A wire type CobraCut S of diameter 0.33 mm was used to create this geometry. Silicon nitride workpieces were ground and the workpiece inner and outer radii were measured, which represent, respectively, the outer and inner radii of the profiled grinding wheel. Obtained results are presented in Figure 4.21. It can be seen that both radii are kept relatively constant while grinding a specific material removal of  $3,200 \text{ mm}^3/\text{mm}$ . Regarding the outer radius measured on the workpiece, a profile shift of only  $6 \text{ }\mu\text{m}$  was observed after grinding the above mentioned specific material removal. This grinding profile could not be created by conventional dressing due to the huge amount of wear on the SiC-wheel. Therefore, without this dressing technology, more than one grinding wheel is necessary to grind the relatively simple profile presented in Figure 4.20.

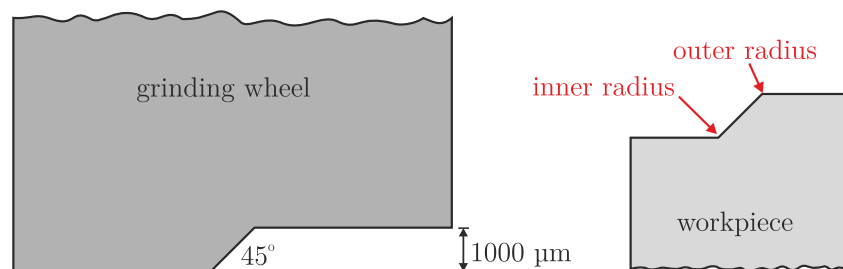


Figure 4.20 – Grinding wheel and ground workpiece profiles indicating the location where inner and outer radius were measured on the workpiece

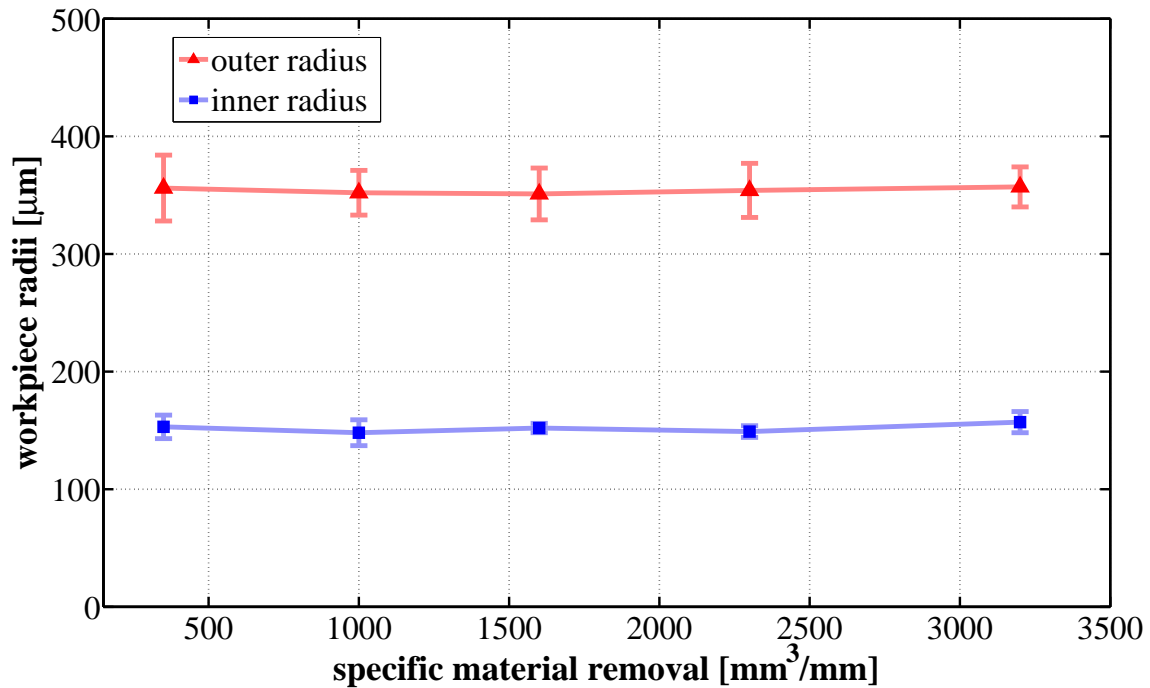


Figure 4.21 – Workpiece radii as a function of specific material removal

To illustrate the way how the grinding wheel wears, Figure 4.22 shows the topography of a grinding wheel in two different conditions and at the same surface location (see red circles to compare similar locations in both figures), namely just after wire electrical discharge dressing (Figure 4.22a) and after grinding a specific material removal of  $V'_w$  of 3,000  $\text{mm}^3/\text{mm}$  (Figure 4.22b). Several diamonds were removed during grinding and in some places there are evidences of frictional bond wear, where flat surfaces were generated. Not every diamond is active during grinding, and some grains are turned into kinematic grains only after the removal of a certain amount of workpiece material. At this point (Figure 4.22b), dressing already needs to be performed aiming to avoid much more heat to be generated due to excessive friction between bond and workpiece.

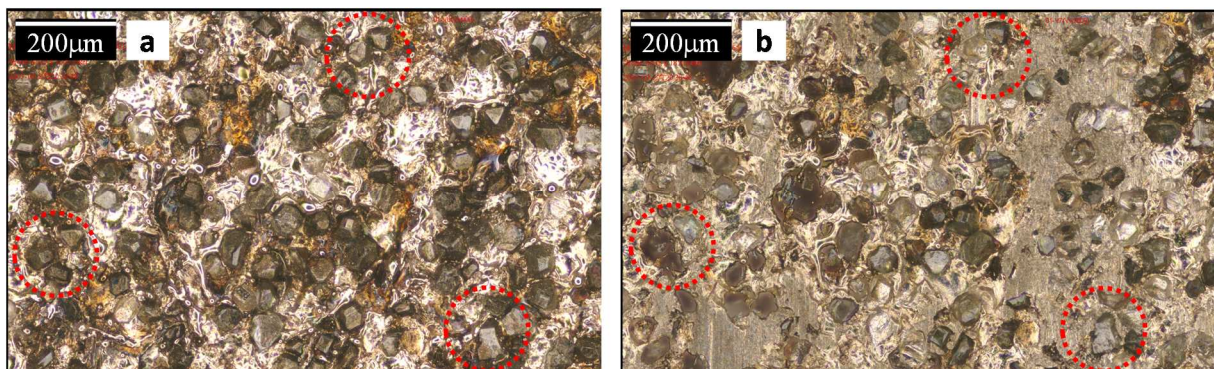


Figure 4.22 – Grinding wheel topography: a) after WED-dressing; b) after grinding a  $V'_w = 3,000 \text{ mm}^3/\text{mm}$  of silicon nitride ( $v_s = 30 \text{ m/s}$ ; B1 D46 C125)

#### 4.2.4 Workpiece surface quality

To evaluate to what extent the dressing process can influence the quality of ground workpieces, silicon nitride workpieces ground by means of WED-dressed and SiC-dressed metal bonded grinding wheels were analyzed. The arithmetical mean roughness  $R_a$ , average peak to valley height  $R_z$  and the waviness height  $W_t$  were measured. Table 4.4 shows erosion and grinding parameters used in these experiments. Figure 4.23 shows results of arithmetical mean roughness  $R_a$  obtained for workpieces ground by means of WED-dressed and SiC-dressed grinding wheels.

Table 4.4 - Erosion parameters, grinding wheel, dielectric and wire specifications

WEDD erosion			Plunge Grinding		
discharge current	$I_{peak}$	223 A	1A1-50-5-20-D46-C125-(M-different)		
discharge duration	$t_e$	1.45 $\mu$ s	wheel speed	$v_s$	45 m/s
pulse interval time	$t_o$	18.3 $\mu$ s	specif. MRR	$Q'_w$	5 mm <sup>3</sup> /mms
wheel speed	$v_{sd}$	20 m/s	speed ratio	$q_s$	100
wire electrode	CobraCut S 0.33 mm		wheel width	$b_s$	10 mm
dielectric	Blasogrind HC5		cutting fluid	Blasogrind HC5	

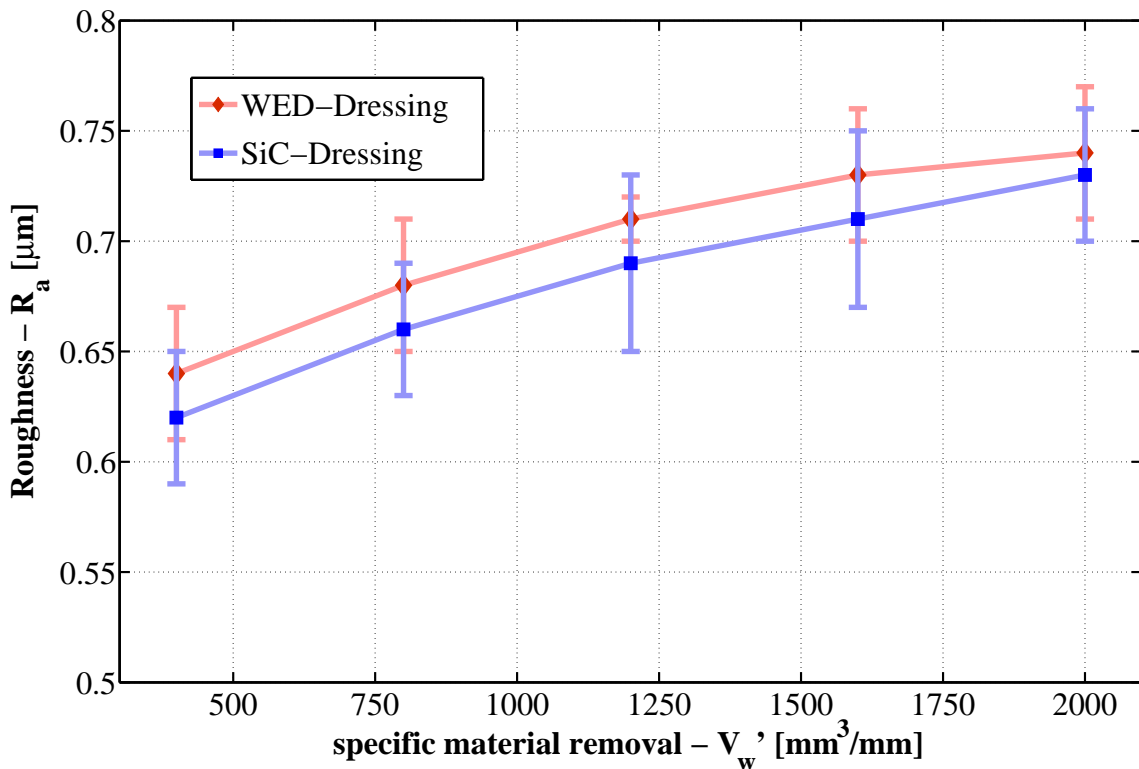


Figure 4.23 – Arithmetical mean roughness  $R_a$  (WEDD vs. SiC-dressing)

Slightly higher arithmetical mean roughness  $R_a$  was measured (mean values) in workpieces ground by the WED-dressed grinding wheel, which however is less than  $0.02 \mu\text{m}$  for all different specific material removals (not significant). Figure 4.24 shows results of average peak to valley height  $R_z$ , indicating a similar trend as for  $R_a$ , i.e.  $R_z$  is slightly higher in workpieces ground with WED-dressed grinding wheels. Although WED-dressing creates more aggressive grinding wheels, it can be stated, from the results presented so far, that the surface quality of ground workpieces is not significantly affected by this method when compared to SiC-dressing.

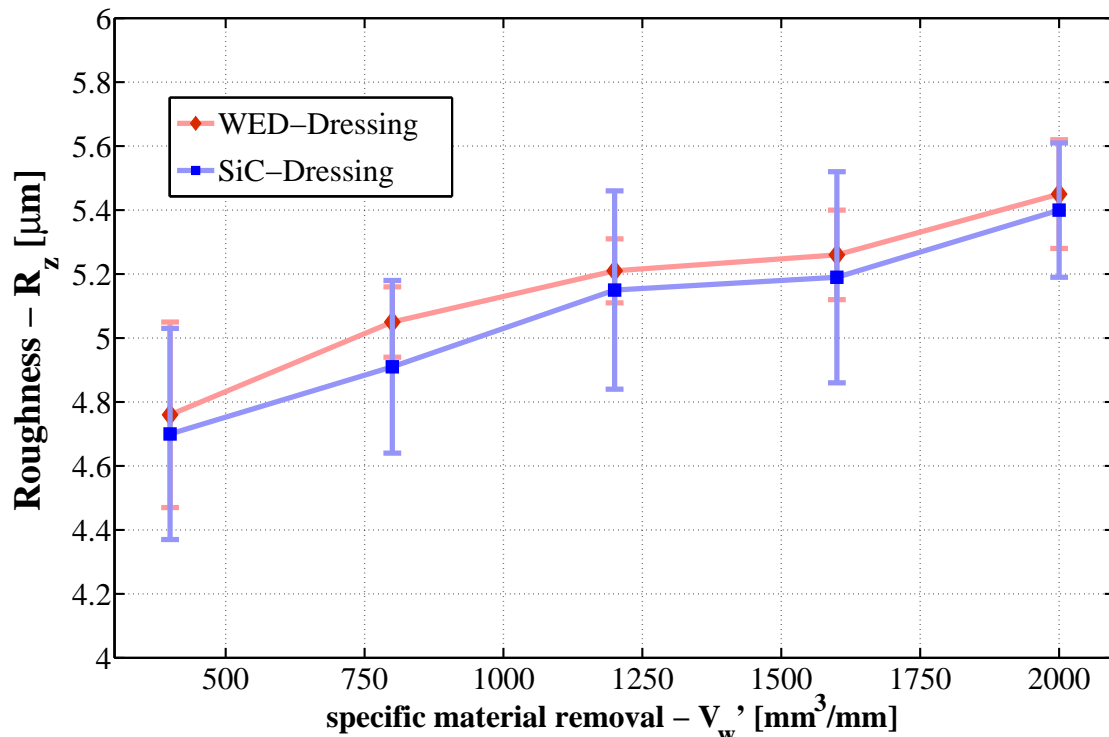


Figure 4.24 – Average peak to valley height  $R_z$  (WEDD vs. SiC-dressing)

Figure 4.25 shows a comparison of waviness height  $W_t$  measured in workpieces ground with metal bonded grinding wheels conditioned with both dressing methods. Lower waviness results were achieved using WEDD. In conventional dressing, the SiC-wheel wears very quickly, which leads to poor dressing accuracy. Moreover, the repeatability of WED-dressing is better in comparison to SiC-dressing. When thicker and larger metal bonded diamond wheels are used, problems concerning accuracy in SiC-dressing are even worse, since even relatively easy grinding wheel geometries such as a straight profile (A1A) can represent a big technical challenge for this dressing technique.

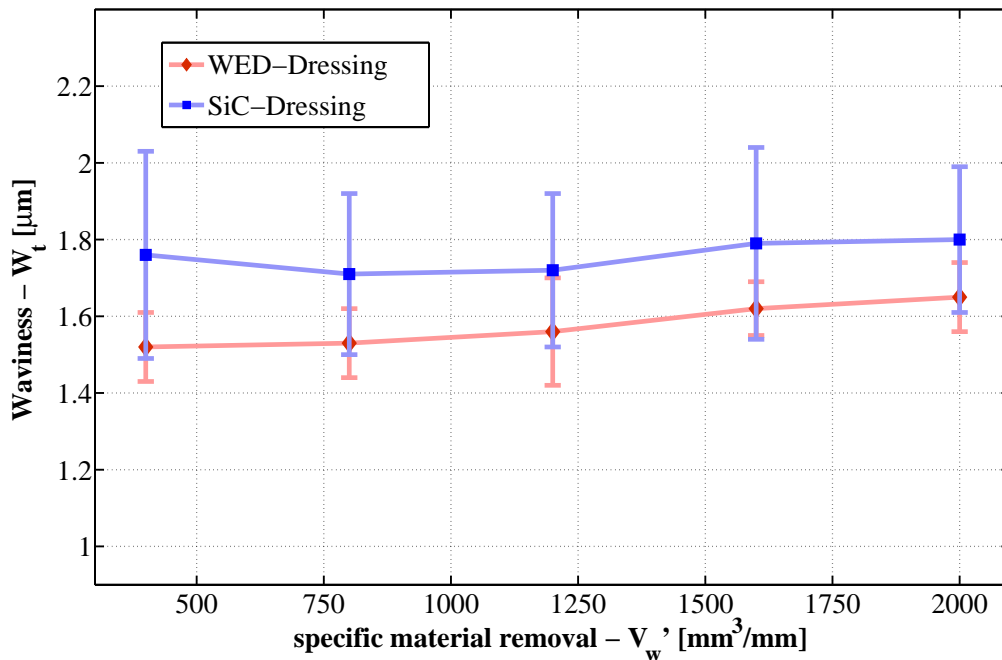


Figure 4.25 – Waviness height  $W_t$  (WEDD vs. SiC-dressing)

#### 4.2.5 Discharge concentration around diamonds in EDD

In die-sinking and wire electrical discharge machining, a stable process is achieved when discharges are uniformly distributed over the discharge gap [KUNI90]. However, in some special cases, a concentration of discharges can occur. The dielectric strength can be reduced, for example, in locations where the gap is contaminated with eroded particles or if not enough time is given to the dielectric to recover from the previous ionization. If the electric field is concentrated in some places over the workpiece, discharges are more likely to occur at these locations, e.g. at the corner of sinking electrodes. In a non-homogeneous workpiece, such as a grinding wheel, this phenomenon can also occur, in this case however around the diamonds. As a consequence, diamonds can be damaged or stay less strongly attached to the metal bond after electrical discharge dressing.

As mentioned in chapter 2, some authors [CHEN00a, CHEN00b, KLIN10] pointed out that electric field is likely to concentrate around the diamonds. Figure 4.26 shows a 3D measurement carried out on a pellet with diamonds of equivalent diameter equals 151  $\mu\text{m}$  and a SEM micrograph of the same workpiece. This pellet was eroded in a die-sinking machine Agitron SPIRIT 2 from GF AgieCharmilles, using a hydrocarbon-based dielectric. One can see that bond material was strongly removed around the diamonds. Moreover, the SEM micrograph reveals that the diamonds have lost their original shapes, i.e. they were damaged during erosion. This surface topography is not appropriate, since diamonds are not enough anchored to the bond, and can pull-out during grinding.



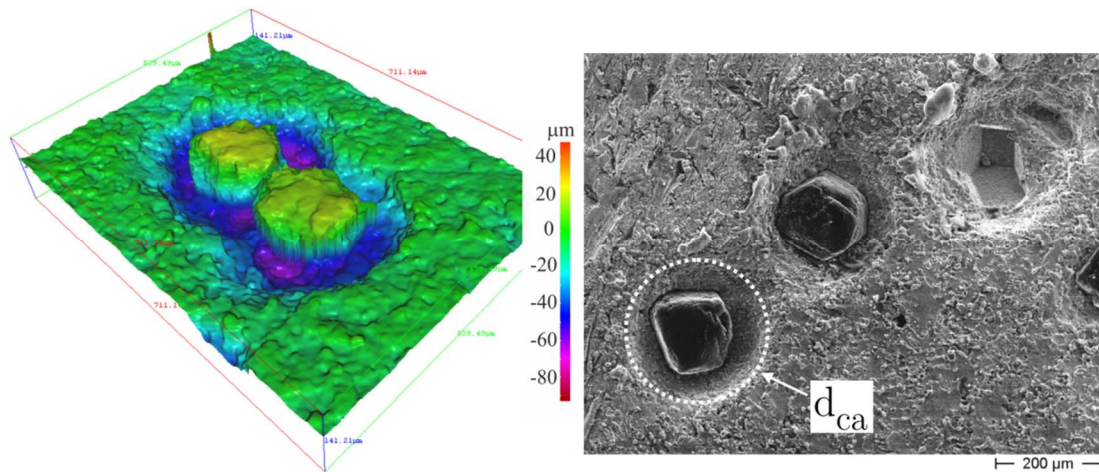


Figure 4.26 – Concentrated erosion around diamonds after die-sinking ( $d_{ca}$  represents the diameter of the surrounding crater)

Deionized water was also used and similar results were achieved, where even larger craters were found around the diamonds. The size of the craters surrounding the diamonds  $d_{ca}$  was measured and is presented in Figure 4.27, in which a D151 pellet was eroded. Crater diameter increases as discharge energy increases and is in agreement with the size of craters measured in single discharge experiments, as presented later in chapter 6 (Figure 6.12).

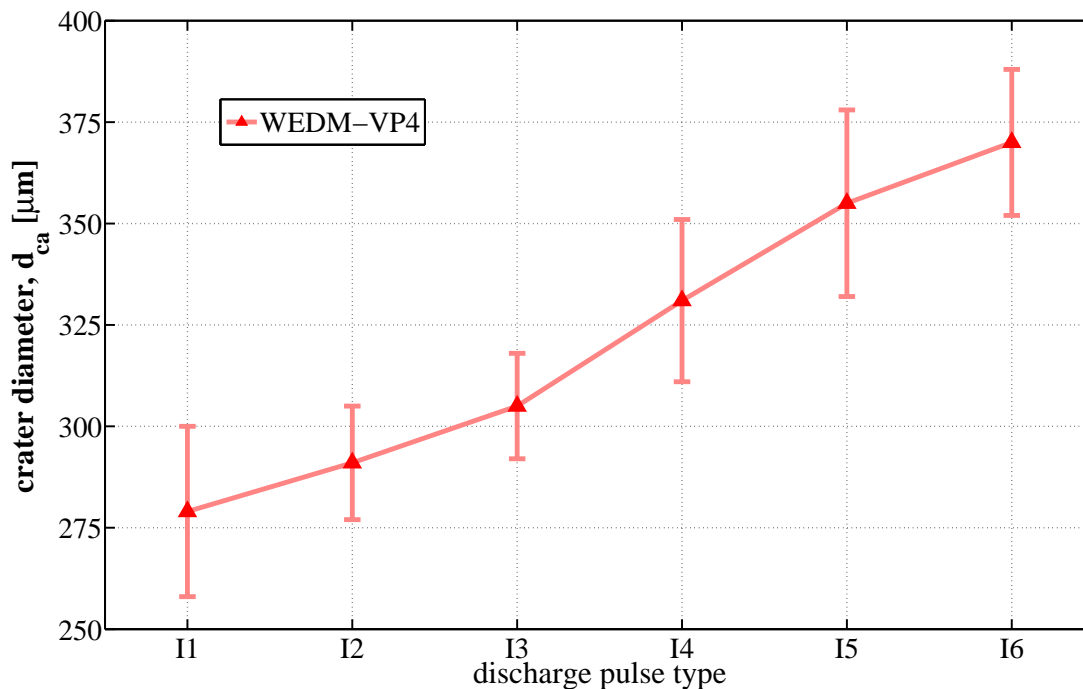


Figure 4.27 – Diameter of eroded craters around the diamonds on a D151 pellet due to concentration of discharges at the boundary diamond/metal

To evaluate the phenomenon of discharge concentration, the erosion of a pellet with embedded diamonds of equivalent diameter 151  $\mu\text{m}$  and concentration C25 was

recorded using a high-speed camera. The schematic representation of this experiment is presented in Figure 4.28. It was carried out in a wire cut machine type Progress VP4 from GF AgieCharmilles, using deionized water. The discharge pulse  $II$  was used ( $I_{peak} = 88$  A,  $t_e = 1.0$   $\mu$ s). The recording speed used in the experiment described in Figure 4.28 was set to thousand frames per second with an exposure time of almost 1000  $\mu$ s per frame. The pulse interval time was set to 100  $\mu$ s, meaning that more than one discharge can be recorded per acquisition frame. The recorded frames were then edited, so that only one line was cut out of the frames (represented by F1 to Fn in Figure 4.28), and put together side by side to form a sequence of discharges. Thus, a mapping of discharges is generated and can be further analyzed.

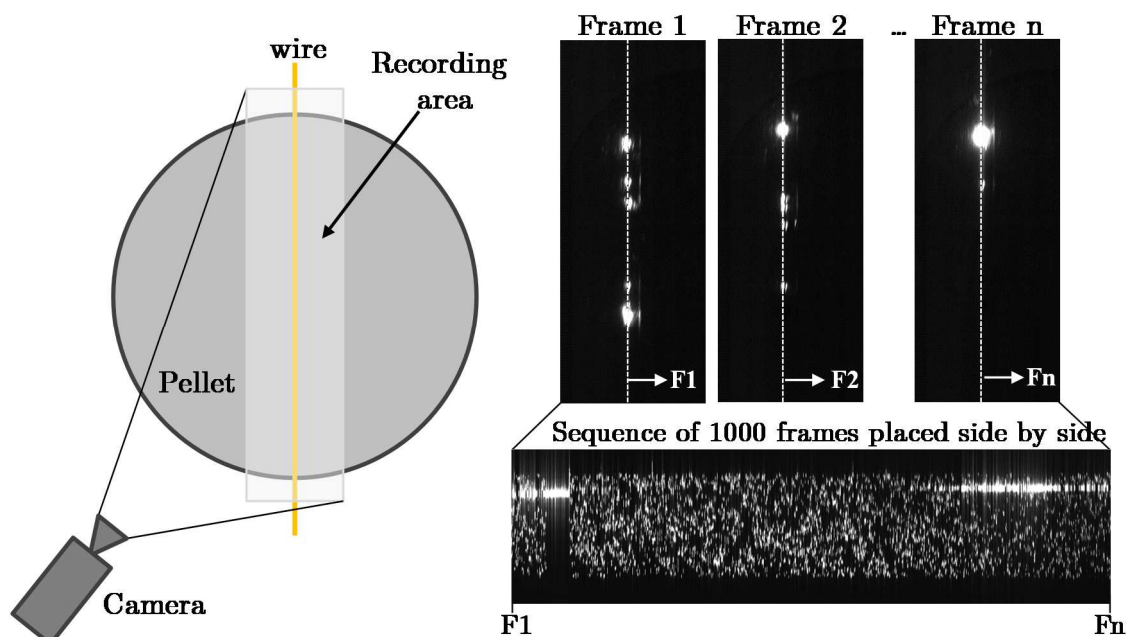


Figure 4.28 – Representation of camera setup for recording discharge sequences

Figure 4.29 shows three sequences of discharge distribution, each one representing thousand frames, i.e. a total acquisition time of one second per sequence. A region of uniform distribution of discharges can be observed in sequence 1 and some regions where discharges are concentrated are visible in all three discharge sequences. The position of the wire electrode relative to the workpiece during the acquisition was known (in x and y direction). Thus, it was possible to correlate the location of discharges with the topography of the pellet. The concentration of discharges happens just around the diamonds, having negative consequences for the grinding wheel as mentioned before.

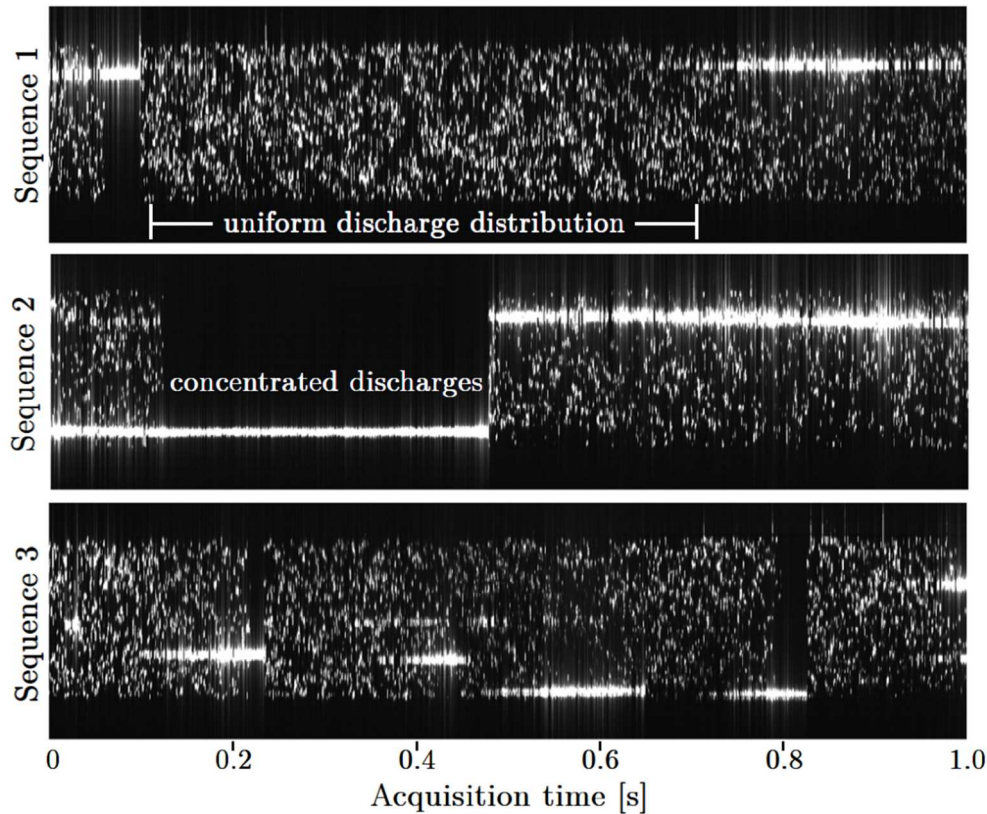


Figure 4.29 – Discharge mapping showing different discharge distribution patterns

From the results presented in Figure 4.29, it can be stated that the electric field around the diamonds triggers an arcing-like phenomenon during the erosion of the pellet. According to Ginzel et al. [GINZ04], arcing usually occurs in EDM when the gap does not recover sufficiently between any two consecutive discharges. During the interval time, the discharge channel has to deionize before the open voltage is applied to the system again. During this time, thermal recovery and electrode cooling also take place. If the gap space has not recovered sufficiently, there is a high probability that consecutive discharges will occur at the same location on the workpiece surface. This phenomenon is known as “arcing” [BART75, GINZ04, KLOC07d] because it has essentially the same destructive effect on the workpiece as a long duration arc, even though the current waveform comprises discrete pulses. According to Bartel and Hockenberry [BART75], if consecutive discharges occur at the same location, the workpiece and tool electrode become overheated in a localized region and a relatively large mass of the workpiece becomes molten. Moreover they stated that due to this cumulative heating effect on the workpiece, the recovery interval increases as a result of longer thermal recovery times. According to the authors, when arcing takes place, the required recovery time may be as much as 5 to 6 times longer than the normal recovery time. Thus, the consecutive discharges around the diamonds lead to a large removal of material at these locations, and the consequent heat concentration is the reason why diamonds can even lose their shapes (thermal damages).

Although the above mentioned results represent a negative impact on WED-dressed grinding wheels, it was found that this phenomenon is more evident for larger diamonds. Grinding wheels D46, D91 and D126 were evaluated, and concentration of discharges was observed in all but the grinding wheel D46. Larger diamonds are more isolated in the surface of the grinding wheel when compared to smaller diamonds for the same concentration of abrasives. For example, the same arbitrary volume of the grinding wheel should have around 8 times more diamonds D46 than D91, and thus when smaller diamonds are used they stay more close together, which consequently impacts the electric field around the diamonds. The grinding wheels were also conditioned at speeds up to 80 m/s, and even in these cases, the concentrated erosion was observed, although it was found to be less intensive. When there is a relative speed between the tool electrode and the grinding wheel, arcing cannot take place since two consecutive discharges cannot occur at the same location. However, the electric field concentration can still cause the discharges to occur more likely just around the diamonds.

The results presented in this session indicate that electrical discharge dressing is more suitable for small abrasive grains and for the case where relative speed is applied between the tool electrode and the grinding wheel. EDD of grinding wheels with larger diamonds is thus critical, and will be discussed in the following session.

#### 4.2.6 WEDD – Process limitations

Electrical discharge dressing has proved to be a suitable dressing method so far. It has however limitations, which must be considered. The first limitation is the size of abrasives. In general, EDM gap is very small, only a few tens of micrometers, which on the one hand is important to achieve high machining accuracies, but on the other hand represents a challenge to good flushing, and, in the context of EDD, limits the applicable grain sizes. It was found that when Blasogrand HC5 is applied, contact between diamonds and the wire electrode already occur for a D91 grinding wheel. Figure 4.30 shows a picture of a new wire electrode (TopasPlus H 0.36 mm) and two pictures of wire electrodes used for dressing grinding wheels of diamonds D91 and D126. Marks left by the contact between grains and the electrode are visible.

To illustrate the aforementioned issue, the gap-size was measured in brass workpieces machined in the wire cut machine Progress VP4. Different discharge peak currents were applied and deionized water was used as dielectric. As shown in Figure 4.31, gap-sizes varied from 33 to 38  $\mu\text{m}$  when the discharge peak current was increased from  $I_3$  to  $I_6$ . The gap-size was also measured using grinding oil as dielectric (Blasogrand HC5) by applying a peak current of  $I_{peak} = 223 \text{ A}$  ( $I_5$ ). In this particular case, the size of the gap was found to be around 20% smaller when compared with

deionized water. Measurements of gap-size were also performed for bond materials B1, B2 and B3, using a peak current of  $I_{peak} = 152 \text{ A}$  ( $I_4$ ), two different open voltages and deionized water. The results obtained in these experiments are presented in Table 4.5. The size of the gap varied between around 27 and 30  $\mu\text{m}$  and was not much influenced by the applied open voltage, although it showed a small increase when 127 V was used. Open voltages, however, cannot be increased unlimitedly, and one has to keep in mind that larger gaps can negatively impact machining accuracy.

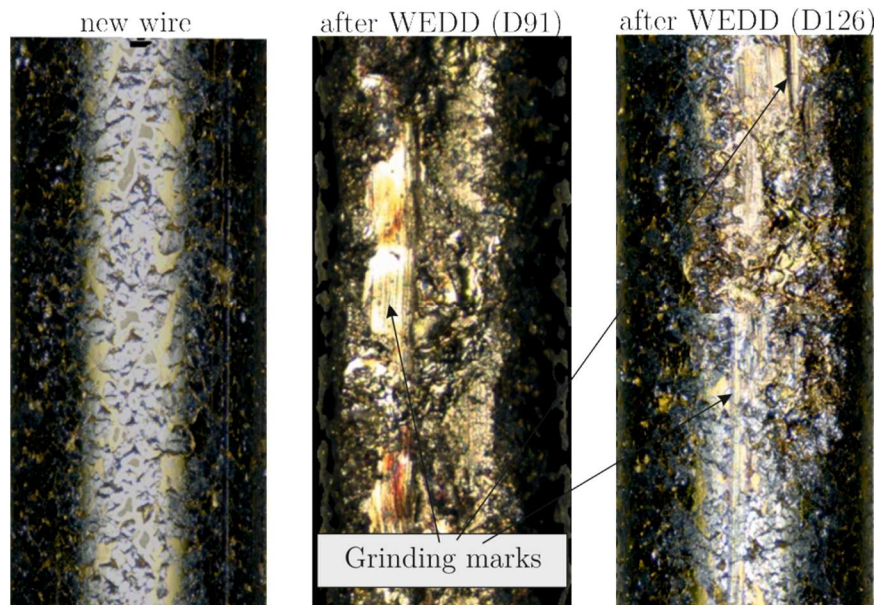


Figure 4.30 – New wire electrode (left) compared to used electrodes (middle and right) containing grinding marks due to WED-dressing of D91 and D126 grinding wheels

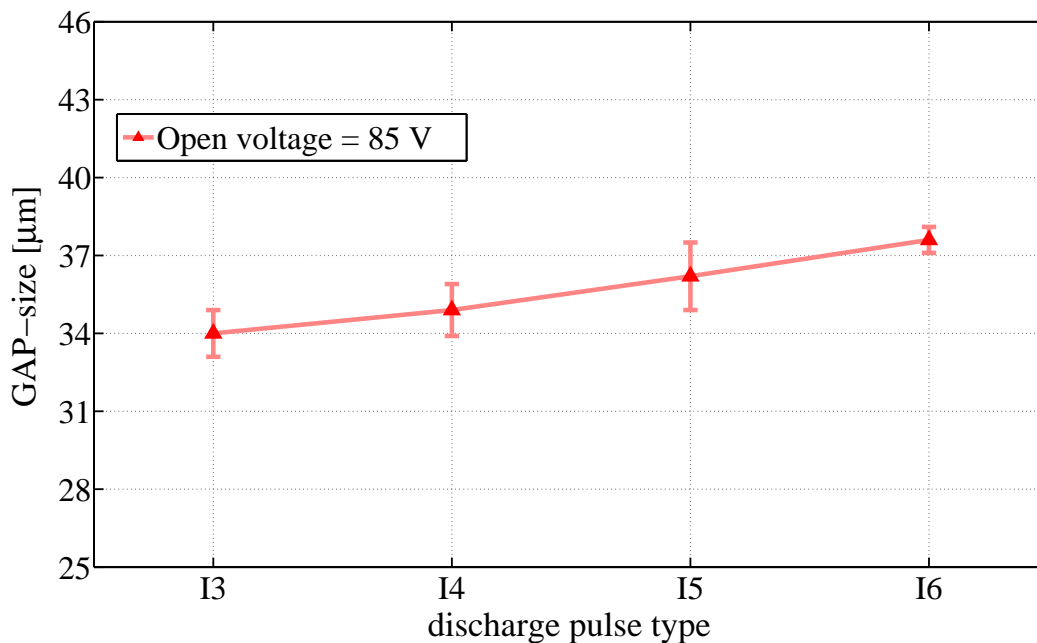


Figure 4.31 – Gap-sizes for brass workpieces as a function of different peak currents, using an open voltage of 85V and deionized water

Table 4.5 – Gap-size for different bond materials and two different open voltages, using a peak current of  $i_{peak} = 152$  A ( $I_A$ ) and deionized water

Open voltage	Bond material		
	B1	B2	B3
Gap (85 V)	27.6 $\mu\text{m}$	28.7 $\mu\text{m}$	27.9 $\mu\text{m}$
Gap (127 V)	28.4 $\mu\text{m}$	29.3 $\mu\text{m}$	28.5 $\mu\text{m}$

From the results presented in Figure 4.31 and Table 4.5, it can be stated that no much space is left for grain protrusion. As previously presented in section 4.2.1, grain protrusion for diamonds D46, D91 and D126 was found to be around 40 to 50%. This means that grain protrusion for a D46 wheel is still lower than the gap-size, but for larger diamonds it becomes critical. This is the reason why marks are visible in Figure 4.30 and more wire breakage occurs as diamond sizes are increased.

As presented before, the gap-size is influenced by the type of dielectric, since different dielectrics have distinguished dielectric strengths. Powder mixed electric discharge machining (PMEDM) could be applied to increase the gap size and facilitate the application of larger diamonds in EDD. Inside a grinding machine, however, this could worsen grinding performance, since the powder can cause additional friction between the grinding wheel and the workpiece, increasing wheel wear and decreasing the quality of ground workpieces.

Another limitation for EDD is the type of bond material. There are different types of bond materials used in grinding wheels. Among them, ceramic, resin, metal and hybrid bonds (metal-ceramic and metal-resin bonds) are the most important. EDD is only suitable for electric conductive bond materials, meaning that among the aforementioned bonds, only metal bonded grinding wheels can be eroded. Moreover, ceramic and resin bonded wheels still dominate the market, and metal bonded grinding wheels find less applications in comparison to grinding wheels of these types. Moreover, the erodibility of different bond materials can vary significantly. Thus, different MRRs are expected for different types of bond material and consequently dressing has to be adjusted to every new type of bond material. Additionally, erosion gap is influenced by the type of eroded material, as previously presented in Table 4.5, and therefore different erosion offsets have to be used for different bond materials (and abrasive sizes as well), since it impacts dressing accuracy to a great extent.

Although EDD has its limitations, it is an important process that can help broadening the application field of metal bonded diamond wheels.

## 5. On-machine WED-dressing

To increase grinding performance of metal bonded grinding wheels it is important to carry out dressing inside the grinding machine. In this case, non-productive time can be reduced and clamping errors minimized. Thus, inside the grinding machine dressing must be fast, i.e. erosion material removal rates must be high to make this process economically viable. In addition, dressing must be accurate. To improve accuracy in wire electrical discharge dressing (WEDD), special attention should be given to wire vibration. In this context, the use of a specially designed wire guide is presented, which is responsible for both ensuring the wire position stability and improving the efficiency of dielectric delivery to the dressing zone.

In this chapter, a discussion about problems related to the use of a free stretched wire in on-machine wire electrical discharge dressing is first introduced. Then, the use of a special wire guide is proposed as an alternative to increase dressing performance, and results concerning dressing material removal rate and dressing accuracy are presented. Moreover, strategies to achieve better dressing accuracies are discussed, namely the use of constant dressing feed rates and small dressing depth of cuts in WED-sharpening. Finally, in-process WEDD is discussed and some results regarding this dressing method are presented.

### 5.1 WEDD with a free stretched wire

In wire electrical discharge machining (WEDM), wire deviations, wire wear and micro vibrations are major causes of cutting inaccuracy. Different forces acting in the erosion gap, such as hydraulic, electrostatic and electrodynamic forces can deflect the wire and cause geometrical errors on machined workpieces [DAUW89, DAUW94]. In on-machine wire electrical discharge dressing (WEDD) this problem is even more critical. Inside the grinding machine, the grinding wheel cannot be submerged in dielectric fluid (grinding oil). Thus, free jet nozzles must be applied during dressing to supply dielectric to the

erosion gap. This fluid application method directly influences the position stability of a free stretched wire. Furthermore, the boundary layer of air which forms around the rotating grinding wheel, and normally deflects grinding fluid away from the grinding zone [EBBR00], can also cause wire vibration and deflection.

In order to illustrate how sensitive a free stretched wire is to external forces, wire deflection was calculated based on a model proposed by Dauw and Beltrami [DAUW94]. The general differential equation of motion for a wire of length  $l_w$  in a plane along the  $z$  axis can be written as

$$F_D \frac{\partial^2 y}{\partial z^2} - EI \frac{\partial^4 y}{\partial z^4} = \rho S \frac{\partial^2 y}{\partial t^2} + c \frac{\partial y}{\partial t} + q_y \quad (5.1)$$

where  $F_D$  is the wire pretensioning force,  $q_y$  an external force,  $E$  is the young's modulus,  $I$  the moment of inertia,  $\rho$  the wire mass density,  $S$  the wire cross section,  $y$  the wire deflection and  $c$  the damping coefficient. Assuming that no time dependent phenomena influence the wire behavior and that in WEDM the wire is hardly subjected to bending moments, the equation (5.1) can be simplified and rewritten as

$$F_D \frac{\partial^2 y}{\partial z^2} = q_y \quad (5.2)$$

where only  $F_D$  and  $q_y$  play the major role on wire deflection. Solving equation (5.2) for  $z=l_w/2$  gives the maximal deflection of the wire. Hence:

$$y \Big|_{\frac{l_w}{2}} = \frac{q_y \cdot l_w^2}{8 \cdot F_D} \quad (5.3)$$

Figure 5.1 shows maximal wire deflections calculated for free stretched wires using a pretensioning force of  $F_D = 25$  N. When an external force  $q_y$  of 1 N is applied to free stretched wires of length 60 and 110 mm, respectively, deflections of 18 and 60  $\mu\text{m}$  are reached. Even for lower external forces, the deflection is normally larger than 5  $\mu\text{m}$ , which would already represent high dressing errors, since grinding is an accurate machining process, where tight tolerances are a constant requirement. When dynamic forces are considered, even higher deviations are expected to the wire.

To illustrate the above mentioned issues, an experiment was carried out to evaluate the influence of the dielectric fluid application on wire deviation. A jet of grinding oil was applied perpendicular to the wire and its position was measured using a contactless capacitive sensor. Figure 5.2 shows deviation results as a function of dielectric flow rate. A constant wire pretensioning force of  $F_D = 25$  N was applied to the wire electrode type CobraCut S of 0.33 mm in diameter (detailed information about the wire can be found in [BEDR11]). A free jet nozzle with diameter of 4 mm was placed at a distance of 2 mm from the wire. These results indicate that relatively large



deviations are reached for both wire lengths, as predicted and presented in Figure 5.1. By using a free stretched wire of length  $l_w = 110$  mm, deviations greater than  $30\ \mu\text{m}$  were measured. As expected, wire position stability increases by decreasing the wire length. However, in order to dress larger grinding wheels, even longer free stretched wire lengths are required, which would decrease the stability of the wire position.

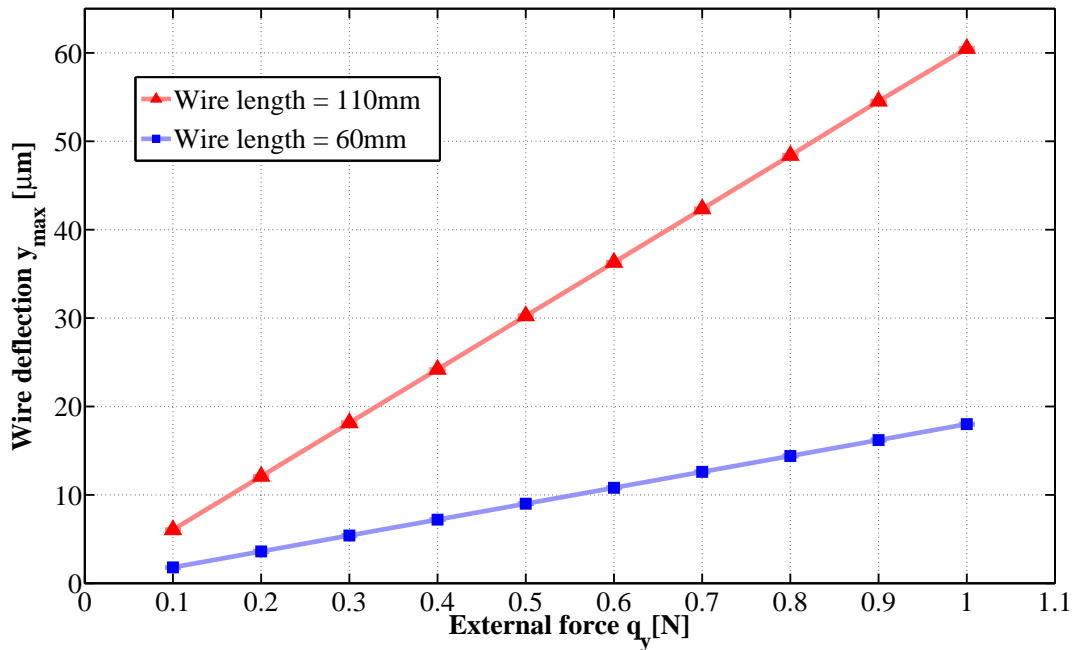


Figure 5.1 – Calculated deflection of free stretched wires of lengths  $l_w = 60$  mm and 110 mm under external forces  $q_y$  and wire pretensioning force of  $F_D = 25$  N

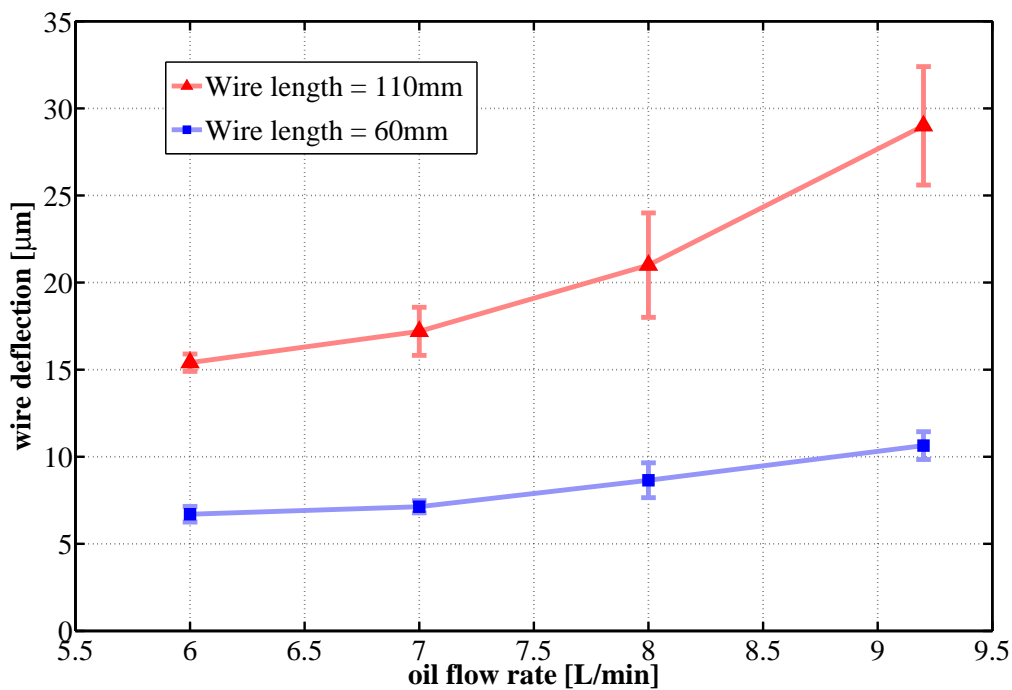


Figure 5.2 – Free stretched wire deflection by increasing oil flow rate (jet nozzle positioned perpendicular to the wire, at a distance of 2 mm in the middle of the wire)

In a second experiment, wire deviation caused by the boundary layer of air that is formed around the grinding wheel was investigated. After WED-dressing an D46 grinding wheel, the wire was kept at the same depth of dressing cut, i.e. at the same radial position as at the end of erosion, and the grinding wheel was driven at different rotational speeds up to  $v_s = 40$  m/s. The position of the wire was measured again using a contactless capacitive sensor. Figure 5.3 shows results of wire deviation for a grinding wheel speed of  $v_s = 40$  m/s. It can be seen that the free stretched wire of length  $l_w = 110$  mm deflected up to  $15\ \mu\text{m}$  and vibrated with amplitudes up to  $3\ \mu\text{m}$ .

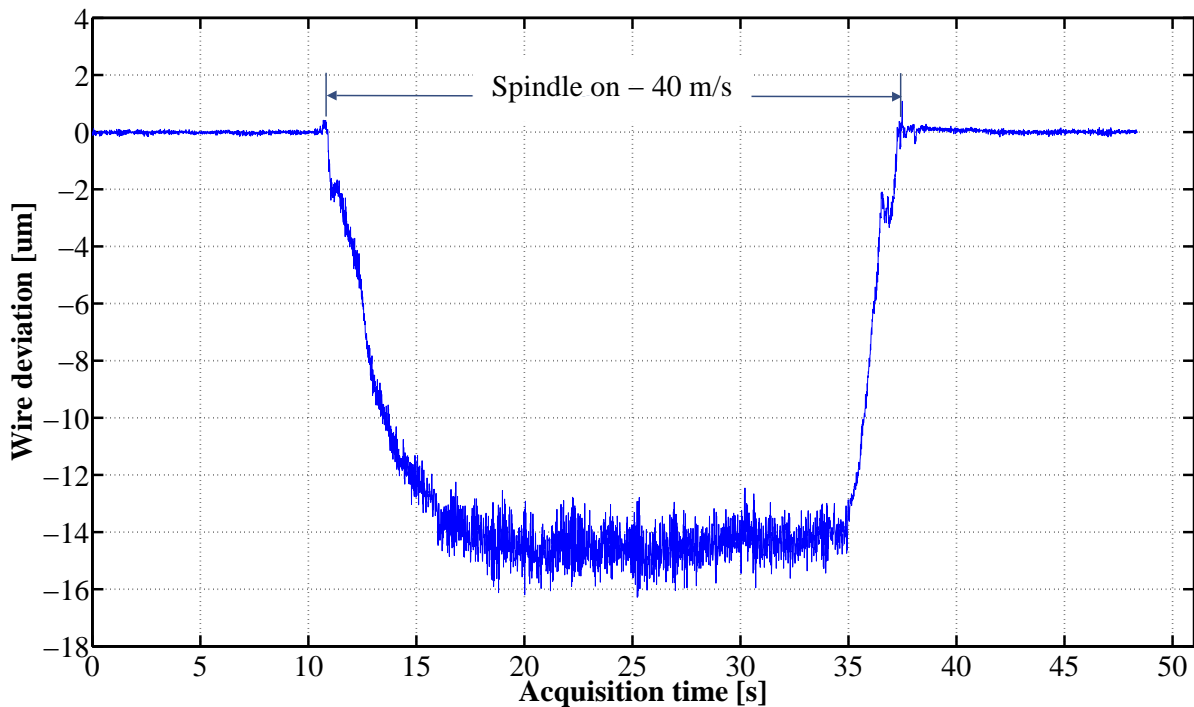


Figure 5.3 – Wire deviation due to dragging forces caused by the boundary layer of air

The results shown in Figure 5.2 and Figure 5.3 indicate that both, dielectric supply and the grinding wheel boundary layer of air can easily affect wire position accuracy. According to equation (5.3), for a given external force  $q_y$ , wire deflection could be reduced either by increasing the wire pretensioning force  $F_D$  or reducing the length of the free stretched wire  $l_w$ . The wire pretensioning force cannot be increased indefinitely. Core materials of standard wire electrodes are typically brass with a tensile strength varying approximately from 500 to 1,000 N/mm<sup>2</sup> [BEDR11]. Typical wire pretensioning forces ranging from 10 to 30 N are applied. Theoretically, however, a free stretched wire of length  $l_w = 0$  mm could be used, if the wire were guided at the erosion zone. On this basis, a wire guide system specially designed for on-machine wire electrical discharge dressing is proposed, as described in the following section.

## 5.2 WEDD with a special wire guide

To minimize the negative effects of wire deviations on dressing results, a special wire guide system was developed [WEIN10a]. This system is responsible for both guiding the wire electrode at the erosion zone and delivering dielectric fluid to the erosion gap. Figure 5.4 shows a schematic representation of the wire guide system and one possible example of its application for dressing a grinding wheel. The wire guide system consists basically of a thin ceramic ring (A) clamped between two flanges (B). The flanges have radial passageways (C) extending from the central bore to its periphery, which allow the dielectric to be delivered to the erosion gap. Dielectric flows from both sides of the ceramic ring. This ceramic ring has a ground groove (D) along its periphery for holding and guiding the wire (E) at the erosion zone (F). The ceramic ring (A) is made out of silicon nitride, since this material is an electric insulator, has a high thermal resistance (very good thermal shock resistance) and a low thermal expansion, which is important when applied near to the erosion zone, where high temperatures occur and the material is subjected to a repetitive cycling of temperatures (thermal fatigue) due to the high discharge frequencies applied in this EDM process.

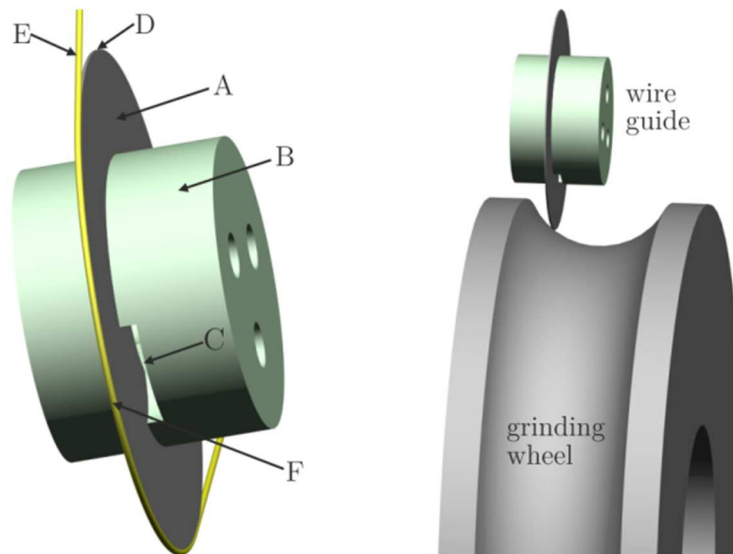


Figure 5.4 – Schematic representation of a wire guide system for WEDD [WEIN10a]

For dressing deep straight edges on grinding wheels and avoiding contact between the wire guide and the diamonds grains, the ceramic ring should be as thin as possible and not exceed a maximal thickness, which depends on the wire diameter, the erosion gap and the diamonds grain size. For example, using a D46 diamond grinding wheel and wire diameter of 0.33 mm, a ceramic ring of thickness 0.38 mm can be used (the ceramic ring can be wider than the wire diameter due to the lateral erosion gap). The same thickness of 0.38 mm was also applied successfully for a wire of diameter or 0.36 mm, what in this case also allows the erosion of larger diamond grains.

As mentioned before, dressing accuracy is crucial for making on-machine wire electrical discharge dressing (WEDD) feasible. Figure 5.5 shows measurements of surface waviness on ground  $\text{Si}_3\text{N}_4$  workpieces after plunge grinding with a D46 grinding wheel (1A1-50-5-20-D46-C125-B1), conditioned by means of WEDD using both the special wire guide and a free stretched wire of length  $l_w = 110$  mm. Table 5.1 lists the applied dressing and grinding parameters. By applying the newly developed wire guide, lower surface waviness was achieved in comparison to results obtained with a grinding wheel dressed using a free stretched wire. Furthermore, surface waviness is not affected when the new wire guide is used and the depth of dressing cut  $a_{ed}$  is increased, in this case, from 3 up to 10  $\mu\text{m}$ . Its use also leads to a significant better dressing repeatability. Dressing with a free stretched wire leads to poor dressing repeatability, which is directly linked to wire deviations and vibration, as discussed before.

Table 5.1 - Erosion parameters, grinding wheel, dielectric and wire specifications

WEDD erosion			Plunge Grinding		
peak current	$I_{peak}$	223 A	1A1-50-5-20-D46-C125-B1		
discharge duration	$t_e$	1,45 $\mu\text{s}$	Wheel speed	$v_s$	50 m/s
pulse interval time	$t_o$	25.2 $\mu\text{s}$	Specif. MRR	$Q'_w$	5 $\text{mm}^3/\text{mms}$
wheel speed	$v_{sd}$	20 m/s	Speed ratio	$q_s$	100
wire CobraCut S	$\varnothing$	0,33 mm	Wheel width	$b_s$	10 mm

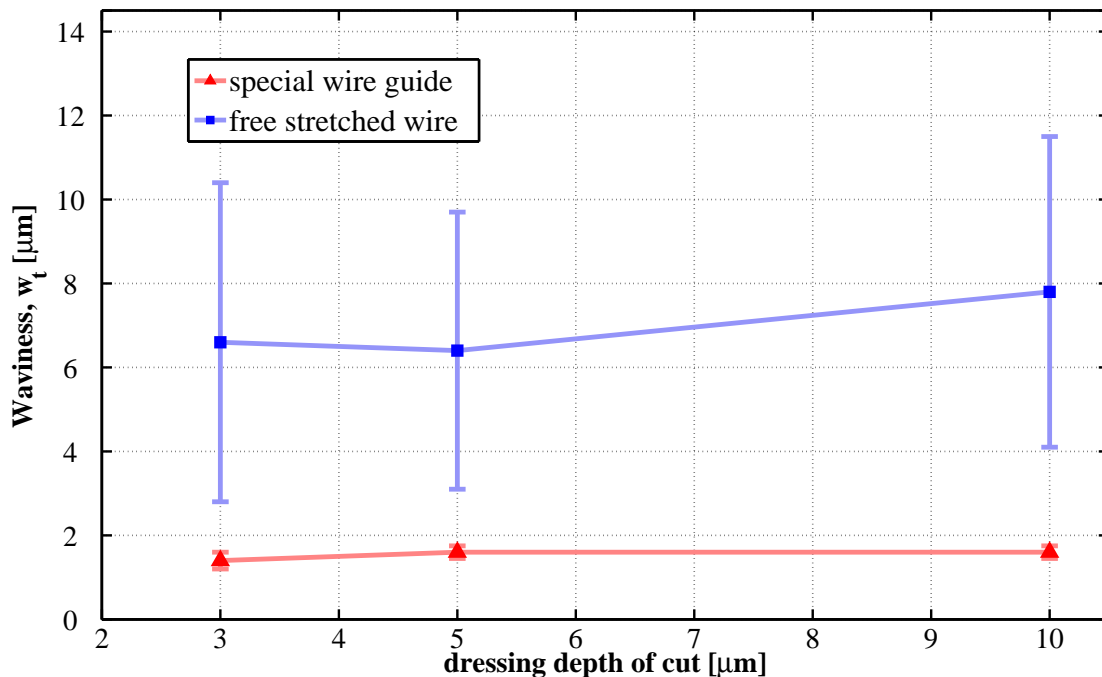


Figure 5.5 – Surface waviness of ground  $\text{Si}_3\text{N}_4$  workpieces after WEDD with a special wire guide and a free stretched wire of length  $l_w = 110$  mm

Figure 5.6 illustrates a 2.5 mm axial wide detail of a grinding wheel surface after WEDD with a free stretched wire. Irregular marks are clearly visible on the grinding wheel surface, which can be directly transferred to the workpiece after plunge grinding.

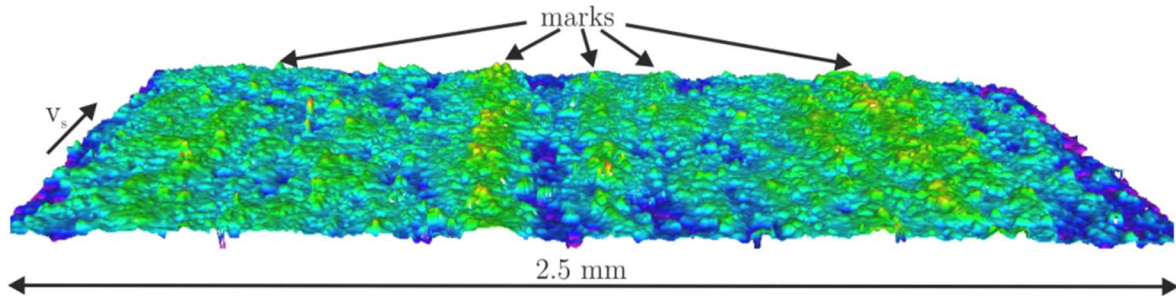


Figure 5.6 – Grinding wheel surface after WEDD with a free stretched wire

Figure 5.7 shows results of roundness  $RONt$ , i.e. the peak-to-valley deviation (Gaussian filter, 1-50  $\mu\text{m}$ ), measured on eroded steel workpieces with diameters of  $d_w = 40$  mm. Erosion parameters used in this case are the same shown in Table 5.1. Lower roundness and better repeatability were achieved by using the special wire guide. In this case, lower depth of dressing cuts leads to better roundness results, indicating that after profiling the grinding wheel, finishing dressing steps (sharpening) help to ensure better dressing accuracy. If the grinding wheel has to be profiled, even higher dressing depth of cuts then  $a_{ed} = 10$   $\mu\text{m}$  can be used, although it is recommended to profile the wheel with several consecutive small depth of dressing cuts, to minimize the risk of instabilities related to the controlled dressing feed rate and to avoid the possibility of braking the wire guide in a collision with the grinding wheel.

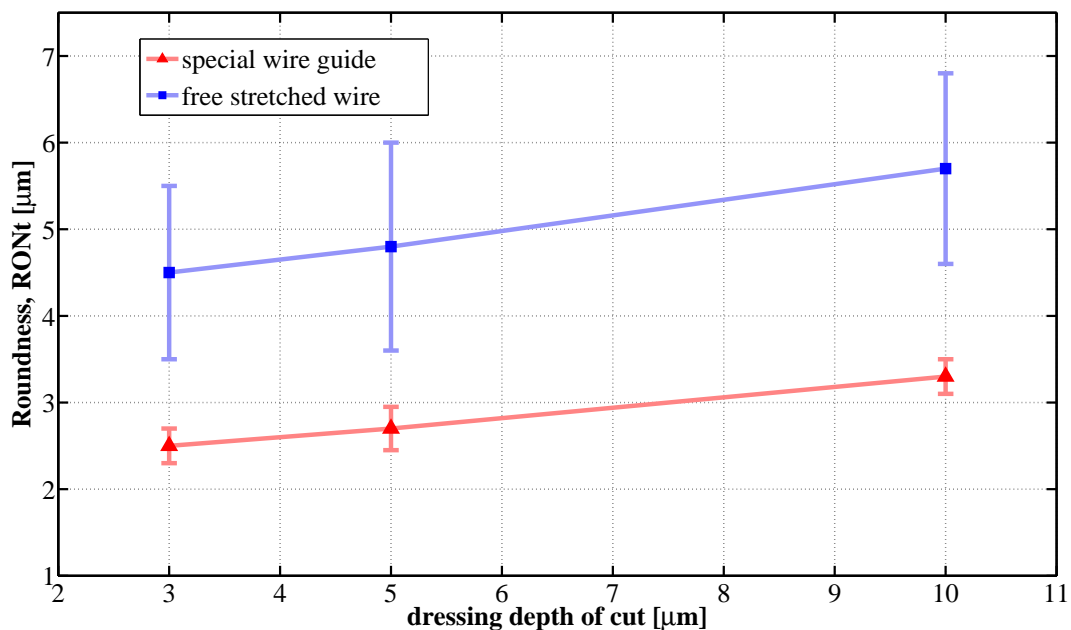


Figure 5.7 – Surface roundness on eroded steel wheels after WEDD with a special wire guide and a free stretched wire of length  $l_w = 110$  mm

To further illustrate the on-machine WEDD method, two D46 grinding wheels were profiled with particular shapes (Figure 5.8). The wheel profile 1 has two diameters differing by a radial depth of  $\Delta r_1 = 1,000 \mu\text{m}$ , and connected by a tapered transition with angle  $\alpha = 45^\circ$ . This profile was measured on ground workpieces of silicon nitride ( $\text{Si}_3\text{N}_4$ ) after plunge grinding specific material removals of  $V'_w = 300$  and  $3,000 \text{ mm}^3/\text{mm}$ . The average values after three measurements were  $\Delta r_1 = 999.7$  and  $998.9 \mu\text{m}$ , and  $\alpha = 45.1^\circ$  and  $44.9^\circ$ , respectively. The grinding wheel profile 2 has two outer radii, differing intentionally by a radial depth  $\Delta r_2$  greater than twice the wire electrode diameter, to show that it is possible to use the wire guide for dressing deep straight edges. However, special attention has to be given when grinding wheels with larger diamonds are dressed, since in this case the diamonds can damage the wire guide and cause the wire to pull out of the ground groove.

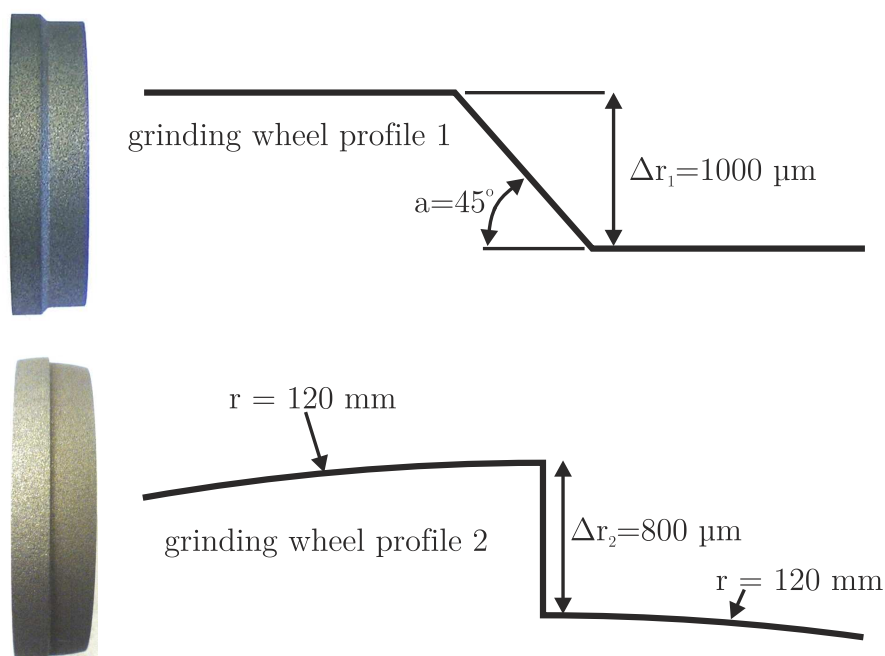


Figure 5.8 – Grinding wheel profiles after WEDD with the new wire guide

To further improve dielectric supply to the erosion zone and to avoid or minimize the possibility of thermal damages to the ceramic ring, the wire guide can also be manufactured with a small frontal opening, as shown in Figure 5.9. In this case, the wire electrode is not completely guided at the erosion zone but rather works like a free stretched wire of a very short length. Since dielectric is supplied through radial passageways contained on the flanges that clamp the ceramic ring, it reaches the erosion zone directly behind the wire, being more effective for the erosion itself and for cooling down the wire (reducing the risk of wire breakage). The ceramic ring shown in Figure 5.9 was first ground to its pre-defined width and the frontal opening manufactured by using a fiber-based pulsed nanosecond laser. In this case, the width of the opening is 5 mm. i.e. the length of the free stretched wire is only 5 mm. By means

of this design, less wire breakage occurred in comparison to the wire guide shown in Figure 5.4, improving thus the reliability of the whole wire guide system.

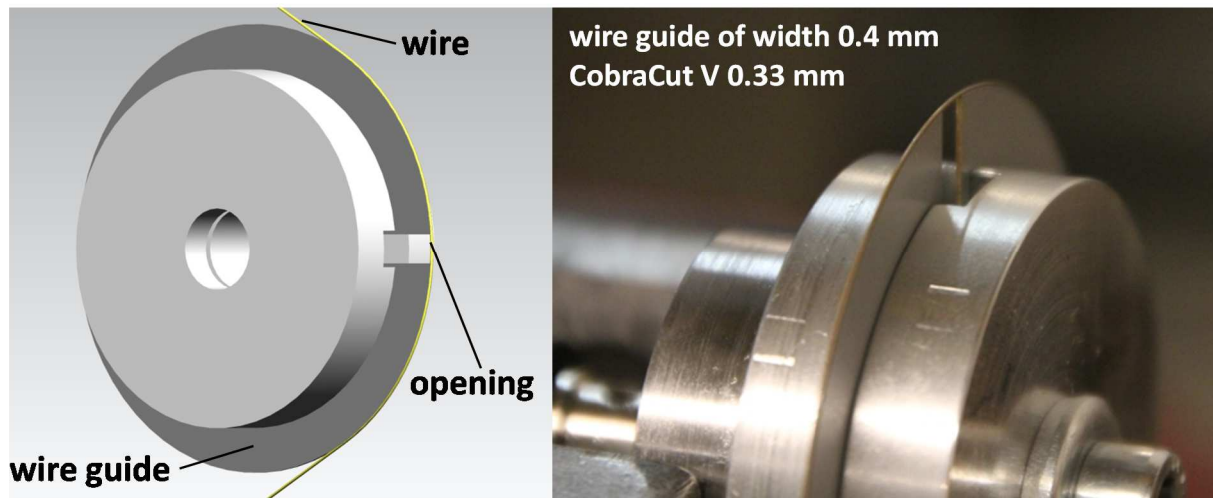


Figure 5.9 – Wire guide with a frontal opening for improving dielectric supply

The wire guide groove, which holds the wire electrode, was ground using a metal bonded diamond wheel D16. This grinding wheel was previously profiled using WEDD, so that the thin ceramic ring (0.38 – 0.4 mm) could be ground on its periphery. Details about this profiled grinding wheel are shown in Figure 5.10 (3D profile measurement).

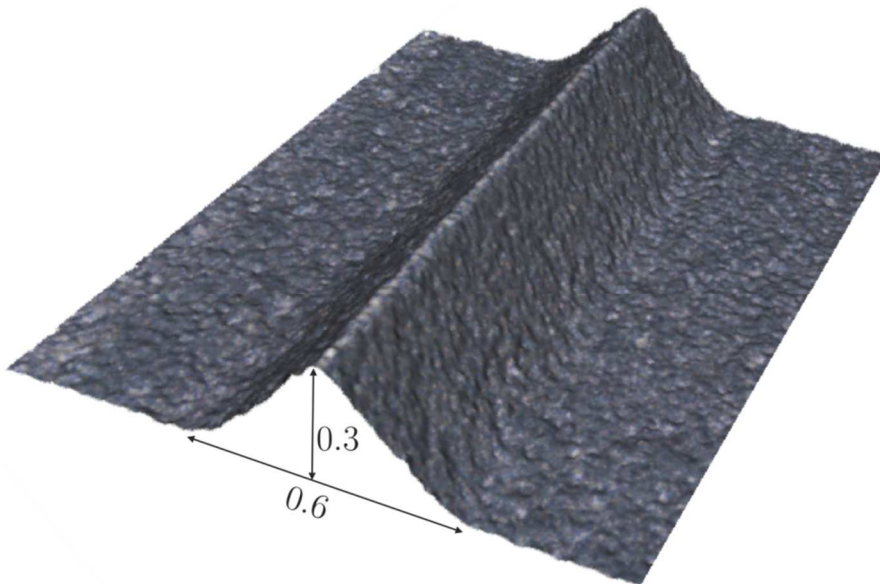


Figure 5.10 – 3D picture of the D16 metal bonded grinding wheel used for grinding the wire guide groove

Figure 5.11a shows the special wire guide mounted inside the grinding machine and a detail of the grinding oil being supplied via the wire guide system perpendicular to the grinding wheel. In Figure 5.11b the same system is being used for dressing a metal bonded grinding wheel.

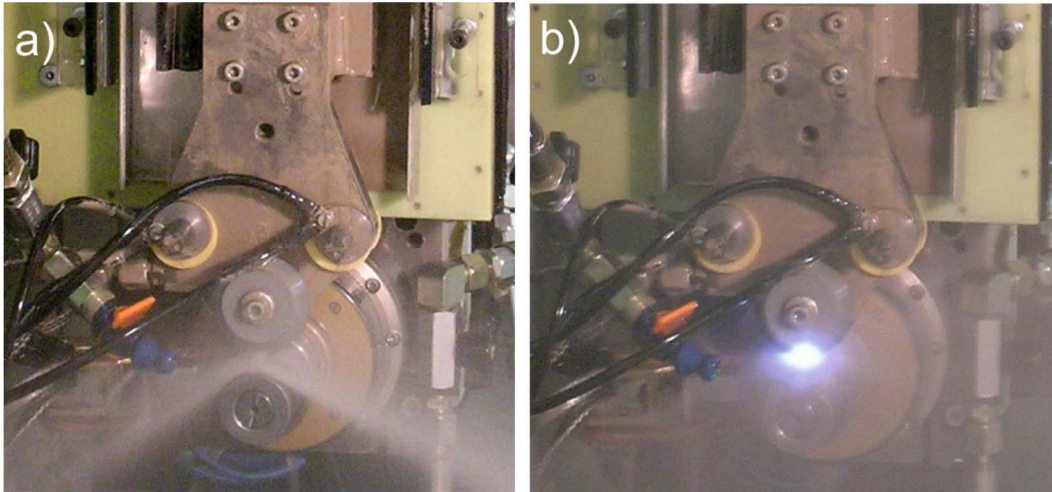


Figure 5.11 – New wire guide: a) Detail of grinding oil supply trough the wire guide system; b) WEDD using a new wire guide

### 5.3 Dressing material removal rate

In manufacturing, short cycle times are usually desired since it often leads to less manufacturing costs, especially because of rising machine and labor costs. According to the guideline published by VDI [VDI94], the machining cycle time  $t_e$  can be defined as follows

$$t_e = t_v + t_{er} + t_g \quad (5.4)$$

where  $t_v$  represents the downtime, i.e. the time in which the machine is in a passive state owing to unforeseen circumstances,  $t_{er}$  is the machine idle time, and  $t_g$  is the sum of the main production time  $t_h$  and non-productive time  $t_n$ . Normally, there is a great potential for reducing machining time when the events which have an associated non-productive time are carefully investigated, such as the dressing process. When grinding wheels are conditioned inside the grinding machine, dressing non-productive time has to be minimized to maximize grinding productivity. In order to have an efficient conditioning process, high dressing material removal rates must be achieved, while keeping appropriate dressing accuracy. To evaluate to what extent the dressing process can influence grinding productivity, WEDD was compared to SiC-dressing, and the obtained results concerning dressing material removal rates are presented in the following section.

#### 5.3.1 MRR in conventional dressing

When metal bonded grinding wheels are conditioned using a silicon carbide dressing tool, a reciprocating dressing strategy is normally applied, i.e. the dressing tool moves back and forth in axial direction with a specific dressing axial feed rate  $v_{fad}$  while a pre-



defined dressing depth of cut  $a_{ed}$  is incremented per dressing stroke. The amount of material removed from the metal bonded grinding wheel has to be measured, since dressing material removal rate depends on the chosen dressing parameters. Thus the dressing process has to be carried out for a pre-defined time and the diameter of the metal bonded grinding wheel has to be monitored to calculate the material removal rate. Table 5.2 shows different dressing parameters used to evaluate the material removal rate in SiC-dressing and Figure 5.12 shows results obtained in these experiments, where different combinations of dressing parameters were used for dressing a D46 metal bonded grinding wheel.

Table 5.2 – Parameters used in SiC-dressing of metal bonded wheels

Circumferential speed of dressing wheel	$v_{sd}$	30 m/s
Circumferential speed of metal bonded wheel	$v_w$	1 m/s
Axial dressing feed rate	$v_{fad}$	750 - 1,250 mm/min
Dressing depth of cut per dressing stroke	$a_{ed}$	10 – 20 $\mu\text{m}$
Dressing principle		Counter-rotation
Grinding oil		Blasogrind HC5
Dressing wheel specification		1A1 500x20x203.2 11C320 G12VPS81
Metal bonded grinding wheel		1A1 400x10x5x203.2 D46 C125 B1

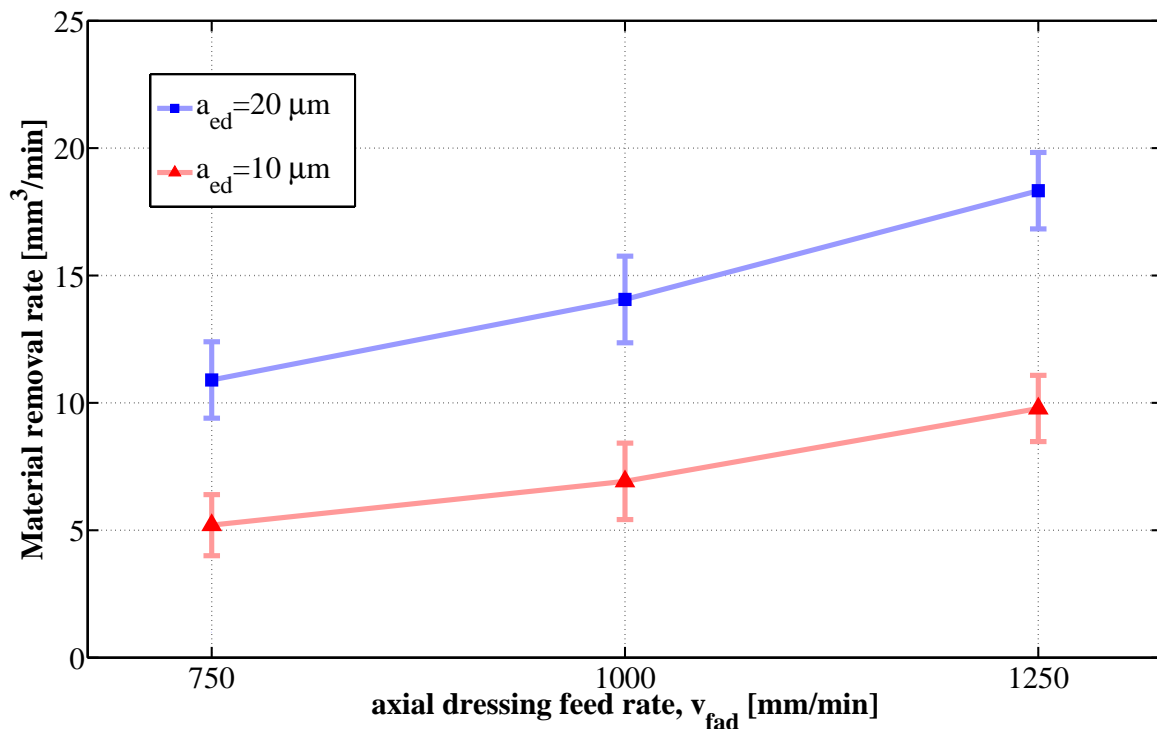


Figure 5.12 – Material removal rate in SiC-dressing of a D46 metal bonded wheel

As shown in Figure 5.12, the material removal rate varies between 5 and 18 mm<sup>3</sup>/min, representing thus a very time-intensive process. The material removal rate increases by increasing depth of dressing cut and/or axial dressing feed rate. Sharpening is recommended to be carried out using dressing depth of cuts equals or lower than 10 μm. Taking a metal bonded grinding wheel of diameter equals 400 mm and width 20 mm, the removal of a total dressing depth of cut of  $a_{ed,ges} = 10 \mu\text{m}$  would take approximately 14 minutes with a material removal rate of 18 mm<sup>3</sup>/min.

Since SiC-dressing is very time consuming, as shown in Figure 5.12, metal bonded diamond wheels are very often conditioned on independent dressing machines, where non-productive time can be reduced, since during the time in which one grinding wheel is conditioned, another is assembled and used in the grinding machine. In the case of using an external independent dressing machine, however, another problem arises, since after dressing the grinding wheel has to be carefully reassembled to the grinding machine, in order to avoid clamping errors [KLOC09b].

### 5.3.2 MRR in WED-dressing

In WED-dressing, the dielectric application method plays a decisive role regarding erosion material removal rate. The erosion gap should be completely filled with dielectric to ensure efficient erosion. Furthermore, the dielectric must penetrate the boundary layer of air which forms around the rotating grinding wheel, to prevent air reaching the erosion gap.

Figure 5.13 shows the achieved material removal rates as a function of peak current for three different dressing methods: *special wire guide*, with internal dielectric supply as proposed in Figure 5.4; *normal wire guide*, which consists of a ceramic wire guide without internal dielectric supply, and free jet nozzles for delivering the dielectric; *free stretched wire*, without using the wire guide, and supplying the dielectric via free jet nozzles. Table 5.3 shows the applied erosion parameters, and specifications of the grinding wheel and wire electrode used in these experiments.

Table 5.3 - Erosion parameters, grinding wheel and wire specifications

WEDD erosion parameters			Grinding wheel and wire electrode		
discharge duration	$t_e$	1.35-1.55 μs	Grinding wheel specification:		
pulse interval time	$t_o$	25.2 μs	1A1-50-5-20-D46-C125-B1		
wheel speed	$v_{sd}$	20 m/s	wire type	CobraCut S	
depth of dressing cut	$a_{ed}$	20 μm	wire diameter	∅	0.33 mm
oil flow rate	$Q_l$	25 L/min	free wire length	$l_w$	110 mm

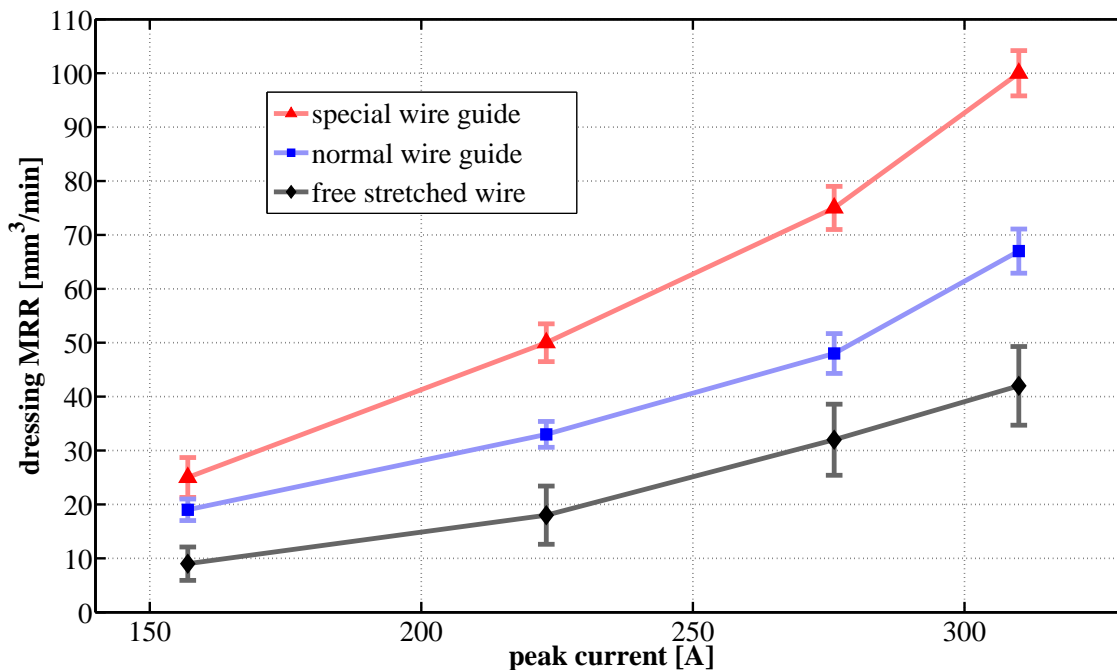


Figure 5.13 – MRR for different WED-dressing conditions.

From Figure 5.13 it can be seen that lower erosion material removal rates are achieved when a free stretched wire is used. This is particularly related to the gap instability, since the wire electrode is subjected to deflections and vibrates during the dressing process. Higher erosion material removal rates were achieved by using the special wire guide. In this case the designed internal passageways to supply dielectric through the flanges significantly impact material removal rate, showing the importance of using the right dielectric delivery method for a non-submerged erosion process. When the open voltage is applied to the system, if the gap is not completely filled with dielectric, the delay time increases, i.e. the time until dielectric breakdown occurs, leading to a lower pulse frequency and consequently lower material removal rates.

High material removal rates guarantee short dressing times, thus minimizing non-productive times and making the integration of this dressing method acceptable inside a grinding machine. For example, eroding a total depth of dressing cut  $a_{ed,ges} = 10 \mu\text{m}$  with an erosion material removal rate of  $100 \text{ mm}^3/\text{min}$  on a diamond grinding wheel diameter  $d_s = 400 \text{ mm}$  and width  $b_s = 20 \text{ mm}$  takes approximately 2.5 minutes of dressing time. This represents a dressing process which is more than 5 times faster than SiC-dressing, as shown previously in Figure 5.12.

To facilitate the integration of a WEDD unit inside a grinding machine, the use of different fluids for grinding and erosion must be avoided, meaning that the best solution would be to use only one type of fluid for both processes. Grinding oil has similar properties as erosion fluids, however contains lots of additives that are not needed in EDM processes. The results presented in Figure 5.13, however, show that

even when using a fluid which is not directly designed for EDM, high material removal rates can be achieved. One particular property of the grinding fluid which is crucial for this erosion method is its flashpoint, since in WEDD the workpiece is not submerged into the dielectric fluid. Important is to use grinding oils with high flashpoints, like the one applied on the WEDD tests shown in Figure 5.13 (Blasogrind HC5). This fluid has a flashpoint of 165°C. According to the VDI guidelines 3400, substances with flashpoints lower than 21°C (danger class AI) are not allowed to be used in electric discharge machining. Most dielectrics used in EDM have flashpoints higher than 55°C. Dielectrics with flashpoints higher than 100°C are classified as non-dangerous [VDI75].

Apart from the importance of supplying dielectric in a right way to improve erosion stability, the material removal rate in electrical discharge machining significantly depends on the thermo-electrical properties of the workpiece. In general, materials with higher melting and boiling temperatures are more difficult to be eroded. The heat conductivity, specific heat, electrical conductivity and mass density are other properties that influence the material removal rate. Figure 5.14 shows how the material removal rate can vary when different types of bond material are used. As a comparison, a standard steel material (AISI1010) was eroded. B1, B2 and B3, are bronze-based alloys, which have melting temperatures lower than 1,000° C. AISI1010, on the other hand melts at approximately 1,400° C, and as shown in Figure 5.14, is more difficult to be eroded. Two different open voltages were applied, and slightly greater MRRs were achieved using a higher open voltage, in this case 127 V.

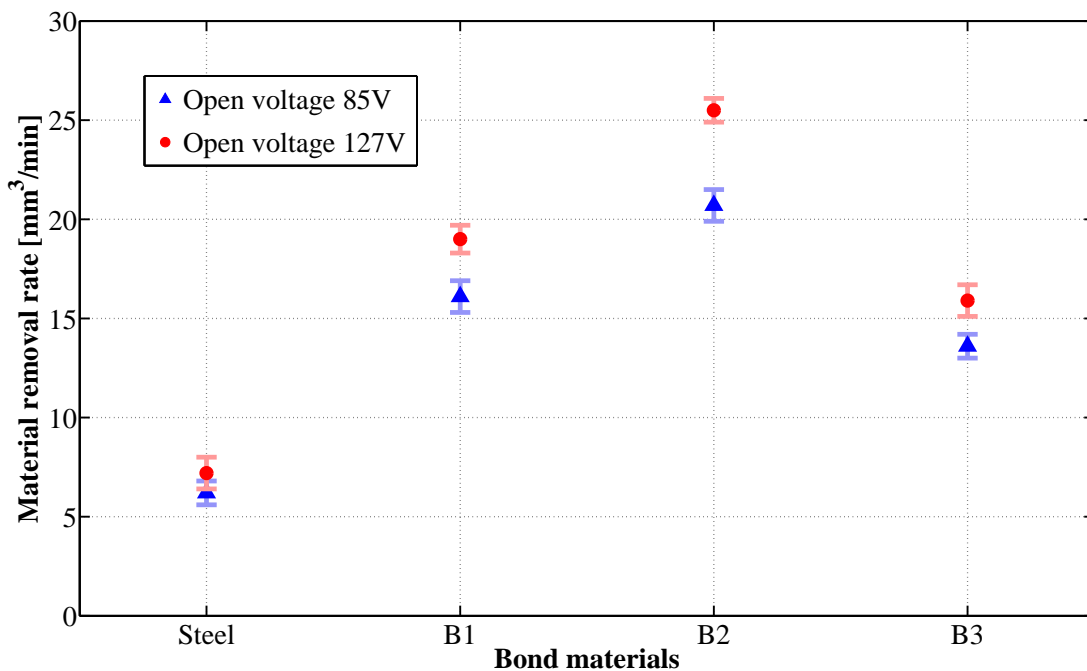


Figure 5.14 – MRR in WEDM of different bond materials and steel AISI1010

In the experiments presented in Figure 5.14, a discharge peak current of  $I_{peak} = 152$  A and a discharge duration of  $t_e = 1.35$   $\mu$ s were applied. A wire type CobraCut A with diameter 0.2 mm was used, and the experiments were carried out on a wire cut Machine Progress VP4, using deionized water. As discussed before, copper and tin are the main components of the above mentioned bond materials. Copper and tin melt respectively at 1,358 K and 505 K. B1 has higher amount of tin in comparison to B3, and less amount of tin in comparison to B2. Thus, B1 has a higher melting temperature in comparison to B2 and lower melting temperature in comparison to B3 ( $T_{melt(B3)} > T_{melt(B1)} > T_{melt(B2)}$ ).

Based on the results shown in Figure 5.14, one can see that different sets of erosion parameters are necessary when eroding different types of materials. Especially during sharpening, as will be discussed later, where a constant dressing feed rate should be applied, it is important to know which material removal rate is expected when a specific set of erosion parameters is used to erode a specific type of material. Here, modeling the erosion process brings benefits since time-intensive experiments can be avoided and the erosion material removal rate can be estimated based on simulation results. This topic will be further discussed in the following chapter 6.

## 5.4 Influence of $v_{fad}$ and $a_{ed}$ on dressing accuracy

In conventional mechanical dressing, the process is influenced, for example, by the geometry of the dressing tool, the depth of dressing cut  $a_{ed}$  and the overlapping rate  $U_d$ , which is defined as the active width of cut  $a_{pd}$  divided by the axial dressing feed per grinding wheel revolution  $f_{ad}$ . Depending thus on the grinding wheel speed, the axial dressing feed rate  $v_{fad}$  is determined. In wire electrical discharge dressing, both the dressing depth of cut  $a_{ed}$  and the axial dressing feed rate  $v_{fad}$  are also input parameters which influence the dressing process. In WEDM, the feed rate is generally controlled, i.e. erosion parameters such as the delay time or average process voltage can be monitored, so that the feed rate continuously changes depending on the erosion conditions. Thus, depending on the erodibility of the workpiece materials, different averaged feed rates are obtained. Moreover, in WEDM, the workpiece generally stays static during erosion, which guarantees a better erosion stability, since less external disturbances are likely to occur. In WEDD, however, the grinding wheel also rotates, which poses another challenge to the process. Disturbances can thus strongly influence the controlled axial dressing feed rate and decrease dressing accuracy.

Regarding the dressing depth of cut  $a_{ed}$ , the larger it is chosen the higher is the possibilities of wire breakage. It can occur since it is more difficult for dielectric to reach the erosion zone (lateral erosion). To minimize wire breakage, a less aggressive

feed control can be used. As a consequence, however, lower material removal rates are achieved. Thus, in WEDD it is recommended to use dressing depth of cuts smaller than the erosion gap, which is as large as approximately 25 to 30  $\mu\text{m}$ , as presented previously in Table 4.5. However, even when dressing depth of cuts of, for example, 20  $\mu\text{m}$  are used, profile inaccuracies can occur. To illustrate this issue, a metal bonded diamond grinding wheel was profiled with a geometry previously shown in Figure 4.20.

Figure 5.15 shows a profile measurement made on a silicon nitride workpiece ground with the above mentioned profiled grinding wheel, where a depth of dressing cut of  $a_{ed} = 20 \mu\text{m}$  was used and the dressing feed rate along the profile was set to be controlled. No wire breakage occurred during these experiments. Profile deviations of the order of magnitude of the dressing depth of cut were measured, especially on the borders of the grinding wheel. In these locations, the dielectric supply condition is different than in the middle of the wheel, since it is mainly delivered through the wire guide, in radial direction to the wheel, what can influence the material removal rate.

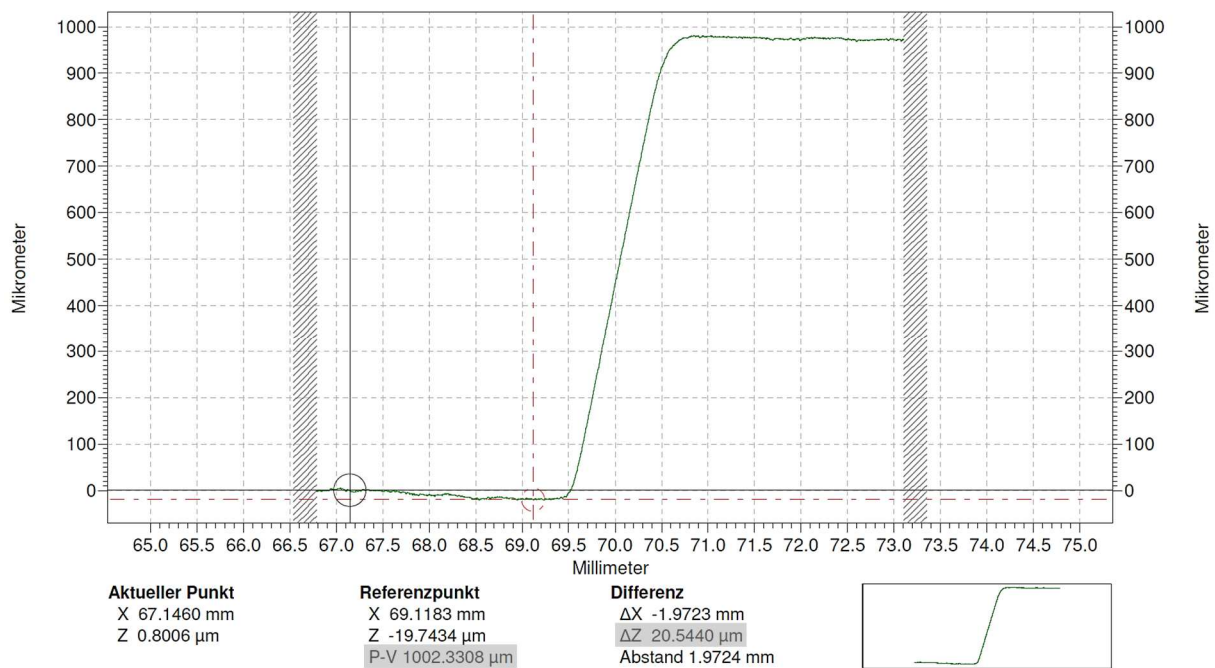


Figure 5.15 – Profile deviation on ground workpiece ( $a_{ed} = 20 \mu\text{m}$  in WEDD)

The same profile was eroded by using a small depth of dressing cut of only  $a_{ed} = 3 \mu\text{m}$ , as shown in Figure 5.16. Profile deviations were clearly reduced when compared to Figure 5.15. These results show that the use of small depth of dressing cuts is necessary to achieve adequate dressing accuracies.

However, even when small depth of dressing cuts are used, deviation can occur if a controlled axial dressing feed rate is applied. Fluctuations on the dielectric supply or other disturbances can lead to fluctuations on the axial dressing feed rate, since the control system can quickly react to it, and consequently cause profile deviations on the

grinding wheel. Figure 5.17 shows a comparison of dressing accuracies when controlled and constant axial dressing feed rates are used. Better dressing accuracies and repeatability were achieved for constant axial dressing feed rates, in this case 40 mm/min (the maximal available feed rate of the WEDD unit during the erosion).

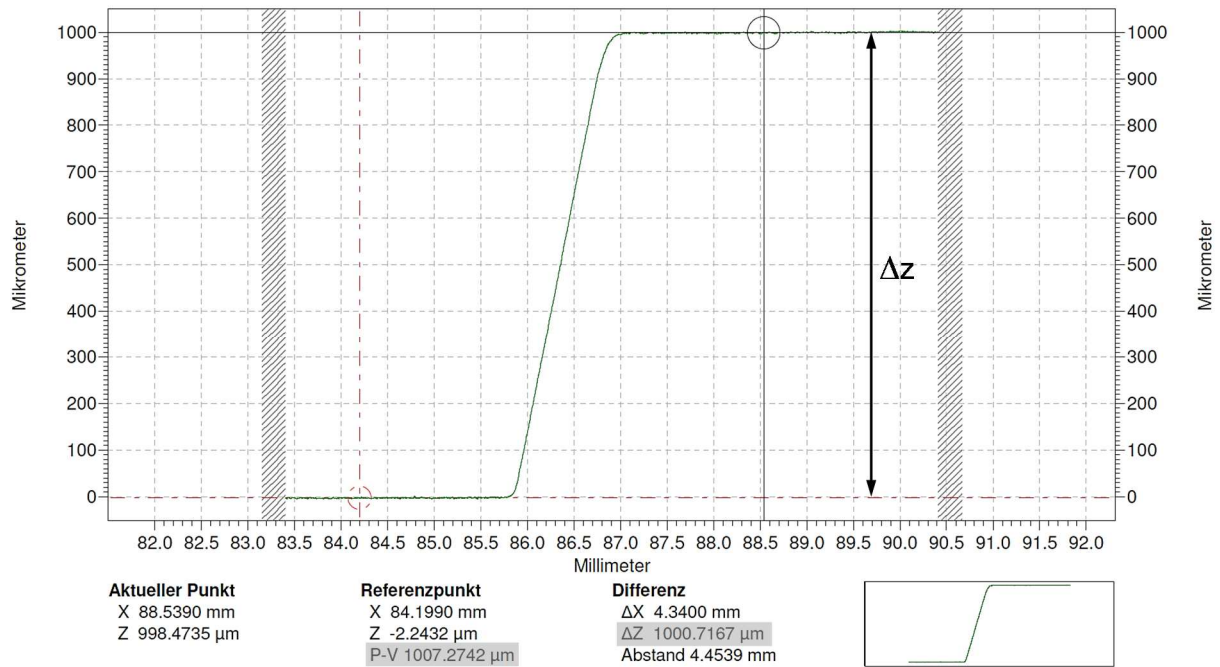


Figure 5.16 – Improved profile accuracy due to the use of small  $a_{ed}$  during WEDD

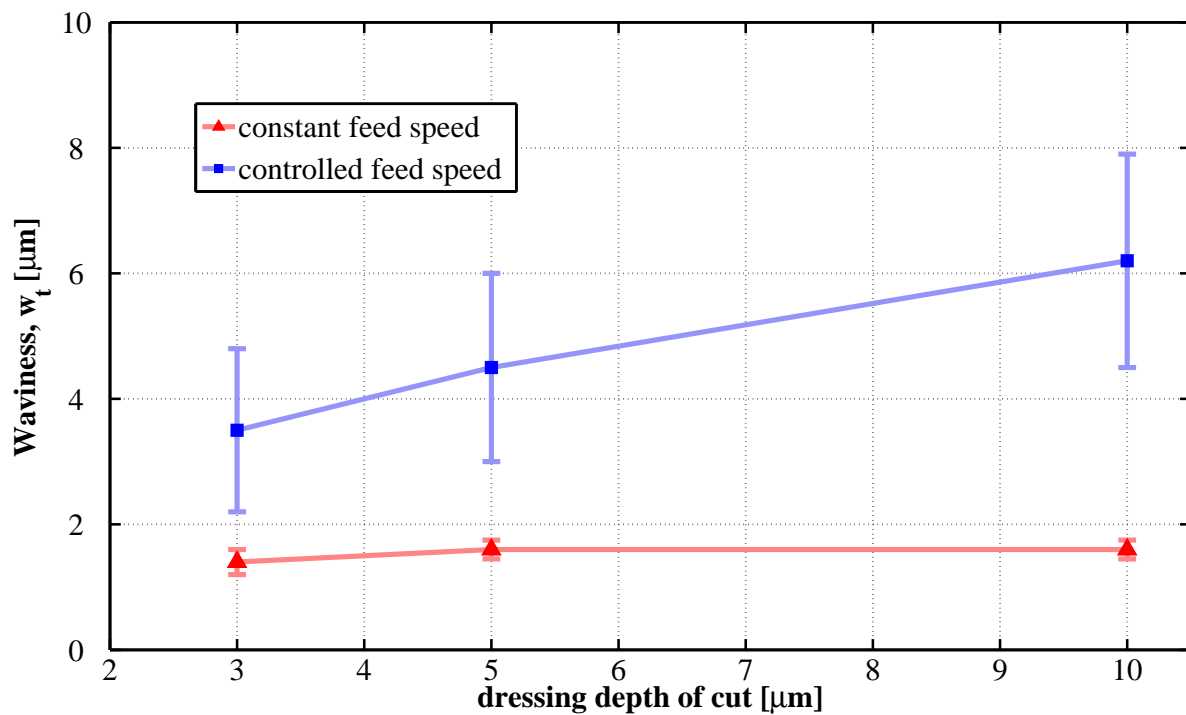


Figure 5.17 – Dressing deviations using controlled feed rate and constant axial dressing feed rate ( $v_{fd} = 40$  mm/min)

Based on the results presented so far, one can say that in WEDD-profiling controlled axial dressing feed rates and larger dressing depth of cuts should be used to maximize material removal rates while in WEDD-sharpening constant axial dressing feed rates and smaller depth of dressing cuts are recommended to achieve better dressing accuracies.

The grinding wheel profile previously illustrated in Figure 4.20 was conditioned using a constant axial dressing feed rate and dressing depth of cut of  $a_{ed} = 3 \mu\text{m}$ , to illustrate the accuracy of this WEDD method. The radial distance of  $1000 \mu\text{m}$  (see Figure 4.20) was monitored. Figure 5.18 illustrates how the workpiece profile was calculated, after being measured with a profilometer Form Talysurf series 2. Two measurement areas were selected, and the average height of the profile was measured. The difference between both measurements gives the radial distance  $\Delta z$ . Figure 5.19 shows the results obtained for  $\Delta z$  and the total profile height  $P_t$ . The latter is obtained directly from the measurement device and takes the roughness into consideration, i.e. gives the distance between the highest peak and the deepest valley over the profile. The results indicate that  $\Delta z$  was kept within a range of only  $2 \mu\text{m}$  even after grinding specific material removals of more than  $3,000 \text{ mm}^3/\text{mm}$ .  $P_t$  also follows the same trend, which also gives approximately a value of  $1,000 \mu\text{m}$  when the roughness  $R_t$  is subtracted from these measurements ( $R_t$  was about  $6.5 \mu\text{m}$ , similar to the  $R_z$  values presented in Figure 4.24).

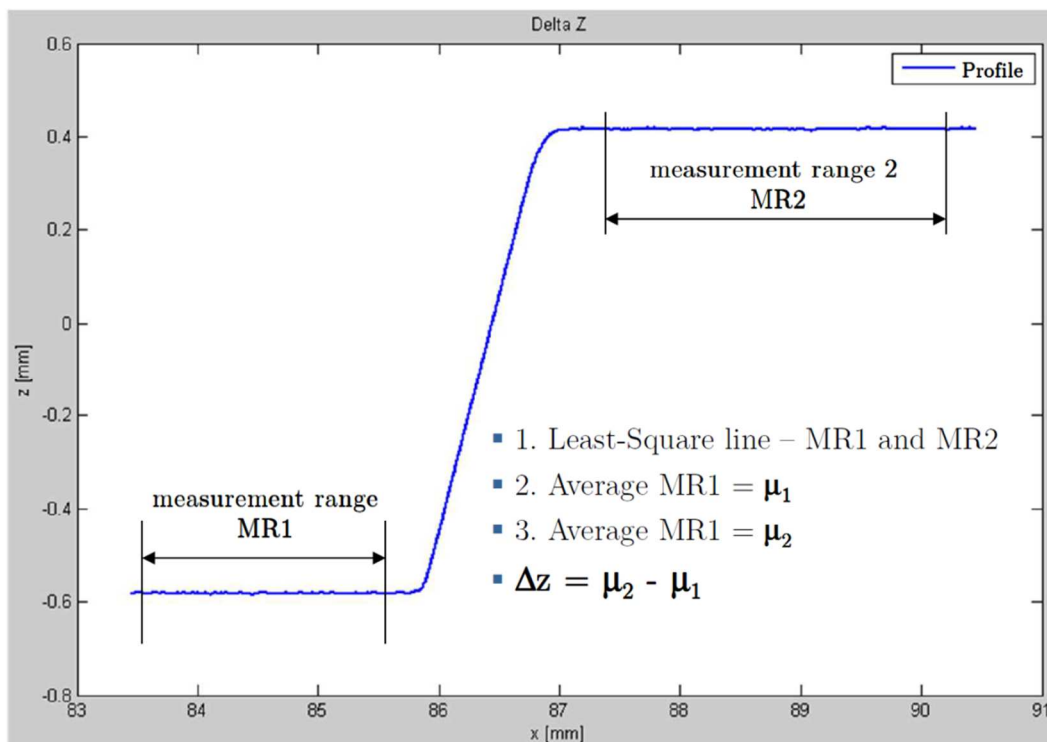


Figure 5.18 – Methodology for measuring the radial profile difference on silicon nitride workpieces ground by means of a WED-dressed metal bonded grinding wheel



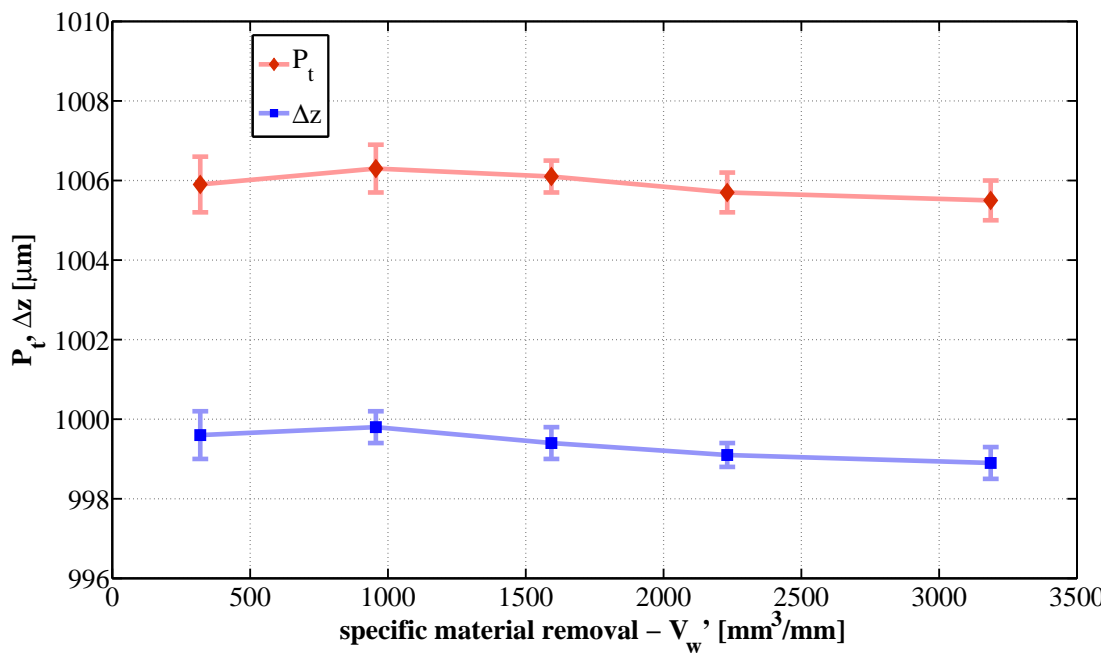


Figure 5.19 – Profile accuracy of  $\text{Si}_3\text{N}_4$  workpieces ground by WED-dressed wheel

All previous results show that WEDD is a suitable process for conditioning metal bonded grinding wheels when beneficial process windows are chosen.

## 5.5 In-process-dressing

In-process dressing is a form of conditioning during grinding, which can be designed as continuous dressing or carried out at pre-defined time steps. There are basically two main advantages when in-process dressing is used [WEIN12c]. First, dressing time no longer influences the machining cycle time  $t_e$ , since it is carried out during the main production time  $t_b$ , i.e. during grinding. Second, the grinding wheel micro and macro geometry can be kept more constant over time, since dressing constantly corrects small deviations caused by wheel wear. Therefore, in-process dressing can positively impact grinding accuracy as well as increase grinding productivity.

Figure 5.20 shows the influence of in-process dressing on grinding forces, where the raw signal acquired using a rotating dynamometer type Z15168 SN473735 from Kistler is presented. It follows a sine curve due to the rotation of the workpiece. Table 5.4 shows grinding and dressing parameters used in this experiment. Four out of seven measurements steps are shown in Figure 5.20, each one corresponding to a specific material removal of  $750 \text{ mm}^3/\text{mm}$ . This specific volume of material is removed within 75 s (main grinding time), since a specific material removal rate of  $10 \text{ mm}^3/\text{mm}$  was used. A total specific material removal of  $5,250 \text{ mm}^3/\text{mm}$  was ground, which corresponds to the fourth measurement step presented in Figure 5.20. In-process-dressing was carried out during the third step, where the acquired signal clearly

dropped to a similar level as during the first grinding step. In this experiment, a large dressing depth of cut of  $a_{ed} = 20 \mu\text{m}$  was used, aiming to clearly show that WEDD can be carried out during grinding and bring the benefits already mentioned before.

Table 5.4 - Erosion parameters, grinding wheel and wire electrode specifications

WEDD erosion parameters			Grinding wheel and workpiece		
discharge duration	$t_e$	1.55 $\mu\text{s}$	1A1-50-5-20-D46-C125-B1		
peak current	$I_{peak}$	276 A	wheel speed	$v_s$	60 m/s
pulse interval time	$t_o$	25.2 $\mu\text{s}$	specif. MRR	$Q'_w$	10 $\text{mm}^3/\text{mms}$
wheel speed	$v_{sd}$	60 m/s	speed ratio	$q_s$	100
depth of dressing cut	$a_{ed}$	20 $\mu\text{m}$	wheel width	$b_s$	10 mm
wire type	CobraCut S		Workpiece material	$\text{Si}_3\text{N}_4$	
wire diameter	0.33 mm		cutting fluid	Blasogrind HC5	

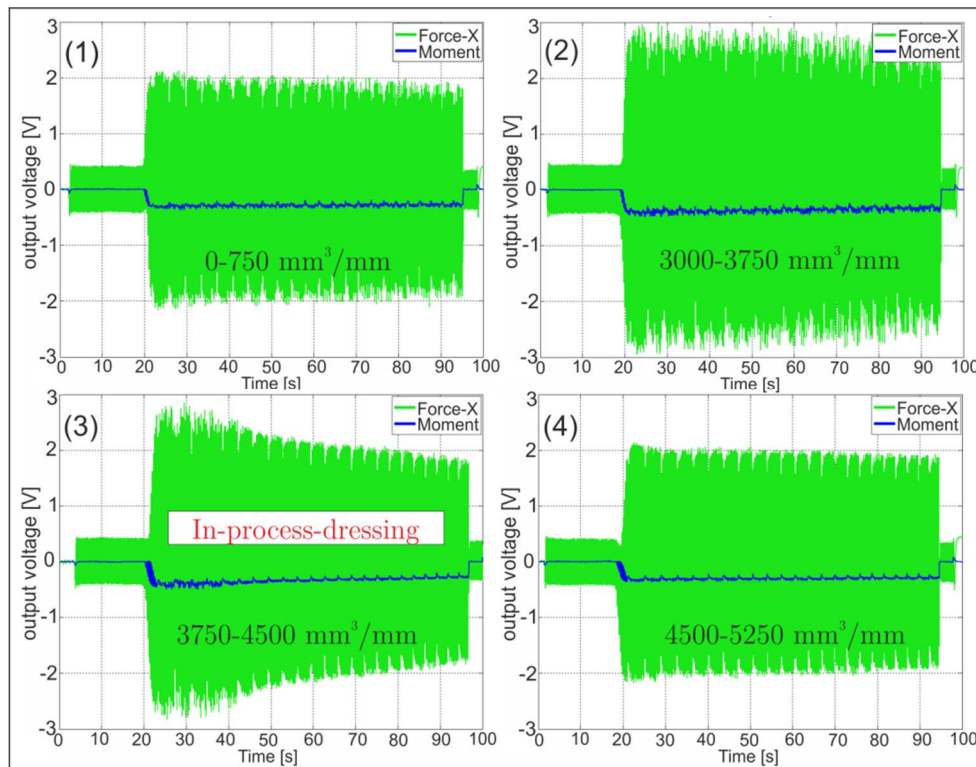


Figure 5.20 – Reduction of grinding forces during in-process-dressing represented by the raw signal acquired using a rotating dynamometer (parameters according to Table 5.4)

Figure 5.21 shows the tangential grinding forces that correspond to the previous experiment. In-process dressing is carried out after grinding a specific material removal of  $3,750 \text{ mm}^3/\text{mm}$ . The tangential forces increase with increasing amount of ground material, and quickly decrease during in-process dressing.

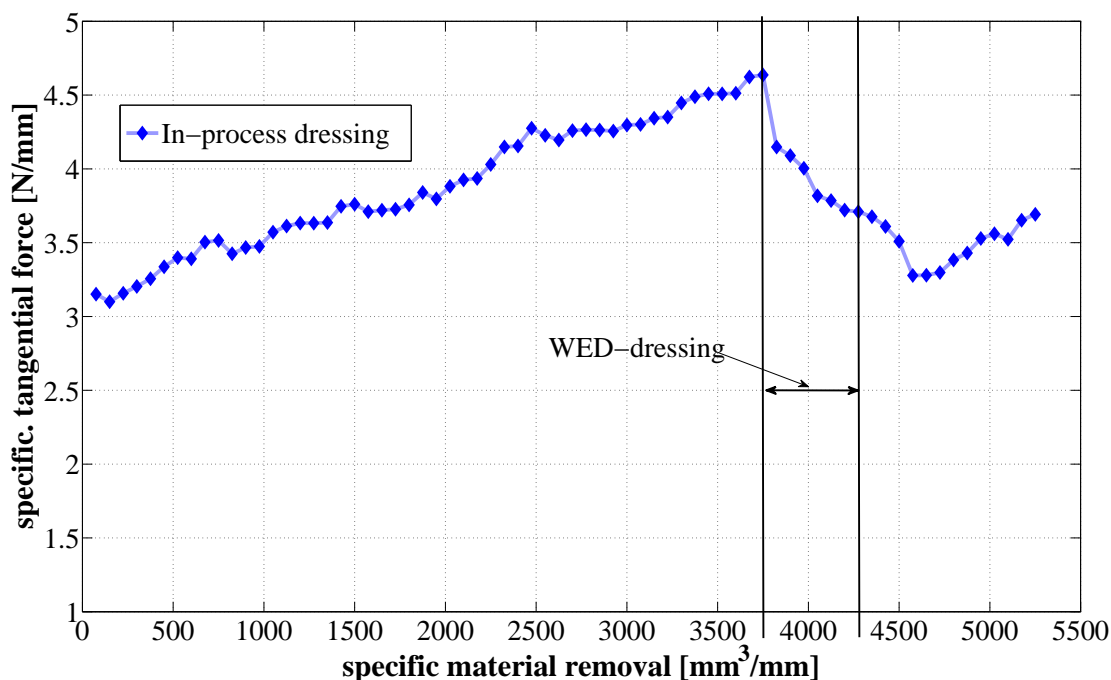


Figure 5.21 – Influence of in-process dressing on specific tangential grinding forces (dressing and grinding parameters according to Table 5.4)

The results shown in both previous figures, however, are not the most important application of in-process dressing. It was shown that dressing can be carried out during grinding and thus non-productive time associated to dressing can be minimized. However, grinding forces still significantly change over time. In-process dressing can be applied to keep grinding forces more constant in case if it is applied more often during grinding, using small depth of dressing cuts. Figure 5.22 shows results of grinding forces, measured in a grinding experiment where in-process dressing was designed to remove dressing depth of cuts of  $a_{ed} = 1 \mu\text{m}$  after every specific material removal of  $100 \text{ mm}^3/\text{mm}$ . Results are then compared to a normal on-machine dressing process, in which a total dressing depth of cut of  $a_{ed,ges} = 10 \mu\text{m}$  (2 times  $a_{ed} = 5 \mu\text{m}$ ) was applied only after grinding a specific material removal of  $1,500 \text{ mm}^3/\text{mm}$ . Table 5.5 shows dressing and grinding parameters used in these experiments. When in-process dressing is carried out, grinding forces are kept more constant over time, and do not reach the same maximum as for on-machine dressing. A total specific material removal of  $4,500 \text{ mm}^3/\text{mm}$  was ground, meaning that the normal on-machine dressing experiment was carried out 3 times, i.e. after each  $1,500 \text{ mm}^3/\text{mm}$  a total depth of dressing cut of  $a_{ed,ges} = 10 \mu\text{m}$  was removed. It can be seen that the specific tangential forces varied between approximately  $2.9 \text{ N/mm}$  and  $3.25 \text{ N/mm}$  in on-machine dressing, while during in-process dressing, specific tangential forces were kept within a small range of  $\pm 0.03 \text{ N/mm}$  around  $3 \text{ N/mm}$ . As a consequence, ground workpieces can be manufactured within tighter tolerances, since grinding conditions are more constant over time, which guarantees better repeatability. Moreover, the total main time and dressing time

needed to grind  $4,500 \text{ mm}^3/\text{mm}$ , when in-process dressing is carried out and the parameters shown in Table 5.5 are used, is equal to 15 minutes. In on-machine dressing, however, at least 1.5 minutes has to be added for the removal of  $10 \text{ }\mu\text{m}$  after each removal of  $1,500 \text{ mm}^3/\text{mm}$ . Thus, in this case, main time plus dressing time would be 19.5 minutes, which represents 30% more than during in-process dressing.

In addition, an averaged radial wheel wear of  $8 \text{ }\mu\text{m}$  was measured for on-machine dressing, meaning that a total of  $18 \text{ }\mu\text{m}$  ( $8 \text{ }\mu\text{m}$  of wear plus  $a_{ed,ges} = 10 \text{ }\mu\text{m}$ ) was removed from the grinding wheel after each removal of  $1,500 \text{ mm}^3/\text{mm}$ . In in-process dressing, however, only  $15 \text{ }\mu\text{m}$  was removed after each removal of  $1,500 \text{ mm}^3/\text{mm}$ , showing another advantage of this dressing process.

Table 5.5 - Erosion parameters, grinding wheel and wire specifications

WEDD erosion parameters			Grinding wheel and workpiece		
discharge duration	$t_e$	$1.55 \text{ }\mu\text{s}$	1A1-50-5-20-D46-C125-B1		
peak current	$I_{peak}$	$276 \text{ A}$	wheel speed	$v_s$	$45 \text{ m/s}$
pulse interval time	$t_o$	$25.2 \text{ }\mu\text{s}$	specif. MRR	$Q'_w$	$5 \text{ mm}^3/\text{mms}$
wheel speed	$v_{sd}$	$45 \text{ m/s}$	speed ratio	$q_s$	$100$
depth of dressing cut	$a_{ed}$	$1 - 5 \text{ }\mu\text{m}$	Workpiece material	$\text{Si}_3\text{N}_4$	
wire type	CobraCut S $0.33 \text{ mm}$		cutting fluid	Blasogrind HC5	

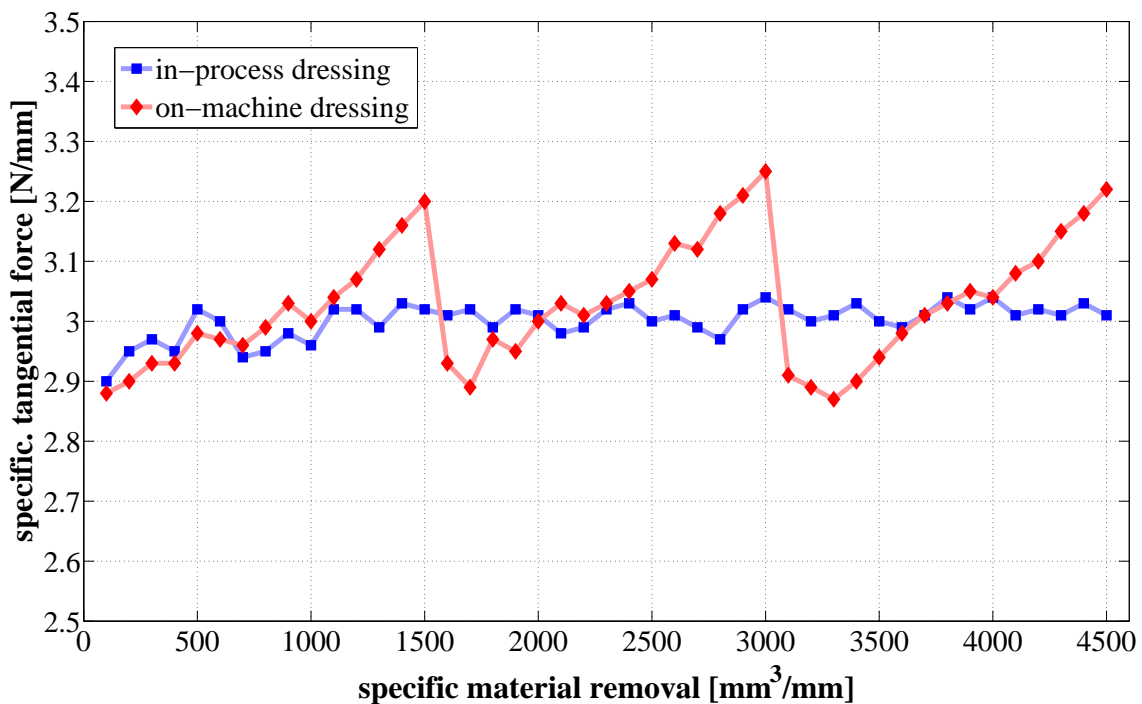


Figure 5.22 – In-process dressing vs. on-machine dressing ( $45 \text{ m/s}$ ;  $Q'_w$   $5 \text{ mm}^3/\text{mms}$ ) (dressing and grinding parameters according to Table 5.5)

Aiming to correctly perform in-process dressing, previous knowledge about the grinding process is necessary, since the way how the grinding wheel wears is of key importance (see Figure 4.19 for details about grinding G-ratios). Wear rate thus defines how often dressing has to be carried out and which volume has to be removed to compensate for wheel wear. If wheel wear is underestimated, it cumulates and leads to an increase of grinding forces, and consequently a decrease on grinding accuracy. On the other hand, an overestimation of wear has an economic impact on the grinding process, since unnecessary volume of expensive abrasives is removed, leading to lower overall process efficiency. Wheel wear depends on a complex set of variables as shown in Figure 5.23. Thus, in-process dressing has to be optimized for each combination of abrasives, bond material, workpiece and grinding process. For instance, if everything is kept unchanged but only the cutting fluid pressure is varied, an impact on wear rate is expected. In another case, similar G-ratios can be achieved when different specific material removal rates are applied, however wear rates are different, and again, in-process dressing has to be adjusted. The same is valid for all the different sets of inputs described in Figure 5.23.

Abrasive	Bond	Workpiece	Grinding process
-Material (diamond, CBN...) -Size (D46, D91, D126...) -Concentration (C75, C100, C125...) -Form (blocky, sharp-shaped...) -Properties (Friability, thermal and chemical stability...)	-Type (metallic, vitrified...) -Mechanical properties (hardness, toughness...) -Stability (thermal, chemical...)	-Material (metal, ceramics...) -Mechanical properties (hardness, toughness...) -Chip formation -Geometry	-Cutting speed -Feed rate -Type of process (plunge, internal...) -Grinding machine (disturbances...) -Grinding wheel profile -Cutting fluid (type, application...)

Figure 5.23 – Variables that influence wheel wear rate

Figure 5.24 shows a comparison of two different in-process dressing strategies. In both cases a dressing depth of cut of  $a_{ed} = 2 \mu\text{m}$  was applied, however after grinding different specific material removals (200 and 300  $\text{mm}^3/\text{mm}$ ). Table 5.5 shows dressing and grinding parameters used in these experiments, where only the grinding wheel speed was increased to 60 m/s. The results indicate that for the particular case in which dressing is performed after every 300  $\text{mm}^3/\text{mm}$ , a dressing depth of cut of only  $a_{ed} = 2 \mu\text{m}$  is not enough to compensate for wheel wear, and grinding forces keep increasing. On the other hand, grinding forces can be kept more constant if the same depth of dressing cut is applied after every 200  $\text{mm}^3/\text{mm}$ . Thus, as mentioned before, it is important to previously know the expected wear rate during grinding so that the right dressing strategy can be chosen.

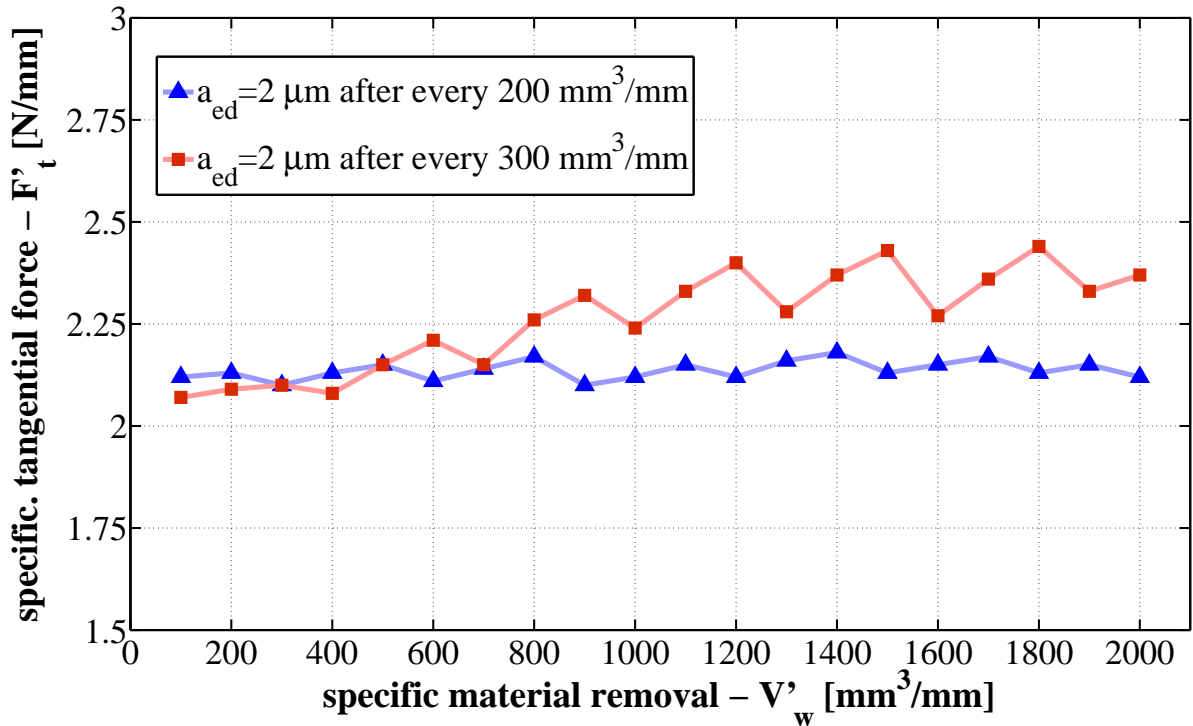


Figure 5.24 – In-process dressing using two different strategies, i.e. same depth of dressing cut but after different specific material removals (parameters according to Table 5.5 where only the grinding wheel speed was increased to 60 m/s)

In-process dressing can also be applied when grinding ductile materials that are normally difficult to grind. In these cases, grinding wheel load is likely to occur since material stays adhered to the grinding wheel, blocking its intergranular spaces and consequently increasing friction. WEDD can be used as a cleaning process, in which the adhered material, in this case an electric conductive material, is eroded during dressing. One example is shown in Figure 5.25, where aluminum was ground using a metal bonded D46 grinding wheel. In Figure 5.25a one can see that aluminum is adhered to the wheel and the mark left by this adhesion,  $b_w$ , gradually disappears after dressing 2 times  $a_{ed} = 2 \mu\text{m}$  (Figure 5.25b and c). Grinding tangential forces were monitored and are presented in Figure 5.26. Aluminum was ground using a specific material removal rate of 3.5 mm<sup>3</sup>/mms and grinding wheel speed of 30 m/s. In normal on-machine dressing, tool load occurred and grinding forces increased fast and suddenly. Loud noise was perceived at this point, after the removal of approximately 400 mm<sup>3</sup>/mm. This occurs due to the increased friction between grinding wheel and workpiece. On the other hand, by applying a dressing depth of cut of  $a_{ed} = 2 \mu\text{m}$  for each removal of 200 mm<sup>3</sup>/mm in in-process-dressing, it was possible to carry on with the grinding process. It also can be seen that grinding forces increased during the removal of 1,000 mm<sup>3</sup>/mm, pointing out that wheel load was not completely removed during dressing. In this case, larger depth of dressing cuts should be applied or dressing should be carried out more frequently.

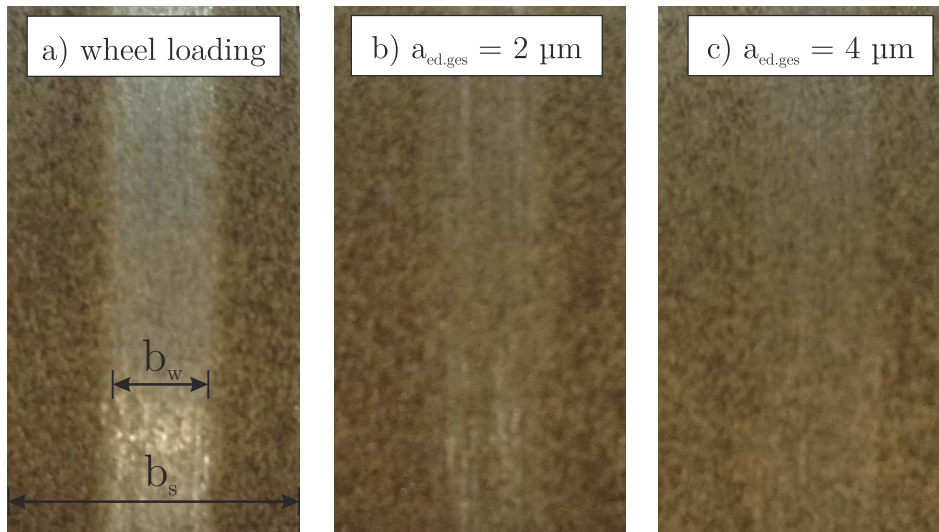


Figure 5.25 – Diamond grinding wheel loaded with aluminum in (a), after dressing  $2 \mu\text{m}$  in (b) and after dressing 2 times a dressing depth of cut of  $a_{ed} = 2 \mu\text{m}$  in (c)

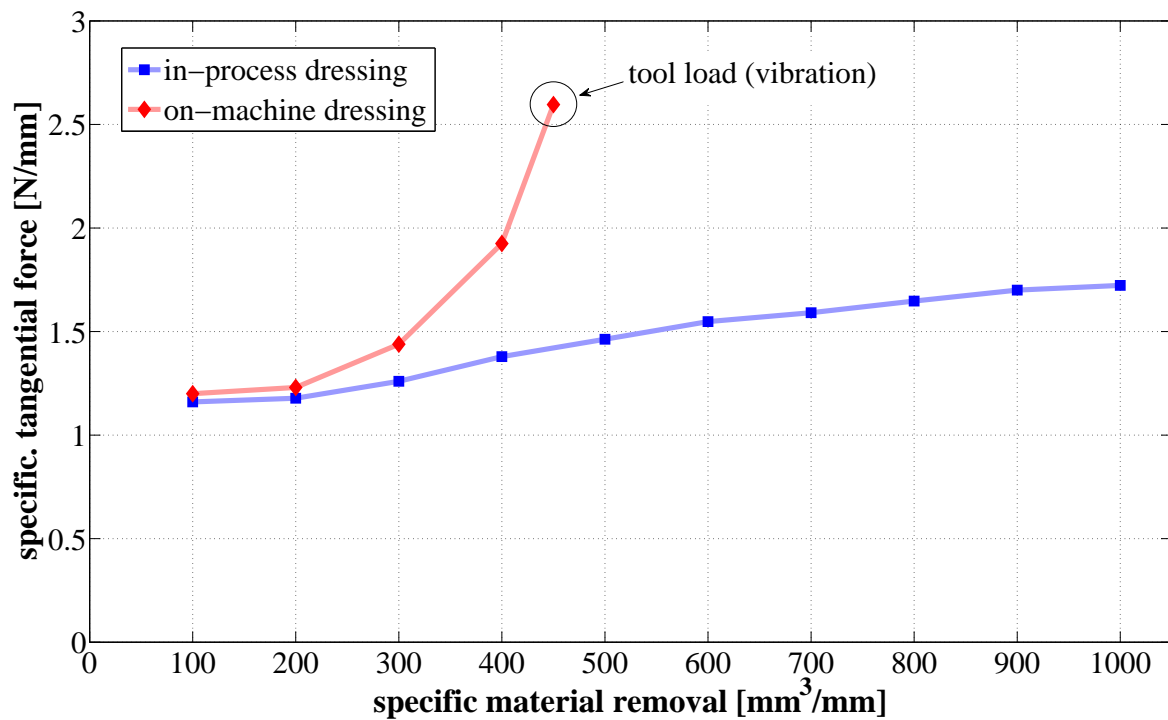


Figure 5.26 – On-machine vs. in-process dressing in grinding aluminum

From the results presented in this section, it can be stated that in-process dressing is an enabling technology that can contribute to improve dressability of metal bonded grinding wheels and consequently allow better use of the advantages offered by this type of grinding tools. Nevertheless, deep knowledge about grinding wheel wear is a pre-requisite for this process to work properly.

## 6. Modeling and simulation of WEDM

Electrical discharge machining involves complex physical processes occurring simultaneously, which lead to removal of material from both the tool electrode and workpiece. This material removal occurs mainly due to a thermal mechanism, where material melts, evaporates and is ejected at the end of the discharge. Modeling the wire electrical discharge machining process can help to better interpret and predict results, which are otherwise difficult to understand. In this context, the evaluation of single discharges is essential to first acquire further knowledge about the erosion process. Single discharges can subsequently be modeled based on erosion process parameters and thermophysical properties of different materials involved in this process. Hence, the dressing material removal rate can be predicted, the influence of high relative speed on WEDM can be better understood and diamond graphitization can be analyzed. This chapter first describes the approach used to model the WEDM process. The validation of the model is then presented. Finally, results obtained from simulations are discussed and compared with experimental results.

### 6.1 WEDM model approach

The WEDM model is based on the heat conduction phenomenon, assuming that heat generated in the plasma is transmitted to the workpiece via a specific heat source, in this case, neither a point heat source nor a disc heat source, but a time-dependent source, which grows from a point to a disc during the discharge duration. The partial differential equation that describes heat conduction in Cartesian coordinates is presented in equation (6.1) and the thermal diffusivity in equation (6.2),

$$\frac{\partial^2 T}{\partial x^2} + \frac{\partial^2 T}{\partial y^2} + \frac{\partial^2 T}{\partial z^2} + \frac{\dot{q}}{k} = \frac{1}{\alpha} \cdot \frac{\partial T}{\partial t} \quad (6.1)$$



$$\alpha = \frac{k}{\rho \cdot c_p} \quad (6.2)$$

where  $T$  is the temperature,  $x$ ,  $y$  and  $z$  represent the Cartesian coordinate system,  $\dot{q}$  is the rate of energy generation per unit volume,  $k$  is the thermal conductivity,  $\alpha$  is the thermal diffusivity,  $t$  represents the time,  $\rho$  the mass density and  $c_p$  is the specific heat at constant pressure.

Analytical methods can be used to solve equation (6.1), but they are limited to special cases in boundary conditions and geometry and are rather applied for steady, two-dimensional conduction problems. Numerical techniques can be extended to three-dimensional problems and better cope with more complex geometries and boundary conditions. The finite-difference method is a numerical technique suitable for solving the heat conduction equation, and is used as basis to model WEDM in this work. The finite-difference method, where time and space are discretized, allows for temperature calculation in different discrete nodal points, as described in the following section.

### 6.1.1 Finite-difference method

Since the finite-difference method is based on the discretization of space and time, the first step in this approach is to define the nodal network. Figure 6.1 shows a schematic representation of a two-dimensional nodal network where coordinates  $x$  and  $y$  are respectively expressed by the  $m$  and  $n$  indices. In a three-dimensional nodal network further parallel planes to the  $xy$  plane are taken into consideration and the coordinate  $z$  is expressed by the  $p$  index.

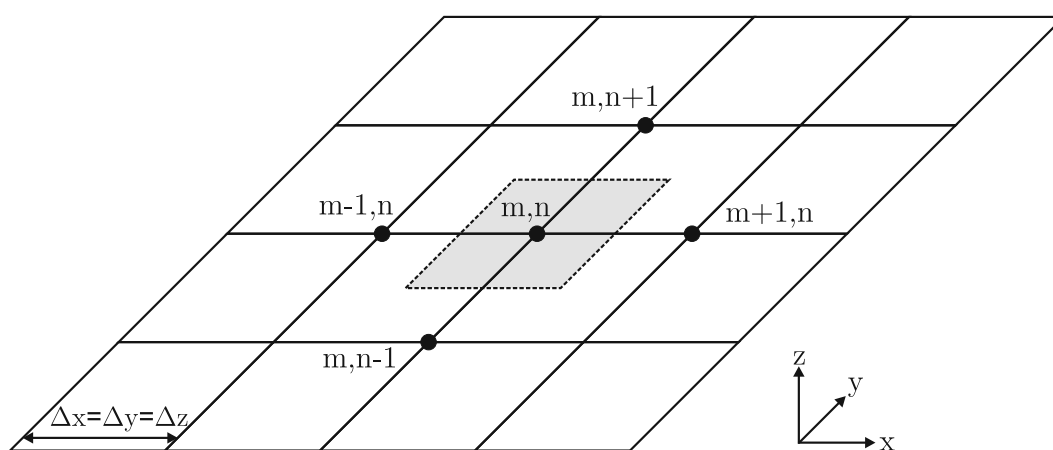


Figure 6.1 – Two-dimensional nodal network

Figure 6.2 shows a schematic representation on how to calculate the temperature of the central nodal point,  $T_{m,n}$ , which represents the average temperature of the surrounding region. Considering the arbitrary temperature distribution

represented in Figure 6.2, one can start by calculating the first derivative of temperature with respect to  $x$  for the locations  $(m-1/2,n)$  and  $(m+1/2,n)$ .

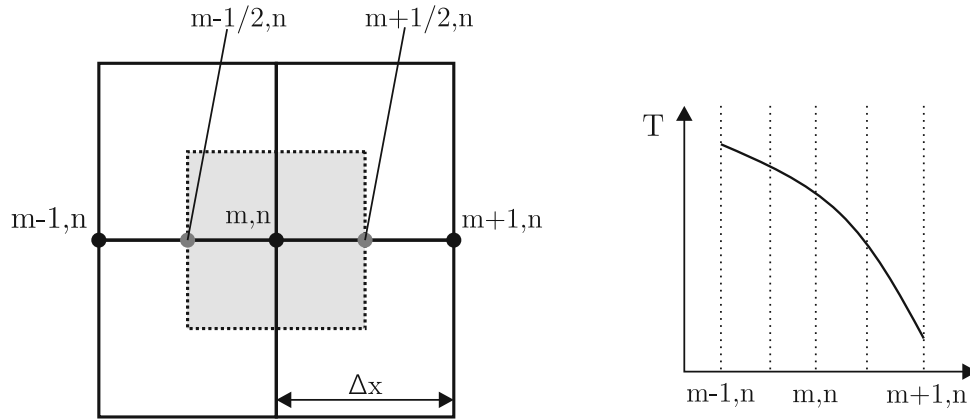


Figure 6.2 – Finite-difference approximation

Equations (6.3) and (6.4) show the approximations made to represent the above mentioned derivatives. The distance between nodal points,  $\Delta x$ , plays a decisive role on the accuracy of this method, i.e. the accuracy can be improved by decreasing  $\Delta x$ . However, choosing a small distance between consecutive nodal points increases the total amount of nodal points that have to be considered, thus increasing the computation time needed for running simulations.

$$\left. \frac{\partial T}{\partial x} \right|_{m-1/2,n} \approx \frac{T_{m,n} - T_{m-1,n}}{\Delta x} \quad (6.3)$$

$$\left. \frac{\partial T}{\partial x} \right|_{m+1/2,n} \approx \frac{T_{m+1,n} - T_{m,n}}{\Delta x} \quad (6.4)$$

Now that the first derivatives are determined, one can calculate the second derivative of temperature with respect to  $x$  for the location  $(m,n)$ , resulting in equation (6.5), which shows the dependency of the second derivative for location  $(m,n)$  on the first derivative for locations  $(m-1/2,n)$  and  $(m+1/2,n)$ . Substituting equations (6.3) and (6.4) into equation (6.5) result in equation (6.6), which shows how the second derivative can be approximated based only on the temperature of the surrounding nodal points and the distance between nodal points.

$$\left. \frac{\partial^2 T}{\partial x^2} \right|_{m,n} \approx \frac{\left. \frac{\partial T}{\partial x} \right|_{m+1/2,n} - \left. \frac{\partial T}{\partial x} \right|_{m-1/2,n}}{\Delta x} \quad (6.5)$$

$$\left. \frac{\partial^2 T}{\partial x^2} \right|_{m,n} \approx \frac{T_{m+1,n} + T_{m-1,n} - 2 \cdot T_{m,n}}{(\Delta x)^2} \quad (6.6)$$

Proceeding similarly as for equation (6.6), the derivatives can be approximated by finite differences for a three-dimensional system:

$$\left. \frac{\partial^2 T}{\partial x^2} \right|_{m,n,p} \approx \frac{T_{m+1,n,p} + T_{m-1,n,p} - 2 \cdot T_{m,n,p}}{(\Delta x)^2} \quad (6.7)$$

$$\left. \frac{\partial^2 T}{\partial y^2} \right|_{m,n,p} \approx \frac{T_{m,n+1,p} + T_{m,n-1,p} - 2 \cdot T_{m,n,p}}{(\Delta y)^2} \quad (6.8)$$

$$\left. \frac{\partial^2 T}{\partial z^2} \right|_{m,n,p} \approx \frac{T_{m,n,p+1} + T_{m,n,p-1} - 2 \cdot T_{m,n,p}}{(\Delta z)^2} \quad (6.9)$$

The derivative of temperature with respect to time can be approximated in a similar fashion:

$$\left. \frac{\partial T}{\partial t} \right|_{m,n,p} \approx \frac{T_{m,n,p}^{t+\Delta t} - T_{m,n,p}^t}{\Delta t} \quad (6.10)$$

Substituting equations (6.7), (6.8), (6.9) and (6.10) into equation (6.1) and assuming that all distances between nodal points are equal ( $\Delta x = \Delta y = \Delta z$ ) result in the heat conduction equation represented by finite differences:

$$\frac{T_{m+1,n,p}^t + T_{m-1,n,p}^t + T_{m,n+1,p}^t + T_{m,n-1,p}^t + T_{m,n,p+1}^t + T_{m,n,p-1}^t - 6T_{m,n,p}^t}{\Delta x^2} + \frac{\dot{q}}{k} = \frac{1}{\alpha} \cdot \frac{T_{m,n,p}^{t+\Delta t} - T_{m,n,p}^t}{\Delta t} \quad (6.11)$$

The above described finite-difference method can be used to calculate the temperature at nodal points associated with different boundary conditions. Figure 6.3 shows a schematic representation of three different nodal points. These different situations describe all the nodal points contained in a semi-infinite body necessary to model the WEDM process.

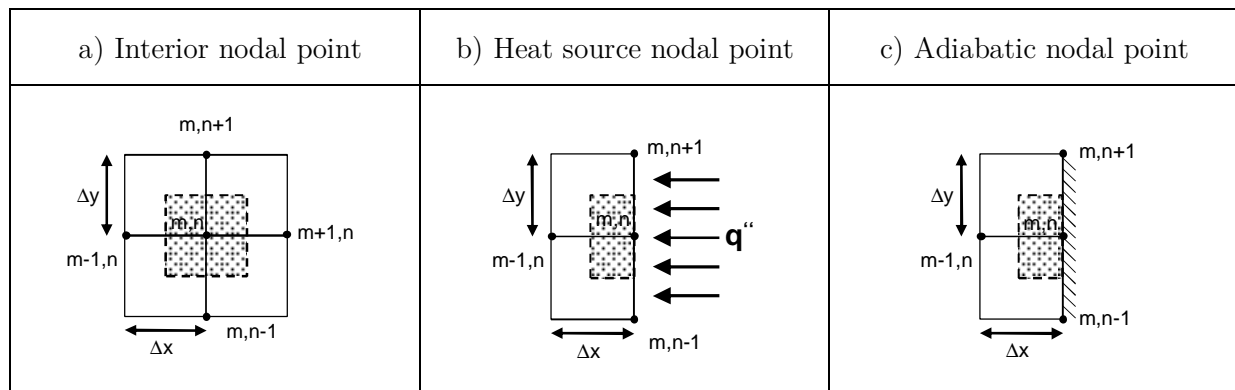


Figure 6.3 – Boundary conditions applied to different nodal points

Considering Figure 6.3a, and introducing  $Fo$ , which is the finite-difference form of the Fourier number as described in equation (6.12), the temperature for an interior nodal point, without heat generation  $\dot{q}$ , can be calculated using equation (6.13). It can be seen that the unknown nodal temperature  $T_{m,n,p}^{t+\Delta t}$  for a new time step ( $t+\Delta t$ ) is calculated based on known nodal temperatures of the previous time step. Thus, this calculation can be repeated continuously for every new time step  $\Delta t$  until the total time is reached, in this case the discharge duration time for a single discharge.

$$Fo = \frac{\alpha \cdot \Delta t}{(\Delta x)^2} \quad (6.12)$$

$$T_{m,n,p}^{t+\Delta t} = Fo(T_{m+1,n,p}^t + T_{m-1,n,p}^t + T_{m,n+1,p}^t + T_{m,n-1,p}^t + T_{m,n,p+1}^t + T_{m,n,p-1}^t) + (1 - 6Fo)T_{m,n,p}^t \quad (6.13)$$

The temperature at nodal points which are in contact with the heat source, as shown in Figure 6.3b, can be calculated using equation (6.14). In this case the heat flux  $q''$  (W/m<sup>2</sup>) entering the region surrounding the nodal point is taken into consideration to calculate the nodal temperature located at position  $(m,n)$ . The heat source is modeled based on different erosion parameters, which will be described later in this chapter.

$$T_{m,n,p}^{t+1} = Fo(2T_{m-1,n,p}^t + T_{m,n+1,p}^t + T_{m,n-1,p}^t + T_{m,n,p+1}^t + T_{m,n,p-1}^t) + \frac{2Fo \cdot q'' \cdot \Delta x}{k} + (1 - 6Fo) \cdot T_{m,n,p}^t \quad (6.14)$$

Taking Figure 6.3c into consideration, the temperature at nodal points situated on an adiabatic surface can be calculated using equation (6.15). This corresponds to a special case of Figure 6.3b in which the heat flux  $q''$  is equal to zero.

$$T_{m,n,p}^{t+\Delta t} = Fo(2T_{m-1,n,p}^t + T_{m,n+1,p}^t + T_{m,n-1,p}^t + T_{m,n,p+1}^t + T_{m,n,p-1}^t) + (1 - 6Fo)T_{m,n,p}^t \quad (6.15)$$

To prevent this numerical method to become mathematically unstable, the Fourier number must be maintained below a certain limit. Hence, to achieve stable numerical calculation for all nodal points of interest in a three-dimensional network, the Fourier number has to be less than or equal to 1/6 ( $Fo \leq 1/6$ ), since the term  $1 - 6Fo$  must be greater than or equal to zero. In summary, the finite-difference equations used to describe different boundary conditions applied in this work to model the WEDM process are presented in Table 6.1.

Table 6.1 - Transient, three dimensional finite-difference equations ( $\Delta x = \Delta y = \Delta z$ )

Interior nodal points		
$T_{m,n,p}^{t+\Delta t} = Fo(T_{m-1,n,p}^t + T_{m+1,n,p}^t + T_{m,n-1,p}^t + T_{m,n+1,p}^t + T_{m,n,p-1}^t + T_{m,n,p+1}^t) + (1-6Fo)T_{m,n,p}^t$		
Adiabatic nodal points (located at top surface)		
$T_{m,n,p}^{t+\Delta t} = Fo(2T_{m-1,n,p}^t + T_{m,n+1,p}^t + T_{m,n-1,p}^t + T_{m,n,p+1}^t + T_{m,n,p-1}^t) + (1-6Fo) \cdot T_{m,n,p}^t$		
Heat source nodal points		
$T_{m,n,p}^{t+\Delta t} = Fo(2T_{m-1,n,p}^t + T_{m,n+1,p}^t + T_{m,n-1,p}^t + T_{m,n,p+1}^t + T_{m,n,p-1}^t) + \frac{2Fo \cdot q'' \cdot \Delta x}{k} + (1-6Fo) \cdot T_{m,n,p}^t$		
Fourier number	$Fo = \frac{\alpha \cdot \Delta t}{(\Delta x)^2}$	Stability Criterion $Fo \leq \frac{1}{6}$

## 6.2 Model inputs

In wire electrical discharge machining (WEDM), short discharge durations and high peak currents are usually applied. This allows for high material removal rates. Furthermore, a relatively long pulse interval time is required to avoid wire breakage. Electric current is in most cases delivered via capacitors, so that both the discharge duration and discharge peak current depend on the system configuration, meaning that different system impedances lead to different discharge durations and peak currents. To assess the erosion process in both the WEDM machine AC Progress VP4 and the WEDD unit, an oscilloscope type LeCroy WaveRunner 44MXi-A was used. The measurements can thus be used as inputs for the WEDM model, as described on the following sections. Furthermore, the thermophysical properties of the workpiece material play a decisive role in EDM, as well as their dependence on the temperature, which are also considered in the erosion model described in this work.

### 6.2.1 Discharge duration and pulse interval time

One of the most important inputs is the discharge duration, which represents the time in which the heat source is acting on the workpiece. The discharge duration cannot be directly specified on the system control of both WEDM systems used in this work and therefore has to be measured. Figure 6.4 shows the discharge duration measured for both configurations, the WEDM machine AC Progress VP4 (WEDM-VP4) and the WEDD unit (WEDD-S31), for different discharge pulses, named here *I1* to *I6*. The discharge duration time ranges from 1 to 1.8  $\mu$ s and, as expected, presents a different behavior in both EDM system configurations.

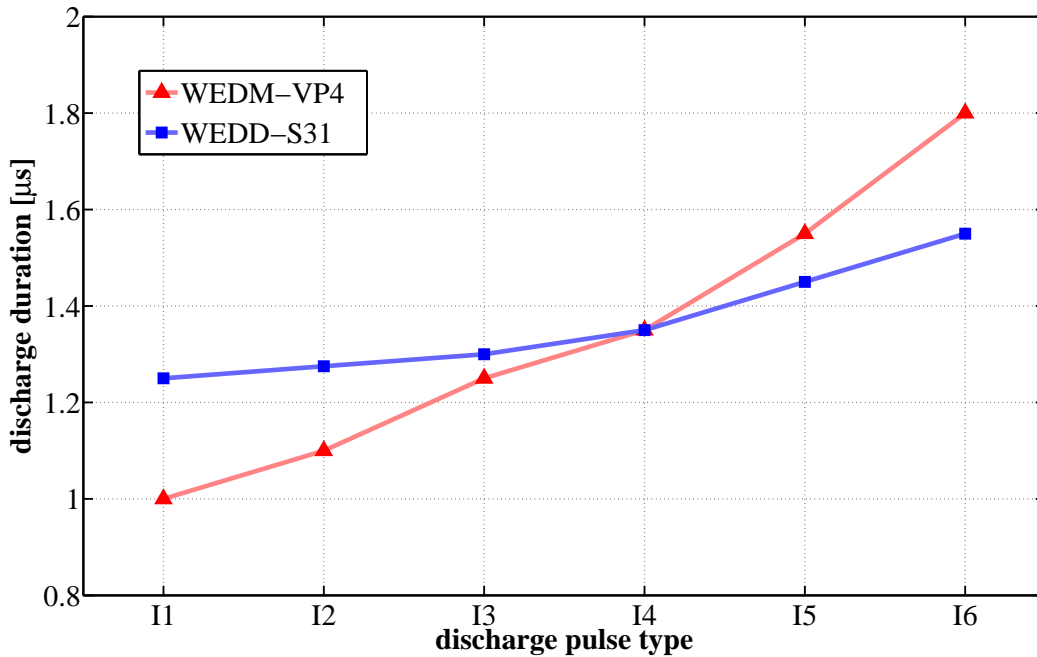


Figure 6.4 – Discharge duration for WEDD unit and wire cut machine Progress VP4

The pulse interval time corresponds to the time starting just after the discharge, when the current reaches zero, until the time when the open voltage is again provided to the system. This time can be precisely controlled by switching on and off the voltage supply source. Hence, this parameter can be reliably obtained directly from the machine catalogue. For both erosion units, the pulse interval time can vary between 2.81 and 409  $\mu\text{s}$ , being possible to be adjusted in short interval steps. The shorter the pulse interval time the higher the pulse frequency, and higher the material removal rate. However, the pulse interval time cannot be too short in all applications, and has to be chosen taking into consideration the discharge energy, wire electrode material and diameter, as well as the type of dielectric and flushing conditions, since high pulse frequencies associated with high discharge energies can easily lead to wire breakage.

The effective pulse frequency  $f_e$  differs from the theoretical one, since the discharges do not occur immediately after the open voltage is applied to the system, but rather after a certain delay time. Moreover, short circuit pulses can be delivered during erosion, which all together lead to a lower effective pulse frequency in comparison to the theoretical one. Hence, the effective pulse frequency, which in fact represents the efficiency of the erosion process, has to be measured. Table 6.2 shows results obtained for five different pulse interval times and three different discharge peak currents, namely  $I3$ ,  $I4$  and  $I5$ . The theoretical pulse frequencies  $f_p$  are also shown and the pulse frequency ratio  $\lambda$  is introduced, which represents the ratio of the effective pulse frequency  $f_e$  to the theoretical pulse frequency  $f_p$ . The theoretical pulse frequency was calculated based only on the theoretical pulse interval time, since discharge durations are significantly shorter than the interval times as shown in see Figure 2.1.

Table 6.2 – Theoretical and effective pulse frequencies

Theoretical pulse interval time [ $\mu\text{s}$ ]		103	71.8	50.5	35	27.2
Theoretical pulse frequency, $f_p$ [kHz]		9.7	13.9	19.8	28.5	36.7
Effective pulse frequency, $f_e$ [kHz]	<i>I3</i>	3.99	5.92	7.95	11.41	14.27
	<i>I4</i>	3.98	5.56	7.91	11.25	14.1
	<i>I5</i>	3.87	5.38	7.85	11.19	13.97
Average effective pulse frequency, $f_e$ [kHz]	<i>I3-I5</i>	3.9	5.6	7.9	11.3	14.1
Pulse frequency ratio, $\lambda = f_e/f_p$ [%]		40.7	40.4	39.9	39.6	38.4

Since the erosion model predicts only the amount of material eroded per single discharge, this has to be multiplied by the effective pulse frequency to obtain the real absolute material removal rate (MRR), which will be discussed later in this chapter. According to the results presented in Table 6.2, a common pulse frequency ratio of  $\lambda = 39.5\%$  was chosen as input for the erosion model.

### 6.2.2 Discharge current waveform

The discharge current  $I_e$  and discharge voltage  $u_e$ , together with the discharge duration  $t_e$ , represent the amount of discharge energy  $W_e$  available per single discharge, as shown in equation (6.16). The discharge current is not constant over the discharge duration time, but depends on the system configuration and has to be measured in order to be used as input for the erosion model. As an approximation, a constant discharge voltage of 20 V was used as input for the erosion model based on measurements done together with the measurements of discharge current.

$$W_e = \int_0^{t_e} u_e(t) \cdot I_e(t) \cdot dt \quad (6.16)$$

Figure 6.5 shows the current waveform of a discharge pulse measured on the wire electrical discharge dressing unit integrated inside the grinding machine Studer S31. A pilot pulse is first released and lasts for approximately 500 ns, in which the discharge voltage is controlled before the strong discharge pulse is delivered. If the discharge voltage stays outside a pre-specified tolerance during the pilot pulse, a short-circuit pulse is released aiming to prevent wire damages, i.e. to avoid wire breakage. As shown in Figure 6.5, the discharge current peaks after approximately half of the discharge duration, and decreases continuously until the end of the discharge pulse. In

this case a pulse type  $II$  was chosen, which represents a peak current of  $I_{peak} = 73$  A and a discharge duration of  $t_e = 1.25$   $\mu$ s. A half sine wave was thus used to model the discharge current.

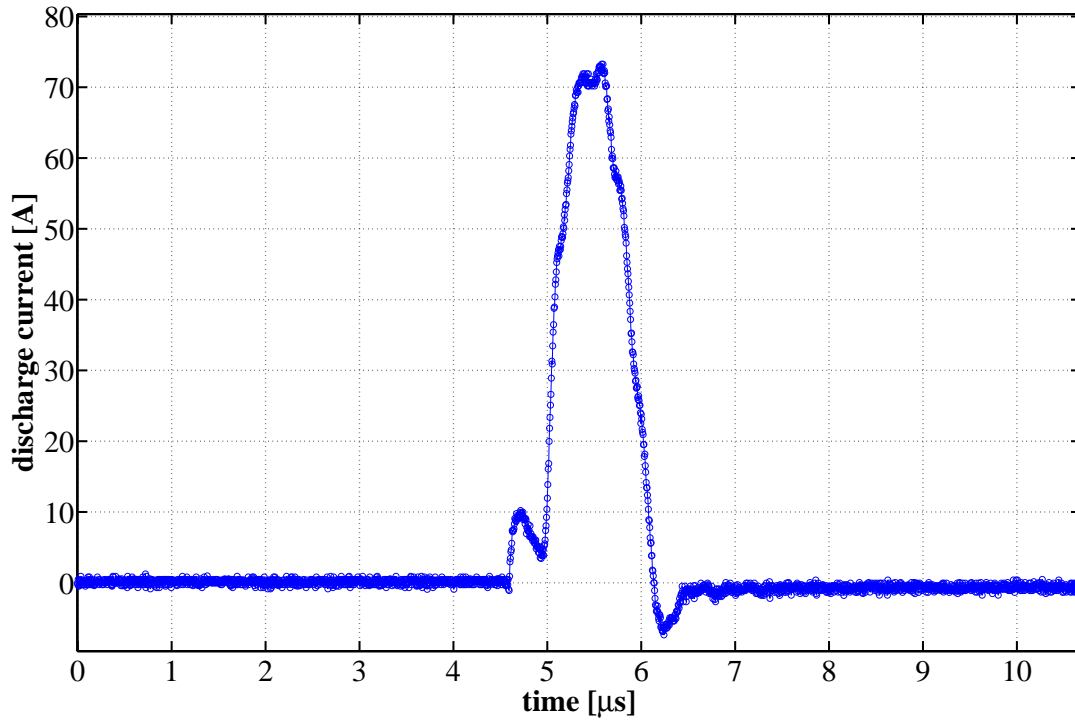


Figure 6.5 – Discharge peak current measured on the WEDD unit ( $II$ )

Similarly to the discharge duration shown before, peak currents are different in both erosion devices due to the difference in the system configurations (different impedances). Figure 6.6 shows values of peak current for different erosion pulses ( $I1$  to  $I6$ ). For the WEDD unit, peak current varies from 73 A for  $I1$  up to 276 A for  $I6$ , while for the WEDM-VP4 machine it varies between 88 A for  $I1$  and 223 A for  $I6$ . The corresponding discharge durations for these pulses were previously shown in Figure 6.4.

As shown on equation (6.14), a heat flux  $q''$  ( $W/m^2$ ) flowing from the plasma channel to the workpiece represents the heat source used as input in the erosion model. The heat flux is a function of discharge current, discharge voltage and crater radius (simplification), as presented in equation (6.17). In the proposed EDM model, the heat flux is discretized in time, depending on the discharge duration  $t_e$  and time step  $\Delta t$  used during the simulation. Single discharge experiments were carried out to measure the shape and volume of eroded craters and the achieved results are discussed later in section 6.3.

$$q''(t) = \frac{u_e(t) \cdot I_e(t)}{\pi \cdot r_c(t)^2} \quad (6.17)$$



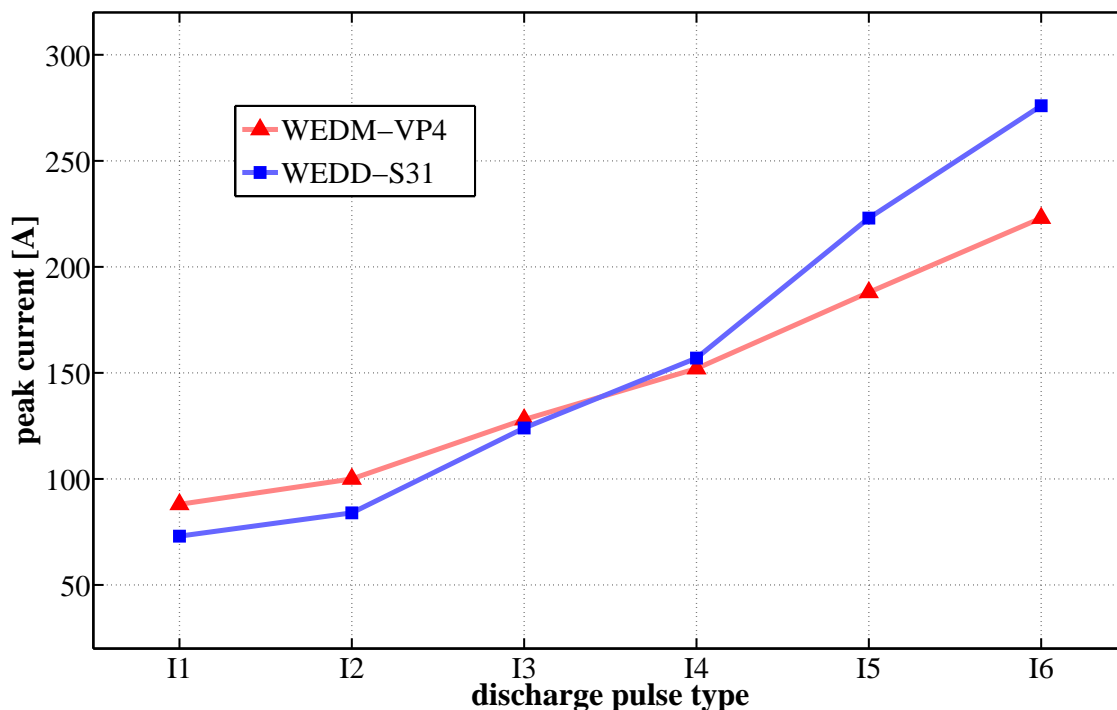


Figure 6.6 – Discharge peak current for different pulses

### 6.2.3 Thermophysical properties of workpiece materials

In equation (6.1) the thermophysical properties of the workpiece material are grouped in an important variable named thermal diffusivity  $\alpha$ . It represents the ratio of the thermal conductivity  $k$  to the heat capacity (the product of mass density  $\rho$  and specific heat  $c_p$ ) and measures the ability of a material to conduct thermal energy relative to its ability to store thermal energy [INCR06]. In several erosion models, these thermophysical properties are assumed to be constant, not depending on the temperature. However, they are significantly affected by the temperature, which must be taken into account for accuracy.

Figure 6.7 shows the temperature dependence of the thermal conductivity and specific heat for pure copper [GATH83, LIDA88, INCR06]. The thermal conductivity varies significantly when copper changes from solid to liquid (melting point of 1,358 K.) and the specific heat increases until the melting temperature is reached, staying relatively constant afterwards. The way how thermophysical properties of different materials respond to changes in temperature can vary considerably [GRIM99], being one of the reasons why discrepancies on simulation results can occur when material properties are assumed constant, i.e. not temperature-dependent. It is, however, difficult to find available data for different materials over a wide range of temperatures, especially for alloys. Data have to be collected from several publications, as shown in Figure 6.7, or, in some cases, have to be approximated based on the different chemical elements that compose the material, although alloys usually have different properties

from those of the basic elements. For all materials used in this work, thermophysical properties were considered as being temperature-dependent.

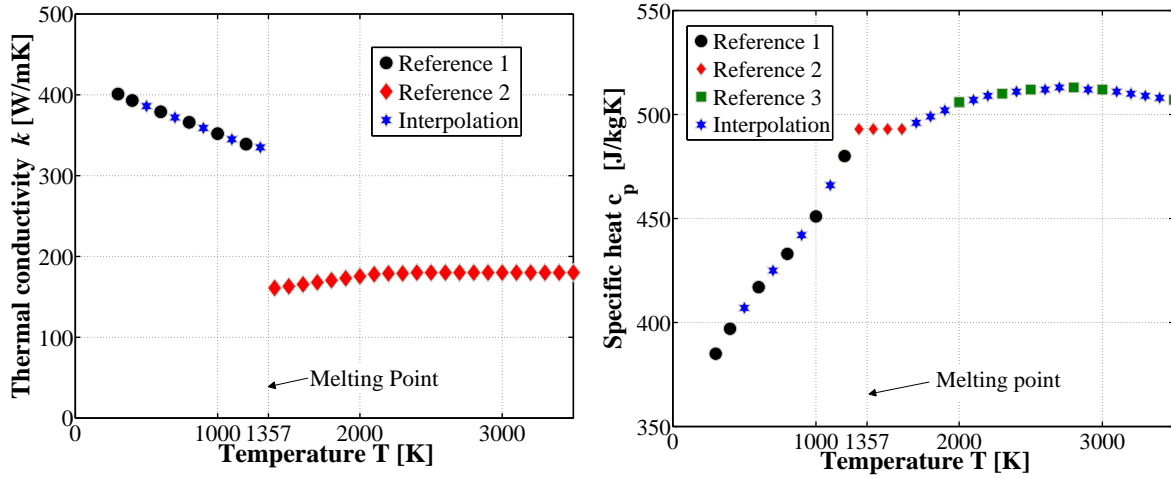


Figure 6.7 – Temperature dependence of the thermal conductivity and specific heat in copper: Reference 1 [INCR06]; Reference 2 [LIDA88]; Reference 3 [GATH83]

#### 6.2.4 Latent heat of fusion and vaporization

When a material is warmed up and phase changes occur, e.g. melting or evaporation, energy is absorbed during these transition processes at constant temperatures. Figure 6.8 shows a schematic representation of these different phases for an arbitrary material (heating, melting and evaporation). The energy associated with phase changes, i.e. the specific latent heat of fusion  $L_f$  and vaporization  $L_v$ , expresses the amount of energy  $Q$  necessary to melt or evaporate 1 kg of material. Equation (6.18) describes the way how to calculate the energy  $Q_f$  necessary to change a specific amount of mass  $m$  from solid to liquid state.

$$Q_f = m \cdot L_f \quad (6.18)$$

Most EDM models do not take the latent heats of fusion and vaporization into account. As a result, deeper craters are created, since the energy associated with phase changes poses a further resistance to the heat to penetrate into the material. To implement the latent heats into the finite-difference method, equivalent melting and evaporation temperatures were defined. It can be calculated by equating the latent heat ( $Q = mL$ ) to the sensible heat ( $Q = mc\Delta T$ ) at phase change temperatures. Thus, the equivalent temperatures represent the ratio of the specific latent heat to the specific heat at melting or boiling temperatures. Equation (6.19) shows how to calculate the equivalent melting temperature  $\Delta T_m$ .

$$\Delta T_m = \frac{L_f}{c_p} \quad (6.19)$$

When melting or boiling temperatures are reached at a nodal point, a temperature increment is first possible after overcoming the equivalent melting or boiling temperatures. Considering an arbitrary material, which melts at 1,000 K and has an equivalent melting temperature of  $\Delta T_m = 500$  K, the equivalent melting temperature starts to be counted at time  $t + \Delta t$  when at time  $t$  the melting temperature was reached. That is, if at time  $t + \Delta t$  the calculated nodal temperature is 1,005 K, the temperature of the nodal point is set back to melting temperature (1,000 K), and the difference of 5 K is accumulated to the equivalent melting temperature. This procedure is repeated until  $\Delta T_m$  is reached (500 K in this case), meaning that the energy  $Q_f$  necessary for melting the volume associated to a nodal point was achieved. After that, the temperature at this nodal point can further increase. The same method is used when the temperature at a nodal point reaches boiling temperature. In this case, an equivalent evaporation temperature  $\Delta T_v$  is considered, which represents the energy  $Q_v$  associated to the latent heat of vaporization that has to be overcome.

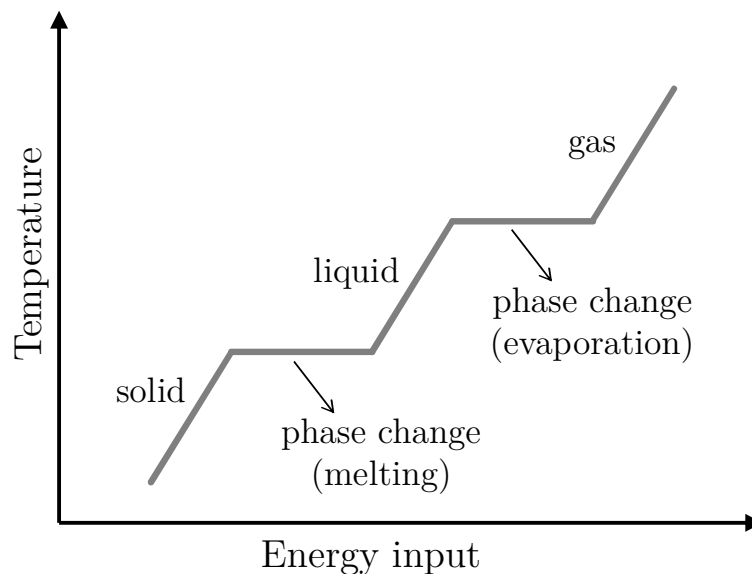


Figure 6.8 – Phase changes of an arbitrary material taking the latent heats of fusion and vaporization into account

### 6.2.5 Energy distribution and recast layer

In electrical discharge machining not the whole available discharge energy  $W_e$  is used to remove material from the workpiece. A so called power factor  $F_c$  has to be introduced to calculate the real absolute eroded volume per crater. The power factor was estimated based on simulation and experimental results of single discharge

experiments. In this case, to quantify the amount of discharge energy which effectively flows to the workpiece/anode, the total volume of molten material per discharge has to be evaluated. Figure 6.9 shows a three-dimensional measurement of a single crater eroded on brass and a schematic representation of the crater's cross section. The total volume of molten material is composed of the recast layer below the reference plane plus the crater volume, which is the eroded volume below the reference plane. The resolidified volume above the reference plane represents ejected material which resolidified and stayed adhered to the workpiece. The crater volume and the resolidified volume can be easily measured using the optical 3D measurement device Alicona InfiniteFocus. The workpiece/anode has to be first ground to allow its surface to be used as a reference plane for the measurements. Knowing the total amount of eroded volume, it can be compared with simulation results to interactively find the “power factor” that should be used as input for the model. The determination of the erosion power factor is presented later in section 6.4.1, where numerical results are discussed.

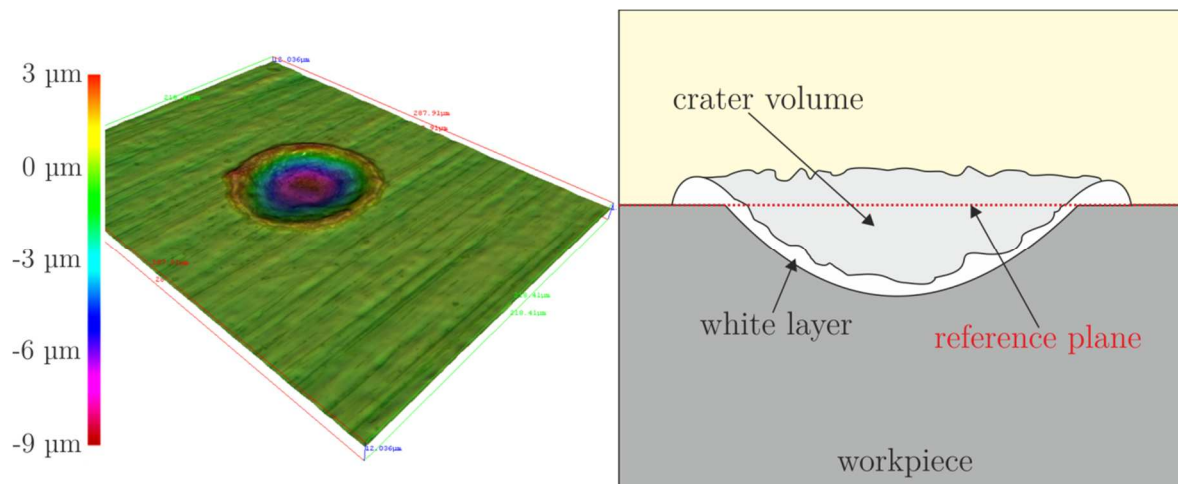


Figure 6.9 – Single crater representation (ejected volume and recast layer)

The recast layer represented in Figure 6.9 can be measured and one example for brass is shown in Figure 6.10. The recast layer was found not to have a constant thickness, but rather varies significantly from place to place. For further simulations, a thickness of 3  $\mu\text{m}$  was assumed for brass and bronze-based materials. This value was used to identify the real amount of eroded volume for a single crater, meaning that a specific amount of material that reached temperatures higher than the melting temperature of the workpiece material during the simulations is not removed from the workpiece (PFE – plasma flushing efficiency), but rather composes the recast layer, which has a specific volume depending on the applied discharge energy, i.e. depending on the size of the eroded craters.

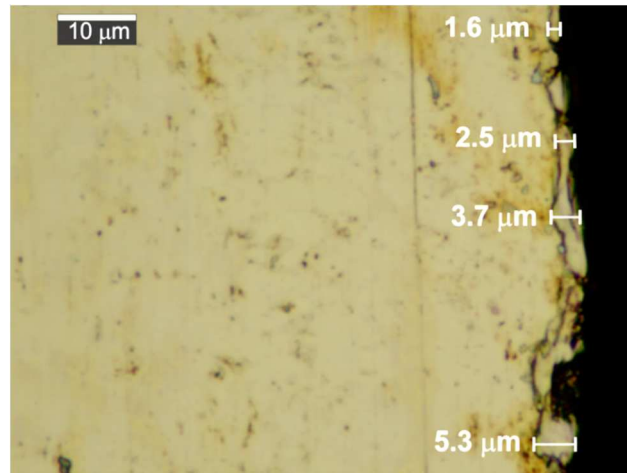


Figure 6.10 – Recast layer measured in brass after wire electrical discharge machining

### 6.3 Single discharge experiments

Single discharge experiments were performed to evaluate the influence of process parameters, materials and the relative speed on the wire electrical discharge machining process. Both erosion systems were used for carrying out these experiments, namely the WEDM Machine AC Progress VP4 and the WEDD unit. The experimental results are later compared with numerical results in section 6.4.

#### 6.3.1 Characterization of eroded craters

To characterize an eroded crater, its shape and volume are first measured using an optical 3D measurement device Alicona InfiniteFocus. The diameter of the crater and its maximum depth were used as characteristic quantities. Figure 6.11 shows a crater eroded on brass and the corresponding measurement of its cross section profile. The crater has a diameter of  $90\ \mu\text{m}$ , is approximately  $6\ \mu\text{m}$  deep and represents an eroded volume of approximately  $13,000\ \mu\text{m}^3$ .

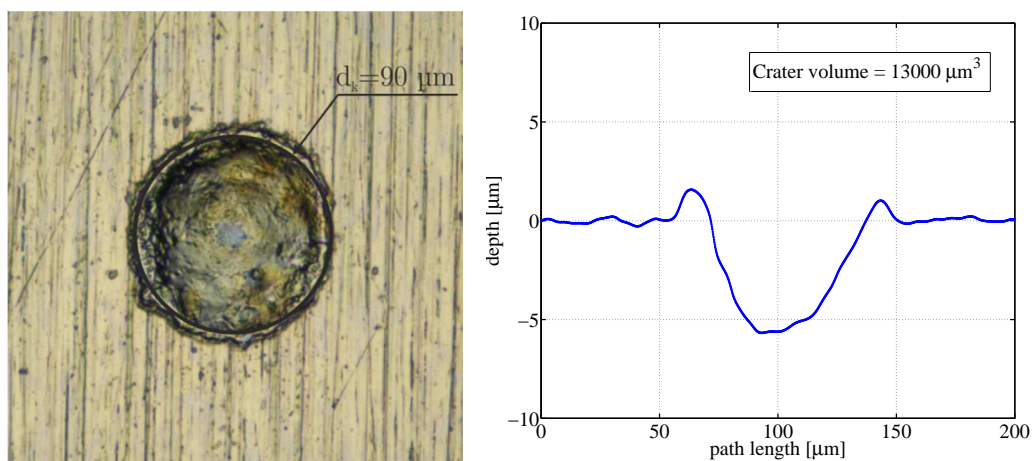


Figure 6.11 – Characterization of an eroded crater (WEDD unit; discharge pulse  $II$ )

Figure 6.12 shows results of measured crater diameters and depth for different discharge pulses in brass. The diameter increases almost linearly starting from 90  $\mu\text{m}$  for pulse type *I1* and ending at 157  $\mu\text{m}$  for pulse type *I6* (see Figure 6.4 and Figure 6.6). Likewise, the crater depth increases from 5.3 to 8.1  $\mu\text{m}$ . The crater diameter is an important input for the model, since the heat source is modeled as a heat flux acting over the diameter of the developing crater, as described in equation (6.17).

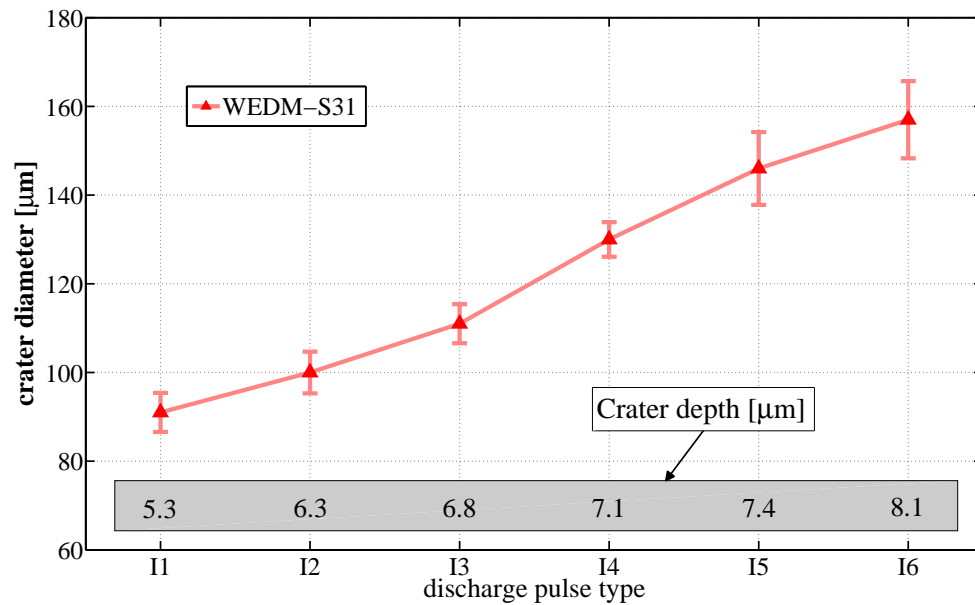


Figure 6.12 – Crater diameter for different discharge pulses in brass

The corresponding eroded volumes per crater for the different discharge pulses shown in Figure 6.12 are presented in Figure 6.13. Volumes ranging from 10,000 to 65,000  $\mu\text{m}^3$  were measured when increasing the discharge peak current from *I1* to *I6*.

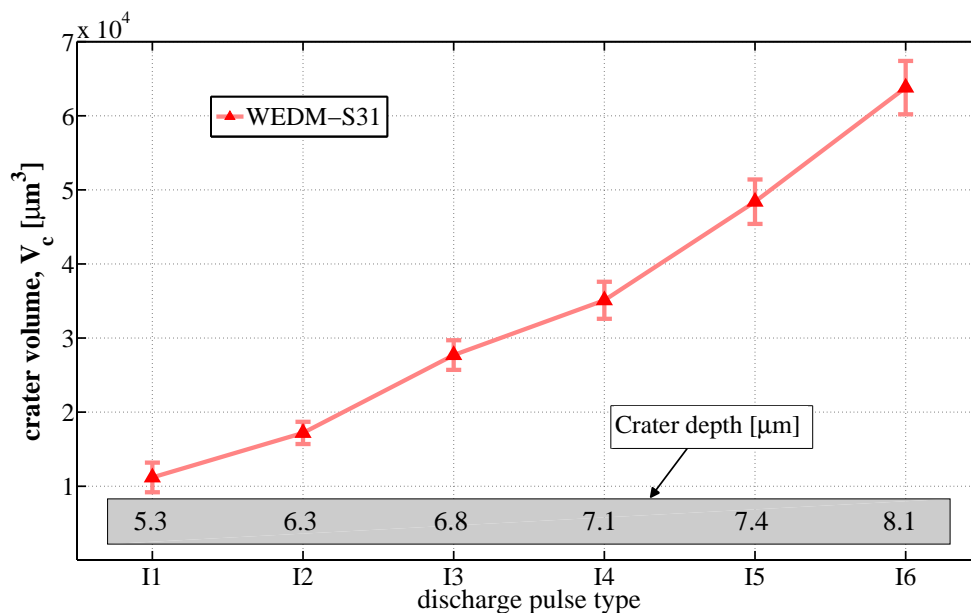


Figure 6.13 – Volume of eroded crater for different discharge pulses in brass

### 6.3.2 Influence of relative speed on eroded craters

In wire electrical discharge machining (WEDM), the wire electrode is fed from a spool at wire run-off speeds  $v_D$  typical ranging from 2 to 20 m/min [GFAC06]. When the discharge duration is taken as a reference, the wire run-off speed can be neglected, since short discharge durations are normally applied in WEDM. As an example, for a run-off speed of 20 m/min and discharge duration of 1.5  $\mu$ s, the relative displacement of the wire electrode during the discharge is only 0.5  $\mu$ m, which is very little when compared to the crater diameters (see Figure 6.12). In on-machine wire electrical discharge dressing (WEDD), however, relative speeds of at least 30 m/s up to over 100 m/s can be applied, since the grinding wheel has normally to be dressed at grinding speeds.

The influence of the relative speed on eroded craters was evaluated based on experiments carried out using the WEDD unit. In this case the workpiece rotates at a specific relative speed  $v_r$  and the wire travels along the workpiece axial direction, tangential to the circumferential surface of the workpiece. The pulse interval time was set to be as long as possible, in this case approximately 400  $\mu$ s, for decreasing the pulse frequency, so that consecutive discharges can be distinguished on the cylindrical surface of the workpiece. Not all the craters can be measured, since some are partially superposed, yet still numerous individual craters can be measured separately.

Figure 6.14 shows the shape of eroded craters for relative speeds up to  $v_r = 80$  m/s. The applied erosion parameters are summarized in Table 6.3. It can be seen that the relative speed has a significant influence on the eroded craters. The plasma channel slides over the workpiece/anode creating a stretched crater along the relative speed direction.

Table 6.3 – Single discharge experiments: WEDM parameters

discharge duration	$t_e$	a) 1.15 $\mu$ s; b) 1.25 $\mu$ s
peak current	$I_{peak}$	a) 58 A; b) 73 A
pulse interval time	$t_o$	400 $\mu$ s
relative speed	$v_r$	0,5-80 m/s
oil flow rate	$Q_l$	25 L/min
wire diameter	$d_w$	0.33 mm
wire type	CobraCut S	(coated brass wire)
wire polarity	negative	
workpiece material	Brass	( <i>CuZn39Pb3</i> )

To quantitatively show how the shape of eroded craters changes due to the relative speed between workpiece and wire electrode, the minor and major diameters of different craters were measured. The major diameter is measured parallel to the

relative speed vector while the minor diameter represents the largest diameter orthogonal to the relative speed vector. Figure 6.15 shows the results obtained by applying a discharge peak current of  $I_{peak} = 73$  A and relative speeds between  $v_r = 0.5$  m/s and 80 m/s. The crater extends along the relative speed direction (major diameter) and slightly decreases perpendicularly to this direction (minor diameter). In this example, the major diameter is almost as large as twice the minor diameter when a relative speed of  $v_r = 80$  m/s is applied. Although it is stated on [KUNI10] that the plasma slides more easily over the cathode rather than over the anode, it can be observed in Figure 6.14 that, at least for this type of WEDM discharges, the plasma can easily slide over the anode, i.e. over the wheel.

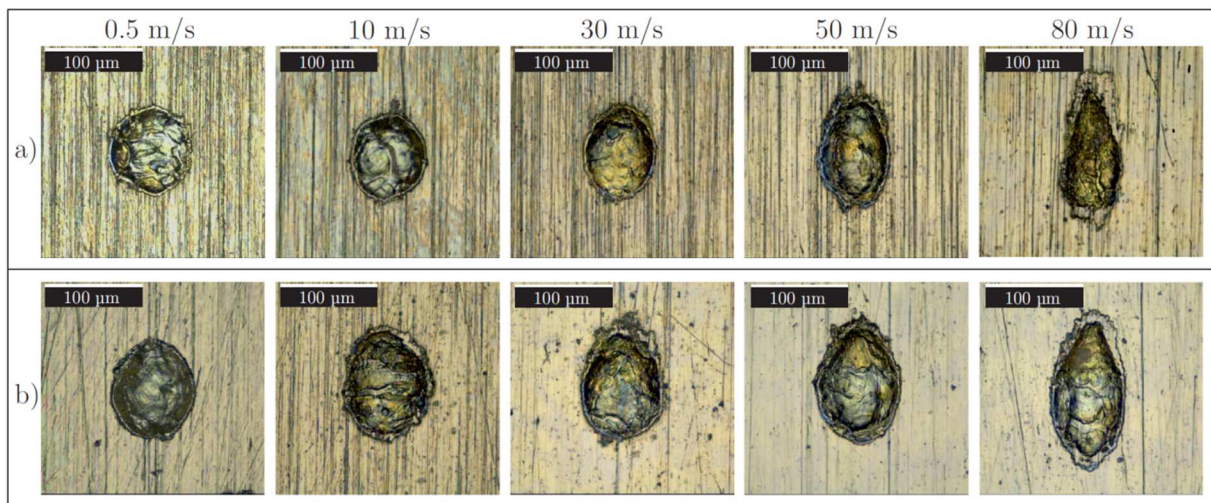


Figure 6.14 – Influence of relative speed on eroded crater shapes

a)  $I_{peak} = 58$  A,  $t_e = 1.15$   $\mu$ s; b)  $I_{peak} = 73$  A,  $t_e = 1.25$   $\mu$ s

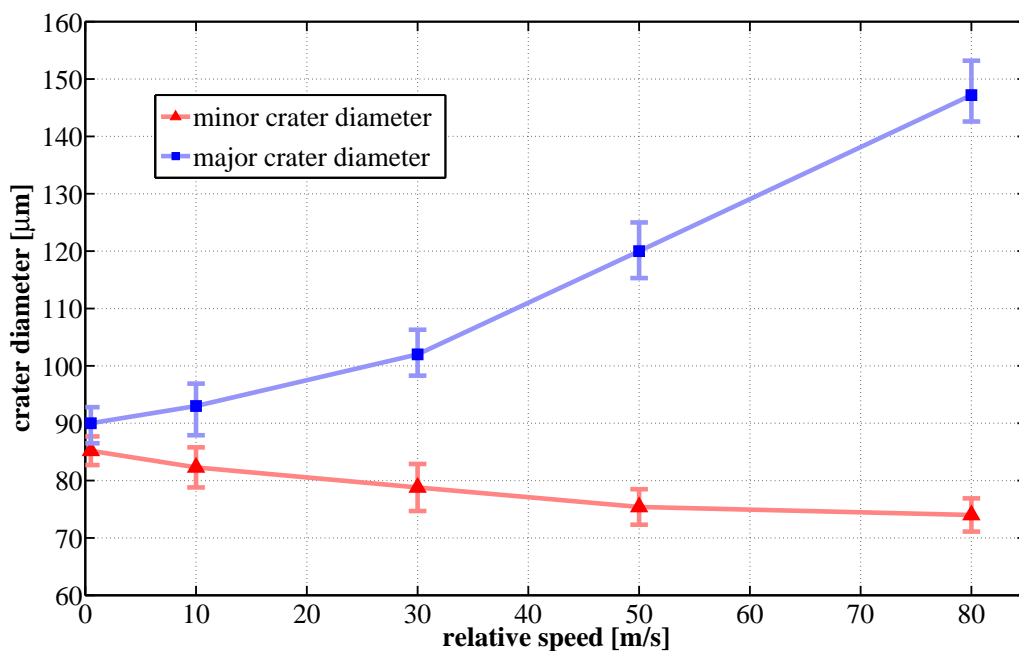


Figure 6.15 – Crater diameter for different relative speeds ( $I_{peak} = 73$  A,  $t_e = 1.25$   $\mu$ s)



In addition, based on the shape of eroded craters, it is possible to measure the slip of the plasma center point during a single discharge. The measured slip can be compared to the theoretical one, which is calculated based on the discharge duration and relative speed. Figure 6.16 illustrates two different craters eroded with different peak currents and the same relative speed ( $v_r = 80$  m/s). In Figure 6.16a, theoretically, the plasma should slide  $92 \mu\text{m}$  during one single discharge ( $80[\mu\text{m}/\mu\text{s}] * 1.15[\mu\text{s}] = 92 \mu\text{m}$ ). The two red circles on each crater, a small and a bigger one, indicate, respectively, the start and end position of the plasma center point. The distance between both centers is  $95 \mu\text{m}$ . In Figure 6.16b, the crater was eroded by applying a discharge peak current of  $73$  A. The slip of the plasma should be, theoretically, equal to  $100 \mu\text{m}$ , and the measured distance between centers is equal to  $102 \mu\text{m}$ . In both cases, theoretical slips correlate well with the measured ones.

Since the theoretical slip of the plasma's center point matches the measured slip, another aspect of the discharge can be evaluated, namely the expansion speed of the crater radius. Figure 6.17a illustrates how to quantify it and Figure 6.17b shows the correspondent approximated diagram of crater radius versus discharge duration. As shown in Figure 6.17a, the crater radius increases almost linearly from the beginning of the discharge until it reaches a maximum. In this particular case, after a slip of  $70 \mu\text{m}$ , the crater reaches a diameter of  $72 \mu\text{m}$ , which is indicated by the largest red circle in Figure 6.17. In other words, the crater radius grows up to  $36 \mu\text{m}$  within nearly  $0.9 \mu\text{s}$  ( $70[\mu\text{m}]/80[\mu\text{m}/\mu\text{s}]$ ), corresponding to a radius expansion speed of approximately  $40$  m/s ( $36[\mu\text{m}]/0.9[\mu\text{s}]$ ). After reaching a diameter of  $72 \mu\text{m}$ , the crater stops increasing. The reason is that the maximum current is reached after half of the discharge duration and starts to decrease significantly until the end of the discharge.

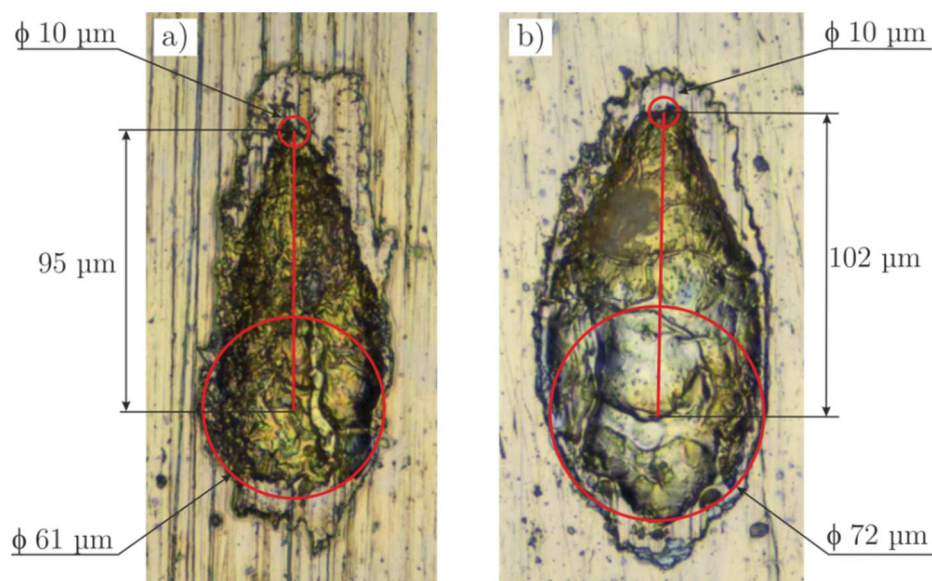


Figure 6.16 – Plasma center point displacement over the anode:

a)  $I_{peak}=58$  A,  $t_e=1.15 \mu\text{s}$ ; b)  $I_{peak}=73$  A,  $t_e=1.25 \mu\text{s}$

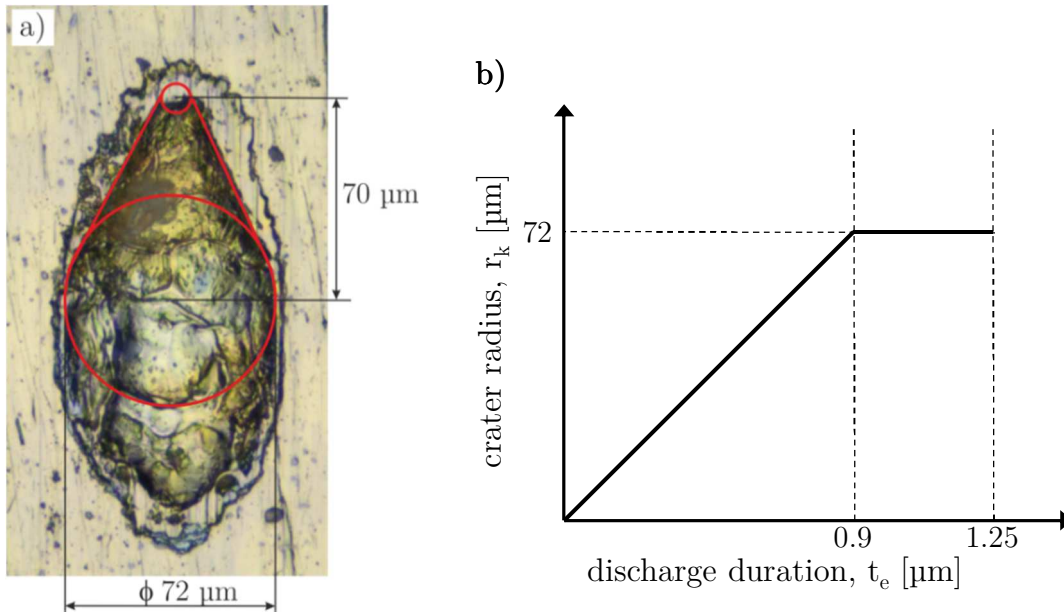
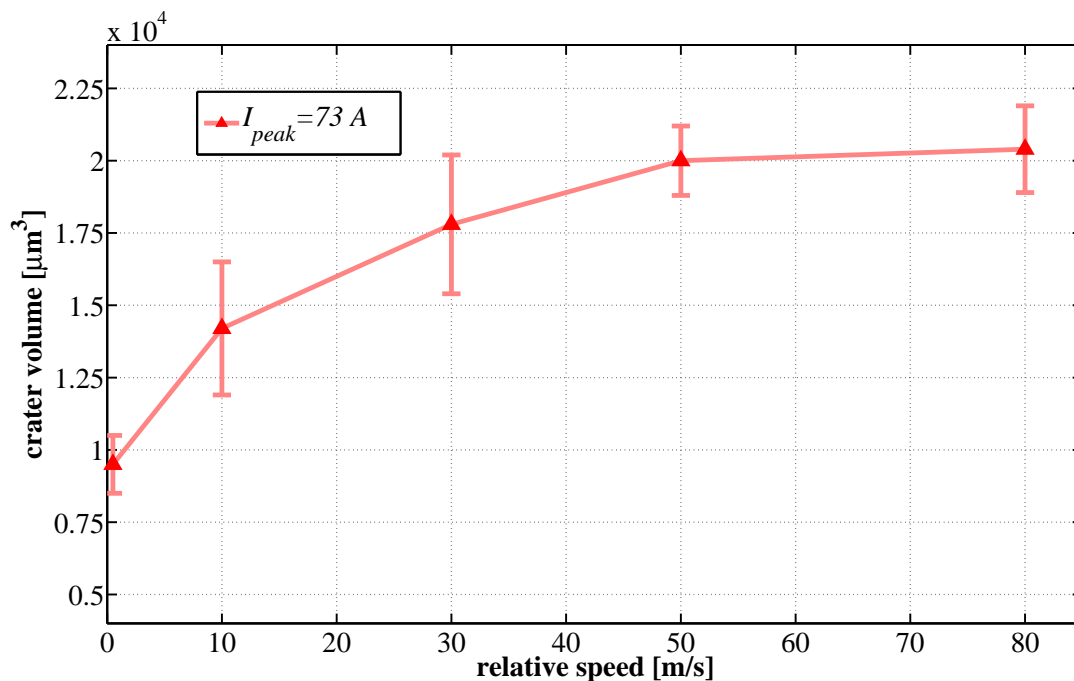


Figure 6.17 – Crater radius expansion speed in brass

The relative speed applied during WEDM was found to influence not only the shape of the eroded craters as presented in Figure 6.14, but also the amount of eroded volume per crater. In general, an increase in relative speed causes an increase in the amount of eroded material. Results obtained by applying a discharge peak current of 73 A are presented in Figure 6.18. The measured volume of eroded material per crater varies in this case from approximately  $10,000 \mu\text{m}^3$  up to  $20,000 \mu\text{m}^3$  by rising the relative speed from  $v_r = 0.5 \text{ m/s}$  to  $80 \text{ m/s}$ .

Figure 6.18 – Influence of relative speed on single craters ( $I_{peak} = 73$ ,  $t_e = 1.25 \mu\text{s}$ )

The same experiment was carried out for a peak current of  $I_{peak} = 157$  A and the obtained results are presented in Figure 6.19. In this case the eroded volume reaches saturation towards very high relative speeds.

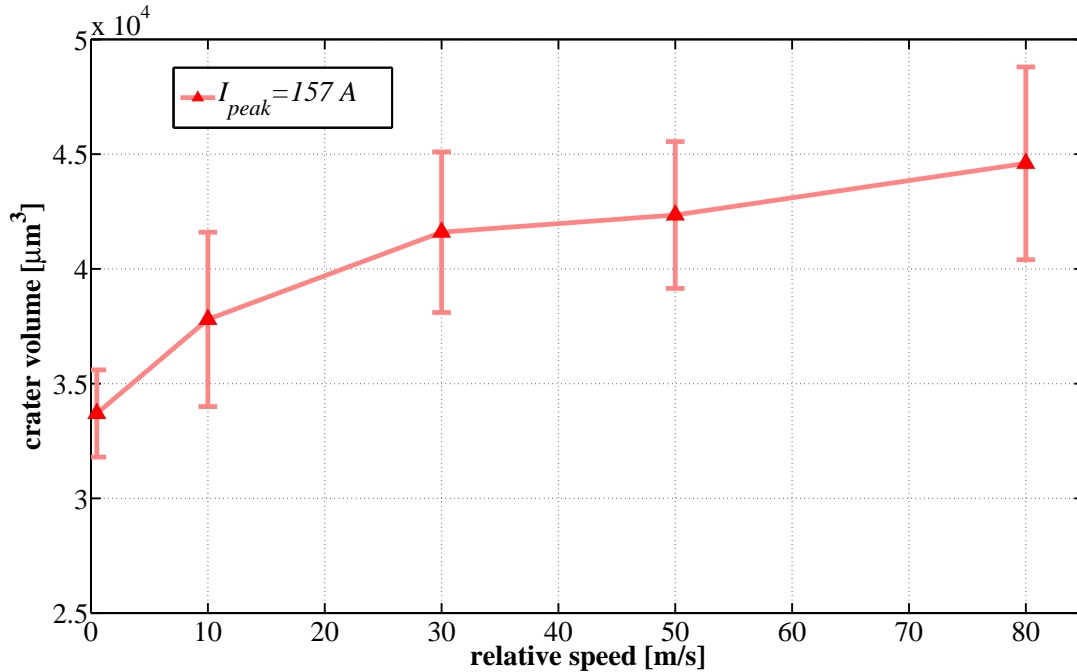


Figure 6.19 – Influence of relative speed on single craters ( $I_{peak} = 157$ ,  $t_e = 1.35$   $\mu\text{s}$ )

The increasing amount of eroded material per single discharges can be related to higher melting efficiencies achieved when relative speed is increased. According to Elsen et al. [VAN07], melting efficiency is defined as the ratio of the minimal amount of energy needed to warm up and melt a given amount of material to the added energy. Thus, lower melting efficiency is achieved using a static heat source, since more heat is used for overheating the melting pool instead of melting more material.

### 6.3.3 Plasma expansion

According to equation (6.17) shown previously, the heat flux depends on the radius of the plasma channel, here assumed to be the crater radius  $r_c$ , which does not increase linearly and depends on erosion input parameters. An empirical equation is derived to describe the crater radius expansion based only on the discharge duration and peak current. It was shown previously in Figure 6.4 and Figure 6.6 that discharge duration and peak current differ in both EDM systems. However, the discharge energy, assuming a burning voltage of 20V and a half sine wave to describe the discharge current, is very similar in both cases as can be seen in Figure 6.20.

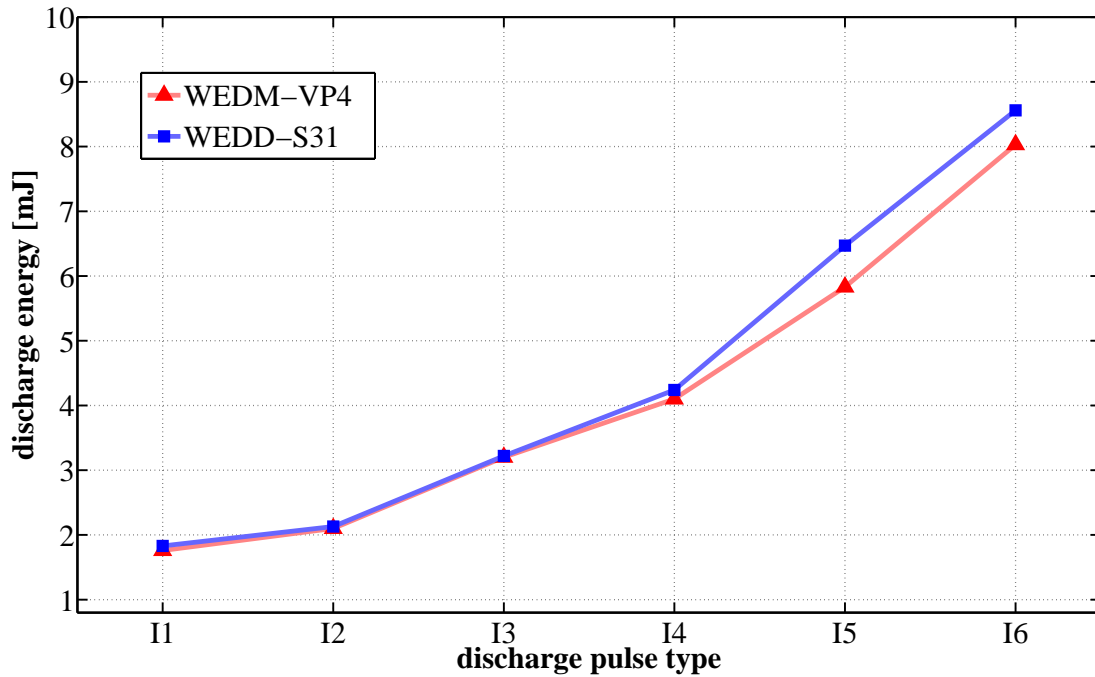


Figure 6.20 – Discharge energy for both EDM systems

Based on the results presented in Figure 6.20, the final crater radius  $r_c$  can be expressed as a function of the product of discharge current and discharge duration. A second-order polynomial can be used to fit this curve:

$$r_c = a_2 \cdot (I_{peak} \cdot t_e)^2 + a_1 \cdot (I_{peak} \cdot t_e) + a_0 \quad (6.20)$$

Using  $I_{peak}$  in amperes and  $t_e$  in microseconds, the following solution was found:  $a_2 = -0.00025$ ;  $a_1 = 0.225$ ;  $a_0 = 27.84$ . However, this equation only shows the final crater radius  $r_c$ , i.e. its value at the end of the discharge. According to Figure 6.17, the crater radius was found to increase almost linearly until around 70% of the discharge duration time, which then stays almost unchanged afterwards. The curve shown in Figure 6.17 can also be fitted by using a second-order polynomial:

$$r_c = b_2 \cdot (t)^2 + b_1 \cdot t + b_0 \quad (6.21)$$

Considering a normalized curve, i.e. with  $r_c$  and  $t$  equal to one at time  $t_e$ , the following solution is achieved for equation (6.21):  $b_0 = -1.188$ ;  $b_1 = 2.061$ ;  $b_2 = 0.125$ . It can be seen that  $b_0$  differs from zero, since we assumed a small plasma diameter at the beginning to avoid almost infinite discharge density at the start.

Now assuming that  $t_e$  differs from one (in our case varies between 1 and 1.8  $\mu\text{s}$ ), crater radius can be normalized by using equation (6.22), where  $t$  varies from 0 to  $t_e$ .

$$r_n = \left(\frac{b_2}{t_e^2}\right) \cdot t^2 + \left(\frac{b_1}{t_e}\right) \cdot t + b_0 \quad (6.22)$$

The crater radius expansion as a function of peak current and discharge duration can thus be calculated at different discrete time steps during the discharge based on equation (6.23) (product of equations (6.20) and (6.22),  $r(t) = r_c \cdot r_n$ ).

$$r(t) = [a_2 \cdot (i_{peak} \cdot t_e)^2 + a_1 \cdot (i_{peak} \cdot t_e) + a_0] \cdot \left[ \left( \frac{b_2}{t_e^2} \right) \cdot t^2 + \left( \frac{b_1}{t_e} \right) \cdot t + b_0 \right] \quad (6.23)$$

Figure 6.21 shows a comparison between the “measured” crater expansion (expected for a discharge pulse type *II*) and the result obtained by applying equation (6.23), assuming the wire cut machine WEDM-VP4. Equation (6.23) is thus used as input for further simulations in this work.

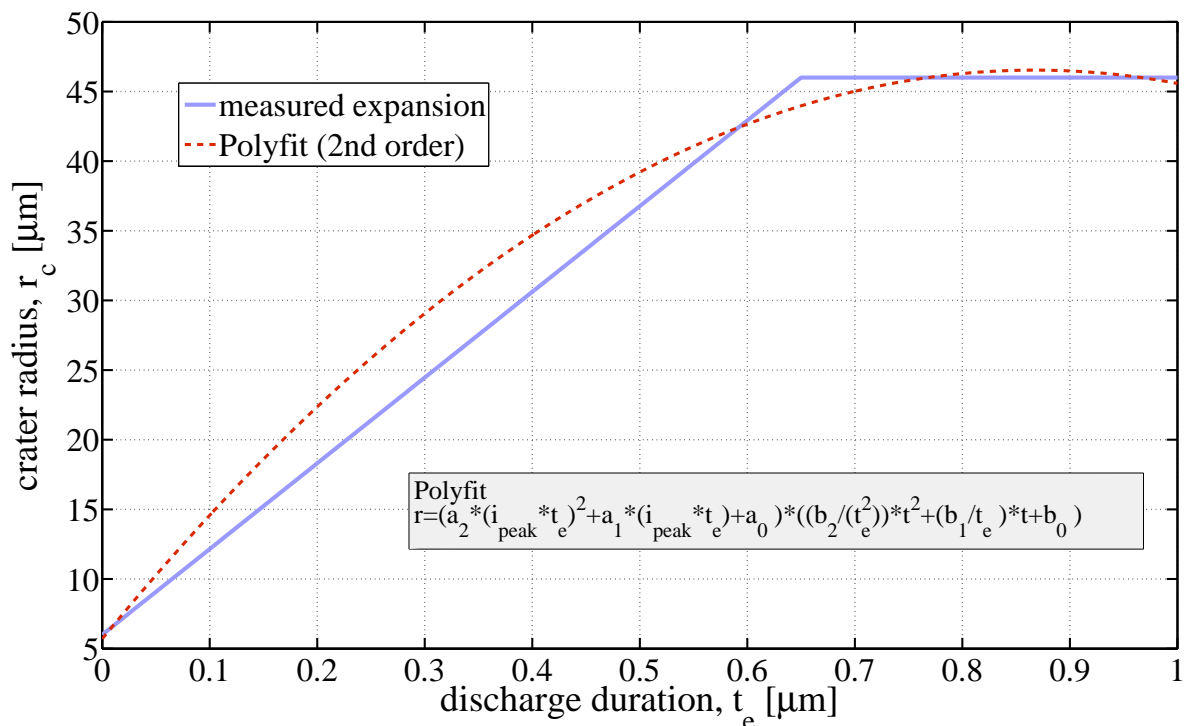


Figure 6.21 – “Measured” crater expansion vs. fitted curve for pulse type *II*

## 6.4 Numerical results

In this section simulation results are presented and discussed. First the approach used to determine the erosion power factor is presented. The influence of the type of heat source and workpiece properties on erosion material removal rates is presented. The influence of the relative speed on eroded craters is also addressed and simulations used to predict constant axial dressing feed rates are shown. Finally, diamond graphitization is discussed based on simulation results.

### 6.4.1 Erosion power factor

The erosion power factor  $F_c$ , i.e. the amount of energy that flows into the workpiece/anode, can be estimated by comparing measurements of the total volume of molten material per discharge and simulation results. Single discharge experiments were carried out using the Wire Cut EDM machine type AC Progress VP4. Erosion pulses  $I1$  to  $I6$  (see Figure 6.4 and Figure 6.6) were used. As an illustrative result, simulated cross sections of two different craters are shown in Figure 6.22 (cross section of  $200\ \mu\text{m} \times 75\ \mu\text{m}$ ). For a pulse type  $I1$  the crater is shallower and has a smaller radius in comparison to  $I6$ .

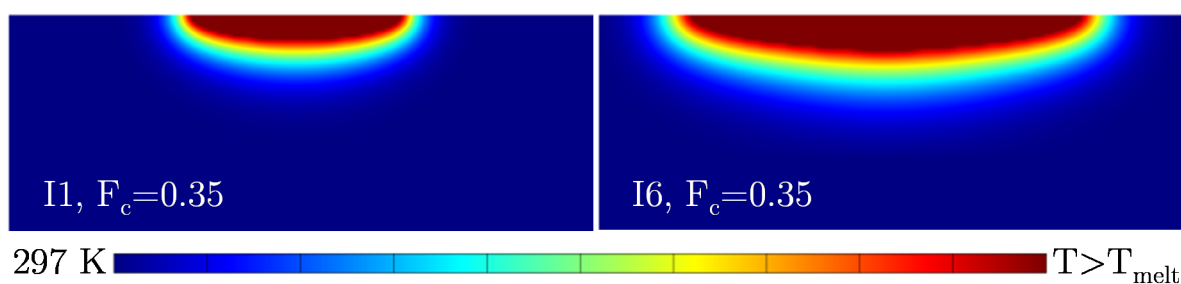


Figure 6.22 – Simulated craters for two different peak currents in copper ( $I1$  and  $I6$ )

Regarding the amount of molten material per single discharge, Figure 6.23 shows a comparison between experimental and simulation results in copper. Simulations were performed using power factors of  $F_c = 0.30, 0.35$  and  $0.40$ , meaning that, respectively, 30%, 35% and 40% of the whole discharge energy is transmitted to the workpiece/anode. According to the presented results, a power factor of  $F_c = 0.35$  was chosen for performing further simulations in this work. This choice is also supported by the work carried out by Xia et al. (cited in Kunieda et al. [KUNI05]), who stated that in die-sinking EDM approximately 34% of the discharge energy flows to the workpiece. One can see that simulation results using  $F_c = 0.35$  do not match the experimental results for all the used peak currents. The reason for that lies in the choice of a common thickness of recast layer for all discharge pulses. In Figure 6.23, the results represent the sum of the measured crater volume and the expected volume of the recast layer, which is larger for higher discharge energies and would represent an increment on the molten volume for these pulses.

### 6.4.2 Influence of heat source type

The heat source that represents the discharge in electrical discharge machining can be modeled in different ways. Generally a point heat source or a disc heat source is applied, since, when compared to expanding heat sources, it is less complex to be described and normally easier to be analytically modeled. However, when these approaches are used, the shape of simulated craters strongly differs from the shape of

measured craters. In this work a time dependent heat source is assumed for the simulations as discussed previously in section 6.3.3. Moreover, considering temperature-dependent thermophysical properties of materials is also important, since several properties are significantly influenced by temperature and thus have an impact on the amount of simulated molten material. The same is valid for the latent heats of fusion and vaporization, which also influence the simulated amount of molten material.

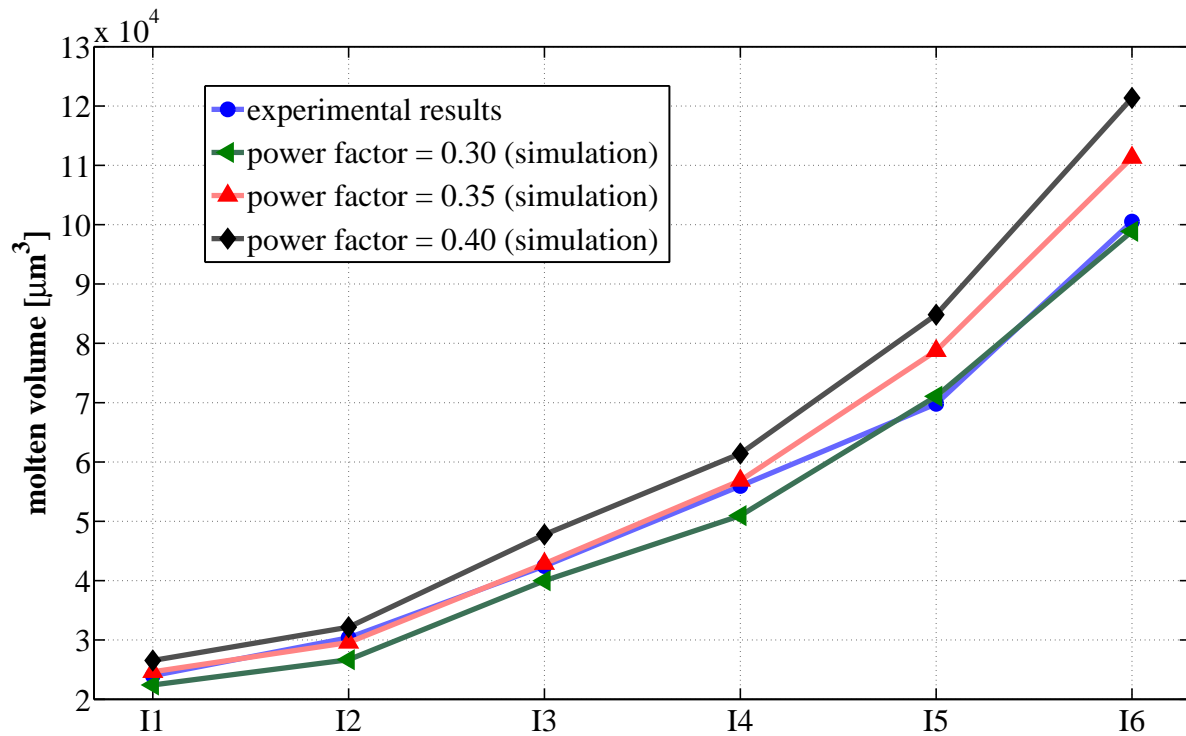


Figure 6.23 – Power factor determination by comparing simulation and experimental results in copper for different discharge pulses

Figure 6.24 shows a sequence of different heat sources and the correspondent results of crater depth  $h_c$  and crater diameter  $d_c$  achieved in these simulations. Pure aluminum was used as base material, the discharge peak current was set to  $I_{peak} = 124$  A, a discharge duration of  $t_e = 1.30$  μs was used, and a power factor of  $F_c = 0.35$  was considered. Aluminum melts at  $T_{melt} = 993$  K and boils at  $T_{boil} = 2,792$  K, has a mass density of  $\rho = 2,702$  kg/m<sup>3</sup>, a specific heat of  $c_p = 903$  J/(kgK) and a thermal conductivity of  $k = 237$  W/(mK). Moreover, the latent heats of fusion and vaporization for aluminum are 10.71 kJ/mol and 294 kJ/mol respectively.

In Figure 6.24a a point heat source was considered, i.e. the heat flux is applied to a point of 5 μm of diameter. The generated crater is a semi-sphere, with a depth of 30 μm and diameter of 60 μm. In Figure 6.24b a disc heat source is used with a diameter of 80 μm, where a crater depth of 20 μm and diameter of 94 μm is created. In Figure 6.24c a time-dependent heat source is considered, i.e. the heat flux is applied to a diameter of 5 μm at the beginning of the discharge and increases up to a diameter of

80  $\mu\text{m}$  at the end. In all the above mentioned types of heat sources, the generated crater is huge when compared to measured craters. Until now, only constant thermophysical properties of the workpiece were considered. In Figure 6.24d, however, temperature-dependent properties are taken into consideration and a time-dependent heat source is applied. Figure 6.25 shows the properties of aluminum used in this simulation. It can be seen that the dimensions of the simulated crater changes considerably, so that a crater depth of  $h_c = 19 \mu\text{m}$  and a crater diameter of  $d_c = 86 \mu\text{m}$  is created. In Figure 6.24e and Figure 6.24f, respectively, the latent heat of fusion and vaporization are implemented. Especially the depth of the simulated craters decreased when the latent heats were applied and the shape of the eroded craters became more and more similar to the shape of measured ones. Figure 6.26 shows a measurement of a crater generated on a single discharge experiment, using the same erosion parameters as for the simulations shown in Figure 6.24. The measured crater has a diameter of  $d_c = 82 \mu\text{m}$  and depth of  $h_c = 8 \mu\text{m}$ , which is very similar to the simulated crater presented in Figure 6.24f. As mentioned before, the recast layer still has to be taken into consideration. Thus, based on the results shown in Figure 6.24, we assume that the best approach to model single discharges in EDM is a time-dependent heat source, where temperature-dependent properties of the workpiece as well as the latent heats of fusion and vaporization are considered.

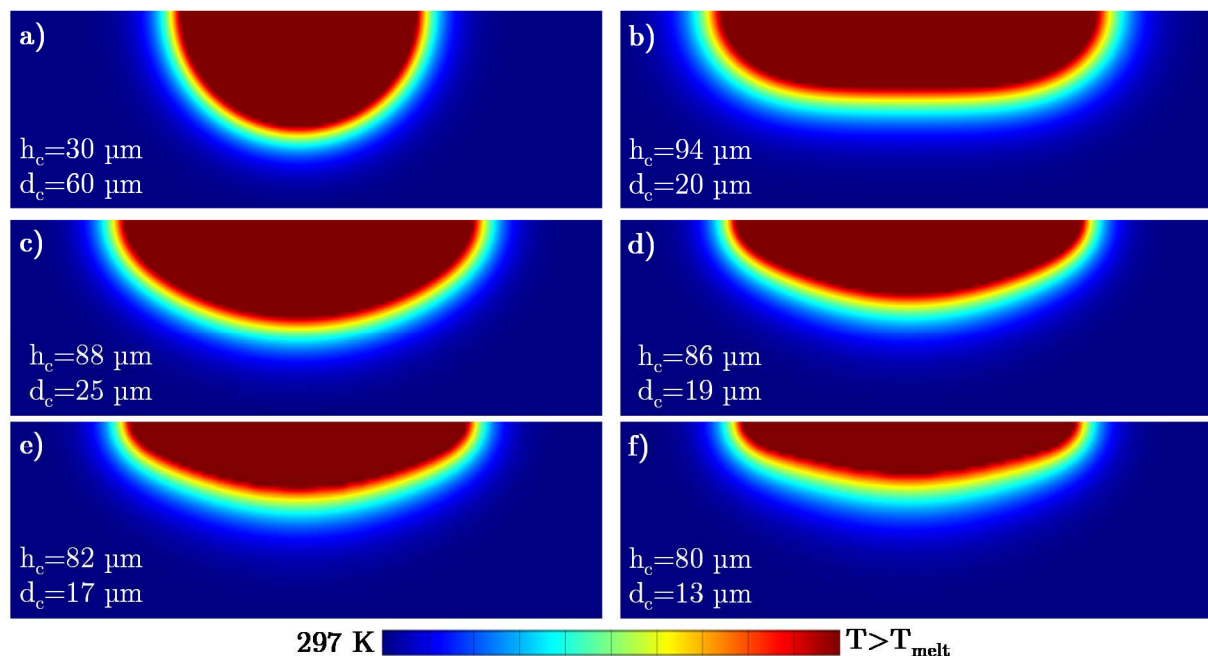


Figure 6.24 – Sequence of cross sections of different simulated craters by changing the type of heat source and thermophysical properties of the workpiece: a) Point heat source; b) Disc heat source; c) Time-dependent heat source; d) Same as in (c) plus temperature-dependent workpiece properties; e) Same as in (d) plus the latent heat of fusion; f) same as in (e) plus the latent heat of vaporization



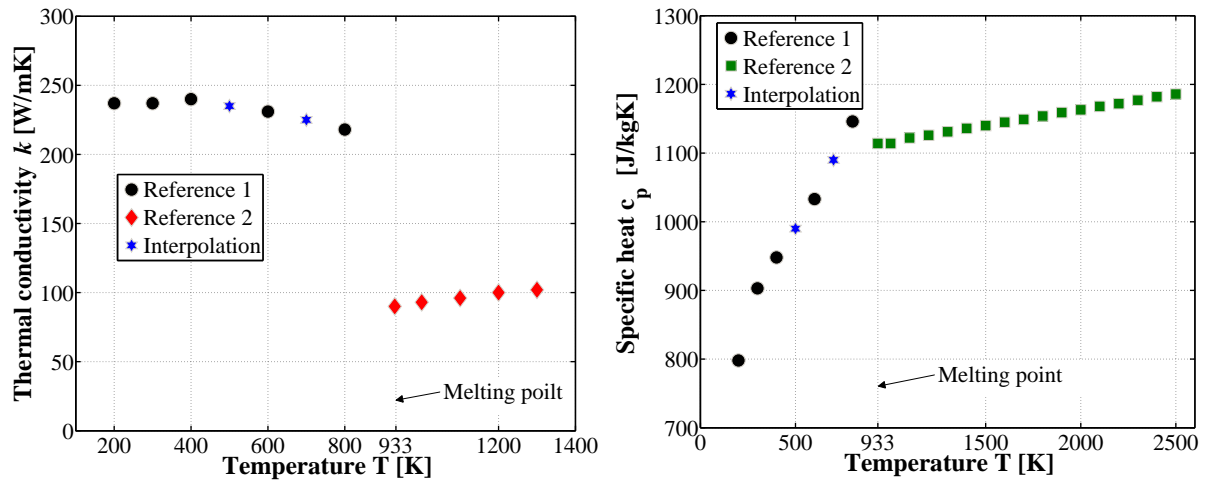


Figure 6.25 – Temperature dependence of the thermal conductivity and specific heat in aluminum: Reference 1 [INCR06]; Reference 2 [GATH83]

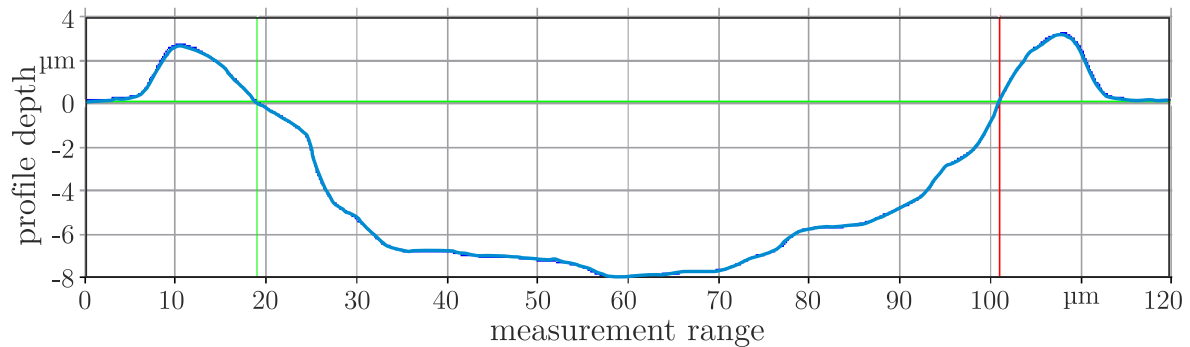


Figure 6.26 – Cross-section of eroded crater in aluminum by applying  $I_{peak} = 124$  A and  $t_e = 1.30$   $\mu\text{s}$ :  $d_c = 82$   $\mu\text{m}$ ;  $h_c = 8.1$   $\mu\text{m}$

### 6.4.3 Thermophysical properties of workpiece materials

In equation (6.1) presented before, the thermal diffusivity  $\alpha$  encompasses the workpiece material properties. Thus, the thermal conductivity  $k$ , mass density  $\rho$  and specific heat  $c_p$  influence the amount of molten material per single discharge, since the thermal diffusivity defines if heat can be more easily stored or conducted into the workpiece. The melting temperature is also an important property, since in general materials with higher melting temperatures are more difficult to be eroded, as for instance molybdenum ( $T_{melt} = 2,896$  K) and tungsten ( $T_{melt} = 3,695$  K) when compared, to tin ( $T_{melt} = 505$  K) and zinc ( $T_{melt} = 692$  K) [KLOC07d].

To illustrate how the above mentioned properties can influence erosion, different single craters were simulated, by varying these thermophysical properties around the properties of aluminum. The main changed property is shown in the following two figures, together with the simulated crater depth  $h_c$  and diameter  $d_c$ . Only constant thermophysical properties were applied in these simulations. An erosion power factor of

$F_c = 0.35$  was used, the discharge peak current was set to  $I_{peak} = 124$  A and a discharge duration of  $t_e = 1.3$   $\mu$ s was applied.

Figure 6.27 shows the influence of the specific heat and the mass density on simulated craters. The specific heat assumed the following values: 700, 903 and 1,100 J/kgK, while the mass density assumed the following values: 1,700, 2,702 and 3,700 kg/m<sup>3</sup>. It can be seen that the dimension of the crater increases when specific heat and/or mass density decrease. As mentioned before, the diffusivity represents the capacity of a material to store energy to its capacity to conduct heat. Thus, the product of mass density and specific heat indicates the ability of a material to store energy. Higher specific heats mean that each node can store more energy, thus leading to higher concentration of energy on the melting pool and consequently to lower amount of molten material. When specific heats of 700 and 1,100 J/kgK were used, the volume of molten material represented, respectively, 125% and 95% of the molten material achieved using a specific heat of 903 J/kgK. Regarding the mass density, a smaller crater was generated by using the mass density of 3,700 kg/m<sup>3</sup>. In addition, when mass densities of 1,700 and 3,700 kg/m<sup>3</sup> were used, the volume of molten material represented, respectively, 150% and 77% of the molten material achieved using a mass density of 2,702 kg/m<sup>3</sup>. Therefore, less material is molten when higher mass densities and specific heats are used.

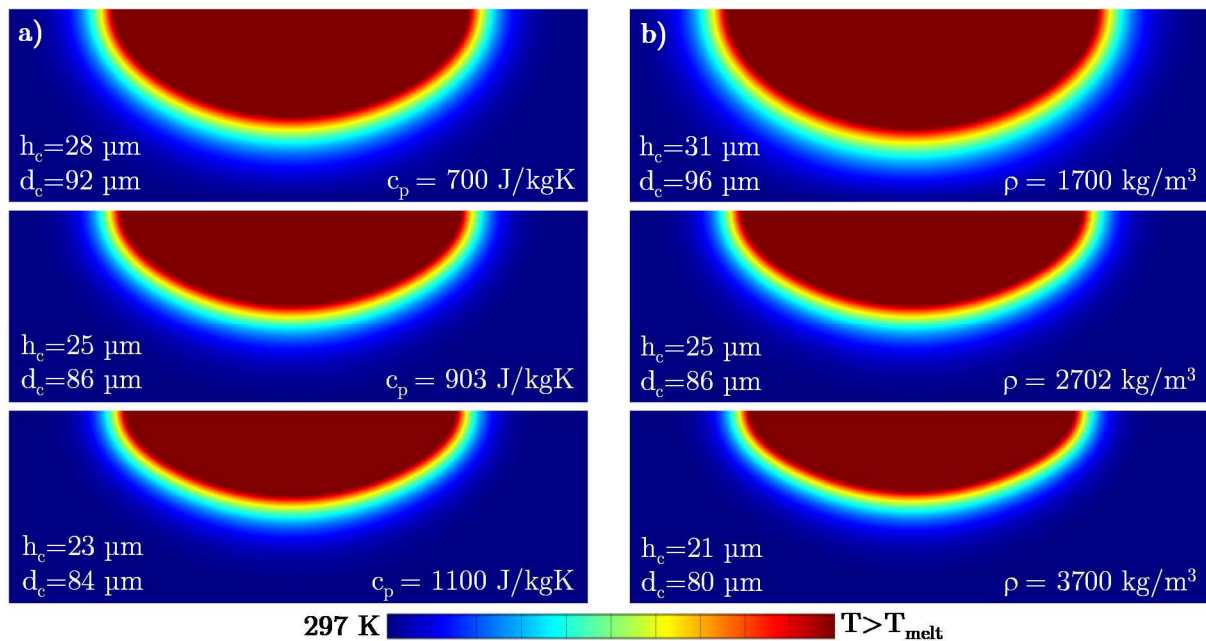


Figure 6.27 – Influence of specific heat  $c_p$  (a: left) and mass density  $\rho$  (b: right) on simulated crater shape and volume

Figure 6.28 shows the influence of the thermal conductivity and melting temperature on simulated craters. Thermal conductivities of 137, 237 and 337 W/mK were applied while melting temperatures of 833, 933 and 1,033 K were used. It can be

clearly seen that the eroded volume increases as the thermal conductivity is increased. Thermal conductivity is responsible for heating up material volume but also for energy losses into the depth of the bulk. If conductivity is too high, so that the conductive heat flux at melting temperature at the surface is larger than the applied heat flux, no further melting occurs. According to the results shown in Figure 6.28, when heat conductivities of 137 and 337 W/mK were used, the volume of molten material is 83% and 115% respectively of the molten material achieved using the thermal conductivity of 237 W/mK.

The melting temperature has a very predictable effect on the amount of molten volume, since for higher melting temperatures more energy is needed to warm up and melt a specific volume of material. When melting temperatures of 833 and 1,033 K were used, the volume of molten material is 110% and 92% respectively of the molten material achieved using melting temperature of 933 K.

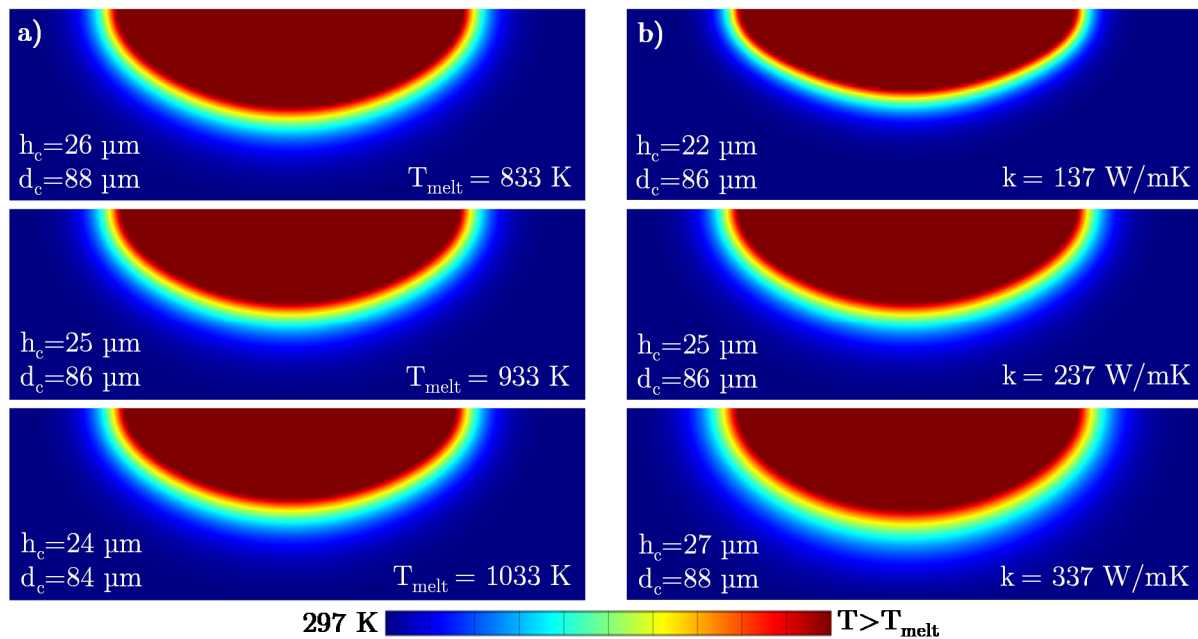


Figure 6.28 – Influence of melting temperature  $T_{melt}$  (a: left) and thermal conductivity  $k$  (b: right) on simulated crater shape and volume

According to both previous figures, it can be stated that changes in the thermophysical properties of the workpiece material significantly influence the amount of molten material. To better illustrate how temperature-dependent material properties and the latent heats of fusion and vaporization influence simulation outputs, Figure 6.29 shows a comparison between experimental and simulation results regarding material removal rates obtained for a brass workpiece (CuZn39Pb3)[WEIN12b]. The material removal rate is obtained by multiplying the amount of molten material per single discharge by the correspondent effective discharge frequency  $f_e$  (see Table 6.2). Four different peak currents ( $I3$ - $I6$ ) and a pulse interval time of 35  $\mu\text{s}$  were considered.

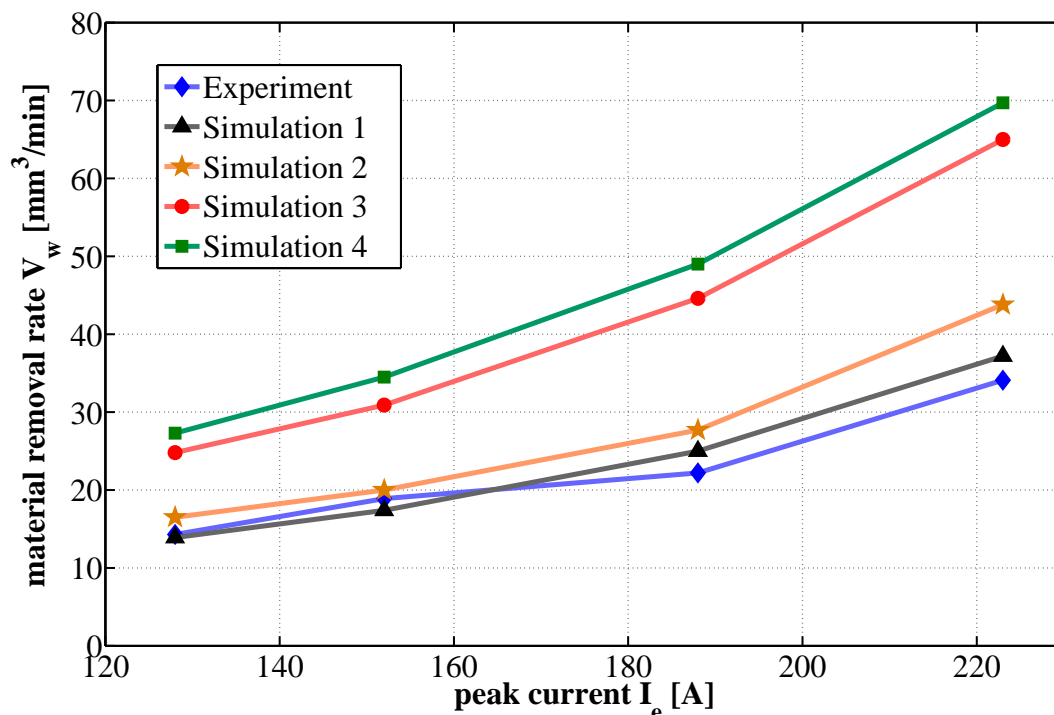


Figure 6.29 - Experimental versus simulation results of material removal rate for brass (CuZn39Pb3): Simulation 1: temperature-dependent material properties and latent heats; Simulation 2: temperature-dependent material properties without latent heat of fusion; Simulation 3: temperature-dependent material properties without both latent heats; Simulation 4: constant material properties without latent heats

In simulation 1, the thermo-physical properties of the workpiece were assumed to be temperature-dependent, and the latent heats of fusion and vaporization were taken into consideration. It is clear to see that simulation results are well correlated with the experimental results. In simulation 2, the latent heat of fusion was neglected, and the simulated amount of molten material increased in comparison to simulation 1. In simulation 3, the simulated material removal rate considerably differs from the experimental results, since the amount of energy involved in phase changes was neglected. Without considering the resistance imposed by these phase changes during the simulation, heat can penetrate more deeply into the workpiece, causing an increase in the amount of molten material. Among both latent heats, the latent heat of vaporization poses a greater resistant to the flow of heat into the material. For copper and zinc, the main components in this alloy, the latent heat of vaporization is, respectively, 22 and 17 times larger than the latent heat of fusion (copper:  $L_f=13.26$  kJ/mol;  $L_e=300.4$  kJ/mol and Zinc:  $L_f=7.32$  kJ/mol;  $L_e=123.6$  kJ/mol). In simulation 4, not only the latent heats were neglected, but also the material properties were assumed to be constant, not dependent on the temperature. A further increase in the simulated material removal rate was observed. This occurs because the specific heat should increase when the temperature is increased, and the assumption that the specific

heat is constant leads to a decrease in the materials' ability to store thermal energy (see Figure 6.27a). On the other hand, the decrease in the thermal conductivity when temperature increases is also neglected, what leads to a decrease in the materials' ability to conduct thermal energy (see Figure 6.28b).

Figure 6.30 shows also the amount of volume that reached temperatures higher than the material's boiling temperature for six different discharge pulses. In comparison to the total amount of removed material, evaporation accounted for approximately 20% in all different simulations, from discharge pulses *I1* to *I6*.

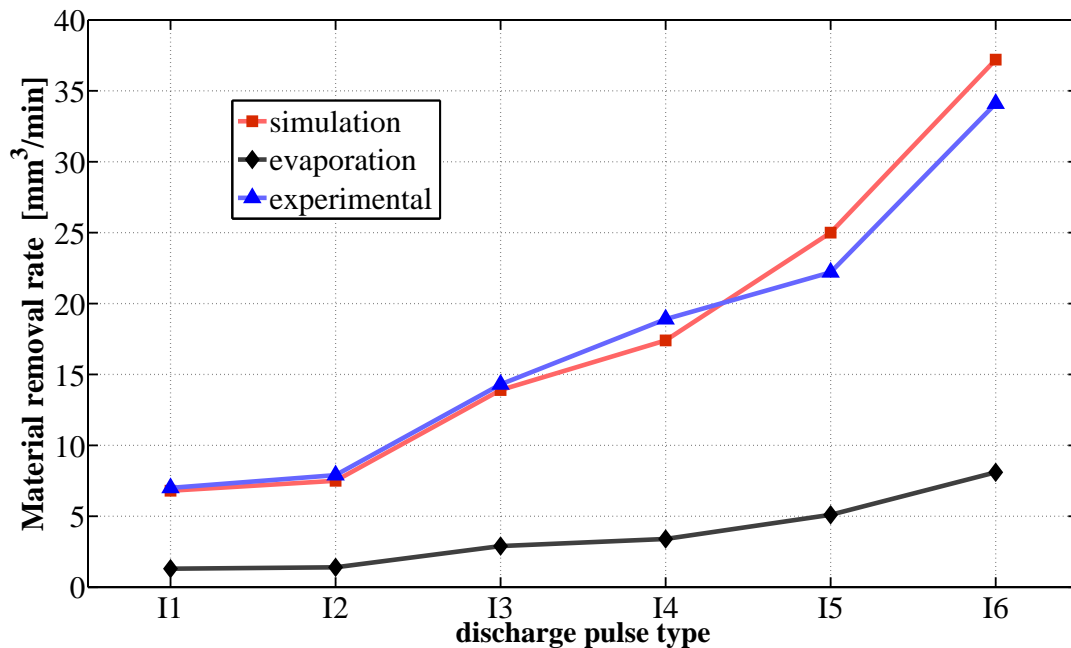


Figure 6.30 – MRR and the amount of evaporation for different discharge currents

Based on the results presented in this section it can be stated that better correlation between simulation and experimental results is achieved for a time-dependent heat source, while considering temperature-dependent material properties and the latent heats of fusion and vaporization. Nevertheless, the lack of data on temperature-dependent properties for different materials is a real drawback.

#### 6.4.4 High relative speeds in WEDM

Experimental results regarding the influence of the relative speed on eroded craters were previously shown in section 6.3.2. To simulate this effect, a time-dependent heat source was used, which slides in the x-axis and creates elongated craters in this direction [WEIN12a]. Figure 6.31 shows different cross sections of simulated craters, by increasing the relative speed  $v_r$  up to 80 m/s. A discharge peak current of  $I_{peak} = 73$  A and discharge duration of  $t_e = 1.25$   $\mu$ s was applied to erode a brass workpiece (CuZn39Pb3). The dimensions of simulated craters are presented in Figure 6.32 and

compared with experimental results. The craters are stretched along the sliding direction of the heat source as relative speed is increased and show a small diameter reduction perpendicular to this direction. Experimental and simulation results do not correlate completely, but deviations are at most around 10%

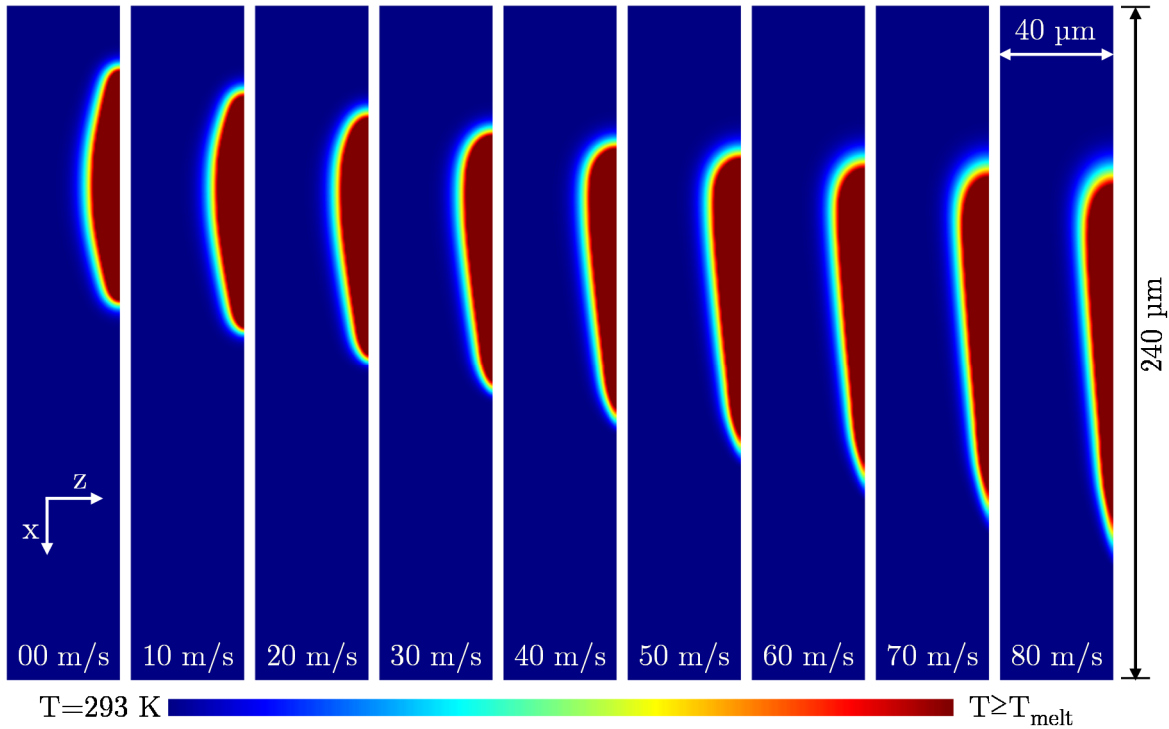


Figure 6.31 – Influence of the relative speed on simulated single discharges in brass (cross section view,  $I_{\text{peak}} = 73 \text{ A}$ ,  $t_e = 1.25 \text{ μs}$ )

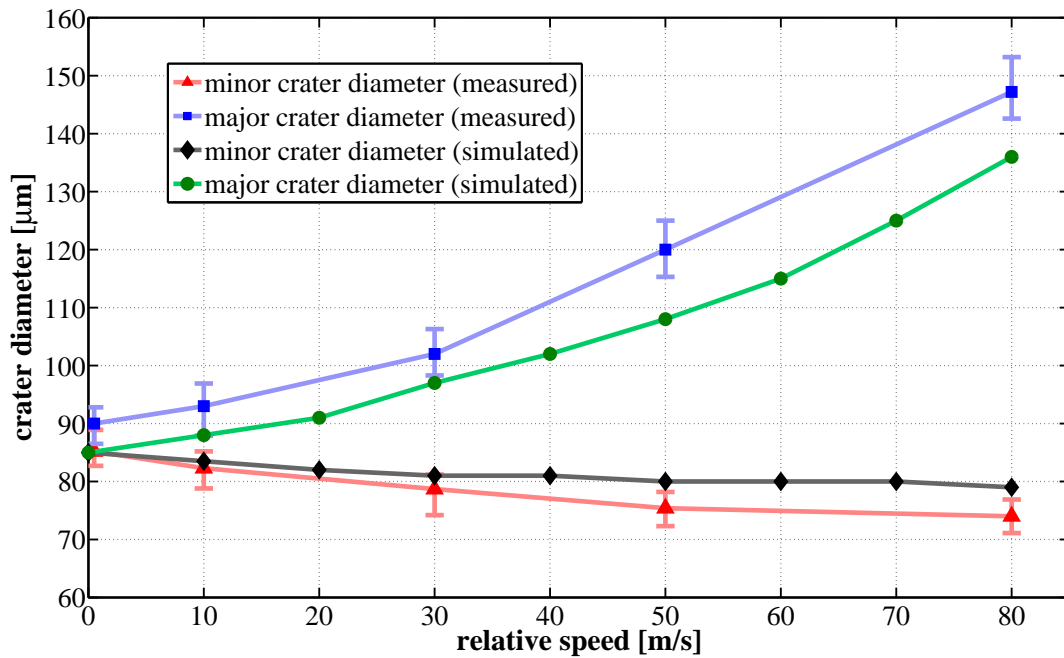


Figure 6.32 – Measured and simulated crater diameters for different relative speeds ( $I_{\text{peak}} = 73 \text{ A}$ ,  $t_e = 1.25 \text{ μs}$ )

Figure 6.33 shows a comparison between simulated and measured craters regarding their top views, showing the similarities between its shapes.

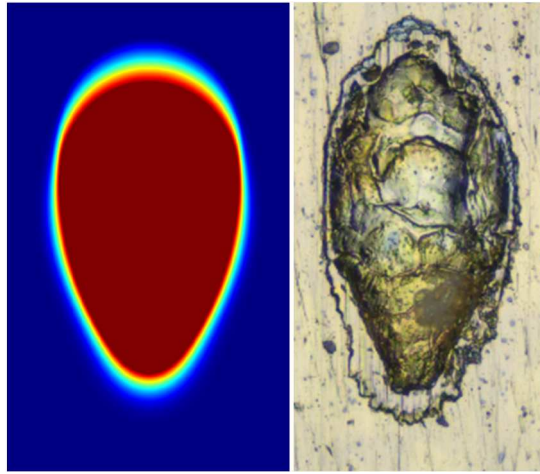


Figure 6.33 – Comparison between simulated and measured craters, 80 m/s (top view)

The influence of the relative speed on the volume of simulated craters in brass is presented in Figure 6.34. It can be seen that it increases as relative speed increases, being consistent with the results presented in Figure 6.18. Furthermore, the average nodal temperature, taking into consideration all nodes that reached temperatures higher than the melting temperature ( $T_{melt} = 1180$  K), was calculated for different relative speeds and is presented in Figure 6.35. It decreases by increasing the relative speed, indicating that higher melting efficiencies are achieved when higher relative speeds are applied, i.e. for higher relative speeds the discharge energy is more efficiently used for melting more material rather than for overheating the melting pool.

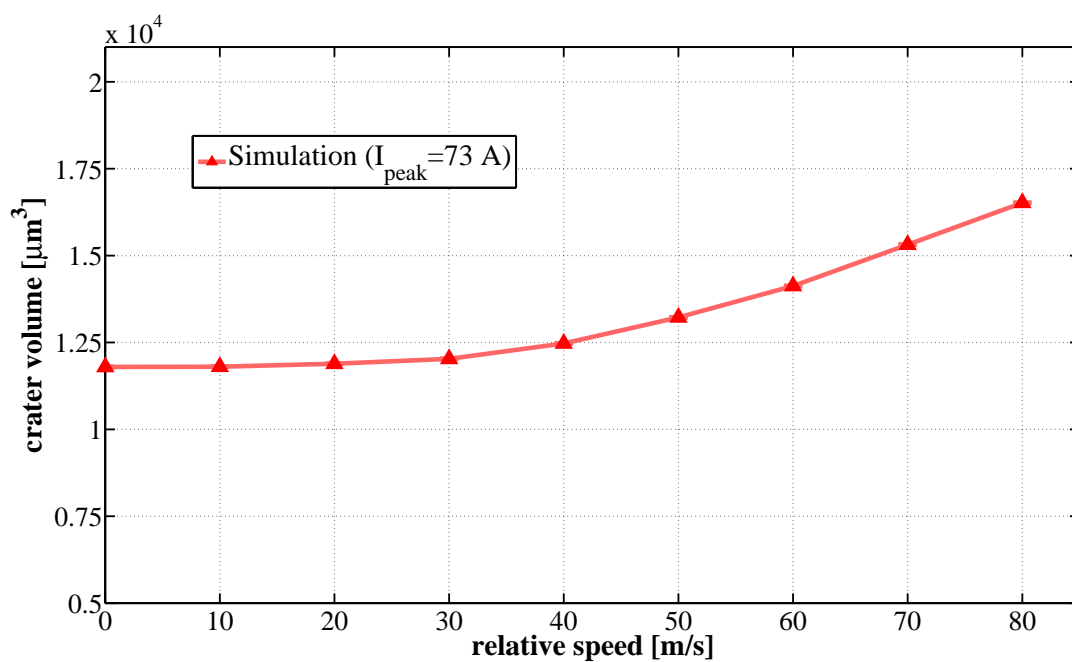


Figure 6.34 – Crater volume by increasing relative speed ( $I_{peak} = 73$  A;  $t_e = 1.25$   $\mu\text{s}$ )

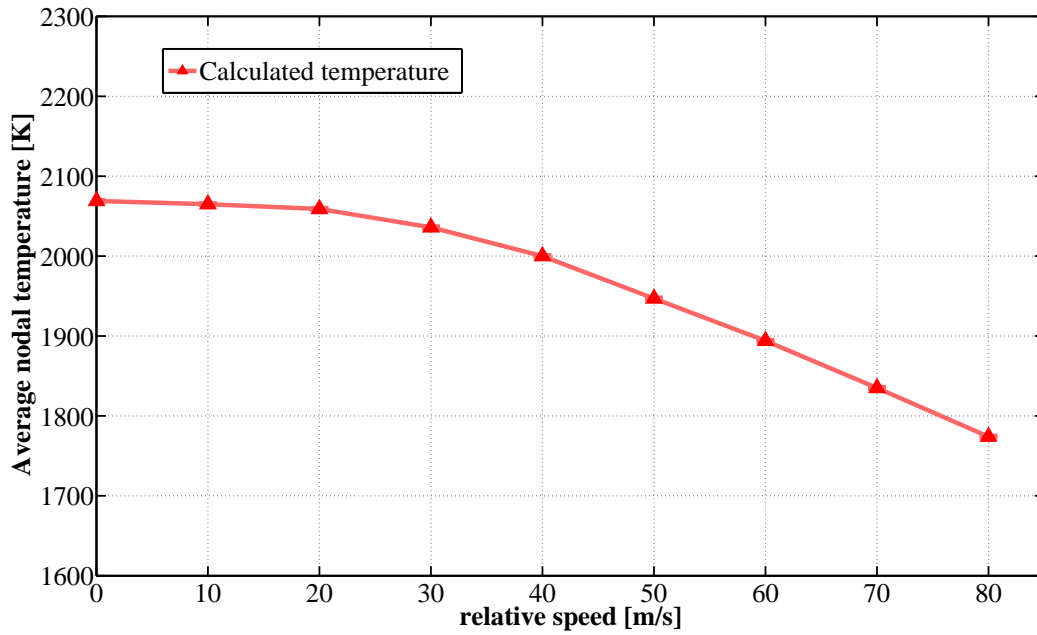


Figure 6.35 – Influence of relative speed on the average nodal temperature within the melting pool for brass ( $I_{peak} = 73$  A;  $t_e = 1.25$   $\mu$ s)

Accuracy of the simulations results presented in Figure 6.34 can be improved if the thickness of the recast layer is considered not to be constant for all the relative speeds. Since the average temperature within the melting pool decreases as the relative speed is increased (Figure 6.35), smaller recast layer thickness is expected for higher relative speeds. This is shown in Figure 6.36, where a better correlation of results between simulation and experiments is achieved when the recast layer (WL) is assumed to decrease with increasing relative speeds.

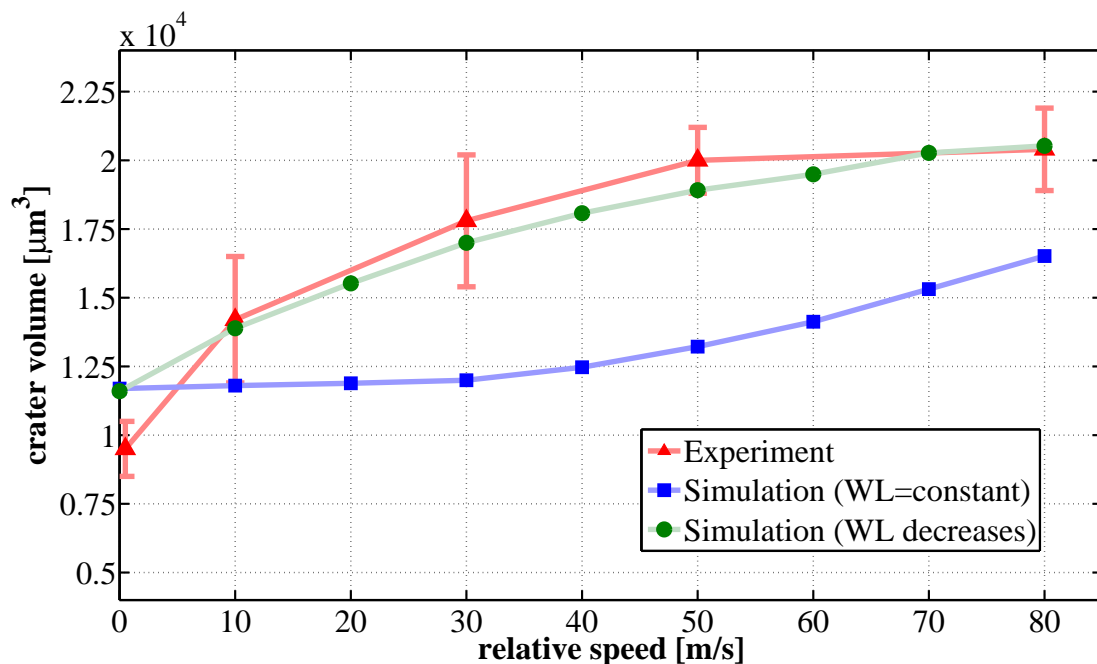


Figure 6.36 – Influence of the recast layer on simulation results ( $I_{peak} = 73$  A;  $t_e = 1.25$   $\mu$ s)



### 6.4.5 WED-dressing strategy

High dressing accuracy is the pre-requisite for a successful grinding process. In WEDD the use of a special wire guide, as previously shown in this work, helps increasing dressing accuracy, since wire vibrations are minimized, leading to a more stable and constant erosion process. However, not only wire vibration is an important issue when it comes to dressing accuracy, but also the way how the erosion process is controlled, i.e. whether a controlled or constant axial dressing feed rate is applied. As shown in section 5.4, constant axial dressing feed rates lead to better dressing accuracies and is thus recommended to be used in WEDD [WEIN12c].

Depending, for instance, on the grinding wheel size, type of metal bond and erosion parameters, different axial dressing feed rates have to be used when different dressing depth of cuts are applied. Thus, the right choice of the axial dressing feed rate  $v_{fad}$  has to be made, to guarantee better dressing results. To support calculating suitable  $v_{fad}$ , the proposed thermal model is used.

In wire electrical discharge dressing, the axial dressing feed rate  $v_{fad}$ , the dressing material removal rate  $Q_d$  and the dressing material removal  $V_d$  can be written as follow

$$v_{fad} = b_s/t_d \quad (6.24)$$

$$Q_d = V_d/t_d \quad (6.25)$$

$$V_d = \pi(r_s^2 - (r_s - a_{ed})^2) \cdot b_s \quad (6.26)$$

where  $b_s$  is the grinding wheel width,  $t_d$  is the time per dressing pass, covering the wheel width  $b_s$ ,  $a_{ed}$  is the dressing depth of cut and  $r_s$  represents the grinding wheel radius. By substituting equation (6.24) and equation (6.25) in equation (6.26) and rearranging this equation, the axial dressing feed rate  $v_{fad}$  can be expressed as

$$v_{fad} = Q_d/\pi(2r_s \cdot a_{ed} - a_{ed}^2) \quad (6.27)$$

The dressing material removal rate  $Q_d$  is thus the only variable in equation (6.27) that cannot be directly chosen, but rather has to be either previously measured or calculated. As an example, for a  $Q_d$  of 50 mm<sup>3</sup>/min,  $a_{ed}$  of 3 μm, and  $r_s$  of 200 mm, the resulting axial dressing feed rate  $v_{fad}$  equals 13.2 mm/min. One has to consider, however, that this axial dressing feed rate represents a maximum for the above mentioned conditions. For practical reasons, a factor of safety should be used, aiming to guarantee that the entire circumferential surface of the grinding wheel is eroded.

In order to reduce the amount of experiments needed for measuring dressing material removal rates, the proposed erosion model can be used to estimate it.

Knowing the effective eroded volume per crater  $V_c$ , the dressing material removal rate  $Q_d$  can be estimated based on simulation results and be written as

$$Q_d = V_c \cdot f_e / (1 - V_a) \quad (6.28)$$

where  $f_e$  is the effective pulse frequency and  $V_a$  represents the volume percentage of abrasives in the bond.  $V_a$  depends on the concentration of diamonds, which is usually specified in the grinding wheel designation by the letter C followed by a number. For example, typical concentrations are C75, C100, C125 and C150, which represent, respectively, a volume percentage of 18% ( $V_a = 0.18$ ), 24%, 30% and 36%. The term  $(1 - V_a)$  used in equation (6.28) is necessary, since the diamonds (insulators) are not eroded, but rather pulled-out of the bond after achieving a certain protrusion, as previously presented in Figure 4.12, in which marks left by diamonds after pulling-out were illustrated in a SEM-micrograph of a WED-dressed diamond wheel D46.

Knowing  $V_c$ , the final equation used to calculate the axial dressing feed rate is obtained by substituting equation (6.28) in equation (6.27) and can be expressed as

$$v_{fad} = \frac{V_c \cdot f_e}{\pi(2r_s \cdot a_{ed} - a_{ed}^2) \cdot (1 - V_a)} \quad (6.29)$$

Figure 6.37 shows a comparison between experimental and simulation results regarding MRRs obtained for a brass workpiece. Three different discharge peak currents ( $I_4$ ,  $I_5$  and  $I_6$ ) and three effective pulse frequencies (7.9, 11.3 and 14.1 kHz) were used. Deviations of at most 10% between experiments and simulation were achieved, showing a good correlation of results.

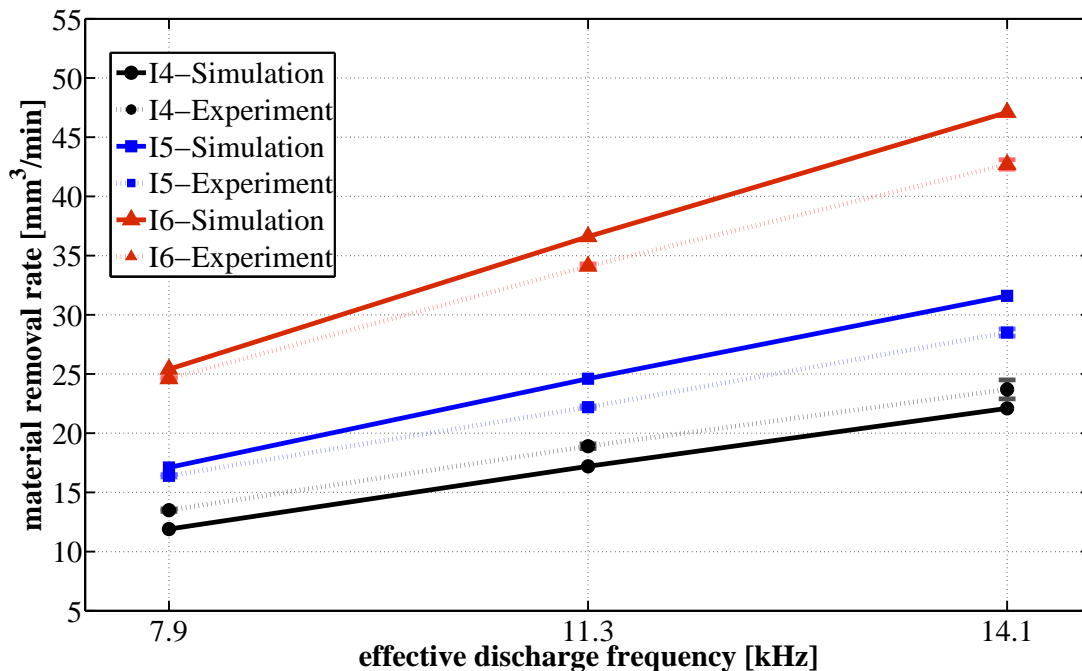


Figure 6.37 – Material removal rate obtained for a brass workpiece

Figure 6.38 shows a comparison between simulations and experimental results regarding the material removal rate using a grinding wheel type 1A1 50x10x5x20 D46 C125 B1. A bronze material (89% Cu, 11% Sn) was used in this case as basis for this simulation. Based on equation (6.28), simulation results with and without the volume percentage of diamonds C125 ( $V_a = 0.3$ ) are presented. The results show a good correlation between experimental and simulation results when  $V_a = 0.3$  is applied.

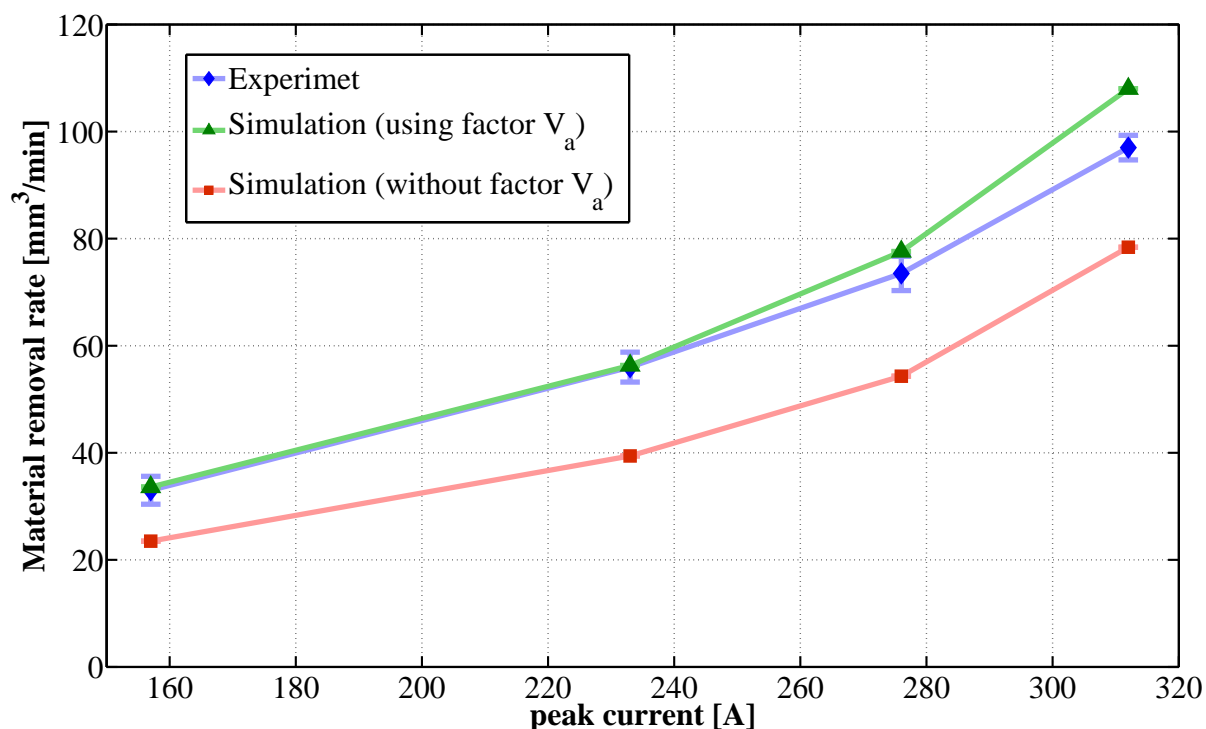


Figure 6.38 – Erosion material removal rate obtained for a diamond grinding wheel type 1A1 50x10x5x20 D46 C125 B1

One can see in Figure 6.38 that for higher peak currents the deviations between experimental and simulation results are higher. One reason for that is that a constant pulse frequency ratio of  $\lambda = 39,5\%$  is assumed for all different peak currents and discharge frequencies (see Table 6.2), which in reality is not correct. As presented in Table 6.2, the effective pulse frequency decreases when higher peak currents are used, so that using the above mentioned constant pulse frequency ratio leads to higher material removal rates for higher peak currents. This can be adjusted if  $\lambda$  is exactly measured for all different pulses, rather than using a constant value of pulse frequency ratio. Nevertheless, assuming this pulse frequency ratio already gives a first good estimation of material removal rates.

Since a good correlation of calculated and measured results has been found, the axial dressing feed rate can be calculated based on equation (6.29). Figure 6.39 shows some examples of  $v_{fad}$  obtained for a grinding wheel 1A1 50x10x5x20 D46 C125 B1, when eroded using different peak currents, an effective pulse frequency of  $f_e = 14.1$

kHz, two different dressing depth of cut  $a_{ed}$ , namely 2 and 3  $\mu\text{m}$ , and different wheel diameters. For smaller grinding wheel diameters, smaller dressing depths of cut and for higher peak currents, higher axial dressing feed rates can be used.

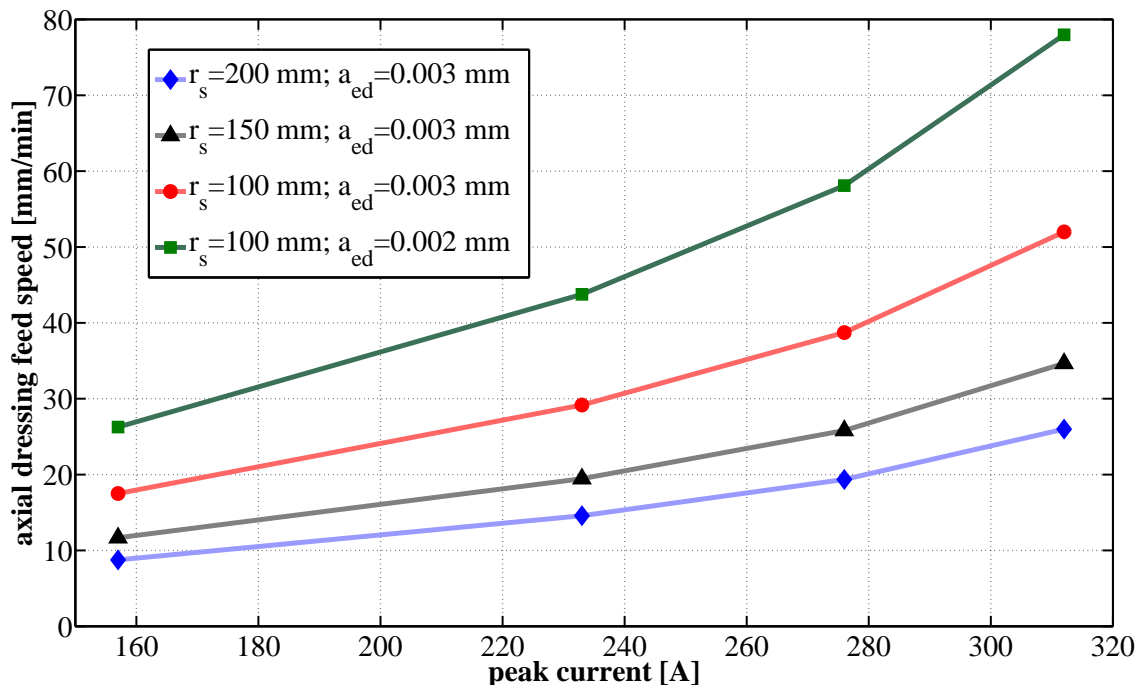


Figure 6.39 – Axial dressing feed rate  $v_{fd}$  calculated for different dressing parameters

Since constant axial dressing feed rates combined with small depth of dressing cuts lead to better dressing accuracies, one could expect that in on-machine wire electrical discharge dressing of metal bonded grinding wheels no controlled axes with gap regulation would be needed. If dressing using the grinding machine axes were possible, the integration of a WEDD unit into a grinding machine would be much easier, the same way as one would expect better acceptance of this technology by the grinding machine users. This possibility still has to be tested, and is addressed here as a recommendation for future work in this area.

#### 6.4.6 Diamond graphitization

Diamond is a material with exceptional properties [SEAL92]. It is an electric insulator, transparent, the material with the highest heat conductivity and known as the hardest material found in nature. For this reason, diamonds find several applications in different fields, ranging from optical to machining processes [FIEL79]. Diamond is not the thermodynamically stable form of carbon at standard conditions for temperature and pressure, but rather graphite [FIEL79]. Graphite, in contrast to diamond, is a good electric conductor, widely used as electrode in die-sinking EDM, and soft, being easily machined by standard machining operations. When electrical discharge machining is

applied for conditioning metal bonded diamond wheels, one would expect thermal damages to the diamonds. Electrical discharge machining is a thermal removal process, in which discharges with highly concentrated energies warm-up, melt and evaporate material from the workpiece [KUNI05]. The graphitization process, i.e. the transformation of diamond to graphite, in air, already starts at temperatures around 700°C [FIEL79]. As mentioned in Chapter 2, Klink et al. [KLIN10] measured a graphite layer of about 0.5  $\mu\text{m}$  on fine diamond grains (5 to 20  $\mu\text{m}$ ) after wire electrical discharge dressing in deionized water and different studies have shown that EDM is a suitable dressing process for metal bonded diamond wheels. However, none of these studies explained why little or no thermal damage occurs to the diamonds in EDD.

When it comes to the process of diamond graphitization, different aspects must be considered. Although graphitization can start when a diamond is heated over 700°C in air, Berman and Simon [BERM55] pointed out that the conversion of diamond to graphite, at zero pressure and in an inert environment, is not detectable experimentally for temperatures below 1,500°C. Davies and Evans [DAVI72] measured graphitization rates at different temperatures, and obtained activation energies of  $728 \pm 50$  KJ/mol and  $1159 \pm 75$  KJ/mol, for (110) and (111) surfaces respectively. Besides that, the thermal conductivity of diamonds is another important aspect. At room temperature, it is as large as five times the thermal conductivity of copper. This has to be taken into consideration, since the heat generated by discharges, for example, can be quickly dissipated to the whole diamond, instead of staying highly concentrated at its surfaces, as for other materials with lower thermal conductivities.

The above mentioned aspects are considered for a thermal model used to calculate the temperature distribution inside a diamond due to different erosion discharges, assuming the same heat source used before (power factor of  $F_c = 0.35$ ). The thermal properties of diamond were chosen as constant, not dependent on the temperature. The following properties were considered: thermal conductivity of  $k = 2,000$  W/mK [FIEL79]; specific heat at constant pressure of  $c_p = 509$  J/kgK; mass density of  $\rho = 3500$  Kg/m<sup>3</sup>; graphitization temperature of  $T_{graph} = 1,800$  K; activation energy of 728 and 1,159 KJ/mol [DAVI72]. The activation energy required to transform diamond into graphite was modeled similarly as for the latent heats presented before (section 6.2.4). In other words, after reaching the graphitization temperature, the activation energy has first to be overcome before graphite is formed.

A diamond of size D46, approximated as a cube of length 46  $\mu\text{m}$ , was used as a reference shape for the model. First, the heat source was assumed to be a disc heat source of the same diameter as the length of the cube, although the diameters of eroded craters are larger than that (see Figure 6.12). This assumption was made aiming to apply the whole discharge energy directly to the diamond. The heat source was placed

on the top surface of the cube while the other five cube faces were considered adiabatic. Figure 6.43 shows a schematic representation of the assumptions made to model the temperature distribution inside the diamond.

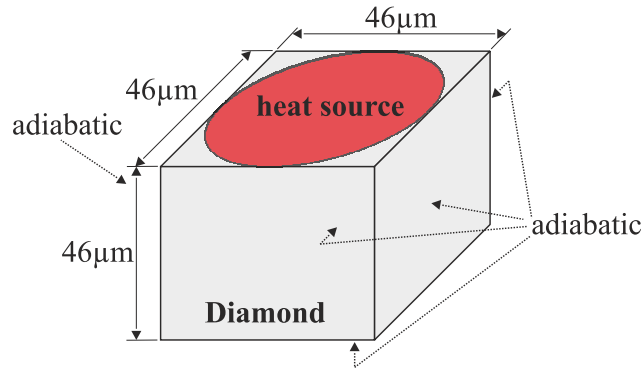


Figure 6.40 – Schematic representation of the heat source applied to a cubic diamond

Pulse discharge types *I1* to *I6* were applied in the simulations. The cube was spatially discretized with an equal distance of 1  $\mu\text{m}$  between consecutive nodes ( $\Delta x = \Delta y = \Delta z$ ) resulting in a total of 97,336 nodes in a cube of length 46  $\mu\text{m}$ . Figure 6.41 shows the amount of nodes which reached enough energy for graphitization. One can see that for the highest discharge energy (*I6*), the volume of graphitization can reach up to 6% of the whole diamond volume. This would represent a layer of approximately 2.5  $\mu\text{m}$  on the top surface of the diamond. The possible amount of graphitization increases as discharge energies are increased and less graphitization is expected for higher activation energies.

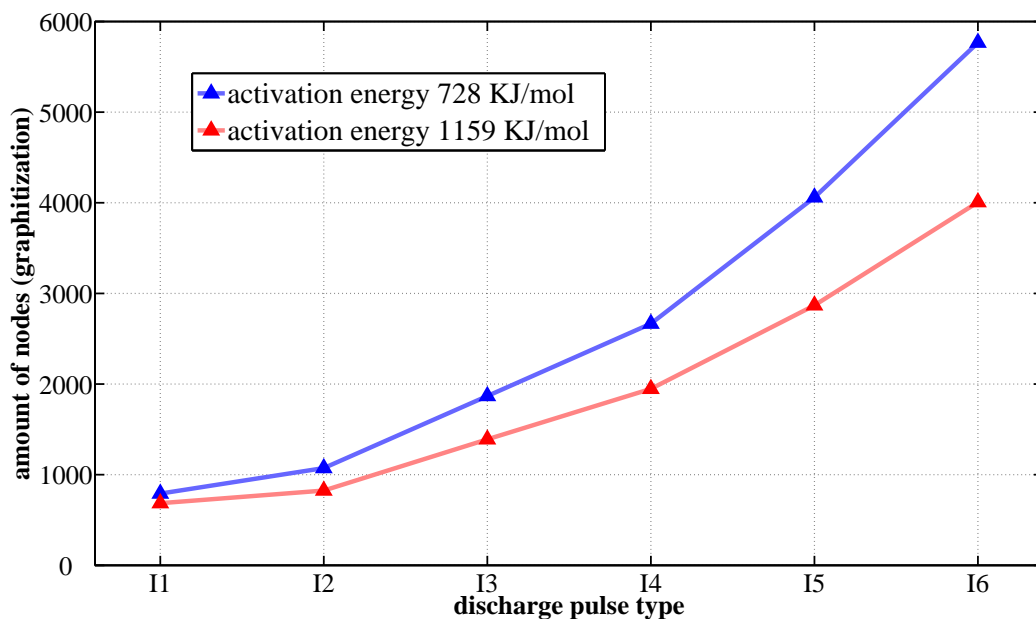


Figure 6.41 – Simulation of diamond graphitization due to single discharges, by considering a disc heat source applying the whole discharge energy to the diamond

Although Figure 6.41 indicates the possibility of thermal damages, the transmission of the whole discharge energy to the diamonds, assumption made to evaluate the worst case scenario, is unlikely to happen. Diamonds are not electric conductors and, for this reason, discharges are not likely to occur directly on the diamonds, but rather nearby. Moreover, diamonds have no adiabatic surfaces, meaning that heat which enters the diamond can also be conducted to the bond material at the contact surfaces. Still, the plasma channel can achieve diameters larger than the diamonds D46, distributing the discharge energy over a larger area.

The first approach was mainly used to check the validity of the model. Considering the molar mass of diamond (12.01 g/mol) and its density (3.5 g/cm<sup>3</sup>), the activation energy can be written as a function of volume, which in this case is equal to 212 J/mm<sup>3</sup> (728 kJ/mol). Assuming now the discharge energy of different pulses used (*I1* to *I6*) and an erosion power factor of  $Fc = 0.35$ , one can calculate which maximal volume of graphitization would be expected if these discharge energies were considered only to overcome the activation energy. This is not directly possible, since due to heat losses more energy is required to achieve the transition state, but can be used as a first approximation. Figure 6.42 shows results obtained by these calculations, where the volume of graphitization is represented as an amount of nodes, in order to facilitate comparison with simulation results presented in Figure 6.41. Higher volume of graphitization was achieved when performing these theoretical calculations in comparison to the simulations, since in the latter energy losses as conduction are not neglected, and thus less energy is available to overcome the activation energy. Since a good agreement of results was found, further thermal simulations can be performed.

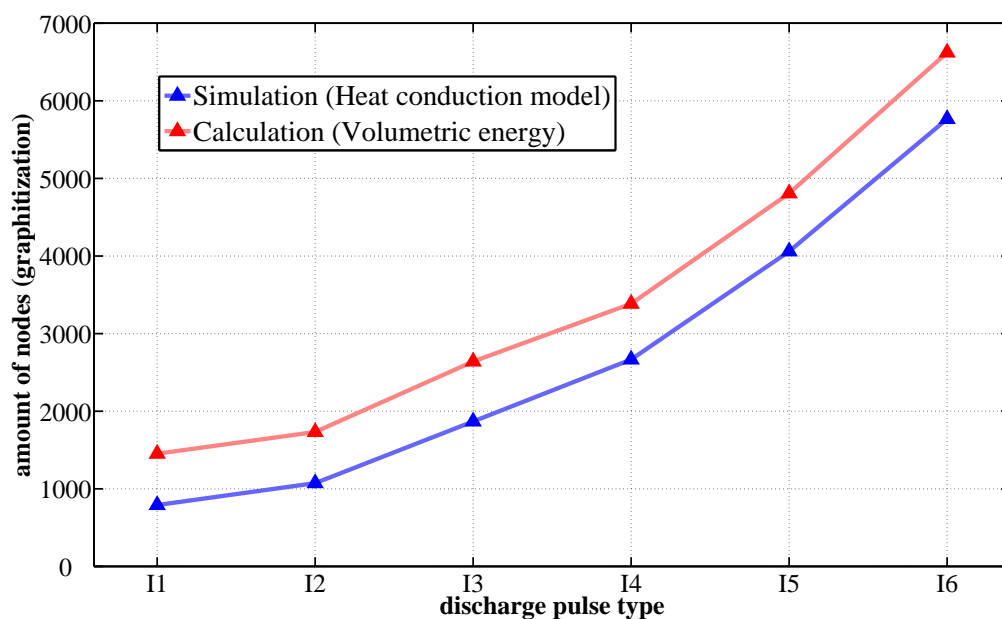


Figure 6.42 – Comparison between thermal simulation and theoretical calculation of the maximal volume of graphitization due to different discharge energies

Another model approach was then used, in which a diamond embedded in bronze was assumed. Now, a time-dependent heat source was considered, which grows larger than the diamond itself. Figure 6.43 illustrates a schematic representation of the assumptions made to simulate graphitization in this case.

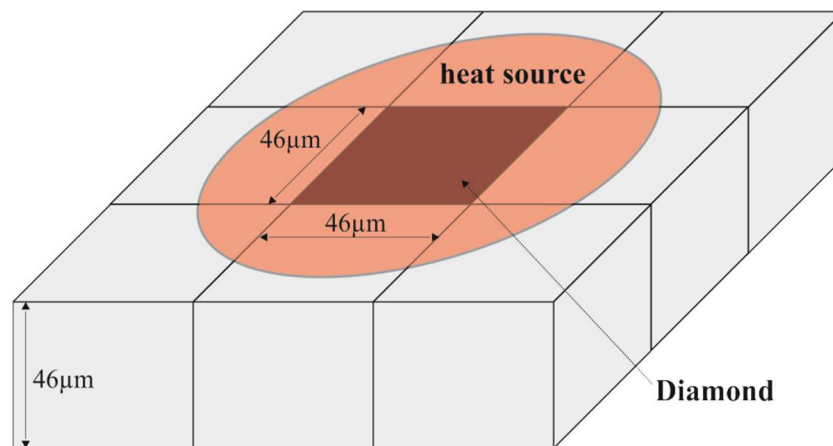


Figure 6.43 – Schematic representation of heat source applied to a diamond (D46) embedded in bronze

Figure 6.44 shows the amount of nodes that reached enough energy for graphitization, now taking into consideration two different diamond sizes, namely D26 and D46, modeled as cubes. The activation energy of 728 KJ/mol was assumed and again pulse discharge types *I1* to *I6* were applied. The cubes were spatially discretized with an equal distance of 1  $\mu\text{m}$  between consecutive nodes ( $\Delta x = \Delta y = \Delta z$ ), resulting in a total of 17,576 and 97,336 nodes, respectively in cubes of length 26 and 46  $\mu\text{m}$ . The heat source was applied on the top surface of the diamond and other five cube faces of the diamond were not considered as being adiabatic. For a D46 diamond, one can see that the amount of graphitization reduces considerably when compared to the results presented in Figure 6.41, where for a peak current *I6* the amount of nodes in the diamond that reached enough energy for graphitization reduced from approximately 6,000 to less than 500. On the other hand, smaller diamonds proved to be more sensitive, since thermal energy can stay more concentrated in smaller diamonds, which have a smaller volume in comparison to a D46 diamond. This second approach also does not represent the reality, since the discharge was placed exactly in the center of the diamond, which should, however, occur near to the diamonds rather than directly on its top surface, as already discussed in section 4.2.5 (discharge concentration around diamonds).

Another approach was tested in which a moving heat source was applied, i.e. the heat source was assumed to start near to the diamond and slip over it. All six different pulses used before were considered and a relative speed of 80 m/s was used. For diamonds D46, graphitization was not obtained for all types of discharges, while for



D26 diamonds, only in the case of using the *I6* discharge pulse, 8 nodes out of a total of 17,576 reached enough energy for graphitization. This approach is closer to reality and indicates that even using high discharge energies, little or no thermal damages are expected to the diamonds during EDD.

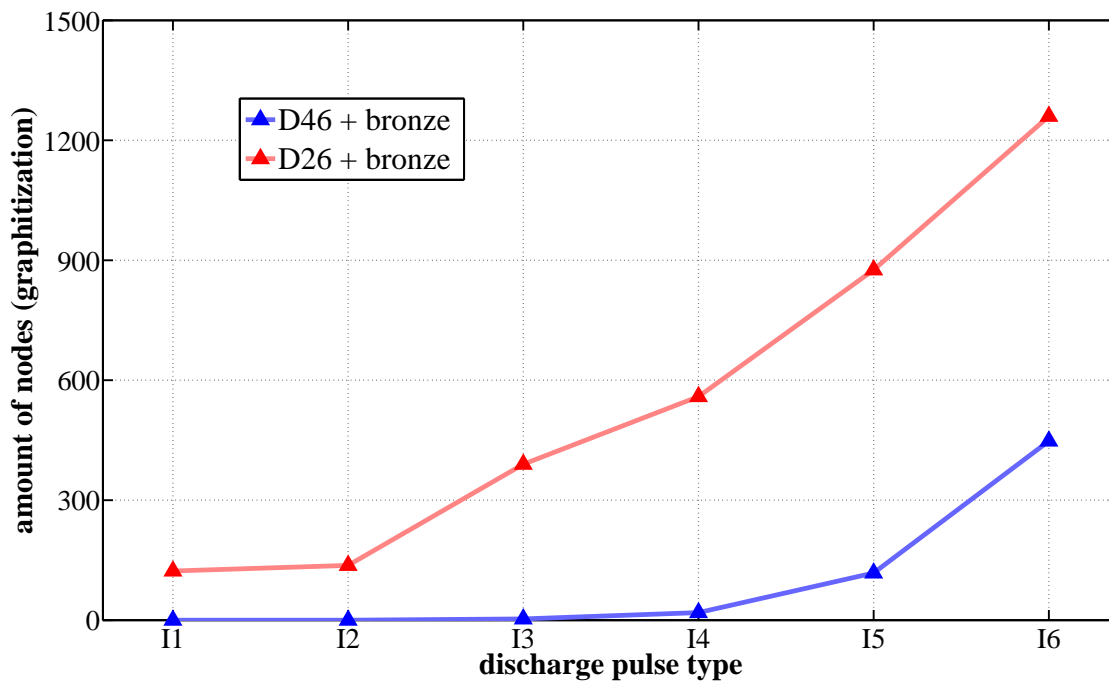


Figure 6.44 – Simulation of diamond graphitization due to single EDM discharges modeled as time dependent heat sources that grow larger than the diamonds

To complement the results presented in this section, diamonds were evaluated in terms of micro Raman-spectroscopy. The characteristic fingerprint of diamond is a single sharp Raman line at  $1,332\text{ cm}^{-1}$  [FILI05]. According to Filik [FILI05], a single crystal of graphite produces a single peak at  $1,575\text{ cm}^{-1}$  whereas in other graphite materials a second feature appears at  $1,355\text{ cm}^{-1}$ . Figure 6.45 shows Raman-spectras of D46 diamonds in different conditions: pure diamond, i.e. loose diamonds which are used to manufacture the grinding wheel; after erosion of a B1 D46 grinding wheel using an *I6* discharge pulse and two different relative speeds, namely 10 and 50 m/s. First of all, the  $1,332\text{ cm}^{-1}$  Raman line is evident in all three cases and there is no presence of graphite, since the Raman lines of  $1,355\text{ cm}^{-1}$  and  $1,575\text{ cm}^{-1}$  are not present. A Raman line appeared at around  $1,435\text{ cm}^{-1}$  in all the cases, also in pure diamond, indicating that it is not caused by the WEDD process. The same Raman line was found after performing conventional dressing of D46 B1 grinding wheels.

After WEDD, some material stills stays attached to the surface of the diamonds, as can be seen in Figure 6.46 (image taken using the Raman microscope). Two locations where measurements were performed are shown and the correspondent Raman-spectras are presented in Figure 6.47. It can be seen that a characteristic

Raman line for graphite appeared for the attached material, while for the top of the diamond the characteristic diamond spectra was revealed. The graphite peak can be the consequence of a coating process which can take place during erosion, where graphite can be deposited over the electrode surface (condensation of graphite on more cold surfaces, creating a layer of pyrolytic graphite).

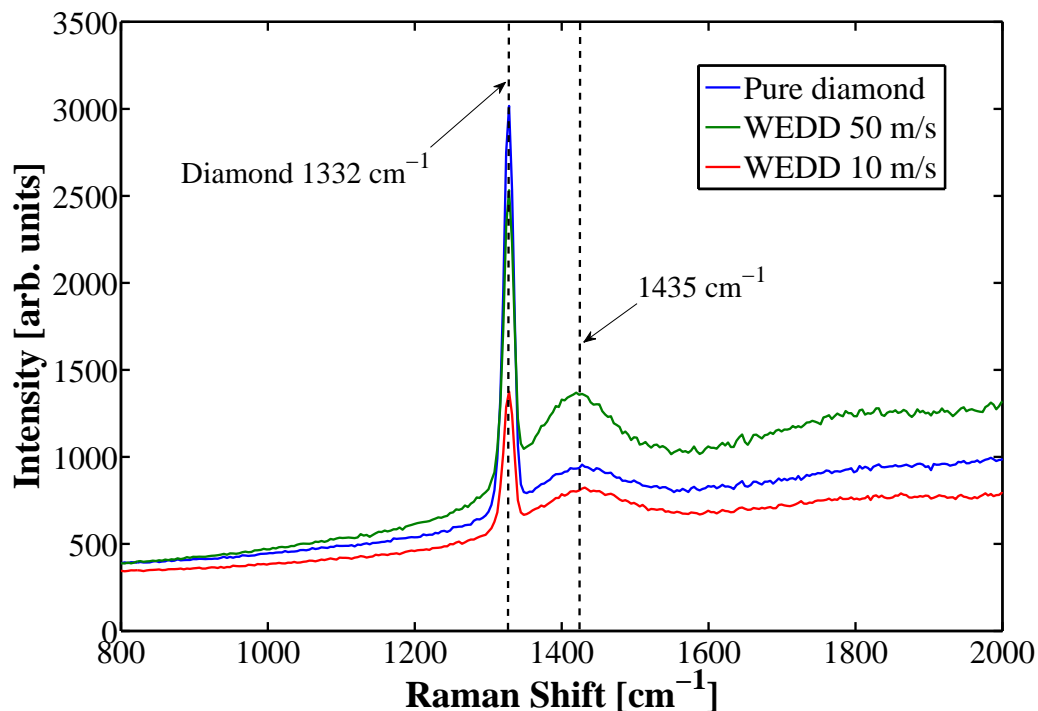


Figure 6.45 – Raman-spectra for D46 diamonds before and after erosion

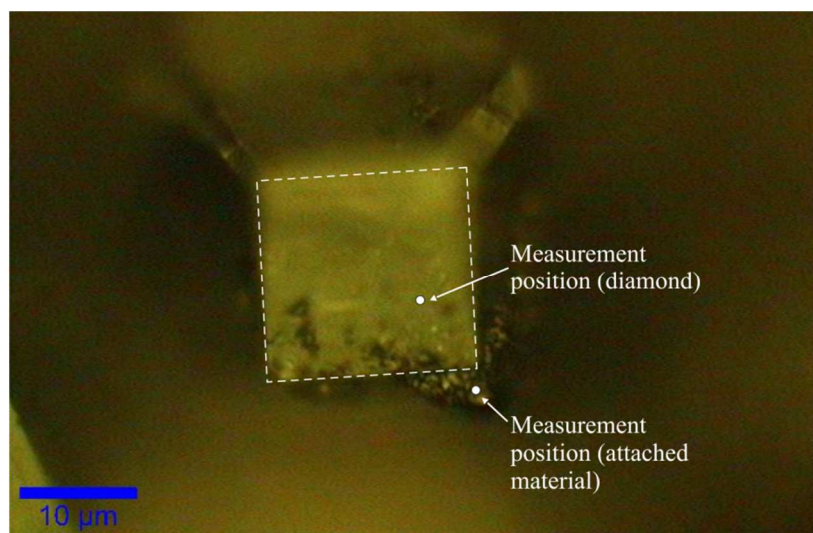


Figure 6.46 – Material attached to a D46 after WEDD at dressing speed of 10 m/s (small circle indicates the position where a Raman measurement took place)

Figure 6.48 shows two SEM-micrographs of WED-dressed grinding wheels with diamond sizes D46 and D91. Geometrically well-defined diamonds with high protrusion

are visible, which still have some metal adhered to their surfaces. No damages were found on the surface of these diamonds after EDD and high G-ratios were achieved after grinding  $\text{Si}_3\text{N}_4$  workpieces, as presented previously in Figure 4.18.

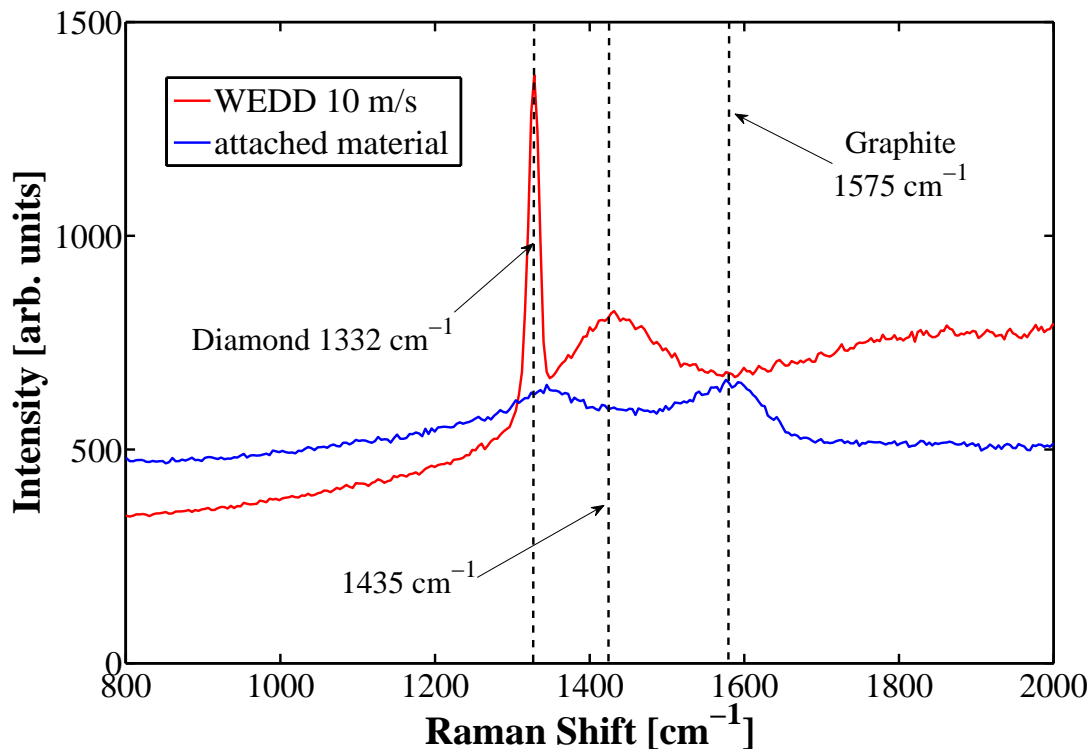


Figure 6.47 – Raman-spectra for D46 diamond and attached material after WEDD

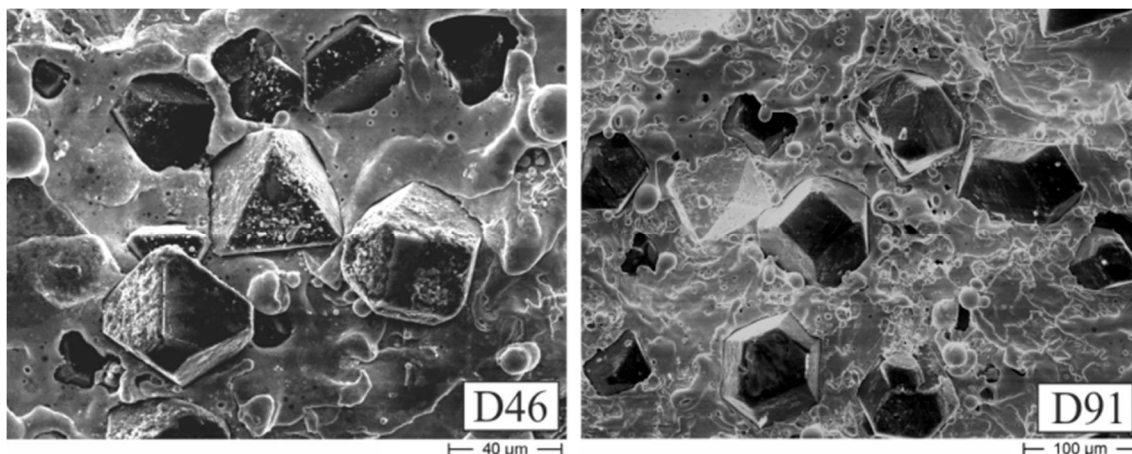


Figure 6.48 – SEM-micrograph of WED-dressed wheels of diamonds D46 and D91

From the results presented in this section, it can be stated that less graphitization is expected for higher activation energies and bigger diamonds and that the properties of diamond helps keeping graphitization at lower rates, i.e. at an acceptable level for a grinding wheel. These results help explain the fact that discharge machining processes are suitable for conditioning metal bonded diamond wheels, leading to minimal thermal damages of the diamonds.

## 7. Conclusions and outlook

In this work, on-machine wire electrical discharge dressing for conditioning metal bonded diamond wheels was evaluated. A compact and flexible WEDD unit was manufactured and integrated inside a grinding machine, enabling on-machine dressing experiments to be carried out. WEDD is more flexible in comparison to SEDD, since with a wire electrode different grinding wheel profiles can be created, instead of having to manufacture different shaped electrodes for SEDD. Moreover, electrode wear plays different roles in WEDD and SEDD. In SEDD, the tool electrode has to be reshaped from time to time, while in WEDD the wire is continuously pulled from a spool, so that electrode wear is constantly compensated.

Comparing electrical discharge dressing with a conventional dressing method, in which a silicon carbide dressing wheel is used, the following can be stated:

- Wire electrical discharge dressing (WEDD) enables the generation of higher grain protrusion on metal bonded diamond wheels. The grinding wheel is thus more aggressive, which is an important characteristic in such a tool. With a more open structure, less friction between the bond and the workpiece is likely to happen, which directly impacts the amount of heat generated during grinding. It also influences the cooling and lubricating efficiency, since more grinding fluid can be transported to the grinding zone. Furthermore, since more chip pockets are available, tool load is also less likely to occur;
- Lower cutting forces are achieved when a WED-dressed grinding wheel is applied. In this case, again, the more suitable grinding wheel topography reduces the grinding forces;

- Grinding wheel wear is also affected by the type of dressing method. Less wheel wear was measured using WED-dressed grinding wheels. The higher cooling and lubrication efficiency together with less bond friction creates a better cutting condition, having a positive impact in wheel wear. The diamonds are also less damaged by WEDD in comparison to SiC-dressing;
- The surface quality of ground  $\text{Si}_3\text{N}_4$  workpieces were similar when metal bonded grinding wheels conditioned with both dressing methods were used. Higher surface roughness was expected using WED-dressed grinding wheels, since it has a more open structure, with high grain protrusion, but only slightly higher values of  $R_a$  and  $R_z$  were measured. Concerning waviness height  $W_t$ , better results were achieved using WEDD.

It was also found that in electrical discharge dressing a concentration of discharges can occur around the diamonds (arcing-like phenomenon), causing large craters to be eroded around these abrasives. Even when a relative speed between tool electrode and workpiece is applied, this selective erosion occurs, which negatively impacts the topography of the grinding wheel. However, this effect is more evident for larger diamonds, such as D91 and D126, which anyway are already larger than the erosion gap, causing the diamonds to touch the tool electrode during dressing. Thus, electrical discharge dressing is more suitable for smaller diamonds.

To reduce non-productive time and minimize the negative effects of clamping errors, it is recommended to carry out dressing inside the grinding machine. Thus on-machine wire electrical discharge dressing is an important conditioning method, since conventional dressing with silicon carbide wheels inside the grinding machine is limited to non-complex shapes, such as a straight profile (A1A). Therefore, the achievable dressing material removal rate plays a decisive role in on-machine dressing. Moreover, dressing accuracy is very relevant, since “grinding is dressing”, i.e. grinding is significantly influenced by dressing. Concerning these aspects, the following can be stated:

- On-machine wire electrical discharge dressing using free stretched wires is not suitable. Poor dressing accuracy and low dressing material removal rates were achieved with this method. The free stretched wire can easily be deviated during dressing either by the cutting fluid/dielectric or by the air barrier which is formed around the grinding wheel. Deviations higher than 10  $\mu\text{m}$  were easily detected, which are not tolerated in a dressing process;
- The use of a special wire guide helps improve dressing performance. The proposed wire guide system is composed of a thin ceramic ring clamped between two flanges, and is responsible for guiding the wire at the erosion

zone and supplying dielectric to the dressing process. Since wire vibration is almost eliminated in this case, a stable erosion process can be carried out. As a consequence, higher dressing material removal rates were achieved as well as better dressing accuracy;

- The use of grinding oil for both grinding and erosion processes is suitable. Erosion material removal rates up to 100 mm<sup>3</sup>/min were achieved using a standard grinding oil type Blasogring HC5, allowing the dressing process to be carried out within a reduced time. This is an important prerequisite to enable an economical application of WEDD inside a grinding machine;
- Better dressing accuracy is achieved when lower dressing depth of cuts  $a_{ed}$  are applied and constant axial dressing feed rates  $v_{fad}$  are used, which are thus recommended in WEDD. In both cases, the influence of disturbances during erosion does not significantly affect the generated macro geometry of the grinding wheel. Controlled axial dressing feed rates and larger depth of dressing cuts are thus better suitable for profiling.

In-process dressing can also be carried out with the designed wire electrical discharge dressing unit, since it was mounted on the clamping system of an internal grinding spindle, and proved to be feasible. In this case, non-productive time can be further reduced in comparison to on-machine dressing, since dressing is carried out during grinding. In-process WED-dressing allows for keeping grinding forces more constant over time, since the grinding wheel is conditioned more frequently, using small dressing depth of cuts, so that the grinding wheel topography tends to change less during grinding. Hence, in-process WED-dressing opens another way for improving the dressability of metal bonded grinding wheels, showing real potential for future applications.

The influence of the relative speed between tool and workpiece electrodes was evaluated for wire electrical discharge machining. Single discharge experiments were carried out for relative speeds up to 80 m/s and the shape and volume of eroded craters were analyzed. According to the measured crater shapes it is possible to state that the plasma channel slides easily over the workpiece/anode. The crater shape extends along the relative speed direction and has a slightly reduction of its diameter perpendicular to it. The theoretical slip of the center point of the plasma channel can be measured and was found to match the theoretical slip, calculated based on the applied relative speed and discharge duration time. The crater radius expansion speed can also be indirectly measured based on the shape of eroded craters. It was found that for specific discharge parameters ( $I_{peak} = 73$  A,  $t_e = 1.25$   $\mu$ s) the crater expansion speed reaches approximately 40 m/s. Eroded crater volumes were found to be dependent on the applied relative speed. They increase as relative speed is increased, having a positive

impact on material removal rates. To help explain the influence of the relative speed on WEDM, an erosion model was proposed based on the heat conduction phenomenon. The finite-difference method was applied to solve the partial differential equation that describes heat conduction. The model was validated by comparing simulation and experimental results, where good correlation of results was found. Based on simulation results, it was found that the amount of nodal points that reached temperatures higher than the melting temperature of the workpiece material increased by increasing relative speed, being in accordance to experimental results. The calculated average temperature within the melting pool was also found to decrease by increasing relative speed, indicating that higher melting efficiencies can be reached when higher relative speeds are applied. In this case, heat is more efficiently used to warm up and melt more material, rather than to extra overheat the melting pool.

Regarding the above mentioned thermal model, it was found that the type of heat source used to describe the plasma channel and the way how material properties are considered play a decisive role in simulation results. In comparison to point and disc heat sources, a time-dependent heat source was found to be more suitable to predict the shape of eroded craters. Moreover, better simulation results were achieved when considering the material properties as temperature-dependent. In addition, the latent heats of fusion and vaporization have a significant influence on simulation results. Thus, to achieve a better correlation between simulation and experimental results, a time-dependent heat source has to be applied, while temperature-dependent material properties and the latent heats of fusion and vaporization must be considered.

The proposed thermal model was also used to calculate the constant axial dressing feed rate necessary in WED-sharpening. An erosion power factor of  $F_c = 0.35$  was applied to different simulations, i.e. it was considered that 35% of the available discharge energy is transmitted to the workpiece/anode. The material removal rate can thus be calculated based on the simulation of single discharges. Good correlation between experimental and simulation results was found. Therefore, the proposed method can be used to calculate the axial dressing feed rate based on different process inputs, such as the grinding wheel diameter and specification, dressing depth of cuts and erosion parameters, so that it is possible to reduce the amount of time-intensive experiments.

Diamond graphitization was also discussed in this work. The thermal model helped showing that thermal damages are not likely to occur to diamonds during WEDD. Some of the reasons why little or no thermal damage occurs to the diamonds during erosion, although high discharge temperatures are reached, are listed below:

- The discharge occurs on a “protected atmosphere”, without oxygen, surrounded by dielectric fluid. In this case, graphitization starts at higher temperatures, at approximately 1,800 K instead of around 1,000 K;
- Diamonds have a very high thermal conductivity, so that heat can be quickly dissipated throughout the whole diamond and does not stay locally concentrated as for other materials;
- High activation energies have to be overcome to transform diamond into graphite. Thus not only the temperature plays a role, but this specific amount of energy must be first achieved in order to start the graphitization process. The discharges applied in this work are very fast, with discharge duration lower than 2  $\mu$ s, also helping to avoid graphitization.

Based on all results achieved in this study, it can be stated that the WEDD technology, as a dressing method to be used directly inside the grinding machine, is suitable, flexible, effective and reliable, ensuring a significant improvement on the dressability of metal bonded diamond wheels. Thus, on-machine WEDD has huge potential for future industrial applications as an enabling technology for dressing metal bonded diamond wheels.

## 7.1 Outlook

Further work should first concentrate on on-machine WEDD of larger diamond grinding wheels. A real industrial application is only possible if this technology also works for larger grinding wheels. In this case, the way how the WEDD unit is integrated inside the grinding machine and thus how discharges are conducted to the erosion zone is determinant. High speed grinding (HSG) using metal bonded grinding wheels also find several applications in industry. Grinding speeds around 150 m/s are usually applied in HSG and WEDD should also be tested in this context. Moreover, WEDD should be tested for a wide variety of bond materials and efforts should focus on enabling this dressing technology to be applied to grinding wheels with larger abrasives (equivalent diameters greater than D91).

Since it was found that better dressing accuracies are achieved when small depth of dressing cuts and constant wire feed rates are used, further work should concentrate on whether dressing using only the grinding machine axes is possible. In this case, a simpler and cheaper WEDD unit may be designed, and even the whole EDM control system could be greatly simplified. Moreover, a smaller unit could be manufactured and easier integrated in different grinding machines. This would allow an easier integration of both EDM and grinding technologies. Fewer efforts would be necessary to guarantee a software integration, which would lead to a better acceptance by the customers. In



this case, a machine user would not need much knowledge of EDM to work with the WED-dressing system and even a conventional dressing cycle, which is already available in modern grinding machines, could be easily adapted to this new dressing technology (with only minor modifications).

In-process dressing should be further pushed, since it proved to be feasible using this WEDD technology. In this context, the wear rate of a certain grinding wheel used to grind a certain workpiece material, under specific grinding conditions has to be well known, so that during grinding, wear can be compensated and the topography of the grinding wheel can be kept more constant over time. Moreover, continuous dressing should be addressed, in which the grinding wheels is sharpened during the whole grinding process, aiming to improve grinding accuracy.

Regarding EDM modeling, efforts should be concentrated on a model that describes the plasma expansion in different liquids and/or gases. Thus, based on erosion inputs, workpiece and tool electrode materials, as well as on dielectric characteristics, one could predict the way how the plasma expands and thus better describe the heat source which is applied to predict the temperature distribution inside the workpiece and tool electrode. Today, this issue is still much based on experimental results and should be rather independent of an empirical method.

Further investigations should focus on the way how to better determine the erosion offset necessary to achieve increased wheel profile accuracies. In a standard erosion process, where the workpiece material is only composed of electrically conductive materials, the determination of an offset is much easier than in the case when grinding wheels are used, since the electrically non-conductive diamonds are kept protruding after dressing, which has to be taken into account when the offset is defined. Thus, different diamond sizes lead to different offsets, even though the bond material and erosion parameters are the same.

## References

- [3M2011] 3M. *Truing and Dressing Machines* [cited 2011 12/11/2011]; Available from: <http://solutions.3m.com>.
- [ATRU12] Atrump. *Diamond Wheel Truing and Dressing Machine*. . 2012 [cited 2012; Available from: [http://www.atrump.com/product\\_detail.php?lang=2&pro\\_id=218#specification](http://www.atrump.com/product_detail.php?lang=2&pro_id=218#specification).
- [BADG11] Badger, J., Murphy, S., O'Donnell, G., *The effect of wheel eccentricity and run-out on grinding forces, waviness, wheel wear and chatter*. International Journal of Machine Tools and Manufacture, 2011. 51(10–11): p. 766-774.
- [BART75] Bartell, E.W., Hockenberry, T.O., *The arcing phenomenon in electrical discharge machining EDM and its effects on the machining process*. Conference on Electrical Methods of Machining, Forming and Coating, 1975: p. 125-131.
- [BECK81a] Beck, J.V., *Transient temperatures in a semi-infinite cylinder heated by a disk heat source*. International Journal of Heat and Mass Transfer, 1981. 24(10): p. 1631-1640.
- [BECK81b] Beck, J.V., *Large time solutions for temperatures in a semi-infinite body with a disk heat source*. International Journal of Heat and Mass Transfer, 1981. 24(1): p. 155-164.
- [BEDR11] Bedra. *Funkenerosionsdraht, Erodierdraht*. 2011; Available from: <http://www.bedra.com/produkte/erodierdraht>.
- [BERM55] Berman, R., Simon, F., *On the graphite - diamond equilibrium*. Zeitschrift Fur Elektrochemie, 1955. 59(5): p. 333-338.

- [BRIN99] Brinksmeier, E., Heinzl, C., Wittmann, M., *Friction, Cooling and Lubrication in Grinding*. Annals of the CIRP, 1999. 48(2): p. 581-598.
- [CAI09] Cai, L.R., Jia, Y., Hu, D.J., *Dressing of metal-bonded superabrasive grinding wheels by means of mist-jetting electrical discharge technology*. Journal of Materials Processing Technology, 2009. 209(2): p. 779-784.
- [CARS05] Carslaw, H.S., Jaeger, J.C., *Conduction of heat in solids*, 2005: Clarendon Press.
- [CERA11] CeramTec. *Products Made of Advanced Ceramics*. 2011; Available from: <http://www.ceramtec.com/products/>.
- [CHEN00a] Chen, H., Li, J.C.M., *Anodic metal matrix removal rate in electrolytic in-process dressing I: Two-dimensional modeling*. Journal of Applied Physics, 2000. 87(6): p. 3151-3158.
- [CHEN00b] Chen, H., Li, J.C.M., *Anodic metal matrix removal rate in electrolytic in-process dressing II: Protrusion effect and three-dimensional modeling*. Journal of Applied Physics, 2000. 87(6): p. 3159-3164.
- [DAUW89] Dauw, D.F., Sthioul, H., Delpretti, R., Tricarico, C., *Wire Analysis and Control for Precision EDM Cutting*. Annals of the CIRP, 1989. 38(1): p. 191-194.
- [DAUW94] Dauw, D.F., Beltrami, I., *High-Precision Wire-EDM by Online Wire Positioning Control*. Annals of the CIRP, 1994. 43(1): p. 193-197.
- [DAVI72] Davies, G., Evans, T., *Graphitization of Diamond at Zero Pressure and at a High Pressure*. Proceedings of the Royal Society of London. Series A, Mathematical and Physical Sciences, 1972. 328(1574): p. 413-427.
- [DERK08] Derkx, J.M., Hoogstrate, A.M., Saurwalt, J.J., Karpuschewski, B., *Form crush dressing of diamond grinding wheels*. Annals of the CIRP, 2008. 57(1): p. 349-352.
- [DIAM09] Diametal. *Conditioning of diamond and CBN grinding wheels*. 2009; Available from: <http://www.diametal.ch>.
- [DIBI89] Dibitonto, D.D., Eubank, P.T., Patel, M.R., Barrufet, M.A., *Theoretical-models of the electrical-discharge machining process .1. A simple cathode erosion model*. Journal of Applied Physics, 1989. 66(9): p. 4095-4103.

- [DOLD11] Dold, C., Transchel, R., Rabiey, M., Langenstein, P., Jaeger, C., Pude, F., Kuster, F., Wegener, K., *A study on laser touch dressing of electroplated diamond wheels using pulsed picosecond laser sources*. Annals of the CIRP, 2011. 60(1): p. 363-366.
- [EBBR00] Ebbrell, S., Woolley, N.H., Tridimas, Y.D., Allanson, D.R., Rowe, W.B., *The effects of cutting fluid application methods on the grinding process*. International Journal of Machine Tools and Manufacture, 2000. 40(2): p. 209-223.
- [ELEM12] ElementSix. *Synthetic diamond's extreme properties*. 2012 [cited 2012; Available from: <http://www.e6.com>].
- [FIEB09] Fiebelkorn, F., *EDM-Abriechtechnologie*, 2009: Annex to CTI-Proposal (WEDD-dressing). p. 8.
- [FIEL79] Field, J.E., *The Properties of diamond*. Vol. 14. 1979: Academic Press. 674.
- [FILI05] Filik, J., *Raman spectroscopy: a simple, non-destructive way to characterise diamond and diamond-like materials*. Spectroscopy Europe, 2005. 17(5): p. 10-17.
- [GATH83] Gathers, G.R., *Thermophysical properties of liquid copper and aluminum*. International Journal of Thermophysics|International Journal of Thermophysics, 1983. 4(3): p. 209-26.
- [GFAC06] GF-AgieCharmiles, ed. *Agiecut Agievision 5 - Equipament Manual C*. 2006.
- [GHOS07] Ghosh, A., Chattopadhyay, A.K., *Experimental investigation on performance of touch-dressed single-layer brazed cBN wheels*. International Journal of Machine Tools and Manufacture, 2007. 47(7-8): p. 1206-1213.
- [GINZ04] Ginzl, J., Behrens, A., Wulfsberg, J.P., *Technology development for EDM using statistical analysis of arcing information*. Journal of Materials Processing Technology, 2004. 149(1-3): p. 232-237.
- [GRIM99] Grimvall, G., *Thermal conductivity*, in *Thermophysical Properties of Materials*. 1999. North Holland: Amsterdam. p. 255-285.

- [HADD08a] Haddad, M.J., Fadaei Tehrani, A., *Material removal rate (MRR) study in the cylindrical wire electrical discharge turning (CWEDT) process*. Journal of Materials Processing Technology, 2008. 199(1-3): p. 369-378.
- [HADD08b] Haddad, M.J., Tehrani, A.F., *Investigation of cylindrical wire electrical discharge turning (CWEDT) of AISI D3 tool steel based on statistical analysis*. Journal of Materials Processing Technology, 2008. 198(1-3): p. 77-85.
- [HOLZ88] HOLZ, R., SAUREN, J., *Schleifen mit Diamant und CBN. Winter Diamantwerkzeuge Bornitridwerkzeuge*. 1988.
- [HOSO06] Hosokawa, A., Ueda, T., Yunoki, T., *Laser dressing of metal bonded diamond wheel*. Annals of the CIRP, 2006. 55(1): p. 329-332.
- [HUAN03] Huang, H., Liu, Y.C., *Experimental investigations of machining characteristics and removal mechanisms of advanced ceramics in high speed deep grinding*. International Journal of Machine Tools and Manufacture, 2003. 43(8): p. 811-823.
- [LIDA88] Iida, T., *The physical properties of liquid metals*. Oxford science publications., ed. Guthrie, R.I.L.1988. Oxford : New York :: Clarendon Press ; Oxford University Press.
- [INCR06] Incropera, F., DeWitt, D., Bergman, T., Lavine, A., *Fundamentals of Heat and Mass Transfer*, 2006: Wiley.
- [INFI11] InfiniteFocus. *InfiniteFocus for form and roughness measurement*. 2011 [cited 2011 23/11/2011]; Available from: <http://www.alicon.com/>.
- [IWAI01] Iwai, M., Ichinose, M., Qun, H.B., Takeuchi, K., Uematsu, T., Suzuki, K. *Application of fluid-free EDM to on - machine trueing/dressing for superabrasive grinding wheels*. in *13th International Symposium on ElectroMachining (ISEM)*. 2001. Bilbao, Spain.
- [JENN84] Jennes, M., Snoeys, R., Dekeyser, W., *Comparison of Various Approaches to Model the Thermal Load on the EDM-Wire Electrode*. Annals of the CIRP, 1984. 33(1): p. 93-98.
- [JOSH10] Joshi, S.N., Pande, S.S., *Thermo-physical modeling of die-sinking EDM process*. Journal of Manufacturing Processes, 2010. 12(1): p. 45-56.
- [KLIN09] Klink, A., *Funkerosives und elektrochemisches Abrichten feinkörniger Schleifwerkzeuge*. Mechanical engineering, 2009: p. 141.

- [KLIN10] Klink, A., *Wire electro discharge trueing and dressing of fine grinding wheels*. Annals of the CIRP, 2010. 59(1): p. 235-238.
- [KLOC05] Klocke, F., *Fertigungsverfahren*, 2005: Springer-Verlag Berlin Heidelberg.
- [KLOC07a] Klocke, F., Brinksmeier, E., Riemer, O., Klink, A., Schulte, H., Sarikaya, H., *Manufacturing structured tool inserts for precision glass moulding with a combination of diamond grinding and abrasive polishing*. Industrial Diamond Review 2007. 4(1): p. 65-69.
- [KLOC07b] Klocke, F., Klink, A., Kamenzky, S., *Electro discharge dressing of fine grained metal bonded grinding wheels*. Proceedings of the 15th International Symposium on Electromachining, 2007: p. 153-158.
- [KLOC07c] Klocke, F., Klink, A., Schneider, U., Grüntzig, A. *EDM and ECM Dressing of Fine Grained Bronze-Bonded Diamond Grinding Wheel Layers*. in *7th Euspen International Conference*. 2007. Bremen, Germany.
- [KLOC07d] Klocke, F., König, W., *Funkenerosives Abtragen (EDM) - Fertigungsverfahren 3*, 2007. Springer Berlin Heidelberg. p. 3-126.
- [KLOC09a] Klocke, F., Kuchie, A., *The Machinability of Various Materials*, in *Manufacturing Processes 2 - Grinding, Honing, Lapping*. Klocke, F., Editor 2009. Springer Berlin Heidelberg. p. 73-111.
- [KLOC09b] Klocke, F., Kuchie, A., *Grinding*, in *Manufacturing Processes 2 - Grinding, Honing, Lapping*. Klocke, F., Editor 2009. Springer Berlin Heidelberg. p. 135-300.
- [KLOC09c] Klocke, F., Kuchie, A., *Structure and Composition of Grinding Sheels*, in *Manufacturing Processes 2 - Grinding, Honing, Lapping*. Klocke, F., Editor 2009. Springer Berlin Heidelberg. p. 1-55.
- [KLOC09d] Klocke, F., *Manufacturing Processes 2 - Grinding, honing, lapping*. RWTH edition, ed. Klocke, F.2009: Springer.
- [KOEN94] Koenig, W., Schulz, A., *Abrichten von CBN-Schleifscheiben mit Diamantformrollen*, in *Industrie Diamant Rundschau*1994. p. 7.
- [KRAM99] Kramer, D., Rehsteiner, F., Schumacher, B., *ECD (Electrochemical In-Process Controlled Dressing), a New Method for Grinding of Modern High-Performance Cutting Materials to Highest Quality*. Annals of the CIRP, 1999. 48(1): p. 265-268.

- [KUNI90] Kunieda, M., Kojima, H., Kinoshita, N., *On-Line Detection of EDM Spark Locations by Multiple Connection of Branched Electric Wires*. Annals of the CIRP, 1990. 39(1): p. 171-174.
- [KUNI05] Kunieda, M., Lauwers, B., Rajurkar, K.P., Schumacher, B.M., *Advancing EDM through Fundamental Insight into the Process*. Annals of the CIRP, 2005. Volume 54(Issue 2): p. 64-87.
- [KUNI10] Kunieda, M., Kameyama, A., *Study on decreasing tool wear in EDM due to arc spots sliding on electrodes*. Precision Engineering, 2010. 34(3): p. 546-553.
- [LAUW07] Lauwers, B.K., J. P.; Brans, K., *Development of Technology and Strategies for the Machining of Ceramic Components by Sinking and Milling EDM*. Annals of the CIRP, 2007. 56(1): p. 225-228.
- [LAZA43] Lazarenko, B.R., *To invert the effect of wear on electric power contacts*. 1943. PhD Thesis.
- [LEE00a] Lee, E.S., *Surface characteristics in the precision grinding of Mn-Zn ferrite with in-process electro-discharge dressing*. Journal of Materials Processing Technology, 2000. 104(3): p. 215-225.
- [LEE00b] Lee, K.W., Wong, P.K., Zhang, J.H., *Study on the grinding of advanced ceramics with slotted diamond wheels*. Journal of Materials Processing Technology, 2000. 100(1-3): p. 230-235.
- [LIAN01] Liang, Y.D., S. P., *Application trend in advanced ceramic technologies*. Technovation, 2001. 21(1): p. 61-65.
- [LIM02] Lim, H.S., Fathima, K., Senthil Kumar, A., Rahman, M., *A fundamental study on the mechanism of electrolytic in-process dressing (ELID) grinding*. International Journal of Machine Tools and Manufacture, 2002. 42(8): p. 935-943.
- [LIN08] Lin, C.-S., Yang, Y.-L., Lin, S.-T., *Performances of metal-bond diamond tools in grinding alumina*. Journal of Materials Processing Technology, 2008. 201(1-3): p. 612-617.
- [MADI96] Madison, J., *CNC Machining Handbook: Basic Theory, Production Data, and Machining Procedure*, 1996. New York: Industrial Press INc. 400.

- [MARA06] Marafona, J., Chousal, J.A.G., *A finite element model of EDM based on the Joule effect*. International Journal of Machine Tools and Manufacture, 2006. 46(6): p. 595-602.
- [MASU85] Masuzawa, T., Fujino, M., Kobayashi, K., Suzuki, T., Kinoshita, N., *Wire Electro-Discharge Grinding for Micro-Machining*. Annals of the CIRP, 1985. 34(1): p. 431-434.
- [MASU05] Masuzawa, T., Yamaguchi, M., Fujino, M., *Surface finishing of micropins produced by WEDG*. Annals of the CIRP, 2005. 54(1): p. 171-174.
- [MATO08] Matorian, P., Sulaiman, S., Ahmad, M.M.H.M., *An experimental study for optimization of electrical discharge turning (EDT) process*. Journal of Materials Processing Technology, 2008. 204(1-3): p. 350-356.
- [MOHA08] Mohammadi, A., Tehrani, A.F., Emanian, E., Karimi, D., *Statistical analysis of wire electrical discharge turning on material removal rate*. Journal of Materials Processing Technology, 2008. 205(1-3): p. 283-289.
- [NAGA12] Nagase-Integrex. *Nagase-i General Catalogue*. 2012 [cited 2012; Available from: <http://www.nagase-i.jp/pdf/catalog-e.pdf>].
- [NOIC12] Noichl, H., *Hochleistungsschleifen von Hartmetall, neue Generation von metallisch gebundenen Diamantschleifscheiben*, in *9. Moderne Schleiftechnologie und Feinstbearbeitung 2012* 2012: Stuttgart - Germany. p. (14-1)-(14-16).
- [OHMO90] Ohmori, H., Nakagawa, T., *Mirror Surface Grinding of Silicon Wafers with Electrolytic In-Process Dressing*. Annals of the CIRP, 1990. 39(1): p. 329-332.
- [OHMO96] Ohmori, H., Takahashi, I., Bandyopadhyay, B.P., *Highly efficient grinding of ceramic parts by electrolytic in-process dressing (ELID) grinding*. Materials and Manufacturing Processes, 1996. 11(1): p. 31-44.
- [OHMO97] Ohmori, H., Nakagawa, T., *Utilization of Nonlinear Conditions in Precision Grinding with ELID (Electrolytic In-Process Dressing) for Fabrication of Hard Material Components*. Annals of the CIRP, 1997. 46(1): p. 261-264.
- [OHMO00] Ohmori, H., Li, W., Makinouchi, A., Bandyopadhyay, B.P., *Efficient and precision grinding of small hard and brittle cylindrical parts by the centerless grinding process combined with electro-discharge truing and*



- electrolytic in-process dressing*. Journal of Materials Processing Technology, 2000. 98(3): p. 322-327.
- [OHMO07] Ohmori, H., Katahira, K., Naruse, T., Uehara, Y., Nakao, A., Mizutani, M., *Microscopic Grinding Effects on Fabrication of Ultra-fine Micro Tools*. Annals of the CIRP, 2007. 56(1): p. 569-572.
- [OLIV10] Oliveira, J.F.G., Bottene, A.C., França, T.V., *A novel dressing technique for texturing of ground surfaces*. Annals of the CIRP, 2010. 59(1): p. 361-364.
- [PAND86] Pandey, P.C., Jilani, S.T., *Plasma channel growth and the resolidified layer in edm*. Precision Engineering, 1986. 8(2): p. 104-110.
- [PARK06] Parker, K., *Advanced ceramics soar to new heights: Advantageous physical properties help these inorganic, nonmetallic materials expand their usage into the manufacture of critical aerospace components*. Metal Finishing, 2006. 104(3): p. 16-18.
- [PATE89] Patel, M.R., Barrufet, M.A., Eubank, P.T., Dibitonto, D.D., *Theoretical-models of the electrical-discharge machining process .2. The anode erosion model*. Journal of Applied Physics, 1989. 66(9): p. 4104-4111.
- [PINT08] Pinto, F.W., Vargas, G.E., Wegener, K., *Simulation for optimizing grain pattern on Engineered Grinding Tools*. Annals of the CIRP, 2008. 57(1): p. 353-356.
- [PIOT07] Piotr, S., *Grinding forces in regular surface texture generation*. International Journal of Machine Tools and Manufacture, 2007. 47(14): p. 2098-2110.
- [RABI11] Rabiey, M., Walter, C., Kuster, F., Stirnimann, J., Pude, F., Wegener, K. *A comparative study on the dressing of hybrid bond CBN wheels using a conventional SiC dressing wheel and a short-pulse fiber laser*. in *Proceedings of the 11th International Conference on Management of Innovative Technologies and 2nd International Conference on Sustainable Life in Manufacturing*. 2011. Fiesca, Slovenia.
- [RAHM09] Rahman, M., Kumar, A.S., Biswas, I., *A review of electrolytic in-process dressing (ELID) grinding*. Key Engineering Materials, 2009. 404: p. 45-59.
- [RHON02a] Rhoney, B.K., Shih, A.J., Scattergood, R.O., Akemon, J.L., Gust, D.J., Grant, M.B., *Wire electrical discharge machining of metal bond diamond*

- wheels for ceramic grinding*. International Journal of Machine Tools and Manufacture, 2002. 42(12): p. 1355-1362.
- [RHON02b] Rhoney, B.K., Shih, A.J., Scattergood, R.O., Ott, R., McSpadden, S.B., *Wear mechanism of metal bond diamond wheels trued by wire electrical discharge machining*. Wear, 2002. 252(7-8): p. 644-653.
- [RODE09] Rödel, J., Kounga, A.B.N., Weissenberger-Eibl, M., Koch, D., Bierwisch, A., Rossner, W., Hoffmann, M.J., Danzer, R., Schneider, G., *Development of a roadmap for advanced ceramics: 2010–2025*. Journal of the European Ceramic Society, 2009. 29(9): p. 1549-1560.
- [SANC08] Sanchez, J.A., Pombo, I., Cabanes, I., Ortiz, R., Lopez de Lacalle, L.N., *Electrical discharge truing of metal-bonded CBN wheels using single-point electrode*. International Journal of Machine Tools and Manufacture, 2008. 48(3-4): p. 362-370.
- [SCHO01a] Schopf, M., Beltrami, I., Boccadoro, M., Kramer, D., *ECDM (Electro Chemical Discharge Machining), a new method for trueing and dressing of metal-bonded diamond grinding tools*. Annals of the CIRP, 2001. 50(1): p. 125-128.
- [SCHO01b] Schöpf, M., *Electro Chemical Discharge Machining (ECDM): Neue Möglichkeit zum Abrichten metallgebundener Diamantschleifscheiben*. Department of Mechanical and Process Engineering, 2001. PhD.: p. 129.
- [SEAL92] Seal, M., *Applications exploiting the extreme properties of diamonds*. Materials Science and Engineering: B, 1992. 11(1-4): p. 167-171.
- [SHEN01] Shen, J.Y., Xu, X.P., Lin, B., Xu, Y.S., *Lap-grinding of Al<sub>2</sub>O<sub>3</sub> ceramics assisted by water-jet dressing metal bond diamond wheel*, in *Advances in Abrasive Processes*. Xu, X.P.S.J.Y.L.Y., Editor 2001. p. 171-176.
- [SPUR93] Spur, G., Schönbeck, J., *Anode Erosion in Wire-EDM - A Theoretical Model*. Annals of the CIRP, 1993. 42(1): p. 253-256.
- [STET74] Stetiu, G., Lal, G.K., *WEAR OF GRINDING WHEELS*. Wear, 1974. 30(2): p. 229-236.
- [STUD11] Studer. *S31 – The Versatile for big tasks*. 2011; Available from: <http://www.studer.com/en/products/universal/s31.html>.
- [SUDI08] Sudiarso, A., Atkinson, J., *In-process electrical dressing of metal-bonded diamond grinding wheels*. Engineering Letters, 2008. 16(3): p. 308-310.

- [SUZU87] Suzuki, K., Uematsu, T., Nakagawa, T., *On-Machine Trueing/Dressing of Metal Bond Grinding Wheels by Electro-Discharge Machining*. Annals of the CIRP, 1987. 36(1): p. 115-118.
- [SUZU04] Suzuki, K., Iwai, M., Uematsu, T., Sharma, A., *Development of a grinding wheel with electrically conductive diamond cutting edges*. Advances in Abrasive Technology Vi, 2004. 257-258: p. 239-244.
- [SUZU05] Suzuki, K., Ninomiya, S., Iwai, M., Tanaka, Y., Murakami, Y., San, S., Tanaka, K., Uematsu, T., *Attempt of electrodischarge grinding with an electrically conductive diamond-cutting-edge wheel*. Advances in Abrasive Technology Viii, 2005. 291-292: p. 63-66.
- [TAN10] Tan, P.C., Yeo, S.H., *Modeling of Recast Layer in Micro-Electrical Discharge Machining*. Journal of Manufacturing Science and Engineering, 2010. 132(3): p. 031001.
- [TARI82] Tariq Jilani, S., Pandey, P.C., *Analysis and modelling of edm parameters*. Precision Engineering, 1982. 4(4): p. 215-221.
- [TARI83] Tariq Jilani, S., Pandey, P.C., *An analysis of surface erosion in electrical discharge machining*. Wear, 1983. 84(3): p. 275-284.
- [TONS00] Tönshoff, H.K., Friemuth, T., *In-process dressing of fine diamond wheels for tool grinding*. Precision Engineering, 2000. 24(1): p. 58-61.
- [UEMA99] Uematsu, T., Iwai, M., Funazawa, T., Takeuchi, K., Suzuki, K., *On Machine Fluid-free Electro Discharge trueing/dressing Method for Superabrasive Wheels*, in *Third International Conference on Abrasive Technology* 1999: Brisbane, Australia. p. 258-265.
- [UHLM05] Uhlmann, E., Piltz, S., Jerzembeck, S., *Micro-machining of cylindrical parts by electrical discharge grinding*. Journal of Materials Processing Technology, 2005. 160(1): p. 15-23.
- [VAN74] Van Dijck, F.S., Dutré, W.L., *Heat conduction model for the calculation of the volume of molten metal in electric discharges*. Journal of Physics D: Applied Physics, 1974. 7(6): p. 899.
- [VAN07] Van Elsen, M., Baelmans, M., Mercelis, P., Kruth, J.P., *Solutions for modelling moving heat sources in a semi-infinite medium and applications to laser material processing*. International Journal of Heat and Mass Transfer, 2007. 50(23-24): p. 4872-4882.

- [VAND74] Vandijck, F.S., Dutre, W.L., *Heat-conduction model for calculation of volume of molten-metal in electric discharges*. Journal of Physics D-Applied Physics, 1974. 7(6): p. 899-910.
- [VDI94] VDI3321, *Optimization of cutting - basics*, Ingenieure, V.D., Editor 1994. p. 16.
- [VDI07] VDI3392, *Trueing and dressing of grinding wheels - Profiling and sharpening*, 2007, VEREIN DEUTSCHERINGENIEURE. p. 35.
- [VDI75] VDI-Richtlinien, *VDI 3400 - Electrical Discharge Machining (DEM) - Definitions, processes, application.*, 1975.
- [WALT12] Walter, C., Rabiey, M., Warhanek, M., Jochum, N., Wegener, K., *Dressing and truing of hybrid bonded CBN grinding tools using a short-pulsed fibre laser*. Annals of the CIRP, 2012. 61(1): p. 279-282.
- [WANG96] Wang, X.K., Ying, B.G., Liu, W.G., *EDM dressing of fine grain super abrasive grinding wheel*. Journal of Materials Processing Technology, 1996. 62(4): p. 299-302.
- [WANG07] Wang, X.Y., Kang, R.K., Xu, W.J., Wang, L.J., Guo, D.M., *Modeling of laser dressing for metal-bond diamond grinding wheel*. Key Engineering Materials, 2007. 329.
- [WANG06] Wang, Y., Zhou, X.J., Hu, D.J., *An experimental investigation of dry-electrical discharge assisted truing and dressing of metal bonded diamond wheel*. International Journal of Machine Tools & Manufacture, 2006. 46(3-4): p. 333-342.
- [WEGE11] Wegener, K., Hoffmeister, H.W., Karpuschewski, B., Kuster, F., Hahmann, W.C., Rabiey, M., *Conditioning and monitoring of grinding wheels*. Annals of the CIRP, 2011. 60(2): p. 757-777.
- [WEIN10a] Weingartner, E., Jaumann, S., Kuster, F., Boccadoro, M., *Special wire guide for on-machine wire electrical discharge dressing of metal bonded grinding wheels*. Annals of the CIRP, 2010. 59(1): p. 227-230.
- [WEIN10b] Weingartner, E., Jaumann, S., Kuster, F., Wegener, K., *On-machine wire electrical discharge dressing (WEDD) of metal-bonded grinding wheels*. International Journal of Advanced Manufacturing Technology, 2010. 49(9-12): p. 1001-1007.

- [WEIN12a] Weingärtner, E., Wegener, K., Kuster, F., *Wire electrical discharge machining applied to high-speed rotating workpieces*. Journal of Materials Processing Technology, 2012. 212(6): p. 1298-1304.
- [WEIN12b] Weingärtner, E., Kuster, F., Wegener, K., *Modeling and simulation of electrical discharge machining*. Procedia CIRP, 2012. 2(0): p. 74-78.
- [WEIN12c] Weingärtner, E., Wegener, K., Kuster, F., *Applying Wire Electrical Discharge Dressing (Wedd) to Improve Grinding Performance of Metal Bounded Diamond Wheels*. Procedia CIRP, 2012. 1(0): p. 365-370.
- [WIMM95] Wimmer, J., *Konditionieren hochharter Schleifscheiben zum Schleifen von Hochleistungskeramik*. PhD-thesis 1995.
- [YEO07] Yeo, S.H., Kurnia, W., Tan, P.C., *Electro-thermal modelling of anode and cathode in micro-EDM*. Journal of Physics D: Applied Physics, 2007. 40(8): p. 2513.
- [YEO08] Yeo, S.H., Kurnia, W., Tan, P.C., *Critical assessment and numerical comparison of electro-thermal models in EDM*. Journal of Materials Processing Technology, 2008. 203(1-3): p. 241-251.